Carbon-Rich SiCN/SiOC Ceramics as Sulfur Cathode Supports in Lithium Sulfur Batteries

TECHNISCHE
UNIVERSITÄT
DARMSTADT

Disperse
Feststoffe

Carbon-Rich SiCN/SiOC Ceramics as Sulfur Cathode Supports in Lithium Sulfur Batteries

Kohlenstoffreiche SiCN/SiOC-Keramiken als Schwefelkathodenträger in Lithium-Schwefel-Batterien

Genehmigte kumulative Dissertation von M.Sc. Fangmu Qu aus Shanxi, China

Fachbereich Material- und Geowissenschaften

Darmstadt, Technische Universität Darmstadt

Jahr der Veröffentlichung der Dissertation auf TUprints: 2024

URN: urn:nbn:de:tuda-tuprints-274900

1. Gutachten: Prof. Dr. Ralf Riedel

2. Gutachten: Prof. Dr. Jan Phillip Hofmann

Tag der Einreichung: 29.02.2024

Tag der mündlichen Prüfung: 08.05.2024

Erklärungen laut Promotionsordnung

§8 Abs. 1 lit. c PromO

Ich versichere hiermit, dass die elektronische Version meiner Dissertation mit der schriftlichen Version übereinstimmt.

§8 Abs. 1 lit. d PromO

Ich versichere hiermit, dass zu einem vorherigen Zeitpunkt noch keine Promotion versucht wurde. In diesem Fall sind nähere Angaben über Zeitpunkt, Hochschule, Dissertationsthema und Ergebnis dieses Versuchs mitzuteilen.

§9 Abs. 1 PromO

Ich versichere hiermit, dass die vorliegende Dissertation selbstständig und nur unter Verwendung der angegebenen Quellen verfasst wurde.

§9 Abs. 2 PromO

Die Arbeit hat bisher noch nicht zu Prüfungszwecken gedient.

Darmstadt, den

_____

(Fangmu Qu)

The present cumulative dissertation summarizes the essential scientific findings reported to the scientific community in the following peer-reviewed articles. Article reprints (1-5) are enclosed in the Chapter Publications at the end of this work.

(1) **F. Qu**, M. Graczyk-Zajac*, D. Vrankovic, N. Chai, Z. Yu*, R. Riedel, Effect of morphology of C-rich silicon carbonitride ceramic on electrochemical properties of sulfur cathode for Li-S battery. *Electrochimica Acta* **384** 138265 (2021). DOI: 10.1016/j.electacta.2021.138265

(2) **F. Qu***, Z. Yu*, M. Krol, N. Chai, R. Riedel, M. Graczyk-Zajac, Electrochemical Performance of Carbon-Rich Silicon Carbonitride Ceramic as Support for Sulfur Cathode in Lithium Sulfur Battery. *Nanomaterials* **12** 1283 (2022). DOI: 10.3390/nano12081283

(3) Q. Wen*[&], **F. Qu**[&], Z. Yu*, M. Graczyk-Zajac, X. Xiong, R. Riedel, Si-based polymer-derived ceramics for energy conversion and storage. *Journal of Advanced Ceramics* **11** 197-246 (2022). DOI: 10.1007/s40145-021-0562-2

(4) A. Zambotti, **F. Qu***, G. Costa, M. Graczyk-Zajac, G.D. Sorarù, Polymer-Derived Ceramic Aerogels to Immobilize Sulfur for Li-S Batteries. *Energy Technology* **11** 2300488 (2023). DOI: 10.1002/ente.202300488

(5) **F. Qu***, Z. Yu*, M. Widenmeyer, C. Tian, R. Yan, H. Tian, A. Kempf, D.M. De Carolis, J.P. Hofmann, A. Weidenkaff, R. Riedel, M. Graczyk-Zajac, In-situ formed porous silicon carbonitride/boron nitride composites to boost cathode performance in lithium sulfur batteries. *Journal of Alloys and Compounds* **984** 174021 (2024). DOI: 10.1016/j.jallcom.2024.174021

Acknowledgments

How time flies! Four years of doctoral studies are fleeting. There are pains and happiness. Looking back on the past, they are all vivid. Over the past four years, with the great help, support and encouragement of my supervisors, friends, and families, I have completed the related work of this dissertation.

First and foremost, I would like to express my deepest appreciation and respect to Prof. Dr. Ralf Riedel who gave me a precious opportunity to work in this group. As my supervisor, he is not only a knowledgeable scholar, but also a life mentor and a good friend. With his continuous support, constructive feedback, and warm encouragements, I am encouraged for the scientific exploration and full of confidence in future work.

I would also like to express my special gratitude to Dr. Magdalena Graczyk-Zajac who always provides support for me. From the demonstration of the topic to the design and implementation of the experiment, and to the discussion of the results as well as further optimization of the experiment, she has been a huge help to me. Thanks to her constant encouragement, I have obtained a more positive attitude for the scientific research and normal life.

I would like to pay my special regards to Prof. Dr. Zhaoju Yu who provides great help for me to have the precious opportunity for studying here. She also gave me a lot of scientific suggestions for my work and keeps encouraging me. Besides, she also provided great help for the creation, revision, and publication of my papers.

I also sincerely thank Prof. Xinmin Liu and Prof. Qingbo Wen for the guidance and help for my experiments. They are the role models for me to keep striving. I am very grateful to Nan Chai for teaching me to perform the Raman spectrometer, element analysis and battery testing, providing advice for my work, and encouraging me in my toughest times. I would like to thank Dario De Carolis for training me to prepare XRD samples and teaching me how to make the Raman and SEM measurements better. Moreover, he is also a very trustworthy good friend in life for me.

I would like to sincerely acknowledge Dr. Dragoljub Vrankovic, Claudia Fasel, Alexander Kempf, Kiefer Samira, Ying Zhan and Mirijam Lederer for their technical support. Many special thanks must be extended to my colleagues. Thanks to Fangtong Xie for being a great

Fangmu Qu (璩方沐)

Darmstadt, February 2024

Abstract

As one of the promising candidates for future energy storage, lithium sulfur batteries have attracted much attention due to their superior energy density and low production cost as compared with that of conventional Li ion batteries. However, the obstacles such as insulated nature, volume expansion and "shuttle effect" significantly hamper the practical commercial application of lithium sulfur batteries. Designing and building novel sulfur cathodes with conductive micro-nanostructure is one of the potential ways to solve the issues of lithium sulfur batteries. C-rich ceramic matrices provide an ideal conductive skeleton for the sulfur host due to their electronic conductivity and robust, stress accommodating mechanical properties. This dissertation presents facile and cost-effective methods for the preparation of C-rich silicon carbonitride (SiCN) ceramics, Silicon oxycarbide (SiOC) ceramics and SiCN-boron nitride (SiCN-BN) composites to be utilized as sulfur host materials for the cathode in lithium sulfur batteries to enhance their electrochemical performance.

First of all, porous C-rich SiCN ceramic matrices were synthesized by crosslinking of silicon-based polymers and subsequent pyrolysis in a temperature range between 1000 °C and 1600 °C under argon. Through the melting-diffusion technique at 155 °C, sulfur was successfully embedded in the obtained porous ceramic matrices. After the characterization and performance testing, the impact of the initial porosity and elemental composition of the SiCN ceramics on the electrochemical performance of SiCN-S composites is addressed. It is shown that the material pyrolyzed at 1000 °C reveals a mesoporous character in line with the presence of a free carbon phase dispersed in the SiCN matrix and demonstrates the best electrochemical stability and the highest capacity (more than 310 mAh/g over 40 cycles) at a high sulfur content of 66 wt.%.

To investigate the electrochemical performance of the C-rich SiCN ceramics pyrolyzed at a relatively low temperature window compared with the first work, sulfur-containing C-rich SiCN composites were processed from SiCN ceramics which were synthesized at temperatures between 800 °C and 1100 °C. The obtained results reveal that a combination of the mesoporous character of SiCN and the presence of a disordered free carbon phase makes the electrochemical performance of the SiCN matrix obtained at 900 °C superior to that of SiCN synthesized at lower and higher temperatures. A capacity value of more than 195 mAh/g over 50 cycles at a high sulfur content of 66 wt.% is achieved.

Then, we further studied the electrochemical performance of three distinct sulfur/PDC cathodes. In two of these cathodes, sulfur is incorporated into PDC aerogels based on the SiOC and SiCN systems, utilizing CO_2 supercritical drying. In the third cathode, sulfur is confined within a mesoporous SiOC produced through the "polymeric spacer" method. The composite cathodes underwent electrochemical characterization, and their performances were analyzed and correlated with the chemical composition and microstructure of the obtained PDC scaffold.

In order to achieve further enhancement of the electrochemical performance of C-rich SiCN ceramic used as sulfur hosts, boron nitride was confined in the SiCN matrix. The SiCN-BN composites were synthesized via annealing mixtures comprised of C-rich SiCN ceramic powder, boric acid and urea at different temperatures (950 °C, 1100 °C, and 1250 °C). The sample SiCN-BN-950/S especially presents 445 mAh/g of the reversible capacity and 62 % of the capacity retention after 60 cycles under 3.5 ~ 3.8 mg/cm^2 of areal density and 66 wt.% of sulfur loading. The excellent cycling stability is attributed to the remarkable synergistic effect of BN and C-rich SiCN ceramic matrix.

The obtained results demonstrate that C-rich SiCN/SiOC ceramics are indeed promising hosts for sulfur as the cathode in lithium sulfur batteries for enhancing their electrochemical performance. Besides, this work also presents facile, cost controllable and efficient synthesis routes for sulfur cathodes in LSB which is suitable for large-scale industrial production, as well as a reference for the utilization of ceramic materials in energy storage systems.

Zusammenfassung

Als eines der vielversprechenden Kandidaten für die zukünftige Energiespeicherung haben Lithium-Schwefel-Batterien seit ihrer Erfindung aufgrund ihrer überlegenen Energiedichte und niedrigen Produktionskosten viel Aufmerksamkeit auf sich gezogen. Die Hindernisse wie die isolierende Natur, die Volumenausdehnung und der "Shuttle-Effekt" behindern jedoch signifikant die praktische kommerzielle Anwendung von Lithium-Schwefel-Batterien. Das Entwerfen und Bauen eines neuartigen Schwefel-Wirtes mit leitfähiger Mikro-Nanostruktur in der Kathode ist ein potenzieller Weg, um die Probleme der Lithium-Schwefel-Batterien zu lösen. C-reiche keramische Matrices stellen aufgrund ihrer elektrischen Leitfähigkeit und robusten, belastbaren mechanischen Eigenschaften ideale Skelettmaterialien für den Schwefel-Wirt dar. Diese Dissertation präsentiert einfache und kosteneffektive Methoden zur Herstellung C-reicher SiCN/SiOC-Keramiken und SiCN-BN-Kompositen als Schwefel-Wirtsmaterialien für die Kathode in Lithium-Schwefel-Batterien mit verbesserter elektrochemischer Leistung.

Zunächst wurden poröse C-reiche SiCN-Keramikmatrices durch Vernetzung eines Si-Polymers und anschließende Pyrolyse im Temperaturbereich zwischen 1000 °C und 1600 °C unter Argon synthetisiert. Über eine Schmelz-Diffusions-Technik wurde Schwefel bei 155 °C in die Poren der SiCN-Keramik erfolgreich infiltriert. Nach Charakterisierung und Leistungstest wird der Einfluss der Anfangsporosität und elementaren Zusammensetzung der SiCN-Keramik auf die elektrochemische Leistung der SiCN-S-Komposite diskutiert. Demzufolge, zeigt das bei 1000 °C pyrolysierte Material Mesoporosität auf. Aufgrund der in SiCN dispergierten und in-situ gebildeten freien Kohlenstoffphase, weist das Material die beste elektrochemische Stabilität und die höchste Kapazität (mehr als 310 mAh/g über 40 Zyklen) bei einem hohen Schwefelgehalt von 66 Gew.-% auf.

Als Nächstes untersuchten wir das elektrochemische Verhalten der bei relativ niedrigen Temperaturen pyrolisierten C-reichen SiCN-Keramiken. Hierzu wurden C-reiche SiCN-Komposite bei Temperaturen von 800 °C bis 1100 °C synthetisiert. Die erhaltenen Ergebnisse der mit Schwefel gefüllten SiCN-Keramiken zeigen, dass eine Kombination aus mesoporösem SiCN und einer darin dispergierten freien Kohlenstoffphase die elektrochemische Leistung signifikant erhöht. Auf diese Weise ist eine bei 900 °C erhaltene SiCN-Matrix überlegen gegenüber SiCN, das bei niedrigeren und höheren Temperaturen synthetisiert wurde. Die bei 900 °C synthetisierte SiCN Kathode erreicht einen Kapazitätswert von mehr als 195 mAh/g über 50 Zyklen bei einem hohen Schwefelgehalt von 66 Gew.-%.

Anschließend untersuchten wir die elektrochemische Leistung von drei verschiedenen Schwefel/PDC-Kathoden weiter. In zwei dieser Kathoden wird Schwefel in PDC-abgeleitete SiOC- und SiCN-Aerogele infiltriert, die durch überkritische CO_2-Trocknung hergestellt wurden. In der dritten Kathode ist Schwefel in mesoporösem SiOC eingeschlossen, das durch eine „Polymer-Spacer"-Methode erzeugt wurde. Die Verbundkathoden wurden einer elektrochemischen Charakterisierung unterzogen und ihre Leistungen wurden analysiert und mit der chemischen Zusammensetzung und Mikrostruktur des PDC-Gerüsts korreliert.

Zusätzlich wurden zur weiteren Verbesserung der elektrochemischen Performanz poröse, C-reiche SiCN-BN Verbundkeramiken synthetisiert. Hierzu wurden Mischungen aus porösem SiCN-Pulver, Borsäure und Urea bei verschiedenen Temperaturen (950 °C, 1100 °C und 1250 °C) erhitzt. Die auf diese Weise bei 950 °C hergestellte Probe SiCN-BN-950/S zeigt eine reversible Kapazität von 445 mAh/g und 62% der Kapazitätserhaltung nach 60 Zyklen unter 3,78 g/cm^2 der flächenbezogenen Dichte und 66 Gew.-% des Schwefelaufladens. Die hervorragende Zyklusstabilität wird dem synergistischen Effekt von BN und C-reicher SiCN-Keramikmatrix zugeschrieben.

Die erhaltenen Ergebnisse zeigen, dass C-reiche SiCN/SiOC-Keramiken vielversprechende Kathodenmaterialien für Lithium-Schwefel-Batterien mit verbesserter elektrochemischer Leistungdarstellen. Vorliegende Arbeit beschreibt kostenkontrollierte und effiziente Synthesewege für die Bereitstellung geeigneter Kathodenmaterialien in Lithium-Schwefel-Batterien, die für eine großtechnische industrielle Produktion geeignet sind und die eine Referenz für die Verwendung von Keramikmaterialien in Energiespeichersystemen darstellen.

Table of Content

List of Abbreviations

SiCN	Silicon carbonitride
SiOC	Silicon oxycarbide
SiCN-BN	Silicon carbonitride/boron nitride composite
EES	Electrical energy storage
LIB	Lithium-ion battery
LIBs	Lithium-ion batteries
LSB	Lithium sulfur battery
LSBs	Lithium sulfur batteries
XRD	X-ray diffraction
BET	Brunauer–Emmett–Teller
CV	Cyclic voltammetry
CNTs	Carbon nanotubes
3D	Three-dimensional
CMK-3	Ordered mesoporous carbon
MWNT	Multi-walled carbon nanotube
MWNTs	Multi-walled carbon nanotubes
BNNT	Multi-walled boron nitride nanotube
BNNTs	Multi-walled boron nitride nanotubes
PPy	Polypyrrole
PT	Polythiophene
SBA-15	Mesoporous silicon dioxide
CVD	Chemical vapor deposition
PDCs	Polymer-derived ceramics
NMR	*Nuclear magnetic resonance*
MAS-NMR	Magic angle spinning nuclear magnetic resonance
SAXS	Small-angle X-ray scattering
DVB	Divinylbenzene
NIB	Sodium-ion battery
NIBs	Sodium-ion batteries
PAN	Polyacrylonitrile
TEOS	Tetraethyl orthosilicate
PSZ	Polysilazane
PHPS	Perhydropolysilazane
SSA	Specific surface area

V_t	Total pore volume
APD	Average pore diameter
L_a	Crystallite size
SEM	Scanning electron microscopy
EDS	Energy-dispersive X-ray spectroscopy

List of Symbols

e	Electron
S_8	Eight-membered sulfur ring
mAh/g	Milliampere hour per gram
Wh/kg	Watt hour per kilogram
Wh/L	Watt hour per liter
S/cm	Siemens per centimeter
g/cm^3	Gram per cubic centimeter
V	Volta
S/m	Siemens per meter
R1–R4	Organic groups or hydrogen
Q_{irr}	Irreversible capacity
Q_{rev}	Reversible capacity
mAh/cm^3	Milliampere hour per cubic centimeter
mAh/cm^2	Milliampere hour per square centimeter
A/g	Ampere per gram
Ar	Argon
kW/kg	Kilowatt per kilogram
F/g	Faraday per gram
m^2/g	square centimeter per gram
nm	Nanometer
mS/cm	Millisiemens per centimeter
μm	Micrometer
P	Pressure
P_0	Pristine pressure
V_t	Total pore volume
L_a	Crystallite size
λ	Wavelength
$I(A_D)$	Intensity of the D band depends on area
$I(A_G)$	Intensity of the G band depends on area
cm^3/g	Cubic centimeter per gram
E	Potential
Q	Capacity
mV/s	Millivolta per second

List of Figures

List of Tables

1. Introduction

The prosperous modern life is dependent on the energy, which is mainly generated from the combustion of fossil fuels. Nevertheless, since the "Industrial Revolution" the use of fossil energy has caused irreversible damage to the natural environment, especially since the twentieth century with the vigorous development of modern industry. Among them, the greenhouse gas carbon dioxide is known as the destroyer of the Earth's atmospheric ozone layer, causing the global warming. Thus, the development of alternative energy technologies such as solar, wind and waterpower has been successfully accelerated. However, the power produced by these new energy technologies cannot be used in the time of the production and it needs to be stored. Therefore, efficient and economic electrochemical energy storage (EES) systems are highly demanded for effective utilization for storing the energy produced by above mentioned new energy technologies [1-4]. The battery system, as one of the most efficient EES systems, has been closely associated with our human civilization since its birth. From simple chemical primary batteries to rechargeable lithium-ion batteries, battery systems have experienced a long evolution. Milestones and foresight of the battery evolution are shown in Figure 1.1.
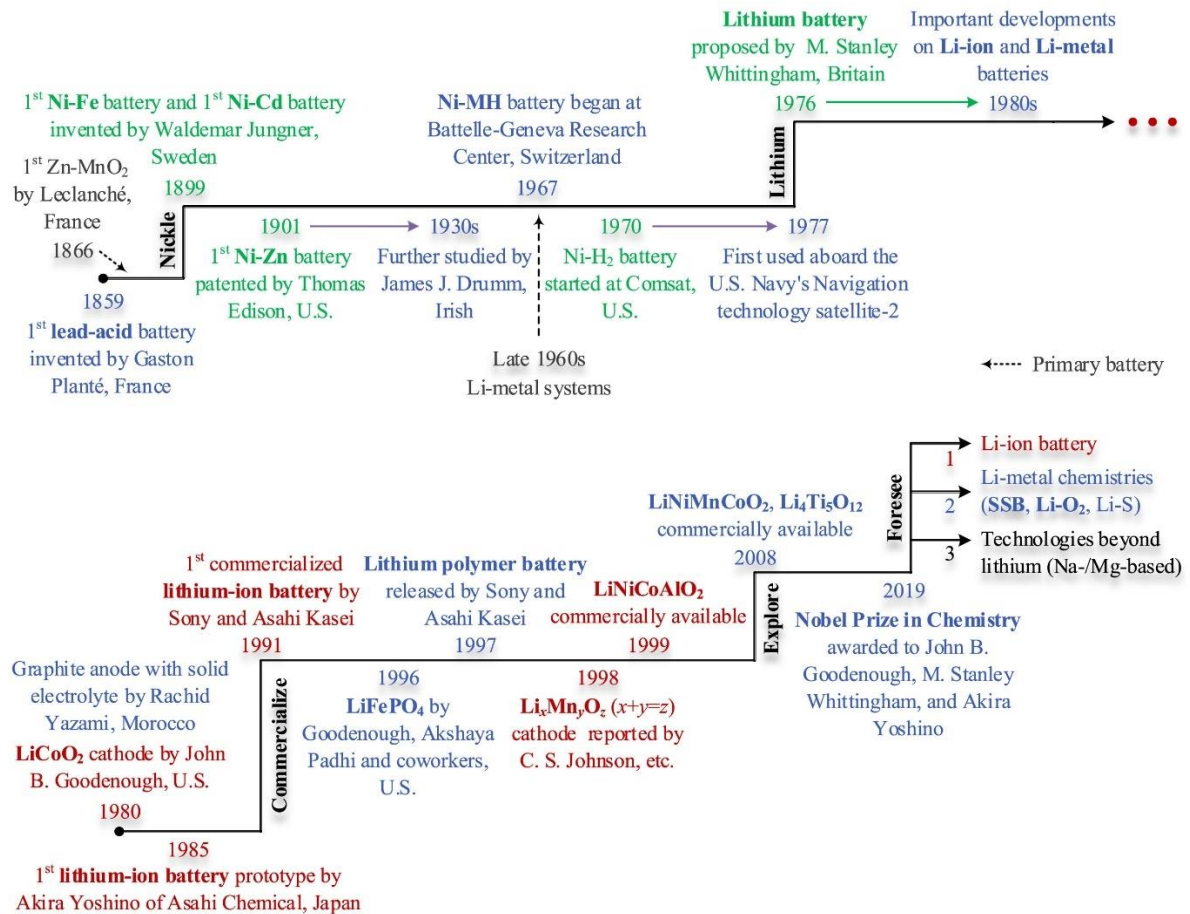
Figure 1.1 Milestones and foresight of battery evolutions. [5]

Rechargeable batteries such as nickel-cadmium, lead-acid, and lithium-ion batteries (LIBs) have been mostly applied in EES. LIBs, since being commercialized by Sony from 1990s, have been first used to power all kinds of portable electronic devices, while nowadays powering electric vehicles. However, the expectations for EV batteries and grid energy storage are hardly to be satisfied for future development since the energy density of the conventional LIBs is low (~420 Wh/kg) as shown in Figure 1.2. The capacity of LIBs is limited by ~250 mAh/g of the theoretical ultimate capacity of the insertion-oxide cathodes and by ~370 mAh/g of theoretical ultimate capacity of the graphite anode. Accordingly, new battery systems with a higher energy density are required [6-9].
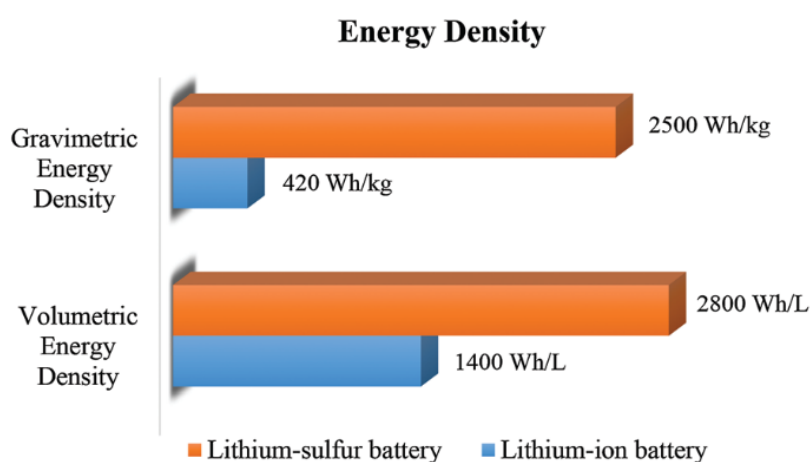
Figure 1.2 Energy density plots of lithium–sulfur vs. lithium-ion batteries. [6]

Lithium sulfur battery (LSB), a promising candidate for the alternative of the LIB, has gained much attention due to its superior cathode theoretical capacity (~1670 mAh/g). Besides, abundant element reserves in earth's crust and low production price of sulfur make it more conducive to large-scale commercial application. However, the electrical insulating property and 80% volume expansion of the sulfur during electrochemical lithiation must be tackled before the successful application of sulfur in LSB. Moreover, the "shuttle effect" caused by the soluble intermediates, polysulfides lead to fast fading of the reversible capacity. All these obstacles impede the practical applications of the sulfur cathode in lithium sulfur battery [2, 3, 6, 10].

In the past two decades, tremendous research has been carried out to develop more reversible, stable, and efficient sulfur cathodes. Providing conductive host materials for sulfur cathode and constructing separators with efficient confinement for polysulfides are the main routes [11-13].

From microporous carbon, mesoporous carbon to graphene and carbon nanotube, plenty of porous carbon materials and carbon-based nanomaterials have been investigated as a potential host for accommodating sulfur and conductive additives [14-20]. Schematic models, SEM observation, and cell performance of a representative S−carbon nano fiber (CNF) composite and a representative S− graphene composite are shown in Figure 1.3. Besides, metal sulfides such as FeS_2 [21], NiS_2 [22], Co_9S_8 [23], metal oxides such as MnO_2 [24], TiO_2 [25] and metal nitrides such as TiN [26], BN [27] are also investigated as additives for the skeleton host materials to enhance the performance of the sulfur cathode. Mechanistically, the performance improvement brought by the above materials is mainly due to their physical confinement and chemical confinement on polysulfide compounds, that is, physical adsorption and affinity of polar chemical bonds. These two effects effectively weaken the "shuttle effect", thus resulting in enhanced electrochemical performance [28]. Though above methods improve the performance of the sulfur cathode, there are still challenges to overcome such as the complicated production process, the low yield, and the expansive cost for producing those materials. Therefore, exploring new conductive host materials with lower cost and easier manufacturing process for large-scale commercial production is still on the way.
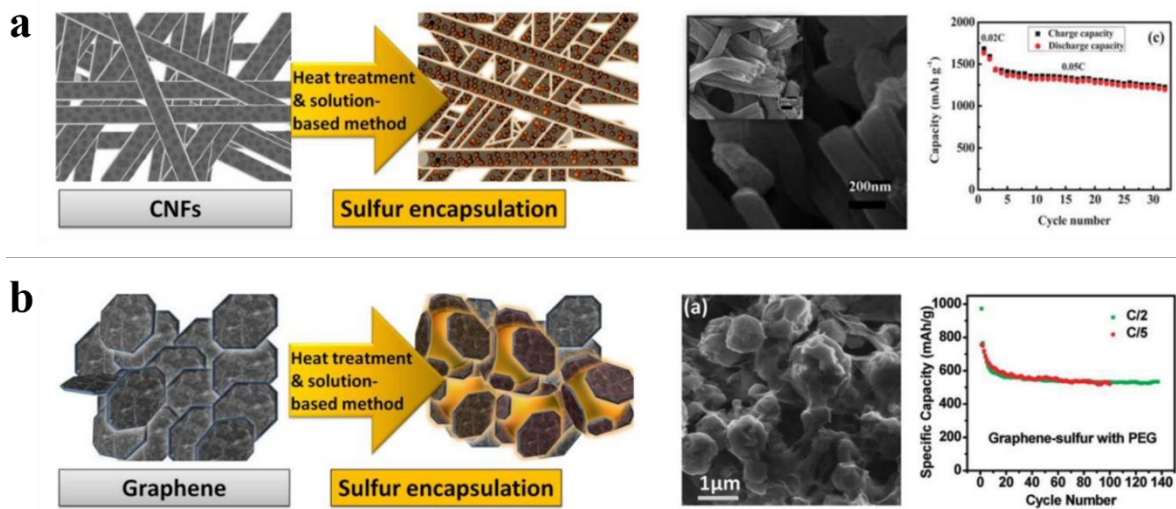
Figure 1.3 Schematic models, SEM observation and cell performance of a representative S−CNF composite (a) and a representative S− graphene composite (b). [29]

In the first section of this work, the basic concepts and electrochemical principles of a lithium sulfur battery are introduced and the detailed literature overview about C-rich ceramic materials utilized in energy storage systems are summarized. Besides, studies about additional modification by boron nitride on conductive carbon-based hosts are also presented. The second

section focuses on the experimental results, namely the synthesis of C-rich SiCN ceramics infiltrated with sulfur by the melting-diffusion method and the characterizations of the final materials by means of X-ray diffraction (XRD), Raman spectroscopy, Brunauer–Emmett–Teller (BET) analysis and elemental analysis. Their electrochemical performance is investigated using cyclic voltammetry (CV) and galvanostatic cycling. As a function of the pyrolysis temperature (800 °C to 1600 °C), different electrochemical performances of the synthesized SiCN samples have been found. Besides, PDCs aerogels in the systems SiOC and SiCN obtained via CO_2 supercritical drying and "polymeric spacer" method are also investigated as host for sulfur cathodes. Subsequently, nanostructured BN has been chemically introduced into the SiCN ceramic matrix to further enhance the performance and to impede the "shuttle effect" via the polar physical adsorption effect. Figure 1.4 presents the schematic diagram of the preparation process of the porous C-rich SiCN host for sulfur cathode. The performed work proves that C-rich SiCN ceramics and their BN composites demonstrate high potential as a host for sulfur cathode in lithium sulfur battery whereas the preparation process is cost efficient, flexible, and inexpensive, being suitable for large-scale commercial production.
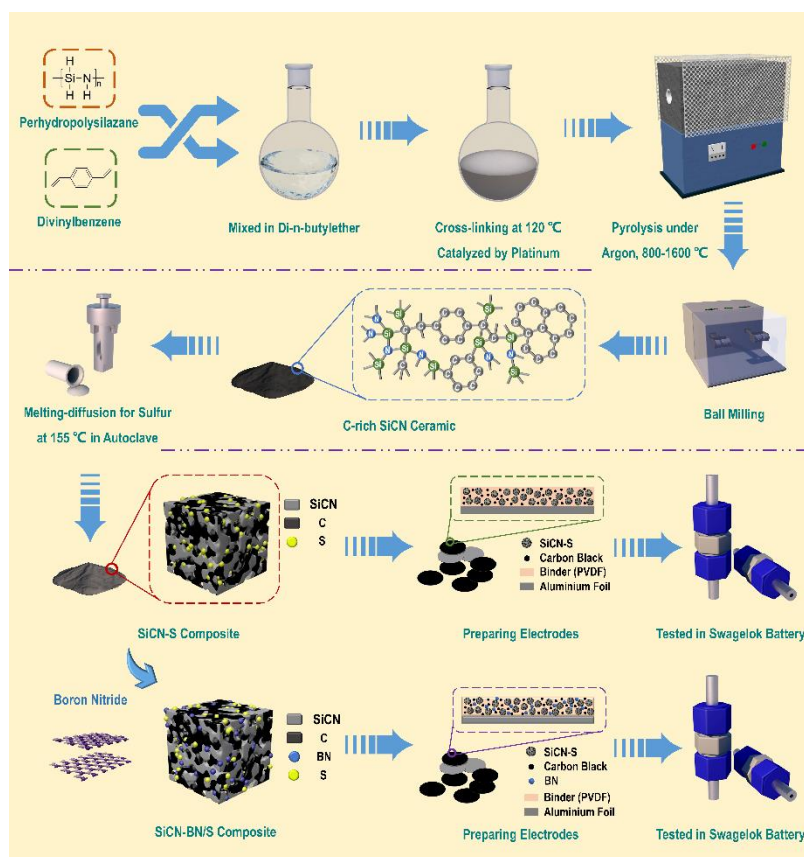
Figure 1.4 Schematic diagram of the preparation process of porous C-rich SiCN host materials for sulfur cathode developed in this work.

2. Fundamentals

This chapter deals with the fundamentals related to LSBs and the polymer-derived ceramics as well as the effect of BN additives in the sulfur cathode with respect to their electrochemical performance. The basic theoretical concepts and the state of the art are summarized in detail.

2.1. Lithium sulfur battery

2.1.1. Basic principles of lithium sulfur battery

In 1962, LSBs were firstly investigated by Herbert and Ulam [30]. They creatively employed sulfur as the cathode material, lithium and lithium alloys as the anode material and aliphatic saturated amines as the electrolyte. Some years later, a 2.35 ~ 2.5 V battery was achieved by introducing organic solvents such as propylene carbonate, dimethyl sulfoxide and dimethylformamide into the battery system. In the late 1980s, the lithium sulfur battery was further improved by employing ether compounds as electrolytes, in particular dioxolane to increase the rechargeable capability [31]. In the next two decades, although intensive research on lithium sulfur battery have been done, there have been no breakthrough in tackling the rapid capacity decay. In 2009, Nazar's team developed a highly ordered nanostructured carbon–sulfur cathode [32]. The real strength of lithium sulfur battery has been firstly demonstrated to the scientific community. The mesoporous carbon was used as host for sulfur and the composite material exhibited high capacity and stable cycling stability over 20 cycles. It is also from this time that LSBs have received much attention leading to a rapid development of various porous conductive materials acting as a sulfur host for enhancing the performance of the LSBs [33, 34].
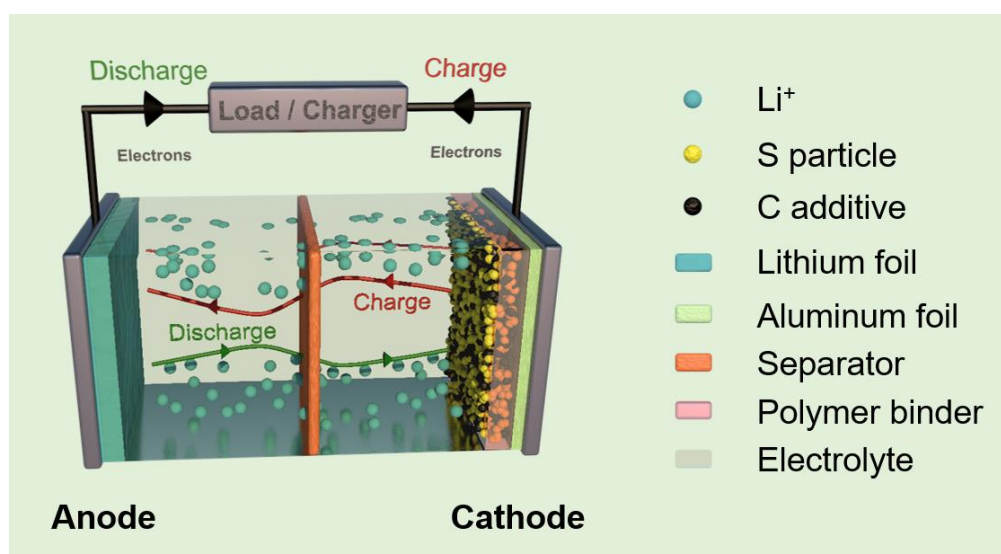
Figure 2.1 Schematic diagram of a LSB with its charge/discharge operations.

Like the traditional LIB, LSB consists of cathode, anode, separator, and electrolyte, whereas the key difference between them lies in the energy storage mechanism. In the traditional LIB, the energy storage is achieved by the intercalation of lithium ions into graphite anode and lithium metal oxide/phosphate cathode. But for the LSB, instead of intercalation, an electrochemical conversion reaction on the sulfur cathode and metal plating and stripping on the lithium anode surface are the main electrochemical processes. A schematic diagram of a lithium sulfur battery and its charge/discharge operations is shown in Figure 2.1. During the discharge process, lithium metal loses electrons and is oxidized to lithium ions. Lithium ions move from the negative electrode to the positive electrode under the combined action of the internal electric field and the ion concentration gradient in the electrolyte, while the lost electrons move from the external circuit to the sulfur side. Elemental sulfur receives the electrons and is reduced, subsequently reacting with previously moved lithium ions to form lithium sulfides. The discharge reaction equation is as follows (The charging process is the opposite) [2, 6]:

Anodic reaction: $16Li \rightarrow 16Li^+ + 16e^-$ (oxidation, loss of electrons)

Cathodic reaction: $S_8 + 16Li^+ + 16e^- \rightarrow 8Li_2S$ (reduction, gaining electrons)

Overall cell reaction: $16Li + S_8 \rightarrow 8Li_2S$

The theoretical anode capacity (~3860 mAh/g) and cathode capacity (1672 mAh/g) according to the above electrochemical reactions result in 1167 mAh/g of the theoretical capacity of the whole LSB with an average battery voltage of 2.15 V, that is ~2500 Wh/kg or 2800 Wh/L of the theoretical energy density. Figure 2.2 shows the typical discharge/charge curves of the LSB operated in ether-based liquid electrolytes. During the initial discharge process, cyclic S_8 molecules are opened, and elemental sulfur is reduced. The reduced sulfur reacts with lithium ions to form high-order lithium polysulfides Li_2S_x ($4 < x < 8$) corresponding to the plateau at around 2.4 V, then to form low-order lithium polysulfide Li_2S_x ($2 < x \leq 4$) corresponding to the plateau at around 2.0 V, and finally generates Li_2S_2 and Li_2S. For the charging process, lithium sulfides undergo a decomposition reaction and are converted back to S_8 via a series of oxidation reactions of the lithium polysulfides. Therefore, a complete reversible discharge and charge process is achieved [3, 6, 34, 35].
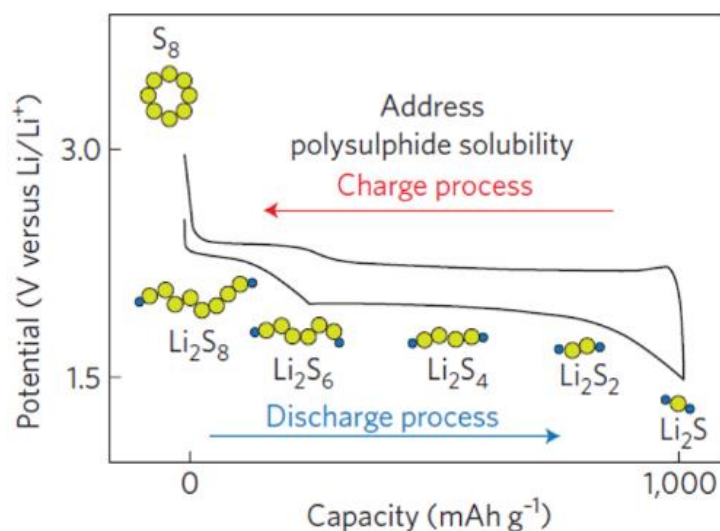
Figure 2.2 Voltage profiles of a LSB. [*2*]

2.1.2. Challenges and solutions

Despite a LSB presents remarkable capacity compared with a conventional LIB, there are several challenges which suppress the practical application of LSB [*2, 3, 6, 33, 36, 37*]. The main challenges are listed below:

(1). Low electrical conductivity. The insulating nature of sulfur results in low, i.e. $\sim 10^{-30}$ S/cm electrical conductivity. In addition, the formed lithium sulfides are also insulating, thus the transport of electrons and ions is hindered during cycling, resulting in unstable electrochemical contact and incomplete use of the active material. Moreover, the formed complex non-conductive lithium polysulfides passivate the surface of the cathode, further reducing the utilization of active materials, leading to poor capacity.

(2). Volume expansion. ~80% of volume change of sulfur during cycling originating from the different density between sulfur and lithium sulfide (2.03 g/cm^3 vs. 1.66 g/cm^3, respectively) cause structural damage of the electrode material, thus leading to constant consumption of the active material to form new solid electrolyte interphase, resulting in low coulombic efficiency and capacity fading.
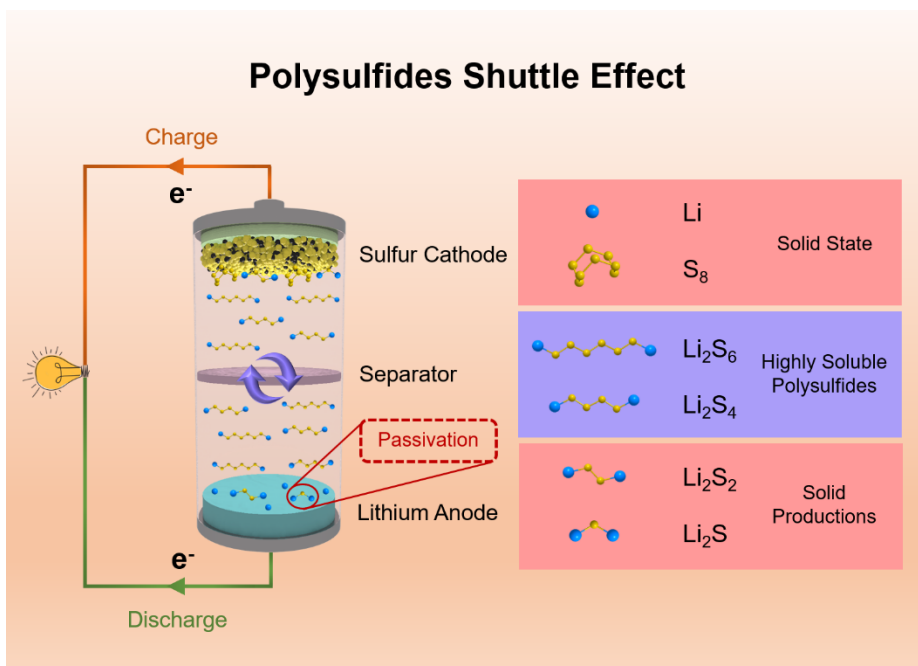
Figure 2.3 Illustration of the shuttle mechanism occurring in LSB.

(3). Shuttle effect. During the first voltage plateau of the discharge process, the generated high-order lithium polysulfides Li_2S_x ($4 < x < 8$) are highly soluble in the ether-based electrolyte. On the one hand, some of them are kept in dissolution state in the electrolyte and don't react to form the final product, lithium sulfide, on the other hand, some of them migrate to the lithium anode side and are reduced chemically to low-order lithium polysulfides and even solid Li_2S_2 and Li_2S. The formed lithium sulfides on the surface of lithium metal are not only difficult to be oxidized back to S_8, but they also passivate the lithium metal surface, leading to a higher impedance. Overall, the shuttle effect results in a poor coulombic efficiency and fast capacity fading. The illustration of the shuttle mechanism is shown in Figure 2.3.

Besides, the dendrite growth of lithium metal as well as the resulting ever-renewing solid electrolyte interphase also irreversibly consume electrolyte, lithium metal and active materials, causing poor cycling stability of the LSB. Furthermore, lithium dendrites may pierce the separator and lead to a short circuit in the battery, with the consequence of severe safety hazards like fire.

Therefore, only if the mentioned issues can be tackled, the true strength of LSB can be brought into play for practical applications. Plentiful efforts have been devoted to increase the conductivity and weaken the volume expansion and the "shuttle effect" of the sulfur cathode. In general, most of the approaches are focused on constructing nanostructured conductive host

materials and other attempts to develop interlayers to trap soluble polysulfides. Pre-lithiation technology and alternate efficient electrolytes have been also studied in the past. All those efforts improve the electrochemical performance of the LSB to some extent. Representative examples of enhancing the performance of the sulfur cathode are given below:
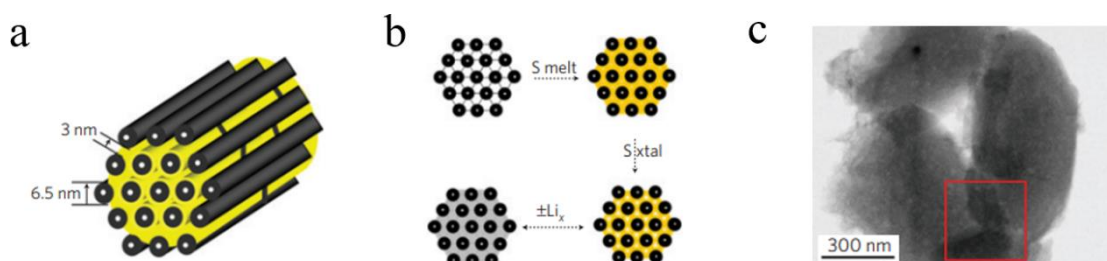
Figure 2.4 (a). A schematic diagram of the CMK-3/S-155 composite, sulfur (yellow) confined in an interconnected pore structure of highly ordered, mesoporous carbon (CMK-3); (b). A schematic diagram of the CMK-3/S-155 composite synthesis by impregnation of molten sulfur, followed by its densification on crystallization. The lower diagram represents subsequent discharging–charging with Li; (c). A TEM image of the CMK-3/S-155 composite particle. [*32*]

(1). Carbon related host materials for sulfur cathode. Porous carbon materials have been extensively studied as a host due to its electrical conductivity, availability and low price [*12*]. In 2009, a highly-ordered, mesoporous C-S cathode was developed by Nazar et al. shown in Figure 2.4, which was considered as a breakthrough of the LSB technology [*32*]. Their work demonstrated that the ordered mesoporous carbon CMK-3 successfully accommodated sulfur as host material due to its special nanostructure and 1005 mAh/g of the specific capacity and remarkable cycling stability over 20 cycles was achieved. With further modification of the carbon surface with hydrophilic polyethylene glycol, the capacity of the composite cathode was improved to 1320 mAh/g. In 2012, Sen et al. investigated the effect of microporous carbon on the performance of the sulfur cathode. Their results revealed that the metastable small sulfur molecules of S_{2-4} synthesized in the confined space of a conductive microporous carbon matrix can totally avoid the unfavorable transition between the commonly used large S_8 and S_4^{2-}, thereby effectively reducing the shuttle effect, resulting in an impressive cycling stability of 1149 mAh/g over 200 cycles [*38*]. Lee et al. firstly developed CNTs-S cathode with simple addition of CNTs into the sulfur cathode in 2003, shown in Figure 2.5. Their work realized 37 % of the capacity retention enhancement after 50 cycles. Besides, CV curves demonstrated that after the addition of carbon nanotubes, the sulfur cathode exhibited a higher reaction current and a diminished ohmic polarization, revealing enhanced electrochemical performance [*39*].

Yuan et al. further improved the performance of the CNTs-S composite by embedding sulfur in multi-walled carbon nanotubes via melt-diffusion at 155 °C, resulting in ~900 mAh/g of the discharge capacity and 74 % of the capacity retention after 60 cycles [40]. In 2011, Dai et al. pioneered the utilization of graphene for the encapsulation of sulfur particles in a sulfur cathode [41]. The composite containing graphene achieved ~750 mAh/g and 70 % capacity retention after 100 cycles at 0.2 C. This excellent performance has been attributed to the superior electrical conductivity and good ductility for accommodating sulfur inside graphene. In the following two decades, other research on CNTs, graphene and even three-dimensional (3D) hollow carbon spheres and carbon related materials as hosts for sulfur emerged [42-51]. Schematic models, SEM observation and cell performance of a representative S−microporous carbon composite, a representative S−mesoporous carbon composite and a representative S−hierarchical porous carbon composite are shown in Figure 2.6.
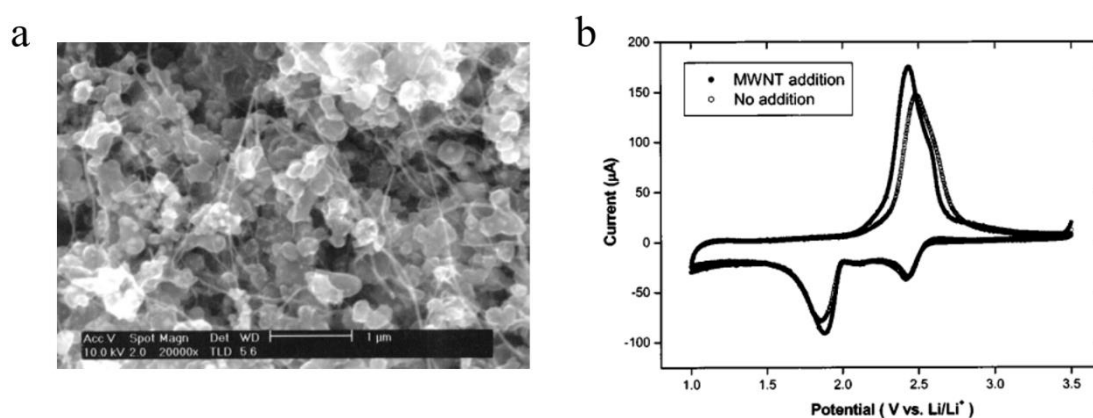
Figure 2.5 (a). SEM images of a cathode of sulfur added to multi-walled carbon nanotubes (MWNT); (b). CV curves of LSB with the cathode described in (a) with cycling. [39]

(2). Polymeric materials as host for sulfur cathode. Wang et al. coated sulfur particles with polypyrrole (PPy) via using oxidative polymerization of pyrrole with iron (III) chloride as the oxidizing agent [52]. The obtained sulfur-polypyrrole composite exhibited 1280 mAh/g of the discharge capacity compared with the pristine case (1110 mAh/g), as shown in Figure 2.7. A sulfur-polythiophene (PT) core–shell composite was synthesized to further improve the confinement of the polysulfides by Wu et al [53]. Besides, other polymeric materials such as sulfur-polyacrylonitrile composites and sulfur-polyaniline composites shown in Figure 2.8 also demonstrated enhanced electrochemical performance due to the following main reasons: 1) the conductive nature of the polymers which provides pathways for electrons; 2) flexible morphology which can accommodate sulfur particles and reduce volume expansion; 3) strong

confinement of the polysulfides by variation of functional groups attached to the polymer [54-57].
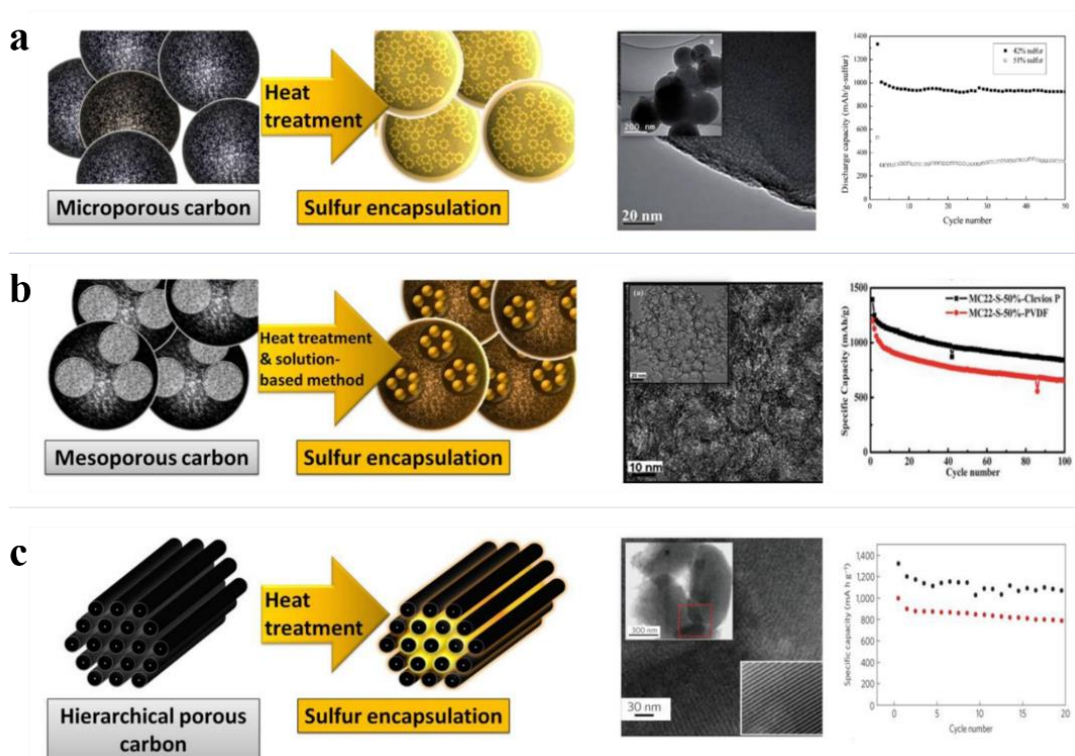
Figure 2.6 Schematic models, SEM observation and cell performance of a representative S−microporous carbon composite (a), a representative S−mesoporous carbon composite (b) and a representative S−hierarchical porous carbon composite (c). [29]
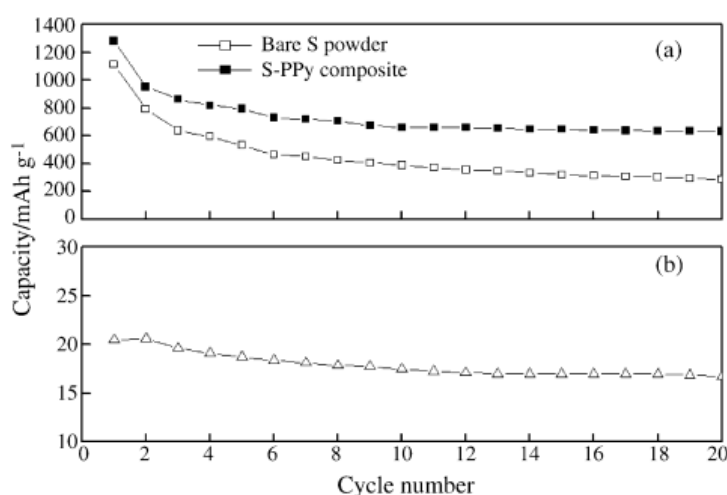
Figure 2.7 Discharge capacities vs. cycle number for cathodes: (a) bare S powder and S-PPy composite and (b) PPy powder. [52]
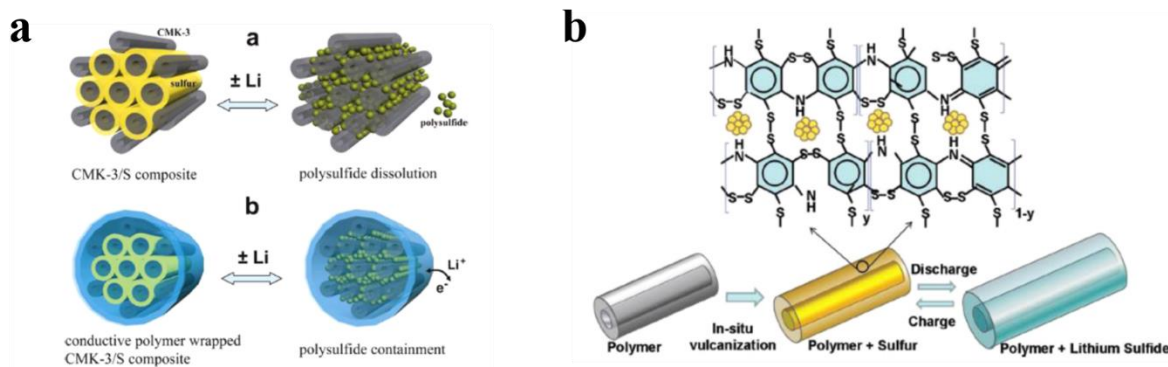
Figure 2.8 Schematic illustration of a PEDOT/PSS-coated CMK-3−sulfur composite (a) and the construction and discharge/ charge process of the S−PANI nanotubes (b). [*29*]

(3). Metal oxides, nitrides and sulfides as host for the sulfur cathode.

In 2004, Lee et al. investigated the nickel oxide ($Mg_{0.6}Ni_{0.4}O$) as additive in sulfur cathode. Their results revealed that the increased specific surface area originated from the $Mg_{0.6}Ni_{0.4}O$ leading to an increase of the specific capacity from 741 mAh/g to 1185 mAh/g [*58*]. Subsequently, aluminum oxide (Al_2O_3) [*59*], mesoporous silicon dioxide (SiO_2; SBA-15) [*60*], TiO_2 [*61*] and MnO_2 [*62*] as well as other metal oxides were also investigated as additive for the sulfur cathode to enhance their performance. In 2016, Zhang et al. developed a route reacting lithium polysulfide (Li_2S_x) with FeS_2 to form active Li_2FeS_{2+x} complexes to achieve a stable cycling performance [*21*]. In 2017, Deng et al. synthesized mesoporous Co_4N to accommodate sulfur and also obtained large reversible capacity of about 1000 mAh/g at 1 C over 100 cycles as shown in Figure 2.9 [*63*]. Therefore, above works demonstrated that addition of metal oxides, nitrides and sulfides to the sulfur cathode indeed provides strong confinement of the soluble polysulfides during cycling.
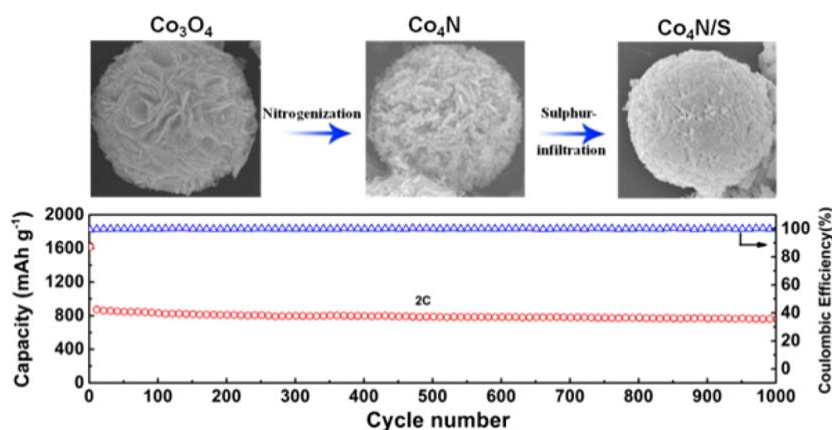
Figure 2.9 Schematic illustration of a Co_4N sphere and discharge capacity of the materials in LSB. [*63*]

As a layered material, hexagonal BN has a graphite-like structure with alternating B and N atoms replacing C-C atoms in graphene layers and regularly stack in planar networks. Similarly, to carbon, BN forms nanosheets and nanotubes (Figure 2.10). Unlike the C-C bonds in CNTs and graphene, B-N bonds in BN possess a partially ionic character leading to "lip-lip" interactions [64] between neighboring BN layers. Thus, continuous superposition of B and N atoms along the axis prefer to form multilayered BN nanosheets [65]. The comparison between the main properties of BNNTs and CNTs is shown in Figure 2.11. To synthesize BN nanomaterials, in addition to the commonly used arc-discharge and chemical vapor deposition (CVD), heating of milled B powders or B-containing reagent mixtures, continuous laser heating at superhigh or ambient pressures, the so-called "substitution reaction" method, and low-temperature plasma-enhanced pulsed laser deposition etc. are also employed [66]. In 1998, Han et al. synthesized BN nanotubes by a low-cost mass production method via the reaction: $B_2O_3 + 3C(nanotubes) + N_2 \rightarrow 2BN(nanotubes) + 3CO$ where the diameters and lengths of the synthesized BN nanotubes were similar to that of the starting CNT templates [67]. BN nanomaterials remained much less explored for a long time in the past. However, due to the specific properties such as electrical insulation, superior chemical and thermal stabilities, high porosity, equal thermal conductivity, and robust mechanical structure of BN nanotubes and nanosheets, they obtained much attention in advanced materials applications in recent years, such as semiconducting nanowires, magnetic nanorods, luminescent nanomaterials, and even sewage treatment [68].
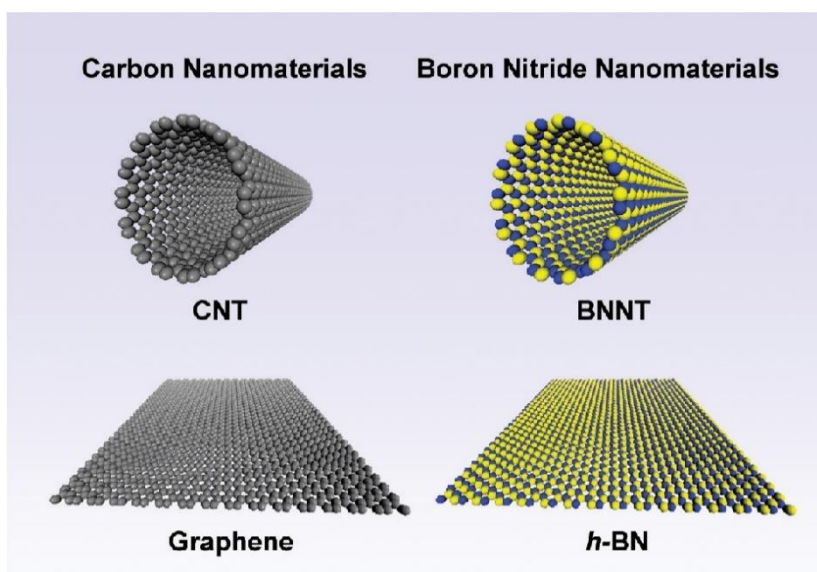
Figure 2.10 One and two-dimensional carbon nanomaterials including CNT and graphene and the corresponding BNNT, and single sheet h-BN. [65]
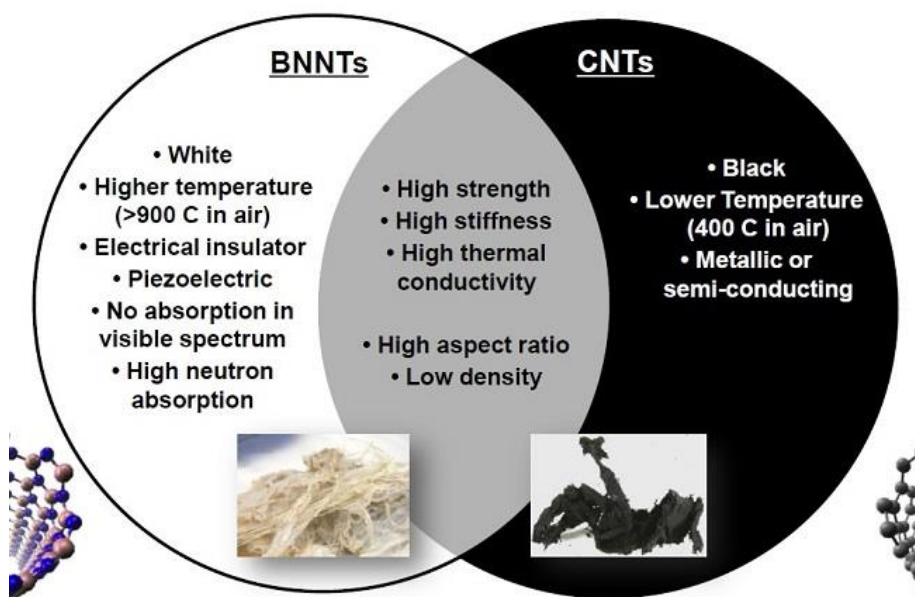
Figure 2.11 Comparison between the main properties of BNNTs and CNTs. [*66*]

The high specific surface area, high thermal conductivity and chemical stability of the BN nanomaterials make them become impressive adsorbents for various substances like organic pollutants also including polar lithium polysulfides [*66, 68*]. Therefore, BN nanomaterials have potential to be used as additive in lithium sulfur batteries as long as the insulation problem is solved. Constructing BN/C composites is an efficient and inexpensive way to overcome the conducting issue. He et al. developed a BN/CNT hybrid as sulfur host via a one-step co-pyrolysis method for LSB [*27*]. The electrochemical performance of the material is shown in Figure 2.12. The contact resistance between non-conducting BN and conductive CNTs is efficiently reduced by the paragenesis structure, and the bandgap of BN is narrowed by the additionally introduced O, resulting in a high conductivity of 1884 S/m. A strong interaction between sulfur and the BN/CNTs hybrid is also confirmed. Besides, the composite cathode exhibits a high specific capacity of 1374 mAh/g at 0.2C, a constant coulombic efficiency of 99% and an excellent rate capability attributed to the high surface and the introduced O. Deng et al. synthesized graphene-supported BN nanosheets to achieve enhanced adsorption feasibility for polysulfides in LSB [*69*]. Based on the synergistic effect between BN and graphene, the composite shows greatly enhanced adsorption for polysulfides, resulting in excellent performance in a wide temperature range (-40 to 70 °C) as shown in Figure 2.13. At 70 °C, the material reveals a reversible capacity of 888 mAh/g over 300 cycles, at -40 °C the recovered capacity was above 650 mAh/g. In 2020, a highly catalytic BN nanofiber in situ grown on pretreated Ketjen Black was prepared by Sun et al. [*70*]. Utilized as sulfur host in LSB, the synthesized material presented a first discharge capacity of 1822.5 mAh/g at 0.1 C. At 2C

charging current, the obtained sulfur cathode exhibited an initial capacity of 1150.9 mAh/g and a high-capacity retention of 51.6% over 1000 cycles. The excellent performance is attributed to the adsorption of BN for polysulfides and the catalysis of BN to promote transformation of polysulfides during chemical reactions as well as the enlarged interlayer distance of graphene for enhanced sulfur loading.
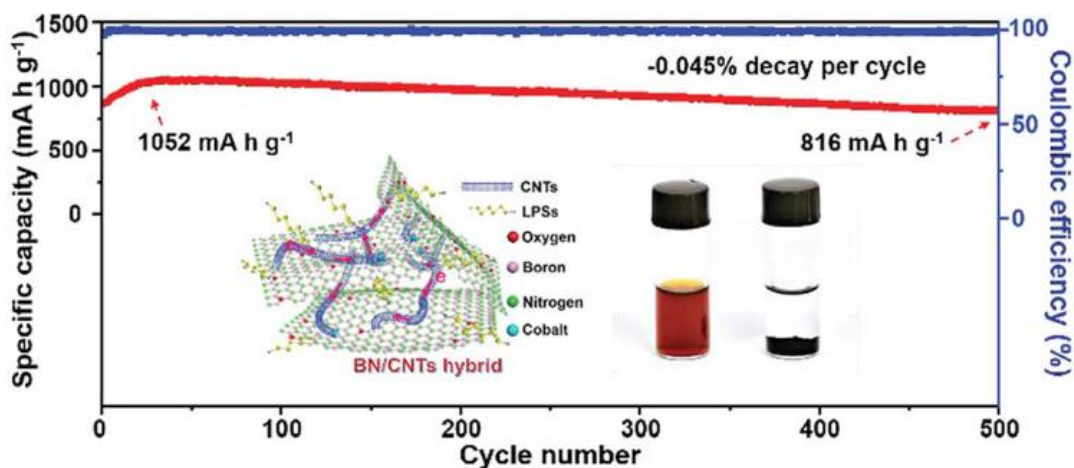
Figure 2.12 Discharge capacity and coulombic efficiency of BN/CNTs–S at 1C. [*27*]
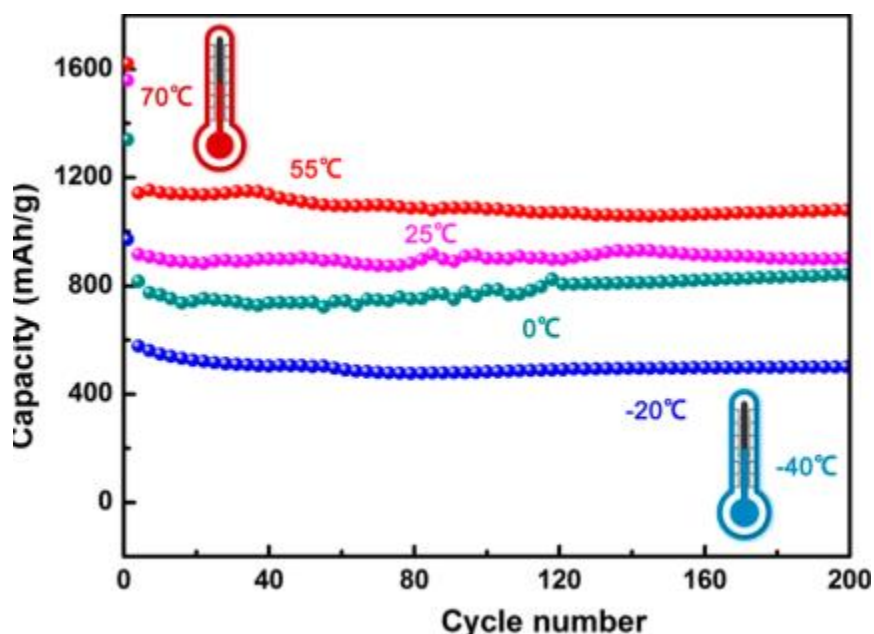
Figure 2.13 Discharge capacity versus cycle number of the BN/graphene from -40 to +70 °C. [*71*]

2.2. Polymer-derived ceramics

2.2.1. General background

Since the initial development by Ainger et al. [72] and Chantrell et al. [73] in the early of 1960s, polymer-derived ceramics (PDCs) pyrolyzed from organo-silicon preceramic polymers attracted great attention in materials applications. It is due to the nature properties of the advanced ceramics such as an outstanding combination of high hardness, high strength, excellent oxidation resistance, great thermal stability, and chemical durability. Besides, they have more capability of designing and tailoring at the molecular level by modifying the chemical/phase compositions and microstructure compared with other traditional powder route and CVD methods [74-83]. In the following decade, Verbeek, Winter, Mansmann and Yajima et al. successfully achieved the first practical transformation of polysilazane, polysiloxane and polycarbosilane preceramic polymers to Si_3N_4 and SiC ceramic fibers [84-86]. The regulation of the microstructure was further achieved by controlling the chemical composition in the 1980s [87, 88]. However, the polymer-derived bulk ceramics based on Si_3N_4, SiC, SiOC, and SiCN systems are hard to meet the demand of particular shapes and properties. Therefore, in the subsequent decades, B, Al, Hf, Zr, Ti, etc. elements were introduced into the above binary and ternary ceramics to form quaternary and multi-element ceramics, resulting in particular morphologies, extremely high temperature resistance, oxidation resistance, and even conductivity as well as ferromagnetism [89-99]. During the manufactory processes, various processing techniques such as fiber drawing [100, 101], dip- or spin-coating [102-104], freeze casting [105-107], and warm pressing [108-110] are employed. Attributed to the remarkable properties, the obtained advanced ceramics are applied in a range of key fields such as thermal/environmental barrier coatings [111, 112], joining/adhesive materials [113, 114], tribological applications [115, 116], electrode materials for secondary batteries [117-122] and supercapacitors [123, 124], electromagnetic absorbing and shielding [125-127], photoluminescent applications [128, 129], biomedical and sensing materials [130-132].

The fabrication of the silicon-based PDCs is realized in 3 steps, i) synthesis of preceramic precursors, ii) crosslinking and iii) transformation from polymer-to-ceramic.

(1). Synthesis of preceramic precursors
Preceramic precursors are typically thermosetting and own the following characteristics: 1) high molecular weight; 2) good solubility or suitable rheological properties for shaping; 3)

controlled polymerization; 4) low volatilization during pyrolysis; 5) containing functional groups for further reactions; 6) defined molecular structure for the synthesis of stoichiometric ceramic compositions. Most of the Si-based preceramic polymers are synthesized from (organo)chlorosilanes as the raw materials. For example, reactions of (organo)chlorosilanes with Na/K, water, and ammonia are used to synthesize polysilanes and polycarbosilanes, polysiloxanes, and polysilazanes, respectively. Poly(silylcarbodiimides) are synthesized by the reaction of bis(trimethylsilyl)carbodiimide with (organo)chlorosilanes. Chemical modification of polysilazanes or poly(silylcarbodiimides) are employed to synthesize ceramics in the system SiBCN. In particular, SiBCN ceramics are obtained by the pyrolysis of boron containing polysilazanes or poly(silylcarbodiimides) via hydroboration of unsaturated carbon bonds containing polymers as well as via dehydrocoupling reactions between B–H bonds of boranes and N–H bonds of polysilazanes [*96, 133*]. The unique synthesis routes of the PDCs are highlighted in Figure 2.14.
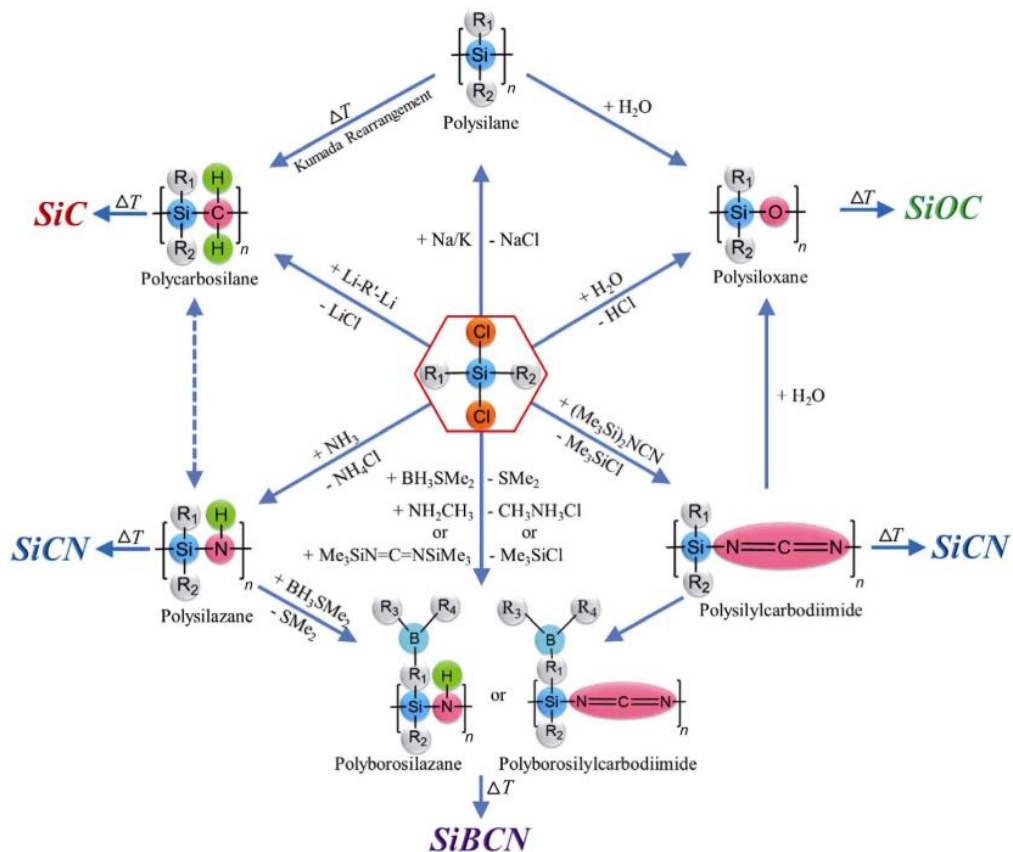
Figure 2.14 Synthetic routes for typical Si-based polymers and associated ceramics from organochlorosilanes. R1–R4 represent organic groups or hydrogen attached to silicon of the polymer backbone. [*134*]

(2). Crosslinking

There is an important procedure before the transformation of the precursor into ceramic, namely crosslinking. This step can not only keep the shapes of the precursor but also increase the production yield of the ceramic because of the formation of a solidified continuous network structure of the precursor inhibiting fragmentation and loss of low molecular weight components during pyrolysis. Here, we focus on the thermal crosslinking, and it is usually performed under a temperature window between 200-400 °C. During the crosslinking in this temperature range, four major reactions, namely hydrosilylation, dehydrocoupling, transamination, and polymerization are involved. Microscopically, polymer molecules are crosslinked to form a network structure. While macroscopically, the polymer changes from a liquid state to a gel or solid state. Moreover, dicumyl peroxide, transition metal ions etc. are sometimes employed as catalysts to decrease the crosslinking temperature. In addition, oxygen, silane, ammonia, electron-beam, UV light, reactive plasma, laser beam, and even highly alkaline solutions etc. are also used to initiate crosslinking processes [*133, 135*].

(3). Transformation from polymer to ceramic

This step, so called ceramization is a pyrolysis process usually occurring at a temperature range between 400 and 1400 °C. With increasing temperature after crosslinking, as the preceramic polymer starts to decompose under the release of gaseous hydrogen and organic fragments and the precursor is gradually converted to an amorphous ceramic matrix. For instance, amorphous SiOC, SiCN, SiC, and SiBCN ceramics are originated from poly(organosiloxanes), poly(organosilazanes)/poly(organosilylcarbodiimides), poly(organocarbosilanes), and poly(organoborosilazanes), respectively. Furthermore, the ceramic yield and the chemical/phase composition of the ceramics are strongly affected by the atmosphere during pyrolysis. For example, under argon or nitrogen, free carbon is hard to avoid due to the existence of hydrocarbon groups in polymers. But the pyrolysis under hydrogen can effectively achieve reduced and even completely removed free carbon phase. Moreover, rapid thermal annealing, laser pyrolysis, plasma spraying, microwave pyrolysis, flash pyrolysis, and ion irradiation can also initiate the ceramization process of the precursors [*96, 133, 135*].
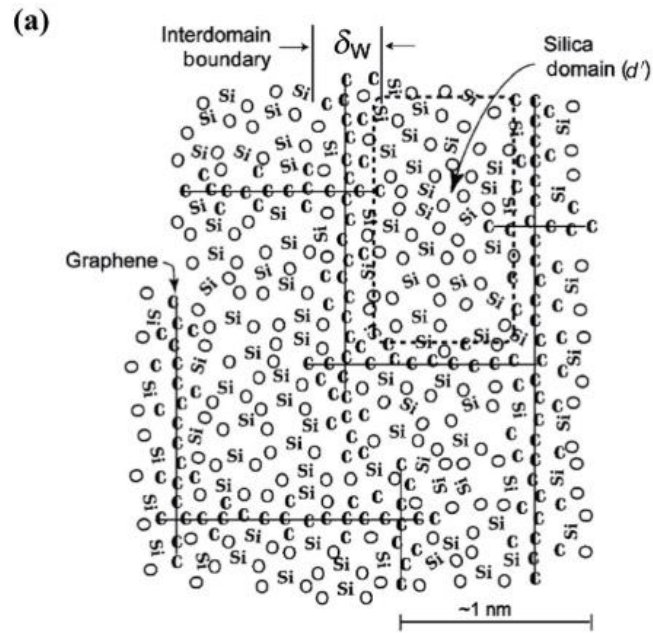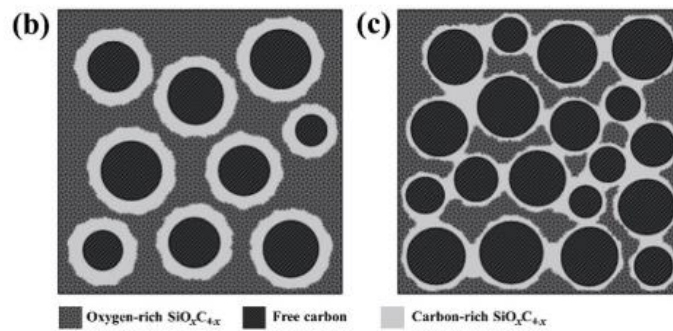
Figure 2.15 Two proposed models illustrating the microstructure of polymer-derived SiOC ceramics. [*134*]

Silicon oxycarbide (SiOC) and silicon carbonitride (SiCN) are two typical representatives of polymer-derived ceramics [*136*]. For the SiOC, it is usually amorphous and constructed by Si tetrahedral cores sited with O and C atoms. There are two structure models shown in Figure 2.15 [*134*]. The first model in Figure 2.15a is experimentally derived from small angle X-ray scattering (SAXS) and from the viscoelastic behavior of SiOC [*137, 138*]. Accordingly, the microstructure is described by 3 constituents: 1) tetrahedral silica cluster cores; 2) a graphene interlayers wrapping the silica sites; 3). SiC_xO_{4-x} mixed bonds ($0 \leq x \leq 4$) between silica and graphene. The second model in Figure 2.15b and Figure 2.15c consists of a silica-rich phase, sp^2-hybridised free carbon and a C-rich SiO_xC_{4-x} interface [*134*]. The results of Widgeon et al. further proved a continuous mass fractal backbone of corner-shared SiC_xO_{4-x} tetrahedral units

with "voids" occupied by free carbon phase which is more consistent with the second model based on the high-resolution ^{29}Si Nuclear magnetic resonance (NMR) spin-lattice relaxation, especially for C-rich SiOC ceramics (carbon content exceeds 20 wt.%) [139]. For the SiCN system, it is also usually amorphous, but its microstructure mainly depends on whether Si-C/N mixed bonds exist. For instance, for the polysilazane-derived SiCN ceramics shown in Figure 2.16a, the tetrahedrally coordinated Si atoms are bonded to carbon and nitrogen in configurations ranging from SiC_4, SiN_4, and SiC_xN_y units [140]. While for the polysilylcarbodiimides-derived SiCN ceramics shown in Figure 2.16b, no significant concentration of the Si–C/N mixed bonds are detected. Si_3N_4, SiC, and free carbon nanodomains exist separately in the polysilylcarbodiimides-derived SiCN ceramics [141, 142]. It is worth noting that PDCs will face phase separation and crystallization if the pyrolysis temperature exceeds about 1200 °C for SiOC and 1400 °C for SiCN depending on their composition. Especially when the temperature rises above 1500 °C, the loss of carbon, oxygen, and nitrogen occurs due to carbothermal reactions [133, 143, 144].
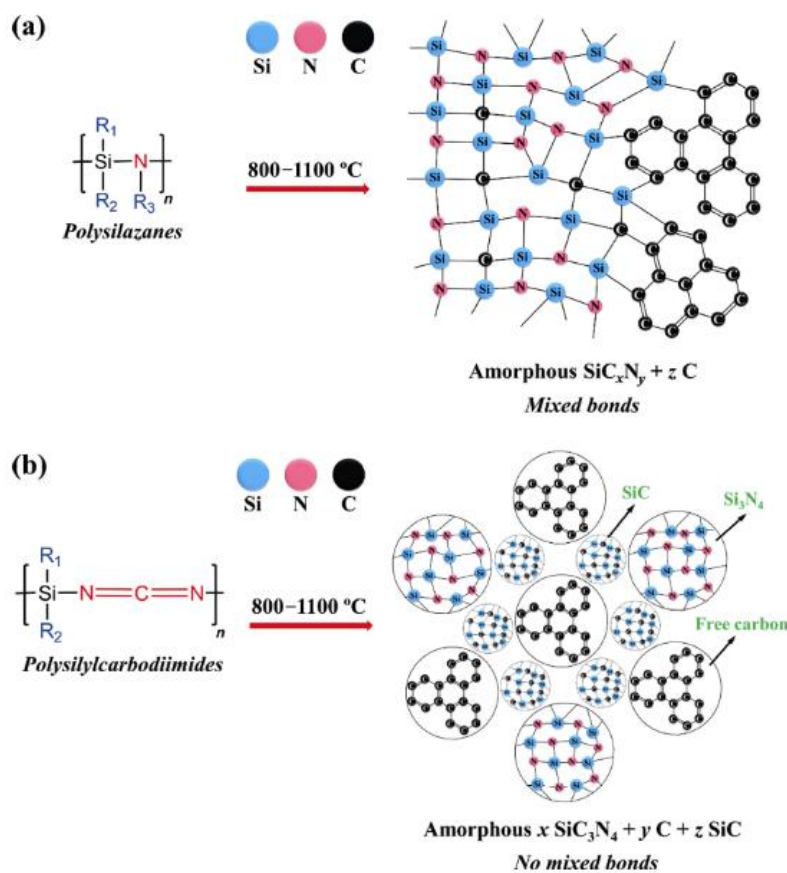
Figure 2.16 Microstructure of amorphous SiCN ceramics derived from two different polymers: (a) polysilazanes, (b) polysilylcarbodiimides. [134]

2.2.2. Polymer-derived ceramics for electrochemical energy storage

Due to their superior chemical and thermodynamic stability, porosity structure, decent electronic conductivity and robust, stress accommodating mechanical properties, etc., PDCs have been evolved as an interesting candidate material for electrochemical energy storage applications in the past two decades [135, 140].

Polymer-derived SiOC and SiCN gained much attention as anode and cathode materials in batteries and supercapacitors in recent years due to the presence of in-situ formed graphene-like sp^2-hybridised carbon network which encases the SiOC- and SiCN-containing nanodomains resulting in an excellent chemical and thermodynamic stability, elevated electrical conductivity (6×10^{-3} S/cm), as well as in robust mechanical properties [133].
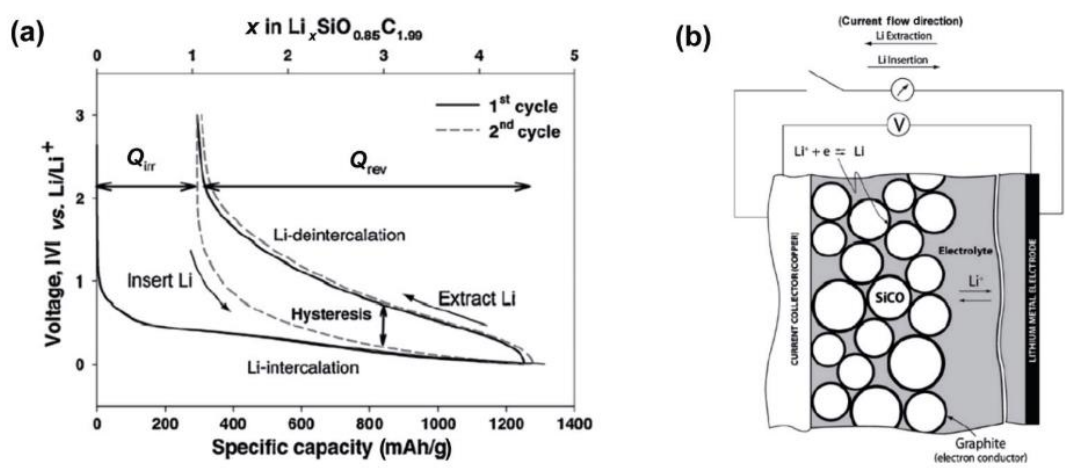
Figure 2.17 (a) Insertion and extraction of lithium into polymer-derived SiOC and (b) a scheme of the microstructure of the SiOC electrode during cycling. [145]

(1). Batteries

In 1994, Wilson et al. firstly reported polymer-derived SiOC used as LIB anode. This SiOC ceramic was pyrolyzed from siloxane polymers and reversibly achieved a specific capacity of 600 mAh/g by intercalating lithium ions lower than 1 V [146]. Dahn's group further investigated the effect of the chemical composition on the electrochemical performance of more than 60 different SiOC materials in the subsequent years and found that the composition of 14% Si and 80% C revealing the best electrochemical performance in LIB [147]. In mechanism of lithium storage and lithium transport, the teams of Ahn [148], Sanchez-Jimenez [149] and Saha [138] claim that the mixed bond configuration (tetrahedrally coordinated silicon from SiC_4 via SiC_3O,

SiC_2O_2, and $SiCO_3$ to SiO_4) is the major lithiation site. A hysteresis at a polarization potential between 250 and 500 mV is demonstrated by the study of Ahn and Raj and they described the lithiation and delithiation processes in SiOC as shown in Figure 2.17 [145]. However, in contrary to these findings, Fukui et al. [150] and other researchers such as Graczyk-Zajac et al. [151], Wilamowska et al. [152] and Pradeep et al. [122] demonstrated that the carbon phase is the host site for effective lithium storage due to the present interstitial and defect sites, edges of graphene sheets, porosity and interfacial adsorption at the interface of graphite nano-crystallites. And the results of ^7Li MAS NMR spectra measurements further confirmed that the carbon phase is indeed the host site for lithium storage [153, 154]. The polyorganosiloxane-derived SiOC anode pyrolyzed from 900-2000 °C by Kaspar et al. demonstrates that the reversible capacity decreases with the rise of pyrolysis temperature and correlates with the formation of crystalline SiC at elevated temperatures (proceeding temperature over 1200 °C, 660 mAh/g for 900 °C to 80 mAh/g for 2000 °C) [155]. A low carbon content resulting in high initial capacity but fast fading during cycling as well as a carbon content being beyond 20 wt% is beneficial for the conductivity and cycling stability were further confirmed by the following studies of Kaspar et al [120]. In 2012, a comparison between dense and porous SiOC anodes had been made by Dibandjo et al. and an enhanced electrochemical performance of the porous sample was confirmed [156]. Pradeep et al. further obtained porous SiOC with 180 m^2/g of specific surface area by a crosslinking process between linear polysiloxane and divinylbenzene (DVB) catalyzed by Pt and subsequent pyrolysis at 1000 °C under argon. Over 600 mAh/g of the specific capacity was achieved due to the porous structure providing enough fast ionic transport paths and accommodating space for the volume changes during cycling [118]. The effect of pyrolysis atmosphere on SiOC was also studied by introducing hydrogen during the pyrolysis of polysiloxane precursors [157]. Figure 2.18 reveals that the carbon content decreases from 55.15 wt.% to 46.37 wt.% caused by introducing 5 % H_2, resulting in an initial capacity enhanced from 568 to 704 mAh/g and a coulombic efficiency increasing from 63 % to 67 % [157]. Hard SiOC microbeads were synthesized by Dong et al. via emulsifying crosslinking and subsequent pyrolysis. When utilized as anode, a discharge specific capacity of 805 mAh/g was achieved after 300 cycles due to an enhanced structural stability of the material [158]. Moreover, nitrogen-doped carbon fibers embedded in a SiOC matrix [159], novel silicone oil-derived SiOC [160], and SiOC composites blended with high-capacity elemental silicon, tin as well as antimony [161, 162] were also investigated as anode material in LIBs and they all exhibited excellent electrochemical performance due to their unique micro-nanostructural features.
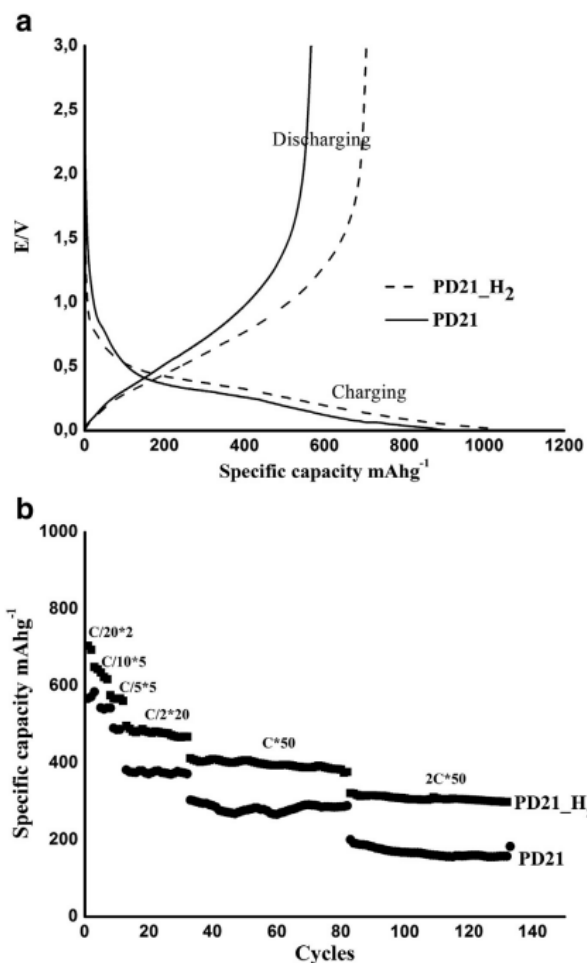
Figure 2.18 Electrochemical performance of PD21 (solid lines) and PD21_H2 samples (dashed lines), a) First cycle at C/20; b) Rate capacities. [*157*]

In 1997, Zank et al. firstly described a polysilazane-derived SiCN ceramic used as anode which had a reversible discharge capacities up to 560 mAh/g [*163*]. The work of Liebau-Kunzmann et al. further demonstrated that the ceramization process performed at 1100 °C in argon yielded Li-containing silicon carbonitride, SiCN:Li. The obtained material is basically amorphous and contains $LiSi_2N_3$ as a crystalline phase, indicating there are active sites between Li and SiCN. This reveals a potential of SiCN to be as anode in LIB [*164*]. A reversible discharge capacity of 754.9 mAh/g and an initial coulombic efficiency of 60.4 % of a SiCN ceramic were achieved via pyrolyzing polysilylethylendiamine at 1000–1300 °C by Su et al [*165*]. Then, C-rich SiCN materials have been extensively investigated by Graczyk-Zajac et al. [*166*], Kaspar et al. [*167*], and Reinold et al. [*168*]. Their works demonstrate that the electrochemical performance of the SiCN ceramics is significantly enhanced due to the presence of a free carbon phase and is affected by the molecular structure of the pre-ceramic polymer. The chemical modification with DVB was found to effectively increase the carbon content of the polyorganosilazane-derived

SiCN by Liu et al. [169], resulting in a capacity improved from 136 to 574 mAh/g. The free carbon phase has also been shown to be the main storage site of lithium in the SiCN by solid-state NMR investigation by Baek et al [170]. And the lithium storage mechanism of the disordered hard-carbon SiCN was further investigated by Graczyk-Zajac et al. via Raman spectroscopy and ^{7}Li MAS NMR [171, 172]. Their work demonstrates that the adsorption-like process in the free carbon phase is in charge of the lithium storage in hard-carbon SiCN ceramics and more than 33% of lithium in the composites is adsorbed in ionic state in pores and on the surface. The influence of the pyrolysis temperature on the electrochemical behavior of porous C-rich SiCN composite was studied by Storch et al.. Their study reveals that the sample pyrolyzed at 900 °C exhibits a capacity of 447 mAh/g and a capacity retention of 534 mAh/g over 100 cycles [173].
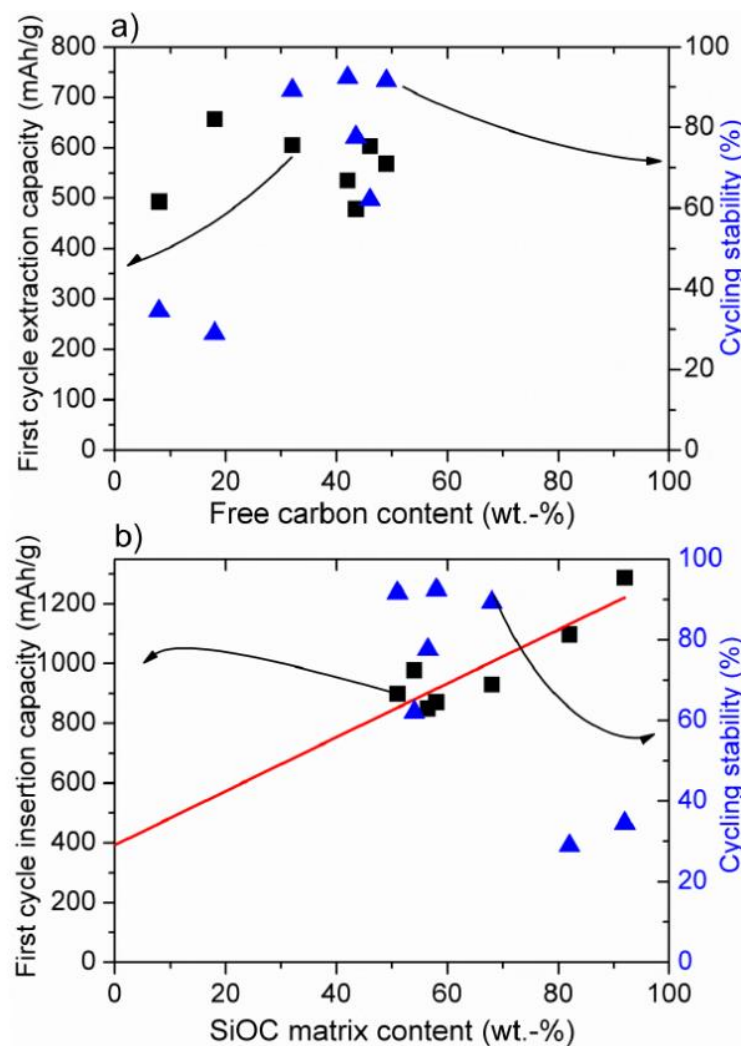
Figure 2.19 Dependence of the lithiation/delithiation capacity of SiOC-derived materials on the amount of free carbon (a) and on the amount of SiOC matrix (b). [174]

Figures 2.19 and 2.20 show the dependence of the lithiation/delithiation capacity of SiOC- and SiCN-anode materials on the amount of free carbon and SiOC or SiCN matrix, respectively. The results of this work also provide a reference for designing a composition of PDC-based anode materials with enhanced electrochemical performance [174].
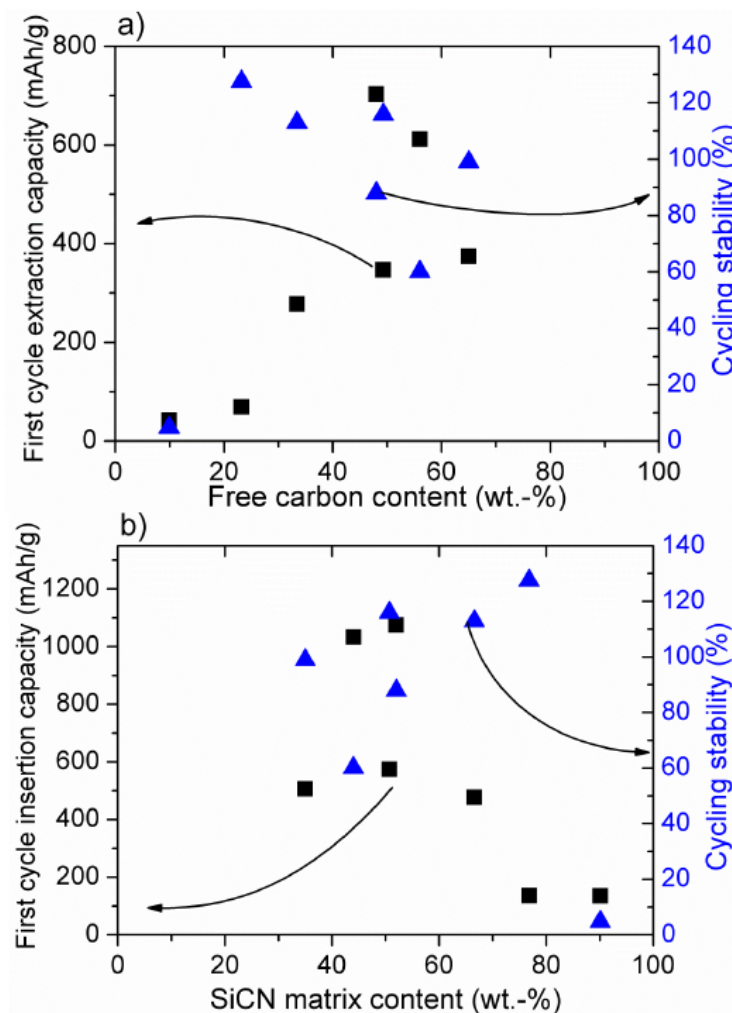
Figure 2.20 Dependence of the lithiation/delithiation capacity of SiCN-derived materials on the amount of free carbon (a) and on the amount of SiCN matrix (b). [174]

In other battery systems, SiOC and SiCN ceramics also exhibit excellent performance as electrode materials. Another promising candidate for high-capacity batteries is a Li-Se battery utilizing the superior theoretical volumetric capacity of Se with 674.9 mAh/g. The Li-Se battery has a substantial electrical conductivity which is 20 times higher than that of sulfur. But the low coulombic efficiency and poor cycle stability caused by the sluggish lithiation reaction kinetics of Se as the cathode and poor structural stability restricted its further development [175]. A

SiOC/Se cathode derived from rice husks was developed by Fang et al. via a bio-templating method assisted with a supercritical CO_2 technique as shown in Figure 2.21 [175]. The fabricated 3D porous SiOC/Se cathode exhibits a high first areal capacity (1012.5 mAh/g at 0.1 C) attributed to the 3D porous conductive network and SiOC units resulting in continuous electron/ion transport pathways. In sodium-ion batteries (NIB), PDCs are also applied as electrodes. A SiOC(N)/hard carbon composite as anode material for NIBs was firstly investigated by Kaspar et al [176]. In their work, they focused on the effect of the microstructure of the ceramic on the electrochemical performance. A strong correlation of the electrochemical performance with the porosity and elemental composition of the SiOC(N) anode was found. The addition of SiOC into hard carbon effectively enhanced the capacity from 44 to 201 mAh/g. Chandra and Kim synthesized a SiCN material from silicone oil as anode for NIBs [177]. The obtained composite calcined at 900 shows an excellent reversible capacity of 160 mAh/g after 200 cycles and the capacity fading of each cycle amounts only 0.09 mAh/g during 650 cycles. The development of potassium-ion batteries is significantly hindered because of the large ionic radius of K. It causes huge volume changes and a low ion diffusion rate during cycling. Sang et al. developed bi-continuous and nano-porous carbon spheres by etching C-rich SiOC ceramics. Utilized in potassium-ion battery, it shows a high first reversible capacity of 336 mAh/g at 0.1 A/g and long cycle life due to the interconnected nanostructure including a carbon framework and various functional groups [178].

Figure 2.21 Schematic of the synthesis of 3D porous SiOC/Se composite. [175]

(2). Supercapacitors

The choice of appropriate electrode materials for supercapacitors is of importance to provide a sufficient performance since the energy density of supercapacitors is usually impeded by the specific surface aera of the electrode materials in practical applications [179]. Figure 2.22 shows a schematic of a supercapacitor containing porous electrode materials [180]. Halim et al.

synthesized a low-carbon SiOC ceramic by pyrolyzing silicone oil under Ar in a temperature window from 700 to 1000 °C [*181*]. A pseudocapacitive behavior of the composite was found by subsequent characterizations. Besides, the material showed a power density of 156 kW/kg and a 90% of energy density retention after 75,000 cycles. Abass et al. prepared a SiOC electrode with embedded BN nanotubes and graphene [*182*]. This material shows high specific capacitance of 78.93 F/g at 1 A/g as well as a great cycling retention of 86% after 185 cycles, demonstrating that the free carbon phase is affected by the BN nanotubes. Kim et al. studied the influence of the oxygen functional group on the surface on the performance of porous SiC in a supercapacitor electrode [*183*]. The one-step carbonization of Si flakes resulted in porous SiC flakes with a high surface area of 1376 m^2/g. It exhibits 85.6% of rate performance from 5 to 500 mV/s and a high specific capacitance of 243.3 F/g at a scan rate of 5 mV/s. David et al. developed a boron-doped SiCN/carbon nanotube/graphene composite paper by vacuum filtration and thermal reduction [*184*]. To be used as electrode in supercapacitors, it delivers a low ohmic resistance and a high specific capacitance of up to 269.52 F/g at 5 A/g due to the unique self-supporting structure. High-performance hierarchical SiCN nanowires (diameter: 23–37 nm) used for supercapacitors reported by Reddy et al. exhibit a capacitance of 188 mF/cm at 5 mA/cm [*123*]. Moyano et al. developed another composite with reduced graphene oxide embedded in a SiCN matrix. Their study revealed that the ceramic composite owns a capacitance of 39 F/g and remains stable after 7000 cycles. This is attributed to the characteristic hybrid cellular structure [*185*].
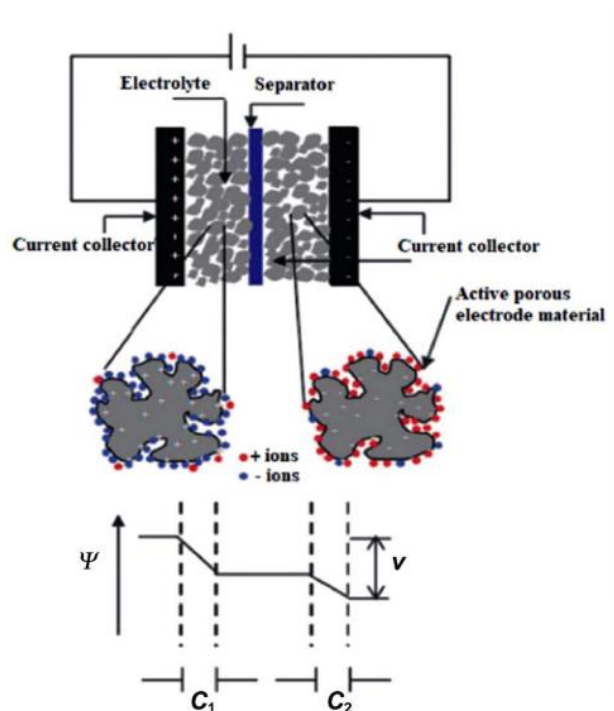
Figure 2.22 Schematic of porous electrode materials used in a supercapacitor. [*180*]

3. Results and Discussion

Within this chapter, the major scientific findings published in our research papers [*133, 186-188*] are summarized and discussed in detail. In section 3.1, C-rich SiCN ceramic matrices were synthesized based on crosslinking at 120 °C and pyrolysis techniques from 800 °C to 1600 °C. With subsequent sulfur embedding via the melting-diffusion method, SiCN-S composites were obtained. It has been shown that the SiCN-S-1000 composite sample demonstrates the best electrochemical stability at a high sulfur content of 66 wt.%. This feature is related to the microstructural integrity of SiCN produced at relatively low temperature in line with an advantage of the presence of nitrogen. Additionally, electrochemical performance of two PDC aerogels based on the SiOC and SiCN systems, as well as one mesoporous SiOC produced through the "polymeric spacer" method were also studied. In section 3.2, a SiCN-BN composite was developed to further enhance the performance of the ceramic host for the sulfur cathode by an annealing technique after polymer pyrolysis. The obtained results demonstrate that besides the benefits achieved from the porous C-rich SiCN ceramic matrix of the sulfur cathode, trapping of polysulfides by the presence of boron nitride significantly enhances the electrochemical performance of the composite cathode.

3.1. C-rich silicon carbonitride ceramic matrix and PDC aerogels for sulfur cathode: microstructural and electrochemical characterization

The content of this Chapter is published in:

(1) **F. Qu**, M. Graczyk-Zajac*, D. Vrankovic, N. Chai, Z. Yu*, R. Riedel, Effect of morphology of C-rich silicon carbonitride ceramic on electrochemical properties of sulfur cathode for Li-S battery. *Electrochimica Acta* **384** 138265 (2021).

(2) **F. Qu***, Z. Yu*, M. Krol, N. Chai, R. Riedel, M. Graczyk-Zajac, Electrochemical Performance of Carbon-Rich Silicon Carbonitride Ceramic as Support for Sulfur Cathode in Lithium Sulfur Battery. *Nanomaterials* **12** 1283 (2022).

(3) Q. Wen*[&], **F. Qu**[&], Z. Yu*, M. Graczyk-Zajac, X. Xiong, R. Riedel, Si-based polymer-derived ceramics for energy conversion and storage. *Journal of Advanced Ceramics* **11** 197-246 (2022).

(4) A. Zambotti, **F. Qu***, G. Costa, M. Graczyk-Zajac, G.D. Sorarù, Polymer-Derived Ceramic Aerogels to Immobilize Sulfur for Li-S Batteries. *Energy Technology* **11** 2300488 (2023).

In the present chapter, aiming at electronically conductive and low-cost sulfur host material, an easy and scalable method for processing such a host and a composite containing sulfur was developed. It consists of crosslinking of the perhydropolysilazane (PHPS) and DVB at 120 °C catalyzed by platinum, pyrolysis at different temperatures from 800 to 1600°C [*189*] followed by an infiltration of sulfur into porous structure of the C-rich silicon carbonitride under solvothermal conditions at 155 °C. Based on the former investigations [*155, 166, 168, 170*], it is already known than porous polymer-derived SiCN ceramics possess a unique combination of high electronic conductivity, porosity and robust, stress accommodating mechanical properties. In a present dissertation the impact of the initial porosity and elemental composition of SiCN ceramics on the electrochemical performance of SiCN-S composites has been discussed in detail. It has been shown that material pyrolyzed at 1000 °C revealing a mesoporous character in line with the presence of a free carbon phase dispersed in SiCN demonstrates the best electrochemical stability and the highest capacity (more than 310 mAh/g over 40 cycles) at a high sulfur content of 66 wt.%.
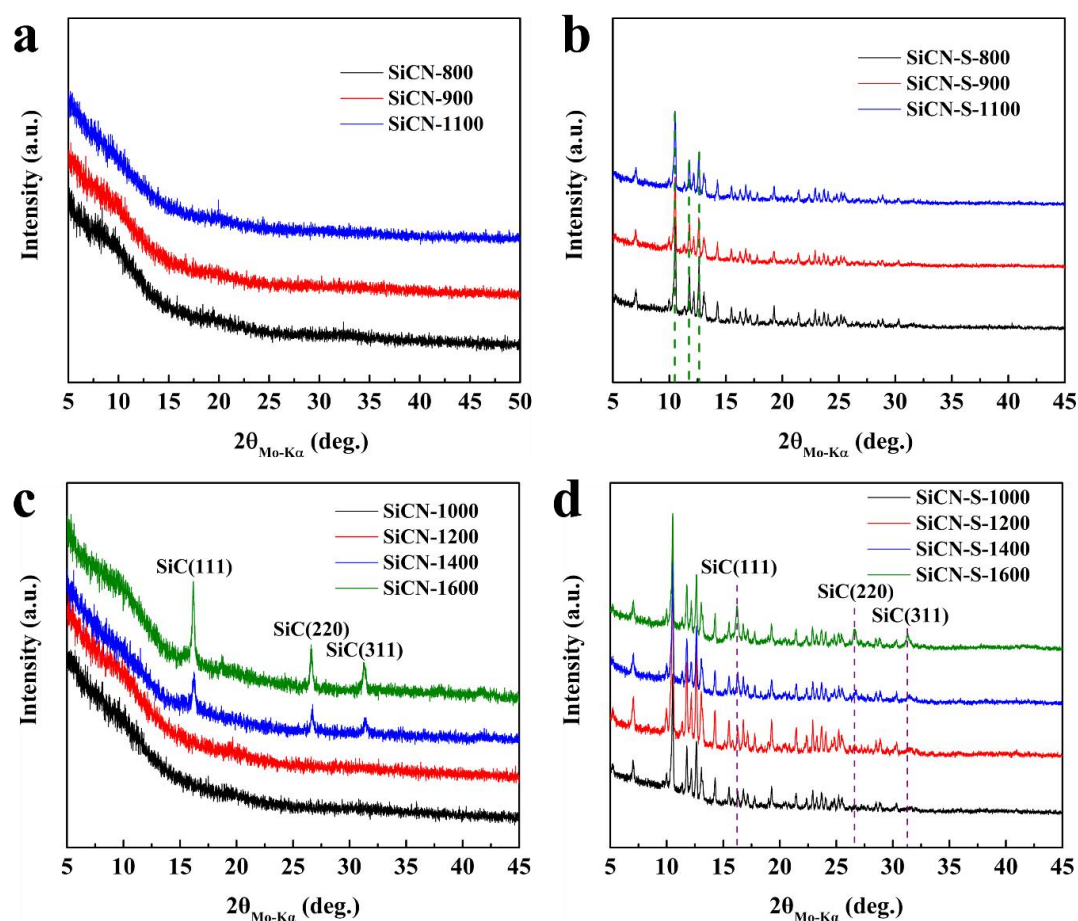
Figure 3.1 XRD patterns of SiCN ceramics (a, c) and SiCN-S composites (b, d) with different thermal treatment temperatures.

Figure 3.1 shows the XRD patterns for both the SiCN ceramics and SiCN-S composites. The results in Figure 3.1a and c indicate that there are no reflections present in the patterns for SiCN-800 to SiCN-1200, revealing their amorphous character. For SiCN-1400 and SiCN-1600, three reflections associated with three planes of crystalline SiC (JCPDS NO. 29-1129) can be seen at 16.21°, 26.61°, and 31.32°, which correspond to the (111), (220), and (311) planes respectively. As the pyrolysis temperature increases, the reflections become clearer and better defined, indicating an increase in crystallinity. Adding sulfur to the mix introduces the reflections of crystalline sulfur, as seen in Figure 3.1b and d.
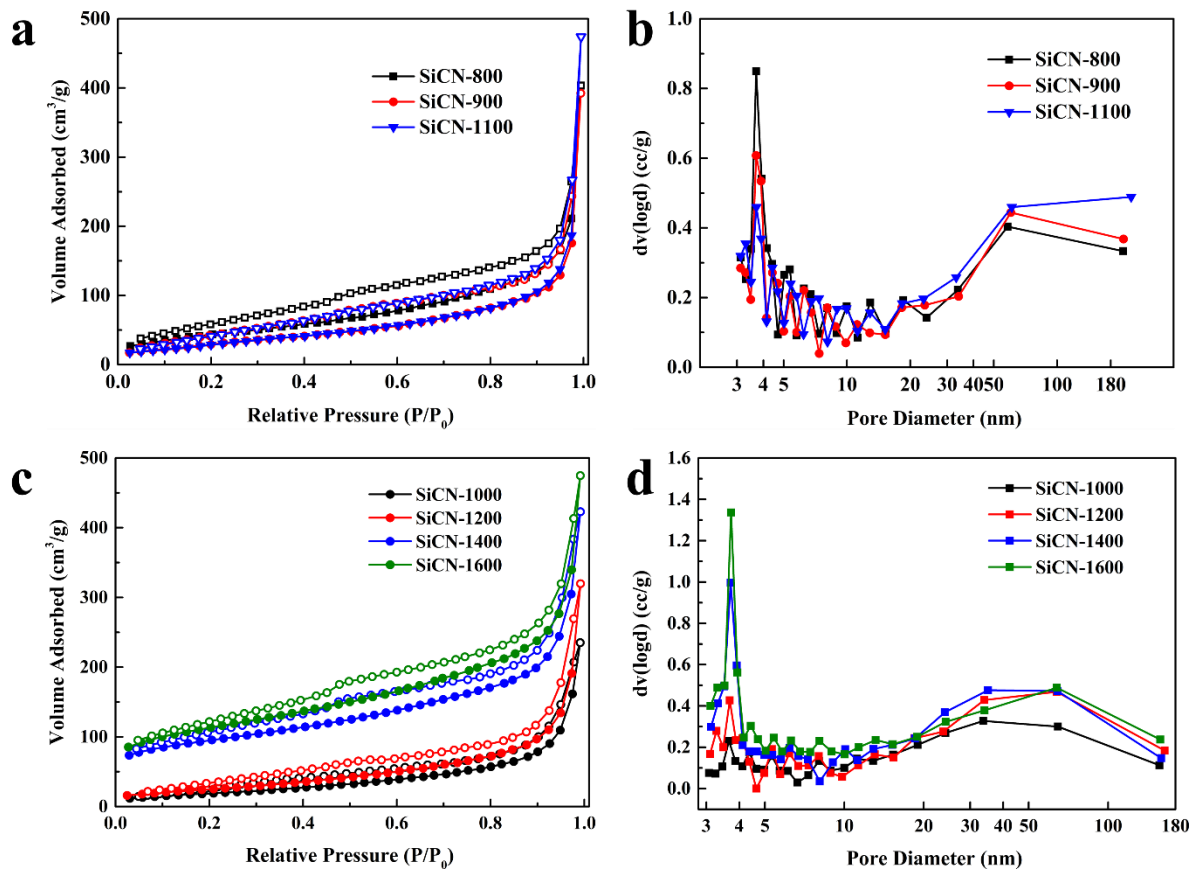
Figure 3.2 Nitrogen adsorption-desorption isotherms (a, c) and pore size distribution (b, d) of SiCN ceramics.

The specific surface area (SSA) and pore size distribution of SiCN ceramics were analyzed using N_2 adsorption-desorption measurement. The results, shown in Figure 3.2a and c, confirm the mesoporous nature of all materials, as indicated by a hysteresis loop at $P/P_0 \approx 0.5$, resulting from capillary condensation of nitrogen in mesopores. Table 3.1 lists the SSA, total pore volume (V_t), and isotherm type for SiCN-800 to SiCN-1600. As the pyrolysis temperature increases from 800°C to 900°C, the SSA and V_t decrease, leading to an increase in pore size (as indicated

by the APD value). However, larger mesopores could not be detected due to equipment limitations. The increase in SSA and V_t from 1000 to 1600 °C is related to the formation of SiC through a carbothermal reduction reaction ($Si_3N_4 + 3C \rightarrow 3SiC + 2 N_2$), leading to a release of nitrogen and an additional microporosity. The Type I isotherm registered for SiCN-1400 and SiCN-1600 supports these findings. Figure 3.2b and d present the pore size distribution of the SiCN ceramics, which firstly show a decrease and then an increase in the amount of mesopores with a size of 3-4 nm as the pyrolysis temperature increases. The average pore diameter (APD) firstly increases and then decreases as the temperature increases.
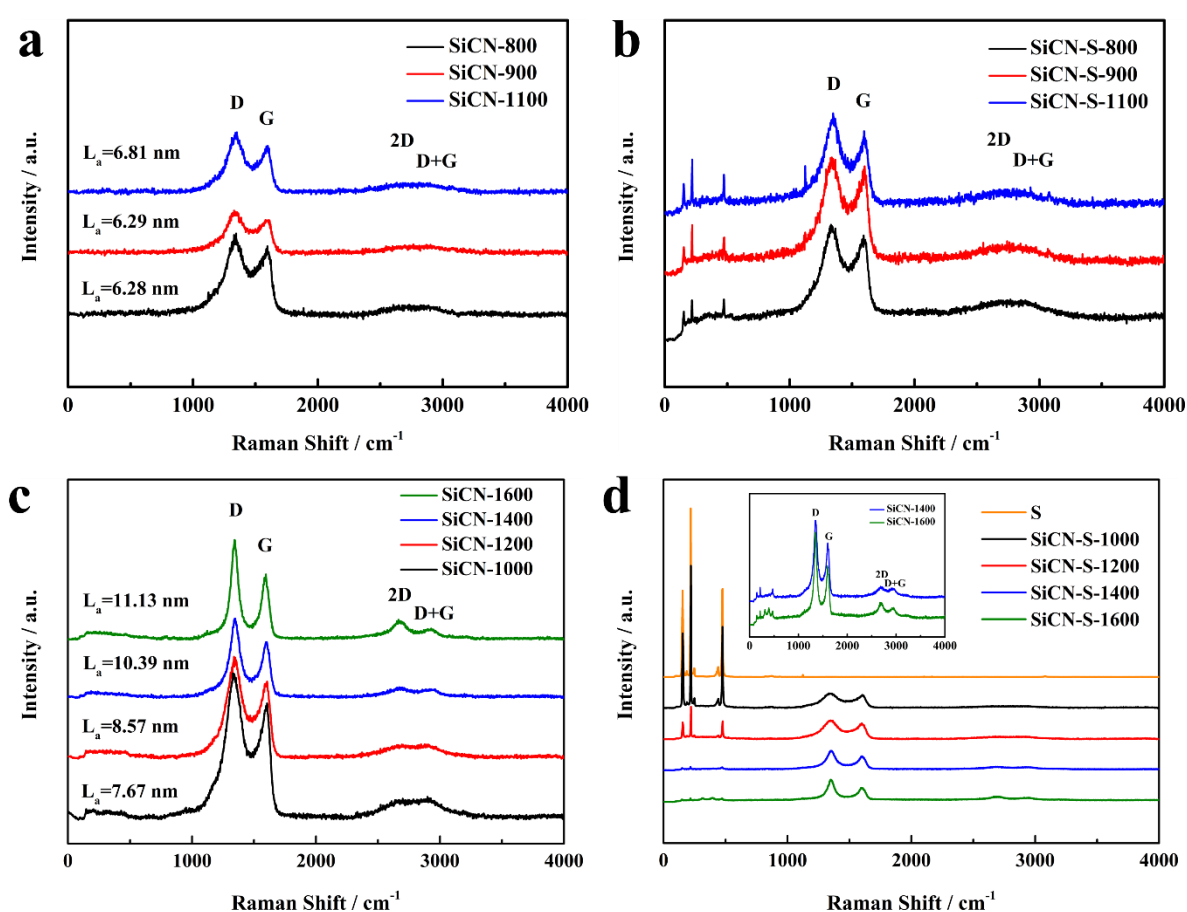
Figure 3.3 Raman spectra of all SiCN ceramics (a, c) and all SiCN-S composites (b, d).

The microstructure of SiCN ceramics, both pure and blended with sulfur, was analyzed using Raman spectroscopy. The results, shown in Figure 3.3a and c, indicate that the SiCN materials contain a disordered carbon phase, as indicated by the D and G bands at around 1346 cm^{-1} and 1585 cm^{-1}, respectively. The intensity of the D band is higher than that of the G band, indicating high disorder in the carbon in the SiCN matrix. As the pyrolysis temperature increases, the intensity ratio of the D and G bands decreases while the intensity of the 2D band at 2685 cm^{-1}

and the D+G band at 2925 cm^{-1} increases. This indicates an increase in graphitic order in the free carbon phase. Table 3.1 also shows an increase in the crystallite size (L$_a$) as the temperature increases. The Raman spectra of the SiCN-S composites are shown in Figure 3.3b and d. Besides the overtones of the carbon phase, the spectra contain characteristic peaks of sulfur (153.67 cm^{-1}, 219.52 cm^{-1}, and 475.11 cm^{-1}).

$$L_a(\text{nm}) = \left(2.4 \times 10^{-1}\right)\lambda^4 \left(\frac{I\,(A_D)}{I\,(A_G)}\right)^{-1} \qquad (Eq.\ 1)[186]$$

Table 3.1 Porous characteristics, I (A$_D$)/ I (A$_G$) ratio and L$_a$ of SiCN-1000 to SiCN-1600 (Gaussian type curve fitting applied).

Sample	SiCN-800	SiCN-900	SiCN-1000	SiCN-1100	SiCN-1200	SiCN-1400	SiCN-1600
SSA (m^2/g)	162	116	72	115	93	318	383
V$_t$ (cm^3/g)	0.62	0.61	0.36	0.73	0.49	0.65	0.73
Isotherm Type	IV	IV	IV	IV	IV	I/IV	I/IV
APD (nm)	15.46	20.94	20.2	25.5	21.2	8.2	7.6
I (A$_D$) / I (A$_G$) ratio	2.68	2.67	2.19	2.47	1.96	1.62	1.51
L$_a$ (nm)	6.28	6.29	7.67	6.81	8.57	10.39	11.13

Figure 3.4a to d present the initial lithiation/delithiation curves of all investigated SiCN-S composites. During the first sulfur lithiation, there are two distinctive voltage plateaus at around 2.4 V and 2.0 V, whereas the slope between them can be considered as a transition state. This represents the conversion of sulfur from S$_8$ to higher order soluble Li$_2$S$_x$ (4<x<8) and subsequent conversion to solid-state Li$_2$S$_2$ and Li$_2$S. It has been addressed in details in Fundamentals [190]. Initial lithiation capacities and corresponding columbic efficiencies of all SiCN-S composites are listed in Table 3.2a and b. The two voltage plateaus of SiCN-S-800 (2.33 V and 2.03 V) reveal a hysteresis compared with SiCN-S-900 and SiCN-S-1100 (2.36 V and 2.06 V) relating to a higher polarization [191, 192]. This phenomenon is also seen in the delithiation curves (2.35 V of SiCN-S-800 vs 2.23 V of SiCN-S-900 and SiCN-S-1100) which is discussed in terms that sample SiCN-S-800 has the lowest degree of graphitization among all composites based on the Raman results. This in turn results in the lowest conductivity of the

free carbon phase in sample SiCN-S-800 [*193*]. The initial lithiation capacity decreases in the row from sample SiCN-S-800 to sample SiCN-S-900 and then increases in sample SiCN-S-1100. This behavior is explained by the amount of accessible sulfur embedded in the ceramic matrix which decreases from SiCN-S-800 to SiCN-S-900 with the decreasing of SSA and average pore volume of the ceramic matrix.
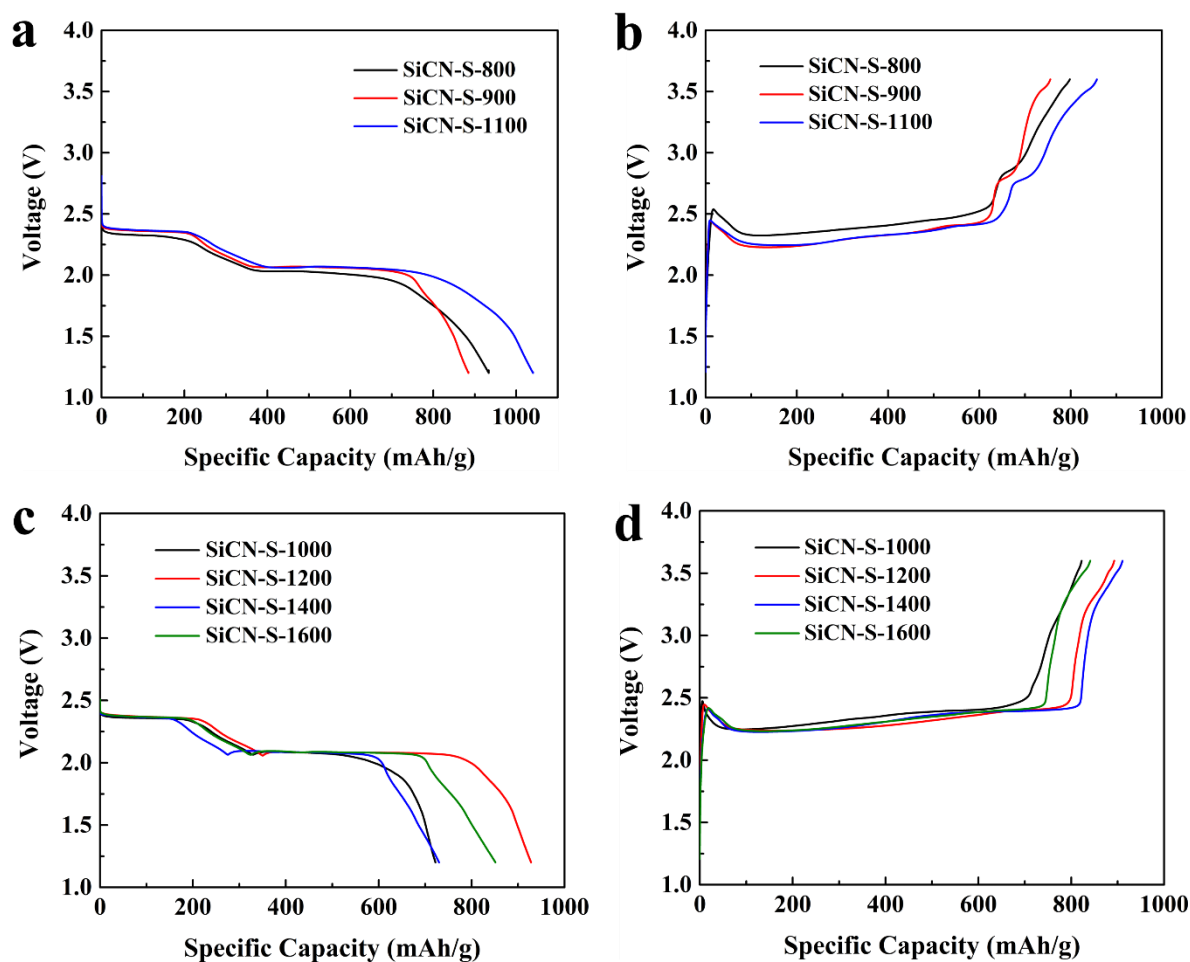
Figure 3.4 Discharge curve (lithiation) of samples (a, c); charge curve (delithiation) of all samples (b, d).

It is known that the "shuttle effect" originating from the diffusion of soluble polysulfides usually leads to a coulombic efficiency higher than 100 % (Define: Efficiency = Delithiation capacity / Lithiation capacity) [191, 203, 204]. For samples with efficiencies over 100 %, the short plateau at around 2.3 - 2.4 V corresponding to the shuttle phenomenon is clearly visible. The voltage for the first plateau varies for the composites (2.35 V for SiCN-S-1000, 2.37 V for SiCN-S-1200, SiCN-S-1400, SiCN-S-1600). For the second plateau the potential values are almost identical (2.08 V), however the transition to the following slope is "smooth" for 1000 °C

and 1200 °C materials, and a very abrupt for SiCN-1400 and SiCN-1600. The last one is typical and comparable to the transitions observed for microporous carbonaceous materials in the literatures [29, 194-196].
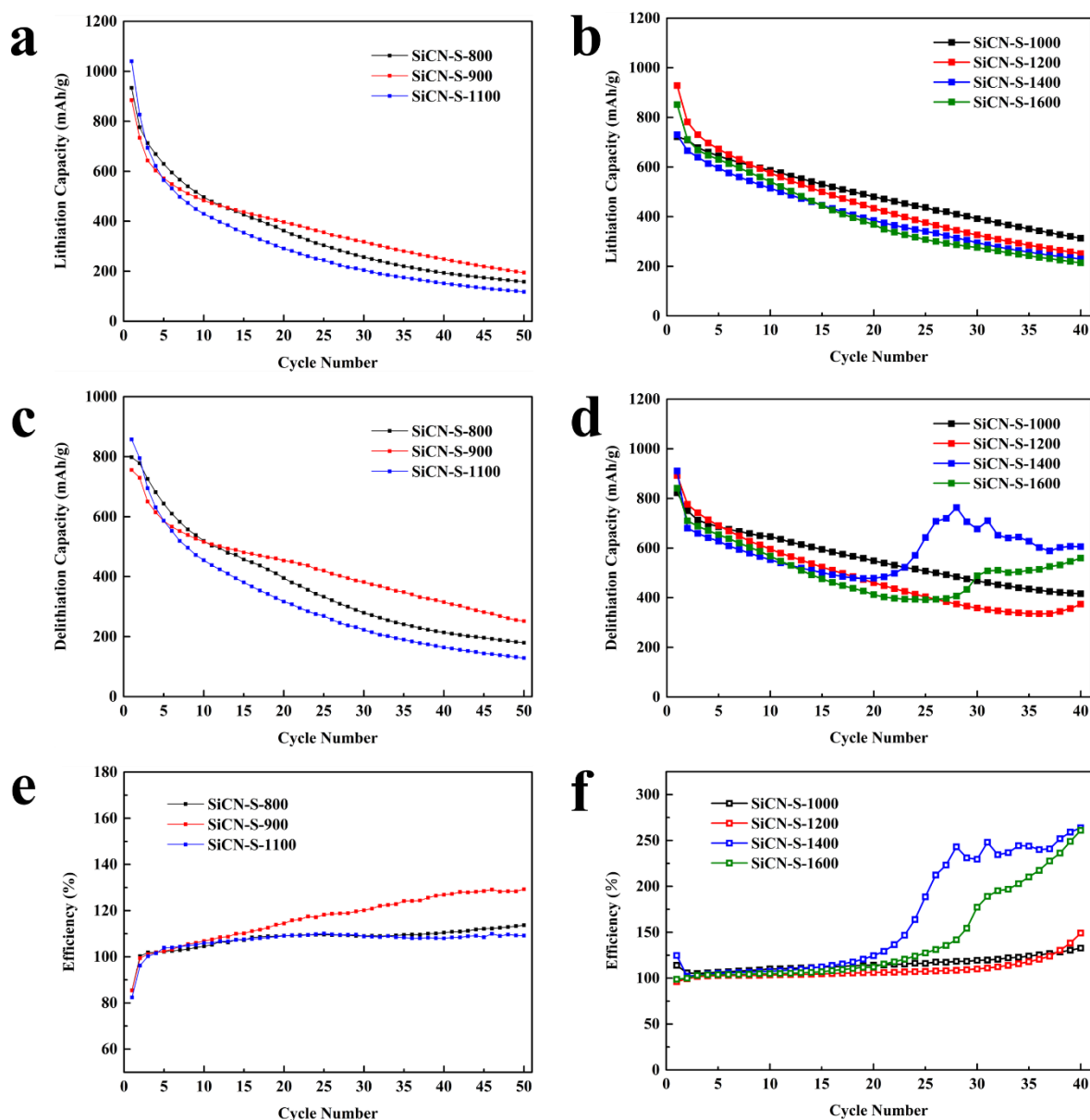
Figure 3.5 Cycling performance of all samples. Lithiation capacity (a, b), delithiation capacity (c, d) and columbic efficiency (e, f).

For extended cycling, lithiation/delithiation specific capacity and the corresponding reversible efficiency of all SiCN-S composites are showed in Figure 3.5, respectively. The initial discharge capacity, coulombic efficiency, reversible capacity, and capacity retention of all samples are listed in Table 3.2 and Table 3.3. As shown in Figures 3.5a, c, e, both lithiation and delithiation

capacities of the sample SiCN-S-900 are the lowest in the first 4 cycles. Nevertheless, after the 4th cycle, its specific capacity surpasses that of the sample SiCN-S-1100. After 12 cycles, the sample SiCN-S-900 even surpasses that of the SiCN-S-800 and remains it until the 50th cycle. The lowest electrochemical performance is registered for the sample SiCN-S-1100. In the end after 50 cycles, the sample SiCN-S-900 exhibits the lithiation retention of 22 %. The enhancement of the electrochemical performance of sample SiCN-S-900 in comparison to that of SiCN-S-800 is mainly due to the enhanced conductivity resulted from the increasing of the degree of graphitization of the free carbon (see Raman spectra of the corresponding samples). Although the SSA of the sample SiCN-900 is lower, its total pore volume V_t changed little in comparison with the sample SiCN-800, and it reveals more mesopores in comparison to SiCN-1100 (results of BET). The presence of mesopores is of advantage for stabilization of sulfur electrochemical behavior [1, 23, 202] which can explain the best electrochemical performance of SiCN-S-900 among measured three samples.

As for the samples SiCN-S-1000 to SiCN-S-1600 shown in Figure 3.5b, d, f, in the beginning of the cycling, SiCN-S-1200 shows the highest initial discharge specific capacity while SiCN-S-1000 reveals the lowest initial discharge specific capacity. In parallel, SiCN-S-1000 exhibits the slowest discharge capacity fading and its discharge capacity exceeds the capacity of the SiCN-S-1200 after 8 cycles. As for SiCN-S-1400 and SiCN-S-1600, before 12th cycle, capacity retention of SiCN-S-1600 is a little bit better than that of SiCN-S-1400 but still worse than SiCN-S-1000 and SiCN-S-1200. Over ca. 20th cycle, the efficiency of both SiCN-S-1400 and SiCN-S-1600 dramatically increases. The reason of this phenomenon is due to an increasing degree of shuttling effect. In case of SiCN-1400 and SiCN-1600, the long-chain polysulfides migrate to Li anode, are chemically oxidized, migrate back and are further oxidized to a long-chain polysulfide, corresponding to a long charge (delithiation) process and efficiency losses. The shuttling phenomenon still does not appear visibly in the potential/capacity transient of SiCN-S-1000, while it is present to a high extend in SiCN-S-1400 and SiCN-S-1600 and to a certain level in E vs Q curves of 1200 °C material. In case of porous carbon supports for sulfur cathode, Li_2S_x trapping relies on the physical adsorption of Li_2S_x on carbon and consequently has only a weak effect on polysulfide diffusion. Some nonconductive adsorbents such as oxides have a better ability to trap soluble polysulfides [197]. However, their insulation properties lead to a high ohmic polarization. Moreover, there is a limited electron transfer from these non-conductive absorbents, which hinders electrochemical redox processes. Polysulfides must desorb and travel to the surface of the conductive host, what results in low reaction rates and

might also lead to the permanent loss of active material if Li_2S_x too strongly adsorbed. In contrast, the N-doped carbon material enables direct and easy redox reactions of adsorbed polysulfides while showing even stronger adsorption [198]. This finding allows us to rationalize the electrochemical properties of SiCN-S composites. Their electrochemical stabilities/capacities decrease with increasing pyrolysis temperature of the SiCN host. Although Raman spectroscopy measurements demonstrate a better embedding of sulfur in those materials, a shuttling effect is strongly pronounced after ca. 20th cycle. A more stable electrochemical performance is found for SiCN-S-1000 and SiCN-S-1200 composites. Both SiCN-S-1400 and SiCN-S-1600 undergo the carbothermal reduction which is accompanied by nitrogen release (for details, please see the discussion of XRD results). Moreover, in consequence of SiC crystallization, the integrity of SiCN ceramic is broken down leading to a phase-separated, nitrogen-poor system consisting in a partially ordered carbon and crystalline SiC. These compositional and microstructural features affect the ability to stabilize sulfur cathode. Thus, the low temperature samples, consisting of free carbon phase uniformly dispersed in an integral SiCN matrix reveal much better electrochemical properties. After 40 cycles, sample SiCN-S-1000 exhibits the highest lithiation capacity retention. The capability of the SiCN ceramic to stabilize the sulfur cathode decreases with increasing synthesis temperature.

Table 3.2 Electrochemical parameters of SiCN-S-800 to SiCN-S-1100.

Samples	Initial Lithiation Capacity (mAh/g)	Reversible Capacity after 50 Cycle (mAh/g)	Initial Coulombic Efficiency (%)	Capacity Retention (%)
SiCN-S-800	934	158	85	17
SiCN-S-900	885	195	85	22
SiCN-S-1100	1040	118	82	11

Table 3.3 Electrochemical parameters of SiCN-S-1000 to SiCN-S-1600.

Samples	Initial Discharge Capacity (mAh/g)	Reversible Capacity after 40th Cycle (mAh/g)	Initial Coulombic Efficiency (%)	Capacity Retention (%)
SiCN-S-1000	722	313	114	43
SiCN-S-1200	928	251	96	27
SiCN-S-1400	730	230	125	32
SiCN-S-1600	851	214	99	25

Cyclic voltammograms allow to get closer insight to the redox reaction. As shown in Figure

3.6a, during the first cycle, the first cathodic peak appears at 2.33 - 2.35 V corresponding to the conversion of S_8 to higher order polysulfides (Li_2S_x, 4<x<8). The second cathodic peak appears at ca. 2.05 V and corresponds to the further reduction of polysulfides to insoluble Li_2S_2 and Li_2S [196]. During the oxidation process, a main anodic peak appears at 2.43 - 2.46 V, which is attributed to the conversion of lithium sulfide to S_8. This behavior originates from the overlap of two peaks corresponding to oxidation of the species reduced within two cathodic peaks. The splitting into two anodic peaks is better visible during the 5th cycle, as shown in Figure 3.6b and d. Both oxidation and reduction peaks are very sharp. It signifies low ohmic losses, namely that the ceramic matrix fulfills their role to provide sufficient electronic/ionic conductivity to embedded sulfur [194, 199]. After 5 cycles, although intensity of all peaks decreases, SiCN-S-1000 still maintains the highest intensity of anodic peak, indicating a good reversibility during cycling.
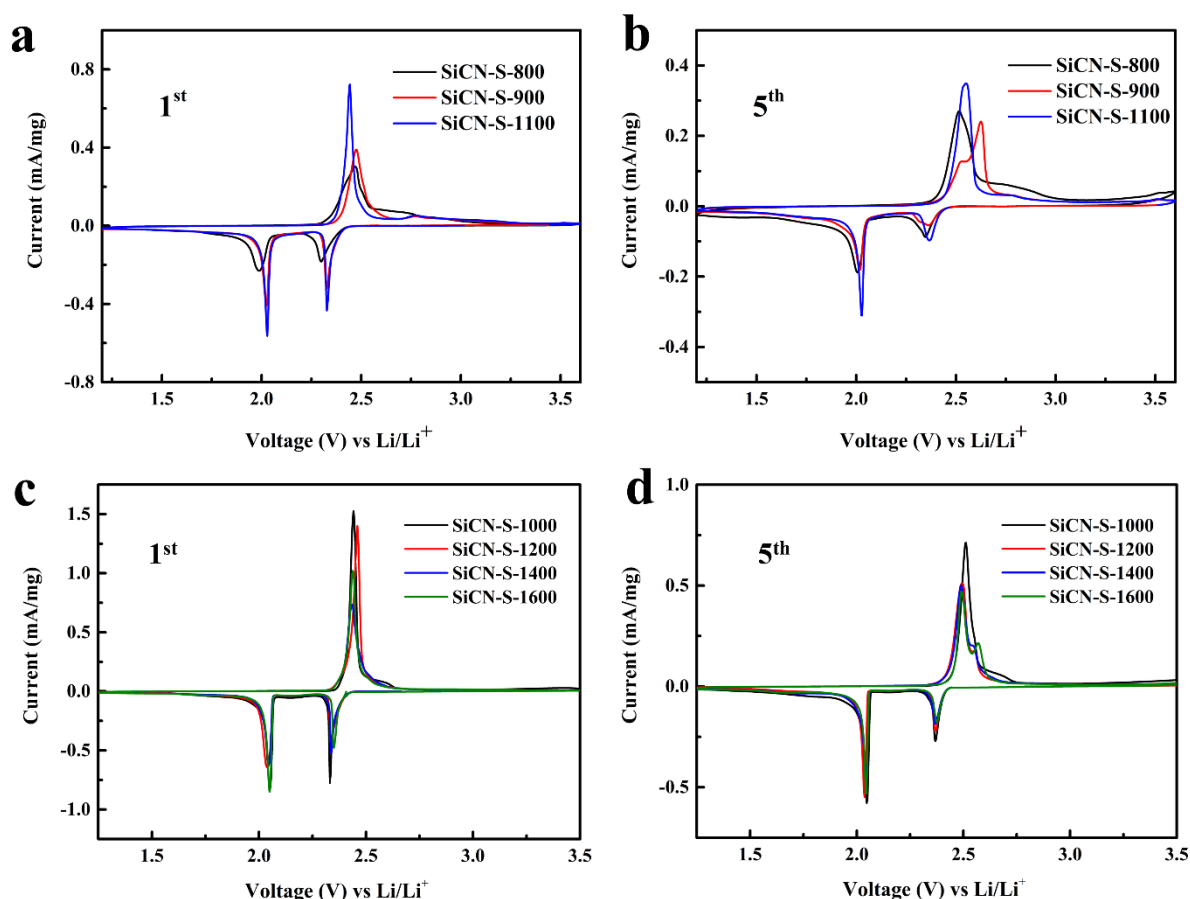
Figure 3.6 Cyclic voltammograms of all samples in the 1st cycle and the 5th cycle.

To summarize, the SiCN ceramic matrix pyrolyzed at 1000 °C shows the best electrochemical performance compared to the materials process at other temperatures. We can conclude that: (1)

the presence of amorphous, highly defective free carbon within the SiCN matrix provides a highly conductive environment for sulfur infiltration, (2) the carbothermal reduction at higher temperatures leads to separation of free carbon and ceramic phases, resulting in less disordered carbon and non-conductive SiC, thus, leading to increased shuttling effect after 20 cycles, (3) the presence of nitrogen at lower temperature materials appears to stabilize polysulfides. This nitrogen presence in the cathode material suppress migration of soluble polysulfides during cycling, resulting in weakened shuttling effect and improved cycling stability. The microporous morphology of the sulfur support is advantageous for cathode stabilization, but it is found not a necessary condition as other properties also play a crucial role. The high columbic efficiency of the low temperature pyrolyzed ceramics is explained taking into account both the beneficial role of the mesoporous ceramic matrix containing nitrogen and the $LiNO_3$ electrolyte additive, which promotes the formation of a stable protective film on the lithium anode. In a word, the electrochemical performance depends on the equilibrium results of all impact factors like microstructure, graphitization level and conductivity, etc..

We further investigated the electrochemical performance of two different PDCs aerogels and one "polymeric spacer" product as host for sulfur cathodes. In this case, the porous ceramics were synthesized using a different approach, namely one SiOC and one SiCN sample were obtained via CO_2 supercritical drying. Another SiOC material was additionally processed via the "polymeric spacer" method. The goal of this work was to find out the role of the processing method/varying type of the porosity on the electrochemical performance of the ceramic.
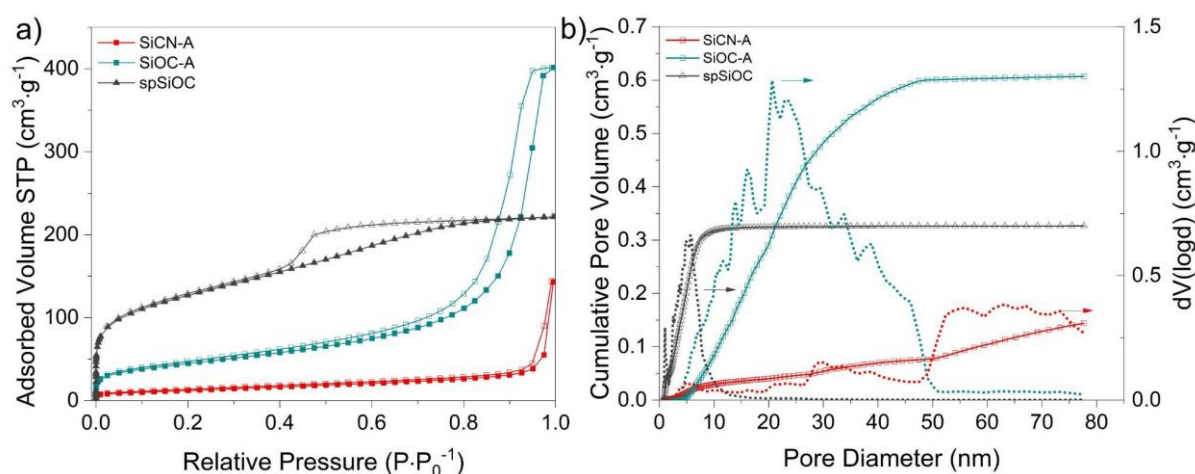
Figure 3.7 N_2 physisorption isotherms (a) and pore size distributions recorded on the porous ceramics before the sulfur infiltration (b).

Figure 3.7 shows adsorption/desorption isotherms and corresponding pore size distribution curves for porous samples before sulfur infiltration. SiOC-A and SiCN-A exhibit type IV and type II isotherms, with SiOC-A displaying a clear H1 hysteresis loop. SiCN-A has a lower total porosity volume (0.15 vs. 0.60 cm^3/g) and a hysteresis shifted to higher relative pressure, indicating the formation of larger mesopores/macropores (ca 70 vs. 20 nm). Mesoporous spSiOC (SiOC ceramic synthesized via the "polymeric spacer" method) displays a type IV isotherm with an H2 hysteresis loop, revealing ordered mesoporous structure. Specific Surface Area (SSA) correlates with pore size distribution: spSiOC reveals an SSA of 455 $m^{2/}$g, SiCN-A has 46 m^2/g due to macropores, and SiOC-A aerogels have a 161 $m^{2/}$g of SSA, aligning with intermediate pore size values. Detailed N_2 adsorption/desorption analysis results are listed in Table 3.4.

Table 3.4 Results from the Ads/Des analysis of the 3 porous PDCs.

Sample	Isotherm	Hysteresis loop	SSA ($m^2 \cdot g^{-1}$)	DFT pore volume (cc/g)	Pore size (nm)
SiOC-A	Type IV	H1	161	0.60	20
SiCN-A	Type II	--	46	0.15	70
SpSiOC	Type I/IV	H2	455	0.32	1 ~ 6
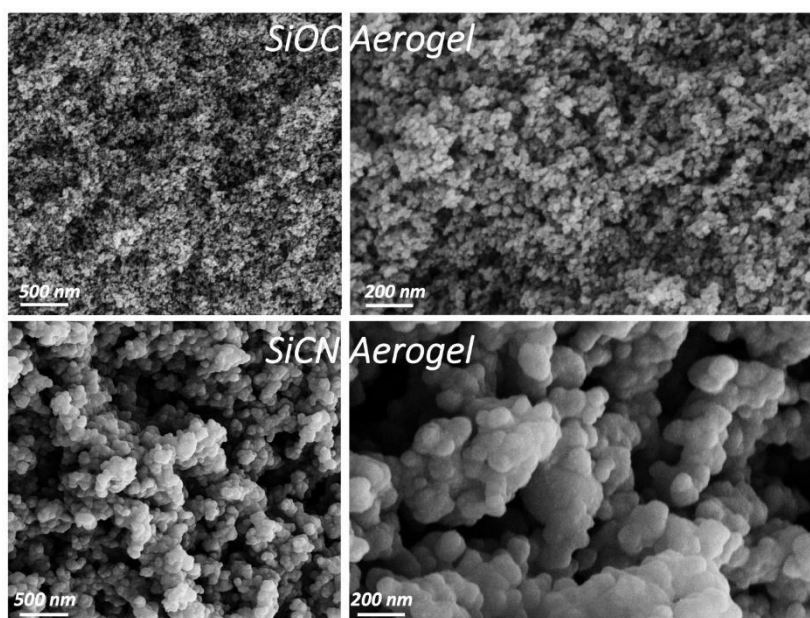
Figure 3.8 SEM picture showing the nanostructure of the ceramic aerogels: SiOC (top) and SiCN (bottom).
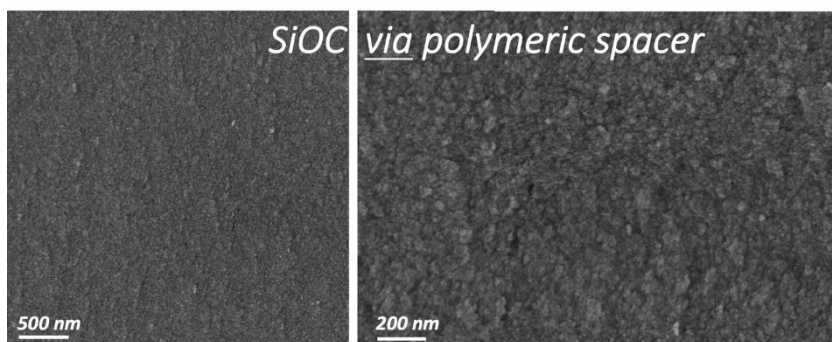
Figure 3.9 SEM of the fracture surface of the mesoporous SiOC obtained via "polymeric spacer". Porosity is indirectly observed from the roughness of the fracture surface which is clearly seen in the picture at the highest magnification (150.000 X).

SEM images of porous samples aid in characterizing ceramic scaffold nanostructures (Figure 3.8). Both aerogel samples consist of colloidal particles, typical for such materials. SiOC-A exhibits finer particles and smaller pores than SiCN-A. At the highest magnification (Figure 3.8, top right), SiOC-A's particle size is estimated in the tens of nanometers, while SiCN-A (Figure 3.8, bottom right) has particles in the hundred nanometer range. SiCN aerogel's pore sizes can extend to several hundred nanometers, including macropores (>50 nm). SEM indicates macropores in SiCN-A, suggesting N_2 sorption underestimation. Mesoporous spSiOC ceramic (Figure 3.9) shows a rough surface, aligning with N_2 sorption's fine porosity. No macropores are observed, supporting the close match between N_2 analysis-derived pore volume (0.32 cm^3/g) and the actual total pore volume.
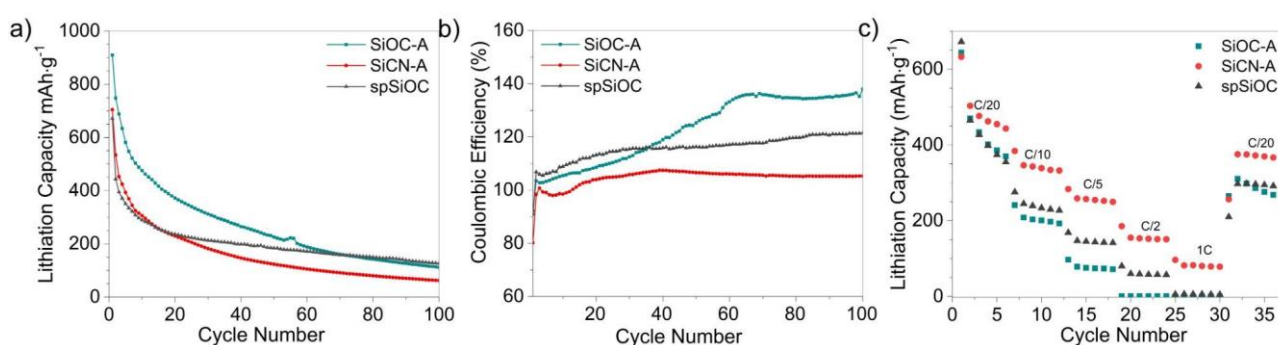
Figure 3.10 Extended constant rate cyclic stability (a); Coulombic efficiency in the 2-100 cycles range (b); Variable rate cycling of the two prepared cathodes (c).

The extended cycling stability of PDC cathodes was assessed at a C/20 rate over 1-100 cycles (Figure 3.10a). A consistent capacity loss occurrs across all PDC cathodes, indicating stabilization of specific capacity over successive measurements. After 100 cycles, SiOC-A,

SiCN-A, and spSiOC cathodes retain 112 mAh/g, 62 mAh/g, and 126 mAh/g, equivalent to 12%, 9%, and 19% of the initial capacity, respectively. Plotting cycle-by-cycle coulombic efficiency revealed efficiencies exceeding 100%, suggesting a shuttle effect as it is seen in Figure 3.10b. SiOC-A and spSiOC show efficiency increases to 140% and 120%, stabilizing after the 60th and 30th cycle, respectively, indicating a growing shuttling effect. SiCN-A's efficiency remain unaffected, attributed to its nitrogen-containing composition hindering polysulfide shuttling. The matrix material's chemical composition is deemed crucial, with SiCN's nitrogen sites chemisorbing polysulfides. spSiOC outperformed SiOC-A, possibly due to smaller pore size more efficiently impeding shuttling compared to SiOC-A's larger mesopores. Figure 3.10c illustrates variable rate cycling, highlighting SiCN-A's superior charge/discharge ability at fast rates. Ionic and electronic conductivity of the matrix material primarily determine rate performance. SiCN-A's high free carbon content enhances electrical conductivity, facilitating ion and electron transport. The slightly better high-rate performance of spSiOC over SiOC-A, despite contradictory parameters (free C content and pore size), is tentatively explained by spSiOC's large specific surface area, potentially facilitating rapid Li^+ adsorption at the contact interface.

In conclusion, polymer-derived ceramic (PDC) SiOC and SiCN aerogels are applied as sulfur-containing scaffolds in Li-S batteries. Electrochemical studies reveal that, despite impressive initial capacities, SiOC and SiCN materials experience capacity decline to the 110-60 mAh/g range, losing about 90% of their initial capacity. SiCN-A, despite having a smaller pore volume, exhibits superior electrical conductivity due to a significant fraction of free carbon, ensuring efficient adsorption of polysulfides. Fine porosity (1-10 nm) in SiOC scaffolds is found crucial in mitigating shuttling phenomena and improving charge/discharge kinetics, contrasting with larger mesopores leading to efficiency losses.

3.2. SiCN-BN composites synthesized by in situ growing boron nitride on porous carbon-containing SiCN ceramic matrix investigated as sulfur cathode supports in Li-S batteries

Porous C-rich SiCN ceramics have been shown to be a suitable host for sulfur cathodes due to its robust and stress-accommodating properties and a sufficient conductive carbon network. In order to further enhance the electrochemical performance of porous SiCN materials, novel SiCN-BN composites have been designed and synthesized. The resulting cathodes show improved electrochemical performance, with the sample SiCN-BN-950/S exhibiting 445 mAh/g of reversible capacity and 62% capacity retention after 60 cycles with 66 wt.% sulfur loading and an electrode areal density of 3.5 ~ 3.8 mg/cm^2. The combination of BN nanosheets and SiCN ceramic matrix resulted in improved structure stability and better electrochemical performance. This is the first time that in situ formation of BN nanosheets on SiCN ceramic matrix has been realized and further applied to enhance the performance of a sulfur cathode.
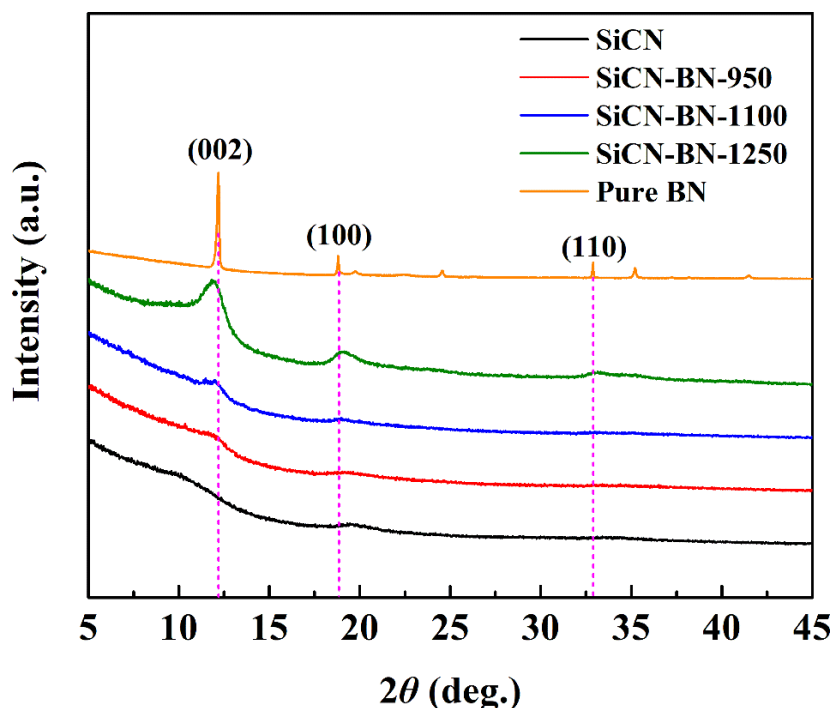
Figure 3.11 XRD patterns of all SiCN-BN samples.

X-ray diffraction (XRD) allows to assess the phase composition of SiCN-BN ceramics. In Figure 3.11, XRD patterns of pure BN, the SiCN (1000 °C) ceramic matrix, and SiCN-BN composites are presented. The pure BN, characterized by a layered hexagonal structure, exhibits distinct reflections at 2θ = 12.2°, 18.8°, and 32.8°, corresponding to the (002), (100), and (110) planes of standard crystalline BN (JCPDS no. 85 - 1068) [71, 200]. In contrast, the pure SiCN material displays an amorphous characteristic. For SiCN-BN-950, SiCN-BN-1100, and SiCN-BN-1250, the reflection at 2θ = 12.2° gradually emerges with the increasing pyrolysis

temperature from 950 °C to 1250 °C. Notably, the sample synthesized at 1250 °C also demonstrates reflections of the (100) and (110) planes of BN at $2\theta = 18.8°$ and $2\theta = 32.8°$. This observation suggests that an elevated pyrolysis temperature is advantageous for the formation of crystalline boron nitride.
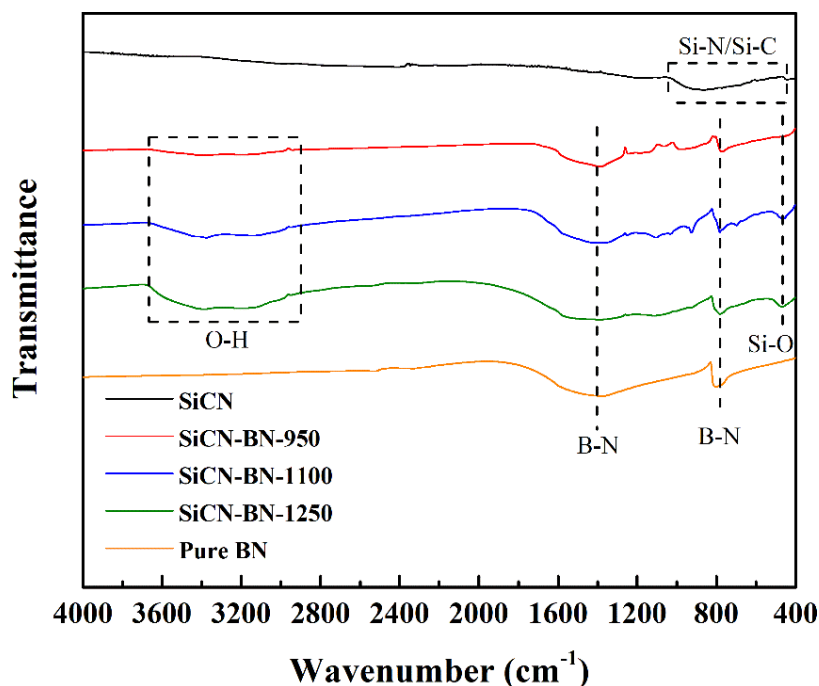
Figure 3.12 FTIR spectra of SiCN-BN samples annealed at three different temperatures compared to SiCN (1000 °C) and pure BN.

To corroborate the presence of boron nitride (BN) in the synthesized composites, Fourier transform infrared (FTIR) spectroscopy measurements were conducted, and the findings are depicted in Figure 3.12. Sample SiCN presents clear Si–N and Si–C bonds between 400 cm^{-1} to 1000 cm^{-1} [201]. In comparison to the SiCN sample, all SiCN-BN composites distinctly display two characteristic peaks of hexagonal BN at 780 cm^{-1} and 1400 cm^{-1}, corresponding to the B-N bending and B-N stretching modes, respectively. This observation aligns with prior investigations [27]. The outcomes validate the incorporation of BN in the SiCN ceramic matrix. Moreover, as the annealing temperature increases, the intensity of BN peaks rises. Additionally, a broad peak between 3000 cm^{-1} and 3700 cm^{-1} is evident, attributed to water molecules or O–H stretching vibrations, typically present in BN composite systems [27, 202].

The results of the elemental analysis are shown in Table 3.5 and Table 3.6. The change in elemental composition during the annealing procedure is mainly due to the following potential

reactions:

$$H_3BO_3 \rightarrow HBO_2 + H_2O \ (T > 140\,°C) \hspace{3cm} (1)[203, 204]$$

$$4HBO_2 \rightarrow H_2B_4O_7 + H_2O \ (T > 180\,°C) \hspace{2.5cm} (2)[203, 204]$$

$$CO(NH_2)_2 + H_2O \rightarrow CO_2 + 2NH_3 \ (200\sim400\,°C) \hspace{1.5cm} (3)[205]$$

$$C + H_2O \rightarrow CO + H_2 \ (T > 200\,°C) \hspace{3cm} (4)[206]$$

$$C + CO_2 \rightarrow 2CO \ (450\sim1000\,°C) \hspace{3cm} (5)[207]$$

$$H_2B_4O_7 \rightarrow 2B_2O_3 + H_2O \ (T > 530\,°C) \hspace{2cm} (6)[203, 204, 208]$$

$$B_2O_3 + 2NH_3 \rightarrow 2BN + 3H_2O \ (T = 900\,°C) \hspace{2cm} (7)\ [209]$$

$$B_2O_3 + CO(NH_2)_2 \rightarrow 2BN + CO_2 + 2H_2O \ (T > 1000\,°C) \hspace{1cm} (8)[209]$$
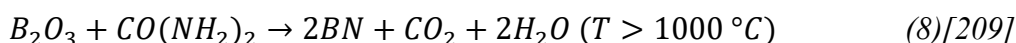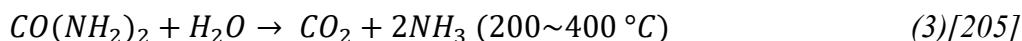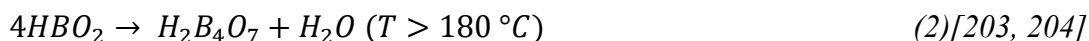
Compared to pure SiCN, the C content in sample SiCN-BN-950 decreases from 67.5 wt.% to 29.5 wt.% due to carbothermal reductions (4) and (5), facilitated by products (CO_2 and H_2O) from reactions (1-3). Additionally, B and N content increases to 14.4 wt.% and 17.7 wt.% from 0 wt.% and 4.76 wt.%, respectively. Normalizing on Si wt.%, assuming no silicon loss during annealing, clarifies the elemental content changes. The increased oxygen content may result from nitrogen replacement with oxygen (from water formed in reactions (1,2,6,7,8)) in the SiCN network and from the alumina furnace annealing environment. XPS analysis also confirms this. Under air storage, Si–O bonds may attract humidity, forming O–H bonds, supported by increased O–H detected in SiCN-BN composites via FTIR. Increasing annealing temperature to 1100 ℃ and 1250 ℃ causes minimal changes in B and N contents but further decreases carbon content to 6.8 wt.% at 1100 °C and 0.5 wt.% at 1250 °C due to continued reaction (8), generating more CO_2 and H_2O, intensifying further consumption of free carbon.

Table 3.5 Results of elemental analysis. Possible trace amount of hydrogen present in the SiCN ceramic has been considered as negligible.

Sample	SiCN	SiCN-BN-950	SiCN-BN-1100	SiCN-BN-1250
Si wt.%	20.5	15.3	19.2	22.9
C wt.%	67.5	29.5	6.8	0.5
N wt.%	4.8	17.7	18.9	22.3
B wt.%	-	14.4	23.1	25.7
O wt.%	7.2	23.1	32.0	28.6

Table 3.6 Result of element analysis after normalization based on Si.

Sample	SiCN	SiCN-BN-950	SiCN-BN-1100	SiCN-BN-1250
Si	1	1	1	1
C	3.29	1.93	0.35	0.02
N	0.23	1.16	0.98	0.97
B	-	0.94	1.20	1.12
O	0.35	1.51	1.67	1.25
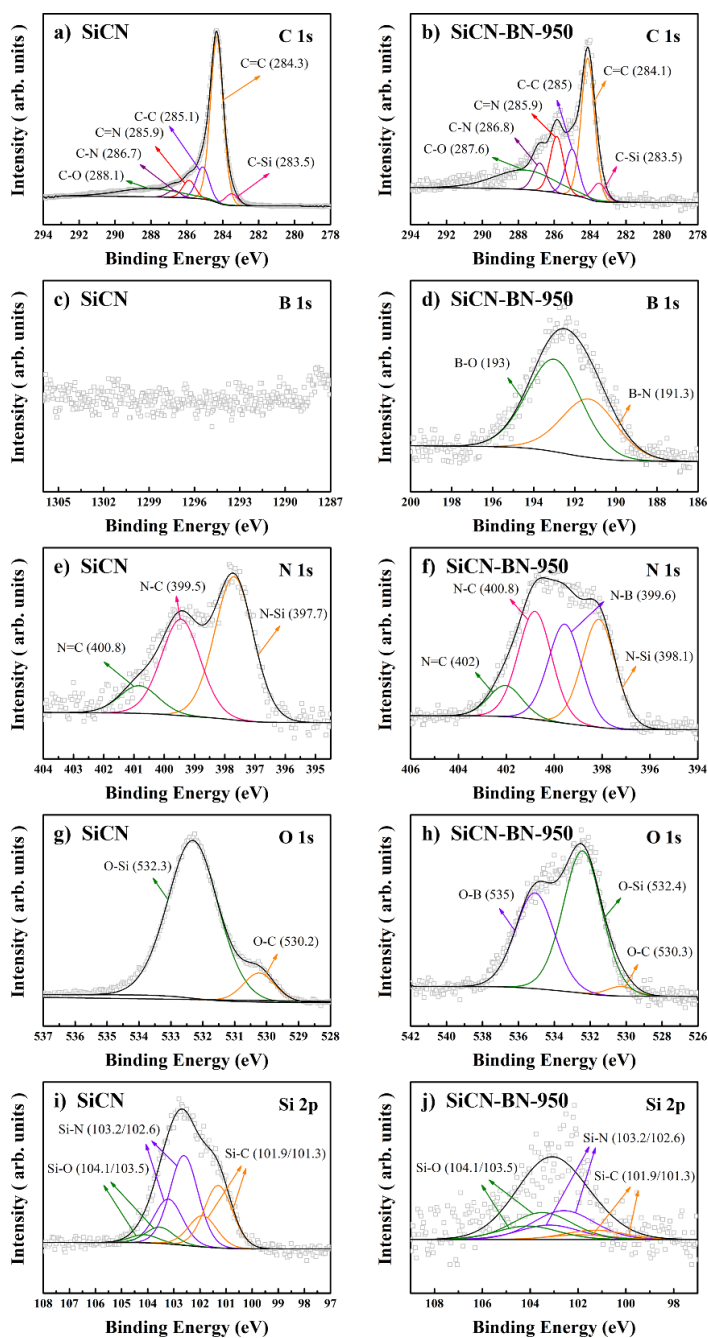
Figure 3.13 XPS spectra of SiCN and SiCN-BN-950: (a,b) C 1s, (c,d) B 1s, (e,f) N 1s, (g,h) O

1s, (i,j) Si 2p.

Covalent bonding in SiCN and SiCN-BN-950 was analyzed via X-ray photoelectron spectroscopy (XPS), with high-resolution spectra presented in Figure 3.13a-j. Both materials exhibit C 1s spectra with six components: C–Si, C=C, C–C, C=N, C–N, and C–O, with C–C/C=C predominating [210]. Annealing increased C=N and C–N, indicating N replacing sp^2 C in the matrix, potentially from urea or BN. Elevated C–N/C=N could improve electrochemical performance by inhibiting polysulfide shuttling. SiCN-BN-950's B 1s spectrum shows peaks at 191.3 eV and 193 eV, indicative of BN presence. Another peak suggests B_2O_3 presence. SiCN's N 1s spectrum displays N–Si, N–C, and N=C peaks, with SiCN-BN-950 exhibiting an additional N–B peak. Both B 1s and N 1s spectra confirm BN presence [27, 70]. SiCN-BN-950 shows increased O–Si relative to SiCN based on O–C content, with an additional O–B peak attributed to B_2O_3 [211]. Si 2p spectra indicate Si–C, Si–N, and Si–O, with decreases in Si–C and increases in Si–N and Si–O after the annealing, consistent with elemental analysis.
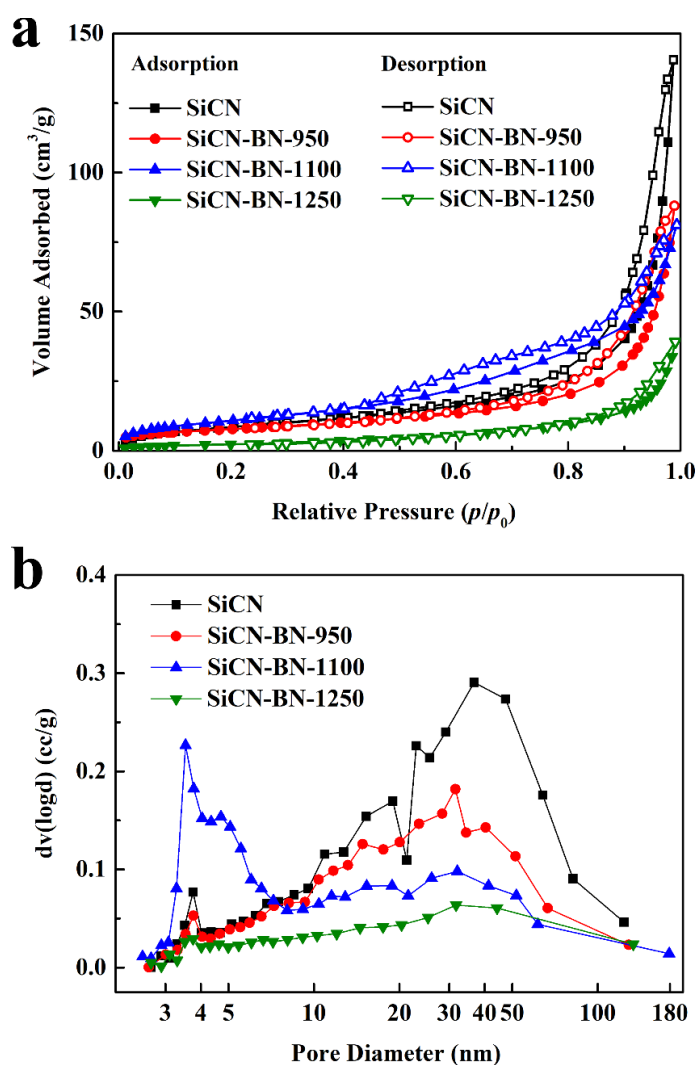
Figure 3.14 Nitrogen adsorption-desorption isotherms (a) and pore size distribution (b) of SiCN

ceramic and SiCN-BN composites.

N_2 adsorption-desorption isotherms (Figure 3.14a) are analyzed via linear BET plots to determine specific surface area (SSA) and pore size distribution. Isotherms shows characteristics of both type II and type IV [212-214]. At high relative pressures ($p/p_0 > 0.4$), all samples exhibit reversible hysteresis loops, indicative of capillary condensation in mesopores (type IV). SiCN-BN-1250 shows hysteresis only at high pressures. However, SiCN, SiCN-BN-950, and SiCN-BN-1100 display adsorption curves trending towards infinity at high relative pressures, suggesting macropores (type II). Pore size distribution (Figure 3.14b) indicates pores ranging from 2 to 180 nm, with SiCN-BN-1100 exhibiting significant small mesopores (3 ~ 10 nm) due to carbothermal reduction. As annealing temperature increased from 950 to 1250 °C, SSA and V_t decrease overall. The decline in pore volume from SiCN to SiCN-BN-1250 suggests BN partially blocks pores. Additionally, SiCN-BN-1250 has low pore volume (0.06 cm³/g), surface area (8.5 m²/g), and a nonporous character, possibly due to BN crystallization at this temperature, leading to pore closure.

Table 3.7 Summary of the results obtained from BET analysis.

Sample	SiCN	SiCN-BN-950	SiCN-BN-1100	SiCN-BN-1250
SSA (m²/g)	32.3	27.6	40.7	8.5
V_t (cm³/g)	0.22	0.14	0.12	0.06
APD (nm)	26.9	19.7	12.0	26.5
Isotherm type	II + IV	II + IV	II + IV	II + IV
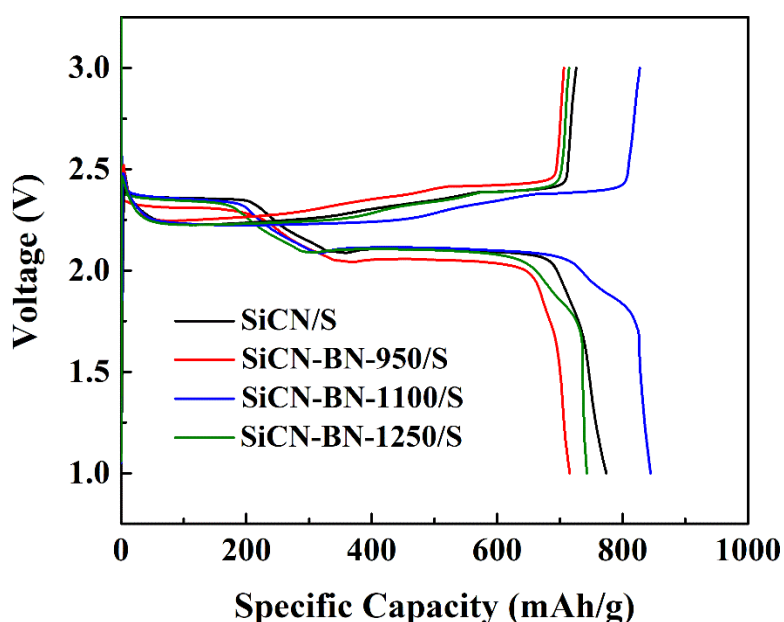
Figure 3.15 Lithiation curves (a) and delithiation curves (b) of SiCN/S and all SiCN-BN/S

samples.

The initial lithiation/delithiation processes recorded for all investigated samples are plotted in Figure 3.15 and the initial discharge capacity as well as a corresponding columbic efficiency of the sample SiCN/S and SiCN-BN/S are shown in Table 3.8. Despite the initial discharge capacity of the sample SiCN-BN-950/S being slightly lower compared to the sample SiCN/S, its initial coulombic efficiency is close to 100 %, indicating a high reversibility of the sulfur cathode. Regarding the sample SiCN-BN-1100/S, the obviously increased initial discharge and charge capacity are attributed to its significantly increased number of small mesopores and degree of graphitization of carbon according to the result of BET and Raman. The initial coulombic efficiency of sample SiCN-BN-1100/S changed little representing the closer reversibility with that of sample SiCN-BN-950/S during the first cycle. As for the sample SiCN-BN-1250/S, in turn reduced mesopores and continued oxidation of the porous carbon according to the results of BET and elemental analysis contributed to the composite exhibiting a compounded adverse effect, resulting in deteriorative initial discharge capacity and coulombic efficiency.
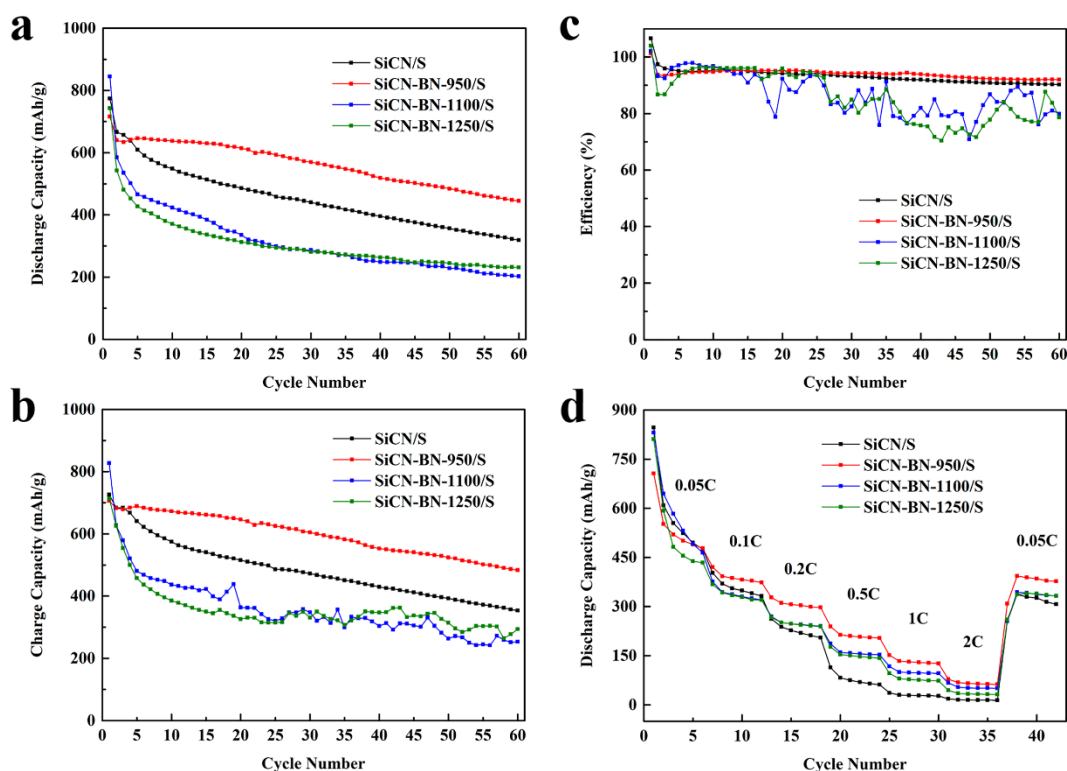
Figure 3.16 Cycling performance of the SiCN/S and SiCN-BN/S. Discharge capacity (a), charge capacity (b), efficiency (c), and rate capacity (d).

Figures 3.16a-c show the extended cycling discharge/charge specific capacity, and coulombic

efficiency of both SiCN/S and SiCN-BN/S (see also the values listed in Table 3.5). Despite that sample SiCN-BN-950/S shows the lowest initial discharge capacity of 716 mAh/g, it surpasses those of samples SiCN-BN-1100/S and SiCN-BN-1250/S from the second cycle and even surpasses that of SiCN/S starting from the 4th cycle. The sample SiCN-BN-950/S retained the highest discharge capacity in all subsequent cycles, with more than 600 mAh/g over the first 23 cycles. After 60 cycles, its reversible capacity was 445 mAh/g, whereas SiCN/S had only 319 mAh/g. The capacity retentions after 60 cycles of SiCN-BN-950/S and SiCN/S were 62 % and 41 %, respectively. This reveals that the introduction of BN into the ceramic matrix significantly enhances the cycling stability of SiCN-BN-950/S. This is mainly attributed to the synergy between BN and the porous free carbon for the polysulfides capturing. Additionally, it is also ascribed to the increased SSA of the mesopores which causes an improvement of physical adsorption for the polysulfides capturing. Therefore, the "shuttle effect" remains suppressed during electrochemical reactions. As concerns the samples SiCN-BN-1100/S and SiCN-BN-1250/S, their extended discharge capacities are very close to each other but significantly lower than SiCN/S. Besides, they also present relatively lower capacity retentions after 60 cycles of only 24 % and 31 %, respectively. This is also expected because an increased annealing temperature leads to significantly decreased porous free carbon resulting in an impaired synergy with BN insufficient for surpassing the "shuttle effect". After 15 cycles, the charge capacity of the samples SiCN-BN-1100/S and SiCN-BN-1250/S fluctuates due to the increased "shuttle effect" resulting from the diminished performance gain from porous carbon [2, 186, 215, 216]. The coulombic efficiencies of samples SiCN-BN-950/S and SiCN/S exhibited remarkable stability over 90 % in 60 cycles, whereas the SiCN-BN-1100/S and SiCN-BN-1250/S presented unstable fluctuations with efficiencies between 80-90 % originating from the increased "shuttle effect".

Table 3.8 Electrochemical parameters of the sulfurized SiCN samples.

Sample	Initial discharge Capacity (mAh/g)	Initial Coulombic Efficiency (%)	Reversible Capacity after 60 Cycle (mAh/g)	Capacity Retention (%)
SiCN/S	774	107	319	41
SiCN-BN-950/S	716	101	445	62
SiCN-BN-1100/S	845	102	202	24
SiCN-BN-1250/S	743	104	231	31

The rate capabilities of all samples are shown in Figure 3.16d. Although the sample SiCN-BN-950/S was unremarkable at the lowest cycling currents of 0.05C, its discharge capacity surpassed all other samples from the 0.1C cycle and remained the best in all subsequent cycles. This signifies that the synergy of BN and porous free carbon also resulted in a superior rate performance of the composites. Interestingly, starting from 0.2 C, the sample SiCN/S presented the lowest rate capacity performance, which indicated it underperforms under high current. Therefore, it reveals that the existence of BN indeed increased rate cycling performance of the samples.
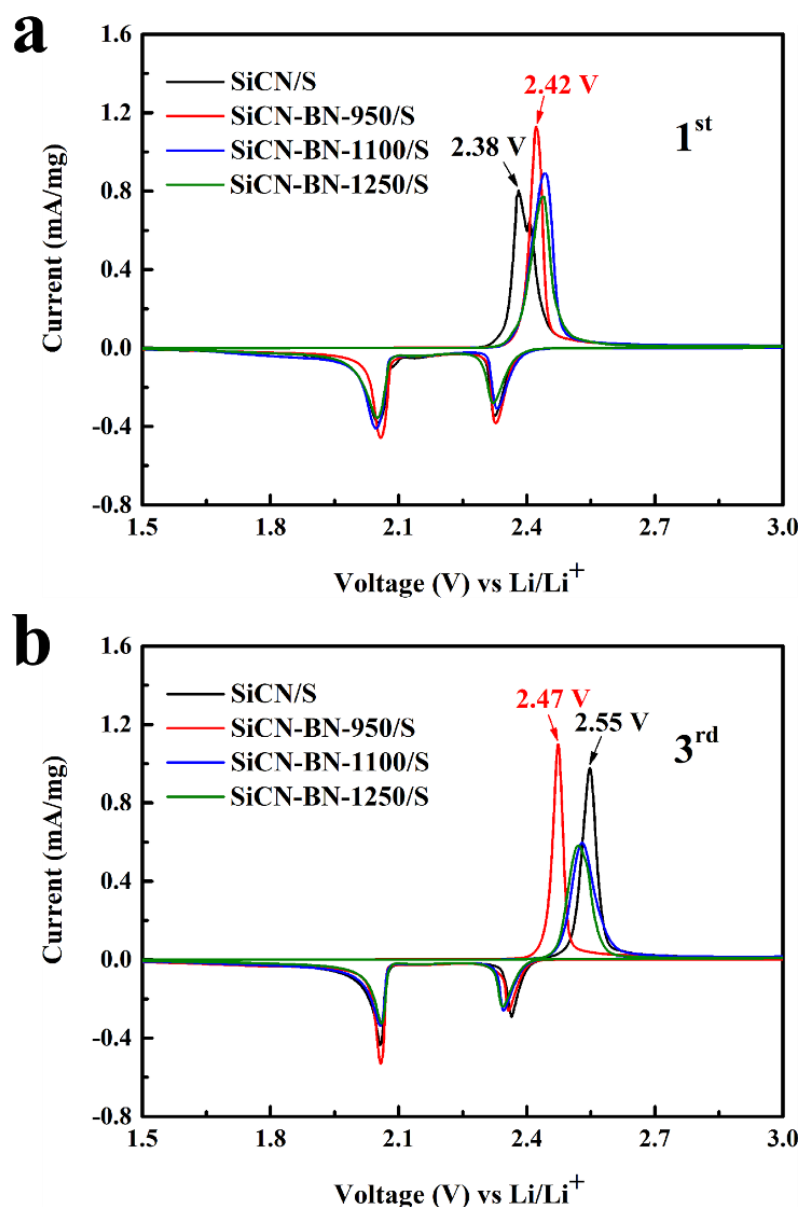
Figure 3.17 Cyclic voltammograms of SiCN/S and SiCN-BN/S in the first (a) and the third (b) cycle.

Cyclic voltammetry (CV) measurements in Figure 3.17 reveal two cathodic peaks and one

anodic peak, representing sequential reduction processes. S_8 molecules transformed into soluble polysulfides Li_2S_x (4 < x < 8), then into solid Li_2S_2 and Li_2S. Lithium sulfide oxidized to elemental sulfur, consistent with galvanostatic discharge/charge profiles. SiCN-BN-950/S exhibited higher initial cycle potentials (2.06 V and 2.33 V) and peak current density, indicating stronger sulfur reduction and minimal cathodic polarization. SiCN-BN-950/S's anodic peak shifted to 2.42 V, suggesting increased electrode polarization, possibly due to decreased carbon and added insulating BN. Higher annealing temperatures (1100 °C) shift cathodic and anodic peaks, increasing polarization due to reduced carbon. SiCN-BN-1250/S maintained equilibrium electrode potential, but current density decreased, indicating weaker electrochemical reactions. In the third cycle, SiCN-BN-950/S showed the lowest anodic peak potential (2.47 V) and strong current density, suggesting superior stability. SiCN/S exhibited pronounced rightward shifting (2.55 V), indicating compromised stability. SiCN-BN-1100/S and SiCN-BN-1250/S showed weakened electrochemical reactions, with rightward-shifting anodic peaks and decreased current intensity. Incorporating BN at 950 °C improved polysulfides capture, but higher annealing temperatures lead to carbon consumption and reduced electrochemical performance.

Summarizing, a porous SiCN-BN composite has been synthesized via a two-step process, involving polysilazane pyrolysis and subsequent annealing with urea and boric acid. This innovative approach facilitated in-situ growth of BN sheets within the porous carbon-rich SiCN ceramic matrix. The SiCN-BN-950/S composite exhibited enhanced electrochemical performance compared to unmodified porous SiCN, with a stable reversible capacity of 445 mAh/g (62% retention after 60 cycles), high active material density (3.5 ~ 3.8 mg/cm^2), and 66 wt.% sulfur loading. The BN-modified SiCN matrix offered structural and chemical stability, especially the BN providing the non-polar adsorption for the polysulfides. Besides, the composite's ample porosity accommodates high sulfur loading. The synergistic effects between BN and SiCN contribute to an excellent electrochemical performance.

4. Summary and outlook

4.1. Summary

This PhD thesis focuses on new materials with a tailored microstructure for the application as sulfur cathode in lithium sulfur batteries. Designed porous C-rich polymer-derived ceramics were used as sulfur host for the cathode in lithium sulfur batteries. The synthesis of these materials includes the crosslinking reaction of a commercial perhydropolysilazane with divinylbenzene by Schlenk techniques and pyrolysis in Schlenk tube furnace in a temperature range from 800 °C to 1600 °C. Moreover, three PDC aerogels were obtained via CO_2 supercritical drying and "polymeric spacer" method. Besides, ball milling, sieving, ultrasonic dispersion, and vacuum drying, etc. were also employed to process the final ceramic with a required microstructure. After the subsequent sulfur embedding into the ceramic matrices by a melting-diffusion process and subsequent cell fabrication, the electrochemical performance was investigated. To further enhance the stability of the synthesized sulfur cathode, nanostructured BN has been introduced in a SiCN ceramic matrix to effectively trap the polysulfides thus hampering the "shuttle effect" of LSB. Figure 4.1 highlights the progress of our research studies obtained within 4 years.

C-rich SiCN 1000-1600

01 C-rich SiCN-1000 reveals > 310 mAh/g over 40 cycles at high sulfur content of 66 wt.%

C-rich SiCN-900 exhibits 195 mAh/g over 50 cycles with a high sulfur content of 66 wt.%

02 **C-rich SiCN 800-1100**

PDC Aerogels

03 All PDC aerogel cathodes show stable capacities in the 60–120 mAh/g range after 100 cycles

SiCN-BN-950/S delivers a 445 mAh/g of the reversible capacity and 62 % of the capacity retention after 60 cycles

04 **SiCN-BN 950-1250**

Figure 4.1 Summary of the obtained research progress related to C-rich SiCN/SiOC ceramics as cathode material in lithium sulfur batteries.

The first part of this work (Chapter 3.1) focuses on the synthesis, characterization, and electrochemical investigations of C-rich SiCN ceramics and PDCs aerogels as sulfur host for the cathode in LSB. For C-rich SiCN ceramics pyrolyzed under 800-1600 °C, different

electrochemical performances were achieved based on the differently developed morphology. Among them, the sample SiCN-1000 pyrolyzed at 1000 °C shows the best electrochemical performance (reversible capacity is more than 310 mAh/g over 40 cycles). Key conclusions drawn from the analysis are as follows: (1) The presence of amorphous, highly defective free carbon within the SiCN matrix creates a highly conductive environment conducive to sulfur infiltration. (2) Carbothermal reduction at higher temperatures results in the separation of free carbon and SiCN ceramic phases, yielding less disordered free carbon and non-conducting SiC, thus, leading to increased shuttling effect after 20 cycles. (3) The presence of nitrogen in SiCN processed at lower temperatures appear to stabilize polysulfides by suppressing the migration of soluble polysulfides during cycling and thereby weakening the shuttling effect with the result of an improved cycling stability. The microporous morphology of the sulfur support is considered to be advantageous for the cathode stabilization, though not a strict requirement, as other properties also play a crucial role. The high efficiency of SiCN ceramics pyrolyzed at low temperatures is attributed to the synergistic effects of the mesoporous ceramic matrix containing nitrogen and the LiNO$_3$ electrolyte additive, which promoted the formation of a stable protective film on the lithium anode. In conclusion, the electrochemical performance of our synthesized SiCN cathode material strongly depends on factors such as the developed microstructure, level of graphitization of the segregated carbon, and its electrical conductivity. Moreover, PDC SiOC and SiCN aerogels were synthesized as scaffolds for sulfur containment in Li-S batteries. Despite initial high capacities, both SiOC and SiCN materials exhibited capacity fading (110-60 mAh/g) with approximately 90% loss of their first specific capacity. The material SiCN-A showed enhanced electrical conductivity despite its low pore volume and the presence of nitrogen contributed to the adsorption of the formed polysulfides. The fine porosity (1-10 nm) present in the obtained SiOC scaffolds contributed to mitigate the shuttling phenomena of polysulfides, while larger pores resulted in efficiency losses.

The second part of this work (Chapter 3.2) is concerned with BN-modified SiCN ceramic as the host for sulfur cathode. After pyrolysis of the SiCN precursor, the synthesized C-rich SiCN ceramic was further mixed with boric acid and urea, subsequently annealed under 950 °C in a Schlenk furnace. Finally, a porous SiCN-BN composite with a unique microstructure comprised of porous SiCN and BN nanosheets was obtained. This blend structure leads to an enhancement of the electrochemical properties of the sulfur cathode. The sample SiCN-BN-950/S delivers an excellent cycling stability, amounting 445 mAh/g of the reversible capacity and 62 % of capacity retention after 60 cycles. Besides, 3.5 ~ 3.8 mg/cm^2 of areal density as well as 66 wt.%

of sulfur loading are achieved. We attribute the enhanced electrochemical performance to a synergistic effect involving the following features: (1) The SiCN ceramic matrix exhibits superior structural and chemical stability; (2) the formed porous free carbon in the SiCN ceramic matrix provides efficient conductive network and physical adsorption sufficient for trapping generated polysulfides; (3) confined porous BN nanosheets embedded in the SiCN matrix strongly contribute to trap polysulfides; (4) both, porous carbon and porous BN, provide sufficient internal space for high sulfur loading; 5) a synergistic effect between BN and carbon-rich SiCN ceramic matrix contributes to an excellent electrochemical performance.

Table 4.1 Comparative table of electrochemical performances of sulfur cathode materials for Li-S battery storage.

Sulfur host material	Sulfur content (*wt.* %)	SSA (m²/g)	Initial capacity (mAh/g)	Reversible capacity (mAh/g)	Number of cycles	Ref.
SiCN-1000	66	72	722	313	40	This work
SiCN-BN-950	66	28	716	445	60	This work
SiCN-A	66.7	46	704	62	100	This work
SiOC-A	64.7	161	909	112	100	This work
spSiOC	62.5	455	671	126	100	This work
SiOCN-5/S- CP	70	38.2	1015	374.5	500	[217]
S-CNTs/SiC	75.6	61.6	1008	316	400	[218]
HPCN11	76	2789	1129	590	400	[219]
S-SiOC	70	235	1420	711	50	[220]
p-BN/CNTs	66	168	1052	816	500	[27]
BN/graphene	75	157	1150	1050	100	[69]
TTCN	71	822.8	1274	918	50	[221]
NG	65.2	643.5	1030	830	100	[222]
SWCNH	80	211	1650	573	200	[215]
CNT@MPC	49	936	1670	1149	200	[223]
MMCS	60.6	1013	>1212	1014	100	[224]
BN-K-1KOH	69	1152	1150.9	593.9	1000	[70]
VN/G	59	37	1471	1252	100	[191]

In summary, a series of C-rich SiCN ceramics, PDC aerogels, as well as boron nitride modified SiCN composites have been synthesized and investigated. The presented results are rationalized

in a view of the microstructural integrity of the synthesized porous C-rich SiCN ceramics in line with an advantage of the presence of nitrogen. Besides, enhancing the electrochemical stability of the sulfur cathode has been achieved in combination with the synergistic effect of boron nitride embedded in the stable C-rich SiCN ceramic matrix. Table 4.1 shows the comparison of electrochemical performance of different sulfur cathode that can be compared with the result presented in this dissertation. Although the electrochemical performance of our ceramic hosts is relatively low, the preparation process of most high-performance materials is complicated and costly, especially for the nanomaterials. They are not suitable for commercial mass production. Of course, our sulfur cathodes are also some distance away from commercial production. However, the PDC methods presented in this PhD dissertation indeed show facile and efficient synthesis routes for the preparation of a sulfur cathode for large-scale commercial applications of lithium sulfur batteries and provides a reference for combining SiCN and SiCO ceramic matrices and boron nitride in the energy storage research field.

4.2. Outlook

This PhD dissertation demonstrates the feasibility of using polymer-derived porous C-rich SiCN, SiOC and SiCN/BN ceramic matrices for sulfur cathodes in lithium sulfur batteries. While a remarkable performance has already been achieved, there is significant room for improvement of these composites.

Firstly, all electrochemical experiments in this work have been realized with the material sulfur mass loading of 66 wt.%. Therefore, it is worthwhile to further explore the effect of varying the ratio of SiCN, carbon, BN, and sulfur in these composites on the electrochemical performance.

Secondly, Chapter 3.2 focuses on the electrochemical performance of BN modified SiCN ceramics. One of the raw materials of the annealing procedure is C-rich SiCN pyrolyzed at 1000 °C which mainly show mesoporous and macoporous features. Employing BN into C-rich SiCN ceramics pyrolyzed at 1400 °C and 1600 °C which exhibit microporous structure as the sulfur cathode could be a promising attempt since the micropores can effectively hinder the shuttle effect. Besides, the higher porosity of the SiCN ceramic pyrolyzed at 1400 °C and 1600 °C may lead to enhanced sulfur loading. The above-mentioned two features may result in enhanced cycling stability.

Thirdly, based on the study of SiCN-BN as sulfur host in cathode, BN modified porous SiOC

as sulfur cathodes is another interesting research direction. In the amorphous network of the SiOC ceramic, oxygen replaces nitrogen. The binding ability of oxygen for the polysulfides [27] may bring unexpected influence to the sulfur cathode.

Fourthly, according to the previous research about polymer-derived SiBCN ceramics of our group, polymer-derived SiBCN ceramics also have potential to be as sulfur host in cathode due to their high strength, low density, excellent high-temperature stability, and resistance to oxidation and creep. More importantly, they already have B-N bonds directly after crosslinking and pyrolysis, without any annealing for the BN formation. Given that research on polymer-derived porous SiBCN is relatively rare, the study will focus on the fabrication and control of pore structure of polymer-derived SiBCN since the ceramics should have enough interspace for accommodating sulfur.

Fifthly, so far, porous C-rich SiCN ceramics are mainly used as sulfur hosts in the cathode of lithium sulfur batteries. Future interesting studies could be devoted to utilizing SiCN- or SiOC-based ceramics as separators in LiSBs. Due to the physical adsorption feasibility to trap polysulfides, which is related to the porous and nitrogen containing SiCN microstructure as well as to the confinement of boron nitride in SiCN/BN composites, separators made from these ceramic matrices could potentially enhance the performance of lithium sulfur batteries. Additionally, introducing other inorganic compounds such as MnO_2, V_2O_5, and MoS_2 embedded in the PDC matrices to replace boron nitride is a promising approach. Based on the existing research, the above-mentioned compounds provide confinement properties like boron nitride, suggesting that their inclusion may also lead to an improved sulfur cathode performance.

In summary, there are numerous areas that require further in-depth PDC related research in future work. Given the cost-effectiveness and efficiency in the synthesis, PDC-based sulfur cathodes are emerging as a promising technology. More broadly, the application of ceramic-based materials in energy conversion and storage will continue to expand worldwide.

5. References

[1]   M. Li, J. Lu, Z. Chen, K. Amine, 30 Years of Lithium-Ion Batteries. *Advanced Materials* **30** 1800561 (2018).

[2]   A. Manthiram, Y. Fu, S.-H. Chung, C. Zu, Y.-S. Su, Rechargeable Lithium-Sulfur Batteries. *Chemical Reviews* **114** 11751-11787 (2014).

[3]   A. Manthiram, Y. Fu, Y.-S. Su, Challenges and Prospects of Lithium-Sulfur Batteries. *Accounts of Chemical Research* **46** 1125-1134 (2013).

[4]   D.R. Rolison, L.F. Nazar, Electrochemical energy storage to power the 21st century. *MRS Bulletin* **36** 486-493 (2011).

[5]   W. Liu, T. Placke, K.T. Chau, Overview of batteries and battery management for electric vehicles. *Energy Reports* **8** 4058-4084 (2022).

[6]   Z.W. Seh, Y. Sun, Q. Zhang, Y. Cui, Designing high-energy lithium-sulfur batteries. *Chemical Society Reviews* **45** 5605-5634 (2016).

[7]   M.S. Whittingham, Electrical Energy Storage and Intercalation Chemistry. **192** 1126-1127 (1976).

[8]   B.R. Thomas, *Linden's Handbook of Batteries, Fourth Edition*. (McGraw-Hill Education, New York, ed. 4th ed., 2011).

[9]   K. Amine, R. Kanno, Y. Tzeng, Rechargeable lithium batteries and beyond: Progress, challenges, and future directions. *MRS Bulletin* **39** 395-401 (2014).

[10]   A. Manthiram, S.-H. Chung, C. Zu, Lithium-Sulfur Batteries: Progress and Prospects. *Advanced Materials* **27** 1980-2006 (2015).

[11]   J. Hou, X. Tu, X. Wu, M. Shen, X. Wang, C. Wang, C. Cao, H. Peng, G. Wang, Remarkable cycling durability of lithium-sulfur batteries with interconnected mesoporous hollow carbon nanospheres as high sulfur content host. *Chemical Engineering Journal* **401** 126141 (2020).

[12]   Z.-L. Xu, J.-K. Kim, K. Kang, Carbon nanomaterials for advanced lithium sulfur batteries. *Nano Today* **19** 84-107 (2018).

[13]   L. Ma, K.E. Hendrickson, S. Wei, L.A. Archer, Nanomaterials: Science and applications in the lithium-sulfur battery. *Nano Today* **10** 315-338 (2015).

[14]   J.-L. Shi, C. Tang, H.-J. Peng, L. Zhu, X.-B. Cheng, J.-Q. Huang, W. Zhu, Q. Zhang, 3D Mesoporous Graphene: CVD Self-Assembly on Porous Oxide Templates and Applications in High-Stable Li-S Batteries. *Small* **11** 5243-5252 (2015).

[15]   L. Ma, R. Chen, G. Zhu, Y. Hu, Y. Wang, T. Chen, J. Liu, Z. Jin, Cerium Oxide Nanocrystal Embedded Bimodal Microniesoporous Nitrogen-Rich Carbon

Nanospheres as Effective Sulfur Host for Lithium-Sulfur Batteries. *Acs Nano* **11** 7274-7283 (2017).

[16]   F. Pei, T. An, J. Zang, X. Zhao, X. Fang, M. Zheng, Q. Dong, N. Zheng, From Hollow Carbon Spheres to N-Doped Hollow Porous Carbon Bowls: Rational Design of Hollow Carbon Host for Li-S Batteries. *Advanced Energy Materials* **6** 1502539 (2016).

[17]   J. Xie, B.-Q. Li, H.-J. Peng, Y.-W. Song, M. Zhao, X. Chen, Q. Zhang, J.-Q. Huang, Implanting Atomic Cobalt within Mesoporous Carbon toward Highly Stable Lithium-Sulfur Batteries. *Advanced Materials* **31** 1903813 (2019).

[18]   J. Park, B.-C. Yu, J.S. Park, J.W. Choi, C. Kim, Y.-E. Sung, J.B. Goodenough, Tungsten Disulfide Catalysts Supported on a Carbon Cloth Interlayer for High Performance Li-S Battery. *Advanced Energy Materials* **7** 1602567 (2017).

[19]   D. Gueon, J.T. Hwang, S.B. Yang, E. Cho, K. Sohn, D.K. Yang, J.H. Moon, Spherical Macroporous Carbon Nanotube Particles with Ultrahigh Sulfur Loading for Lithium-Sulfur Battery Cathodes. *ACS Nano* **12** 226-233 (2018).

[20]   J.T. Lee, Y. Zhao, S. Thieme, H. Kim, M. Oschatz, L. Borchardt, A. Magasinski, W.-I. Cho, S. Kaskel, G. Yushin, Sulfur-Infiltrated Micro- and Mesoporous Silicon Carbide-Derived Carbon Cathode for High-Performance Lithium Sulfur Batteries. *Advanced Materials* **25** 4573-4579 (2013).

[21]   S.S. Zhang, D.T. Tran, Pyrite FeS2 as an efficient adsorbent of lithium polysulphide for improved lithium-sulphur batteries. *Journal of Materials Chemistry A* **4** 4371-4374 (2016).

[22]   C. Ye, L. Zhang, C. Guo, D. Li, A. Vasileff, H. Wang, S.-Z. Qiao, A 3D Hybrid of Chemically Coupled Nickel Sulfide and Hollow Carbon Spheres for High Performance Lithium-Sulfur Batteries. *Advanced Functional Materials* **27** 1702524 (2017).

[23]   T. Chen, L. Ma, B. Cheng, R. Chen, Y. Hu, G. Zhu, Y. Wang, J. Liang, Z. Tie, J. Liu, Z. Jin, Metallic and polar Co9S8 inlaid carbon hollow nanopolyhedra as efficient polysulfide mediator for lithium-sulfur batteries. *Nano Energy* **38** 239-248 (2017).

[24]   X. Wang, G. Li, J. Li, Y. Zhang, A. Wook, A. Yu, Z. Chen, Structural and chemical synergistic encapsulation of polysulfides enables ultralong-life lithium-sulfur batteries. *Energy & Environmental Science* **9** 2533-2538 (2016).

[25]   S.B. Patil, H.J. Kim, H.-K. Lim, S.M. Oh, J. Kim, J. Shin, H. Kim, J.W. Choi, S.-J. Hwang, Exfoliated 2D Lepidocrocite Titanium Oxide Nanosheets for High Sulfur Content Cathodes with Highly Stable Li-S Battery Performance. *Acs Energy Letters* **3** 412-419 (2018).

[26] J. Zhang, C. You, W. Zhang, J. Wang, S. Guo, R. Yang, Y. Xu, Conductive bridging effect of TiN nanoparticles on the electrochemical performance of TiN@CNT-S composite cathode. *Electrochimica Acta* **250** 159-166 (2017).

[27] B. He, W.-C. Li, Y. Zhang, X.-F. Yu, B. Zhang, F. Li, A.-H. Lu, Paragenesis BN/CNTs hybrid as a monoclinic sulfur host for high rate and ultra-long life lithium–sulfur battery. *Journal of Materials Chemistry A* **6** 24194-24200 (2018).

[28] H. Kang, M.J. Park, Thirty-minute synthesis of hierarchically ordered sulfur particles enables high-energy, flexible lithium-sulfur batteries. *Nano Energy* **89** 106459 (2021).

[29] A. Manthiram, Y. Fu, S.H. Chung, C. Zu, Y.S. Su, Rechargeable lithium-sulfur batteries. *Chem Rev* **114** 11751−11787 (2014).

[30] H. Danuta, U. Juliusz, Electric Dry Cells and Storage Batteries. *U. S. Patent* **3043896** (1962).

[31] E. Peled, Y. Sternberg, A. Gorenshtein, Y. Lavi, LITHIUM-SULFUR BATTERY - EVALUATION OF DIOXOLANE-BASED ELECTROLYTES. *Journal of the Electrochemical Society* **136** 1621-1625 (1989).

[32] X. Ji, K.T. Lee, L.F. Nazar, A highly ordered nanostructured carbon-sulphur cathode for lithium-sulphur batteries. *Nature Materials* **8** 500-506 (2009).

[33] Q. Pang, X. Liang, C.Y. Kwok, L.F. Nazar, Advances in lithium-sulfur batteries based on multifunctional cathodes and electrolytes. *Nature Energy* **1** 16132 (2016).

[34] Y.-X. Yin, S. Xin, Y.-G. Guo, L.-J. Wan, Lithium-Sulfur Batteries: Electrochemistry, Materials, and Prospects. *Angewandte Chemie-International Edition* **52** 13186-13200 (2013).

[35] R. Fang, S. Zhao, Z. Sun, W. Wang, H.-M. Cheng, F. Li, More Reliable Lithium-Sulfur Batteries: Status, Solutions and Prospects. *Advanced Materials* **29** 1606823 (2017).

[36] Y. Chen, T. Wang, H. Tian, D. Su, Q. Zhang, G. Wang, Advances in Lithium-Sulfur Batteries: From Academic Research to Commercial Viability. *Advanced Materials* **33** 2003666 (2021).

[37] J.B. Goodenough, Y. Kim, Challenges for Rechargeable Li Batteries. *Chemistry of Materials* **22** 587-603 (2010).

[38] S. Xin, L. Gu, N.-H. Zhao, Y.-X. Yin, L.-J. Zhou, Y.-G. Guo, L.-J. Wan, Smaller Sulfur Molecules Promise Better Lithium-Sulfur Batteries. *Journal of the American Chemical Society* **134** 18510-18513 (2012).

[39] S.C. Han, M.S. Song, H. Lee, H.S. Kim, H.J. Ahn, J.Y. Lee, Effect of multiwalled carbon nanotubes on electrochemical properties of lithium sulfur rechargeable batteries.

Journal of the Electrochemical Society **150** A889-A893 (2003).

[40] L. Yuan, H. Yuan, X. Qiu, L. Chen, W. Zhu, Improvement of cycle property of sulfur-coated multi-walled carbon nanotubes composite cathode for lithium/sulfur batteries. *Journal of Power Sources* **189** 1141-1146 (2009).

[41] H. Wang, Y. Yang, Y. Liang, J.T. Robinson, Y. Li, A. Jackson, Y. Cui, H. Dai, Graphene-Wrapped Sulfur Particles as a Rechargeable Lithium-Sulfur Battery Cathode Material with High Capacity and Cycling Stability. *Nano Letters* **11** 2644-2647 (2011).

[42] X.-B. Cheng, J.-Q. Huang, Q. Zhang, H.-J. Peng, M.-Q. Zhao, F. Wei, Aligned carbon nanotube/sulfur composite cathodes with high sulfur content for lithium-sulfur batteries. *Nano Energy* **4** 65-72 (2014).

[43] M.-Q. Zhao, X.-F. Liu, Q. Zhang, G.-L. Tian, J.-Q. Huang, W. Zhu, F. Wei, Graphene/Single-Walled Carbon Nanotube Hybrids: One-Step Catalytic Growth and Applications for High-Rate Li-S Batteries. *Acs Nano* **6** 10759-10769 (2012).

[44] Z. Yuan, H.-J. Peng, J.-Q. Huang, X.-Y. Liu, D.-W. Wang, X.-B. Cheng, Q. Zhang, Hierarchical Free-Standing Carbon-Nanotube Paper Electrodes with Ultrahigh Sulfur-Loading for Lithium-Sulfur Batteries. *Advanced Functional Materials* **24** 6105-6112 (2014).

[45] Z. Zhang, L.-L. Kong, S. Liu, G.-R. Li, X.-P. Gao, A High-Efficiency Sulfur/Carbon Composite Based on 3D Graphene Nanosheet@Carbon Nanotube Matrix as Cathode for Lithium-Sulfur Battery. *Advanced Energy Materials* **7** 1602543 (2017).

[46] J.-Y. Hwang, H.M. Kim, S.-K. Lee, J.-H. Lee, A. Abouimrane, M.A. Khaleel, I. Belharouak, A. Manthiram, Y.-K. Sun, High-Energy, High-Rate, Lithium-Sulfur Batteries: Synergetic Effect of Hollow TiO2-Webbed Carbon Nanotubes and a Dual Functional Carbon-Paper Interlayer. *Advanced Energy Materials* **6** 1501480 (2016).

[47] X. Liang, Y. Rangom, C.Y. Kwok, Q. Pang, L.F. Nazar, Interwoven MXene Nanosheet/Carbon-Nanotube Composites as Li-S Cathode Hosts. *Advanced Materials* **29** 1603040 (2017).

[48] H.-J. Peng, J.-Q. Huang, M.-Q. Zhao, Q. Zhang, X.-B. Cheng, X.-Y. Liu, W.-Z. Qian, F. Wei, Nanoarchitectured Graphene/CNT@Porous Carbon with Extraordinary Electrical Conductivity and Interconnected Micro/Mesopores for Lithium- Sulfur Batteries. *Advanced Functional Materials* **24** 2772-2781 (2014).

[49] J.-Q. Huang, Z.-L. Xu, S. Abouali, M.A. Garakani, J.-K. Kim, Porous graphene oxide/carbon nanotube hybrid films as interlayer for lithium-sulfur batteries. *Carbon* **99** 624-632 (2016).

[50] D. Gueon, J.T. Hwang, S.B. Yang, E. Cho, K. Sohn, D.-K. Yang, J.H. Moon, Spherical Macroporous Carbon Nanotube Particles with Ultrahigh Sulfur Loading for Lithium-Sulfur Battery Cathodes. *Acs Nano* **12** 226-233 (2018).

[51] W. Kong, L. Yan, Y. Luo, D. Wang, K. Jiang, Q. Li, S. Fan, J. Wang, Ultrathin MnO2/Graphene Oxide/Carbon Nanotube Interlayer as Efficient Polysulfide-Trapping Shield for High-Performance Li-S Batteries. *Advanced Functional Materials* **27** 1606663 (2017).

[52] J. Wang, J. Chen, K. Konstantinov, L. Zhao, S.H. Ng, G.X. Wang, Z.P. Guo, H.K. Liu, Sulphur-polypyrrole composite positive electrode materials for rechargeable lithium batteries. *Electrochimica Acta* **51** 4634-4638 (2006).

[53] F. Wu, J. Chen, R. Chen, S. Wu, L. Li, S. Chen, T. Zhao, Sulfur/Polythiophene with a Core/Shell Structure: Synthesis and Electrochemical Properties of the Cathode for Rechargeable Lithium Batteries. *Journal of Physical Chemistry C* **115** 6057-6063 (2011).

[54] L. Xiao, Y. Cao, J. Xiao, B. Schwenzer, M.H. Engelhard, L.V. Saraf, Z. Nie, G.J. Exarhos, J. Liu, A Soft Approach to Encapsulate Sulfur: Polyaniline Nanotubes for Lithium-Sulfur Batteries with Long Cycle Life. *Advanced Materials* **24** 1176-1181 (2012).

[55] W. Zhou, Y. Yu, H. Chen, F.J. DiSalvo, H.D. Abruna, Yolk-Shell Structure of Polyaniline-Coated Sulfur for Lithium-Sulfur Batteries. *Journal of the American Chemical Society* **135** 16736-16743 (2013).

[56] W. Li, Q. Zhang, G. Zheng, Z.W. Seh, H. Yao, Y. Cui, Understanding the Role of Different Conductive Polymers in Improving the Nanostructured Sulfur Cathode Performance. *Nano Letters* **13** 5534-5540 (2013).

[57] Y. Yang, G. Yu, J.J. Cha, H. Wu, M. Vosgueritchian, Y. Yao, Z. Bao, Y. Cui, Improving the Performance of Lithium-Sulfur Batteries by Conductive Polymer Coating. *Acs Nano* **5** 9187-9193 (2011).

[58] M.S. Song, S.C. Han, H.S. Kim, J.H. Kim, K.T. Kim, Y.M. Kang, H.J. Ahn, S.X. Dou, J.Y. Lee, Effects of nanosized adsorbing material on electrochemical properties of sulfur cathodes for Li/S secondary batteries. *Journal of the Electrochemical Society* **151** A791-A795 (2004).

[59] Y.J. Choi, B.S. Jung, D.J. Lee, J.H. Jeong, K.W. Kim, H.J. Ahn, K.K. Cho, H.B. Gu, Electrochemical properties of sulfur electrode containing nano Al2O3 for lithium/sulfur cell. *Physica Scripta* **T129** 62-65 (2007).

[60] X. Ji, S. Evers, R. Black, L.F. Nazar, Stabilizing lithium-sulphur cathodes using polysulphide reservoirs. *Nature Communications* **2** 325 (2011).

[61] Z. Wei Seh, W. Li, J.J. Cha, G. Zheng, Y. Yang, M.T. McDowell, P.-C. Hsu, Y. Cui, Sulphur-TiO2 yolk-shell nanoarchitecture with internal void space for long-cycle lithium-sulphur batteries. *Nature communications* **4** 1331-1331 (2013).

[62] X. Liang, C. Hart, Q. Pang, A. Garsuch, T. Weiss, L.F. Nazar, A highly efficient polysulfide mediator for lithium-sulfur batteries. *Nature Communications* **6** 5682 (2015).

[63] D.-R. Deng, F. Xue, Y.-J. Jia, J.-C. Ye, C.-D. Bai, M.-S. Zheng, Q.-F. Dong, Co4N Nanosheet Assembled Mesoporous Sphere as a Matrix for Ultrahigh Sulfur Content Lithium-Sulfur Batteries. *Acs Nano* **11** 6031-6039 (2017).

[64] M. Buongiorno Nardelli, C. Brabec, A. Maiti, C. Roland, J. Bernholc, Lip-Lip Interactions and the Growth of Multiwalled Carbon Nanotubes. *Physical Review Letters* **80** 313-316 (1998).

[65] K.J. Erickson, A.L. Gibb, A. Sinitskii, M. Rousseas, N. Alem, J.M. Tour, A.K. Zettl, Longitudinal Splitting of Boron Nitride Nanotubes for the Facile Synthesis of High Quality Boron Nitride Nanoribbons. *Nano Letters* **11** 3221-3226 (2011).

[66] M.B. Jakubinek, B. Ashrafi, Y. Martinez-Rubi, J. Guan, M. Rahmat, K.S. Kim, S. Dénommée, C.T. Kingston, B. Simard, in *Nanotube Superfiber Materials (Second Edition),* M. J. Schulz, V. Shanov, Z. Yin, M. Cahay, Eds. (William Andrew Publishing, 2019), pp. 91-111.

[67] W. Han, Y. Bando, K. Kurashima, T. Sato, Synthesis of boron nitride nanotubes from carbon nanotubes by a substitution reaction. *Applied Physics Letters* **73** 3085-3087 (1998).

[68] D. Golberg, Y. Bando, Y. Huang, T. Terao, M. Mitome, C. Tang, C. Zhi, Boron Nitride Nanotubes and Nanosheets. *ACS Nano* **4** 2979-2993 (2010).

[69] D.R. Deng, F. Xue, C.-D. Bai, J. Lei, R. Yuan, M.S. Zheng, Q.F. Dong, Enhanced Adsorptions to Polysulfides on Graphene-Supported BN Nanosheets with Excellent Li–S Battery Performance in a Wide Temperature Range. *ACS Nano* **12** 11120-11129 (2018).

[70] C. Sun, C. Hai, Y. Zhou, Y. Shen, X. Li, Y. Sun, G. Zhang, J. Zeng, S. Dong, X. Ren, J. Zheng, J. Mao, K. Dai, Highly Catalytic Boron Nitride Nanofiber In Situ Grown on Pretreated Ketjenblack as a Cathode for Enhanced Performance of Lithium–Sulfur Batteries. *ACS Applied Energy Materials* **3** 10841-10853 (2020).

[71] D.R. Deng, F. Xue, C.D. Bai, J. Lei, R. Yuan, M.S. Zheng, Q.F. Dong, Enhanced

Adsorptions to Polysulfides on Graphene-Supported BN Nanosheets with Excellent Li-S Battery Performance in a Wide Temperature Range. *ACS Nano* **12** 11120-11129 (2018).

[72] F.W. Ainger, J.M. Herbert, THE PREPARATION OF PHOSPHORUS-NITROGEN COMPOUNDS AS NON-POROUS SOLIDS. *Angewandte Chemie-International Edition* **71** 653-653 (1959).

[73] C. P, P. P, Inorganic polymers and ceramics. *Spec Ceram* **67** (1965).

[74] P. Colombo, J. Schmidt, G. Franchin, A. Zocca, J. Gunster, Additive manufacturing techniques for fabricating complex ceramic components from preceramic polymers. *American Ceramic Society Bulletin* **96** 16-23 (2017).

[75] P. Colombo, T. Gambaryan-Roisman, M. Scheffler, P. Buhler, P. Greil, Conductive ceramic foams from preceramic polymers. *Journal of the American Ceramic Society* **84** 2265-2268 (2001).

[76] S. Yajima, J. Hayashi, M. Omori, CONTINUOUS SILICON-CARBIDE FIBER OF HIGH-TENSILE STRENGTH. *Chemistry Letters* 931-934 (1975).

[77] D.L. Poerschke, A. Braithwaite, D. Park, F. Lauten, Crystallization behavior of polymer-derived Si-O-C for ceramic matrix composite processing. *Acta Materialia* **147** 329-341 (2018).

[78] S. Yajima, Y. Hasegawa, K. Okamura, T. Matsuzawa, DEVELOPMENT OF HIGH-TENSILE STRENGTH SILICON-CARBIDE FIBER USING AN ORGANOSILICON POLYMER PRECURSOR. *Nature* **273** 525-527 (1978).

[79] Y.D. Blum, R.M. Platz, E.J. Crawford, GLASS STRENGTHENING BY POLYMER-DERIVED CERAMIC COATINGS. *Journal of the American Ceramic Society* **73** 170-172 (1990).

[80] C.H. Park, Y.J. Joo, J.K. Chung, Y.H. Han, C.J. Kim, Morphology control of a silicon nitride thick film derived from polysilazane precursor using UV curing and IR heat treatment. *Advances in Applied Ceramics* **116** 376-382 (2017).

[81] J.D. Torrey, R.K. Bordia, Processing of polymer-derived ceramic composite coatings on steel. *Journal of the American Ceramic Society* **91** 41-45 (2008).

[82] Q.B. Wen, Z.J. Yu, R. Riedel, E. Ionescu, Significant improvement of high-temperature oxidation resistance of HfC/SiC ceramic nanocomposites with the incorporation of a small amount of boron. *Journal of the European Ceramic Society* **40** 3499-3508 (2020).

[83] Q.B. Wen, Y.P. Xu, B.B. Xu, C. Fasel, O. Guillon, G. Buntkowsky, Z.J. Yu, R. Riedel, E. Ionescu, Single-source-precursor synthesis of dense SiC/HfCxN1-x-based ultrahigh-

temperature ceramic nanocomposites. *Nanoscale* **6** 13678-13689 (2014).

[84] W. Verbeek, MOLDED BODIES FROM MOGENIC MIXTURES OF SILICON CARBIDE AND SILICON NITRIDE AND PROCESS FOR THEIR PRODUCTION. *Ger. Pat* **No. DE2218960A1** (1972).

[85] W. Verbeek, G. Winter, Formkoerper aus siliciumcarbid und verfahren zu ihrer herstellung. *Ger. Pat* **No. DE2236078** (1974).

[86] G. Winter, W. Verbeek, M. Mansmann, Formkoerper aus homogenen mischungen von siliciumcarbid und siliciumnitrid und verfahren zu ihrer herstellung. *Ger. Pat* **No. DE2243527** (1974).

[87] K.J. Wynne, R.W. Rice, CERAMICS VIA POLYMER PYROLYSIS. *Annual Review of Materials Science* **14** 297-334 (1984).

[88] D. Seyferth, G.H. Wiseman, C. Prudhomme, A LIQUID SILAZANE PRECURSOR TO SILICON-NITRIDE. *Journal of the American Ceramic Society* **66** C13-C14 (1983).

[89] R. Riedel, L.M. Ruswisch, L.N. An, R. Raj, Amorphous silicoboron carbonitride ceramic with very high viscosity at temperatures above 1500 degrees C. *Journal of the American Ceramic Society* **81** 3341-3344 (1998).

[90] M. Peuckert, T. Vaahs, M. Bruck, CERAMICS FROM ORGANOMETALLIC POLYMERS. *Advanced Materials* **2** 398-404 (1990).

[91] G. Pouskouleli, METALLORGANIC COMPOUNDS AS PRECERAMIC MATERIALS .1. NON-OXIDE CERAMICS. *Ceramics International* **15** 213-229 (1989).

[92] Z.C. Wang, F. Aldinger, R. Riedel, Novel silicon-boron-carbon-nitrogen materials thermally stable up to 2200 degrees C. *Journal of the American Ceramic Society* **84** 2179-2183 (2001).

[93] E. Ionescu, B. Papendorf, H.J. Kleebe, H. Breitzke, K. Nonnenmacher, G. Buntkowsky, R. Riedel, Phase separation of a hafnium alkoxide-modified polysilazane upon polymer-to-ceramic transformation-A case study. *Journal of the European Ceramic Society* **32** 1873-1881 (2012).

[94] E. Ionescu, B. Papendorf, H.J. Kleebe, F. Poli, K. Muller, R. Riedel, Polymer-Derived Silicon Oxycarbide/Hafnia Ceramic Nanocomposites. Part I: Phase and Microstructure Evolution During the Ceramization Process. *Journal of the American Ceramic Society* **93** 1774-1782 (2010).

[95] G.D. Soraru, M. Mercadini, R. Dalmaschio, F. Taulelle, F. Babonneau, SI-AL-O-N FIBERS FROM POLYMERIC PRECURSOR - SYNTHESIS, STRUCTURAL, AND

MECHANICAL CHARACTERIZATION. *Journal of the American Ceramic Society* **76** 2595-2600 (1993).

[96] R. Riedel, A. Kienzle, W. Dressler, L. Ruwisch, J. Bill, F. Aldinger, A silicoboron carbonitride ceramic stable to 2,000 degrees C. *Nature* **382** 796-798 (1996).

[97] S. Dire, F. Babonneau, C. Sanchez, J. Livage, SOL-GEL SYNTHESIS OF SILOXANE OXIDE HYBRID COATINGS SI(CH3)2O.MOX - M = SI, TI, ZR, AL WITH LUMINESCENT PROPERTIES. *Journal of Materials Chemistry* **2** 239-244 (1992).

[98] A.M. Wootton, M. Rappensberger, M.H. Lewis, S. Kitchin, A.P. Howes, R. Dupree, Structural properties of multi-component silicon oxycarbide glasses derived from metal alkoxide precursors. *Journal of Non-Crystalline Solids* **204** 217-227 (1996).

[99] S. Dire, R. Ceccato, S. Gialanella, F. Babonneau, Thermal evolution and crystallisation of polydimethylsiloxane-zirconia nanocomposites prepared by the sol-gel method. *Journal of the European Ceramic Society* **19** 2849-2858 (1999).

[100] O. Flores, R.K. Bordia, D. Nestler, W. Krenkel, G. Motz, Ceramic Fibers Based on SiC and SiCN Systems: Current Research, Development, and Commercial Status. *Advanced Engineering Materials* **16** 621-636 (2014).

[101] A.R. Guo, M. Roso, M. Modesti, J.C. Liu, P. Colombo, Preceramic Polymer-Derived SiOC Fibers by Electrospinning. *Journal of Applied Polymer Science* **131** 39836 (2014).

[102] P. Hernandez-Rodriguez, E. Lopez-Honorato, Polymer derived SiC environmental barrier coatings with superwetting properties. *Ceramics International* **43** 11289-11295 (2017).

[103] G. Barroso, Q. Li, R.K. Bordia, G. Motz, Polymeric and ceramic silicon-based coatings - a review. *Journal of Materials Chemistry A* **7** 1936-1963 (2019).

[104] M. Gunthner, K. Wang, R.K. Bordia, G. Motz, Conversion behaviour and resulting mechanical properties of polysilazane-based coatings. *Journal of the European Ceramic Society* **32** 1883-1892 (2012).

[105] H.X. Zhang, P.D. Nunes, M. Wilhelm, K. Rezwan, Hierarchically ordered micro/meso/macroporous polymer-derived ceramic monoliths fabricated by freeze-casting. *Journal of the European Ceramic Society* **36** 51-58 (2016).

[106] B.H. Yoon, E.J. Lee, H.E. Kim, Y.H. Koh, Highly aligned porous silicon carbide ceramics by freezing Polycarbosilane/Camphene solution. *Journal of the American Ceramic Society* **90** 1753-1759 (2007).

[107] B.H. Yoon, C.S. Park, H.E. Kim, Y.H. Koh, In situ synthesis of porous silicon carbide (SiC) ceramics decorated with SiC nanowires. *Journal of the American Ceramic Society*

90 3759-3766 (2007).

[108] L. Toma, H.J. Kleebe, M.M. Muller, E. Janssen, R. Riedel, T. Melz, H. Hanselka, Correlation Between Intrinsic Microstructure and Piezoresistivity in a SiOC Polymer-Derived Ceramic. *Journal of the American Ceramic Society* **95** 1056-1061 (2012).

[109] S. Kaur, R. Riedel, E. Ionescu, Pressureless fabrication of dense monolithic SiC ceramics from a polycarbosilane. *Journal of the European Ceramic Society* **34** 3571-3578 (2014).

[110] X.M. Liu, Z.J. Yu, R. Ishikawa, L.Q. Chen, X.W. Yin, Y. Ikuhara, R. Riedel, Single-source-precursor synthesis and electromagnetic properties of novel RGO-SiCN ceramic nanocomposites. *Journal of Materials Chemistry C* **5** 7950-7960 (2017).

[111] K.S. Wang, M. Gunthner, G. Motz, R.K. Bordia, High performance environmental barrier coatings, Part II: Active filler loaded SiOC system for superalloys. *Journal of the European Ceramic Society* **31** 3011-3020 (2011).

[112] M.D. Nguyen, J.W. Bang, A.S. Bin, S.R. Kim, Y. Kim, K.H. Hwang, V.H. Pham, W.T. Kwon, Novel polymer-derived ceramic environmental barrier coating system for carbon steel in oxidizing environments. *Journal of the European Ceramic Society* **37** 2001-2010 (2017).

[113] P. Colombo, V. Sglavo, E. Pippel, J. Woltersdorf, Joining of reaction-bonded silicon carbide using a preceramic polymer. *Journal of Materials Science* **33** 2405-2412 (1998).

[114] C.A. Lewinsohn, P. Colombo, I. Reimanis, O. Unal, Stresses occurring during joining of ceramics using preceramic polymers. *Journal of the American Ceramic Society* **84** 2240-2244 (2001).

[115] T. Cross, R. Raj, Mechanical and tribological behavior of polymer-derived ceramics constituted from SiCxOyNz. *Journal of the American Ceramic Society* **89** 3706-3714 (2006).

[116] Z.B. Li, Y.J. Cao, J.B. He, Y.G. Wang, Mechanical and tribological performances of C-SiC nanocomposites synthetized from polymer-derived ceramics sintered by spark plasma Check for sintering. *Ceramics International* **44** 14335-14341 (2018).

[117] J. Kaspar, M. Graczyk-Zajac, R. Riedel, Determination of the chemical diffusion coefficient of Li-ions in carbon-rich silicon oxycarbide anodes by electro-analytical methods. *Electrochimica Acta* **115** 665-670 (2014).

[118] V.S. Pradeep, D.G. Ayana, M. Graczyk-Zajac, G.D. Soraru, R. Riedel, High Rate Capability of SiOC Ceramic Aerogels with Tailored Porosity as Anode Materials for Li-ion Batteries. *Electrochimica Acta* **157** 41-45 (2015).

[119] D. Vrankovic, M. Graczyk-Zajac, C. Kalcher, J. Rohrer, M. Becker, C. Stabler, G. Trykowski, K. Albe, R. Riedel, Highly Porous Silicon Embedded in a Ceramic Matrix: A Stable High-Capacity Electrode for Li-Ion Batteries. *Acs Nano* **11** 11409-11416 (2017).

[120] J. Kaspar, M. Graczyk-Zajac, S. Choudhury, R. Riedel, Impact of the electrical conductivity on the lithium capacity of polymer-derived silicon oxycarbide (SiOC) ceramics. *Electrochimica Acta* **216** 196-202 (2016).

[121] M. Graczyk-Zajac, D. Vrankovic, P. Waleska, C. Hess, P.V. Sasikumar, S. Lauterbach, H.-J. Kleebe, G.D. Sorarù, The Li-storage capacity of SiOC glasses with and without mixed silicon oxycarbide bonds. *Journal of Materials Chemistry A* **6** 93-103 (2018).

[122] V.S. Pradeep, M. Graczyk-Zajac, R. Riedel, G.D. Soraru, New Insights in to the Lithium Storage Mechanism in Polymer Derived SiOC Anode Materials. *Electrochimica Acta* **119** 78-85 (2014).

[123] I.N. Reddy, A. Sreedhar, C.V. Reddy, J. Shim, M. Cho, K. Yoo, D. Kim, J.S. Gwag, High performance hierarchical SiCN nanowires for efficient photocatalytic - photoelectrocatalytic and supercapacitor applications. *Applied Catalysis B-Environmental* **237** 876-887 (2018).

[124] M. Halim, G.C. Liu, R.E.A. Ardhi, C. Hudaya, O. Wijaya, S.H. Lee, A.Y. Kim, J.K. Lee, Pseudocapacitive Characteristics of Low-Carbon Silicon Oxycarbide for Lithium-Ion Capacitors. *Acs Applied Materials & Interfaces* **9** 20566-20576 (2017).

[125] Y. Song, L.H. He, X.F. Zhang, F. Liu, N. Tian, Y.S. Tang, J. Kong, Highly Efficient Electromagnetic Wave Absorbing Metal-Free and Carbon-Rich Ceramics Derived from Hyperbranched Polycarbosilazanes. *Journal of Physical Chemistry C* **121** 24774-24785 (2017).

[126] X.M. Liu, Z.J. Yu, R. Ishikawa, L.Q. Chen, X.F. Liu, X.W. Yin, Y. Ikuhara, R. Riedel, Single-source-precursor derived RGO/CNTs-SiCN ceramic nanocomposite with ultra-high electromagnetic shielding effectiveness. *Acta Materialia* **130** 83-93 (2017).

[127] W.Y. Zhao, G. Shao, M.J. Jiang, B. Zhao, H.L. Wang, D.L. Chen, H.L. Xu, X.J. Li, R. Zhang, L.A. An, Ultralight polymer-derived ceramic aerogels with wide bandwidth and effective electromagnetic absorption properties. *Journal of the European Ceramic Society* **37** 3973-3980 (2017).

[128] L. Ferraioli, D. Ahn, A. Saha, L. Pavesi, R. Raj, Intensely photoluminescent pseudo-amorphous SiliconOxyCarboNitride polymer-ceramic hybrids. *Journal of the American Ceramic Society* **91** 2422-2424 (2008).

[129] Y. Shimokawa, A. Fujiwara, E. Ionescu, G. Mera, S. Honda, Y. Iwamoto, R. Riedel, Synthesis and characterization of luminescent properties of ceramics derived from polysilylcarbodiimides. *Journal of the Ceramic Society of Japan* **122** 895-901 (2014).

[130] M. Gaweda, P. Jelen, E. Dlugon, A. Wajda, M. Lesniak, W. Simka, M. Sowa, R. Detsch, A.R. Boccaccini, M. Sitarz, Bioactive layers based on black glasses on titanium substrates. *Journal of the American Ceramic Society* **101** 590-601 (2018).

[131] E. Ionescu, S. Sen, G. Mera, A. Navrotsky, Structure, energetics and bioactivity of silicon oxycarbide-based amorphous ceramics with highly connected networks. *Journal of the European Ceramic Society* **38** 1311-1319 (2018).

[132] I. Gonzalo-Juan, R. Detsch, S. Mathur, E. Ionescu, A.R. Boccaccini, R. Riedel, Synthesis and In Vitro Activity Assessment of Novel Silicon Oxycarbide-Based Bioactive Glasses. *Materials* **9** 959 (2016).

[133] Q. Wen, F. Qu, Z. Yu, M. Graczyk-Zajac, X. Xiong, R. Riedel, Si-based polymer-derived ceramics for energy conversion and storage. *Journal of Advanced Ceramics* **11** 197-246 (2022).

[134] Q. Wen, Z. Yu, R. Riedel, The fate and role of in situ formed carbon in polymer-derived ceramics. *Progress in Materials Science* **109** 100623 (2020).

[135] P. Colombo, G. Mera, R. Riedel, G.D. Soraru, Polymer-Derived Ceramics: 40 Years of Research and Innovation in Advanced Ceramics. *Journal of the American Ceramic Society* **93** 1805-1837 (2010).

[136] G. Mera, A. Navrotsky, S. Sen, H.-J. Kleebe, R. Riedel, Polymer-derived SiCN and SiOC ceramics - structure and energetics at the nanoscale. *Journal of Materials Chemistry A* **1** 3826-3836 (2013).

[137] A. Scarmi, G.D. Soraru, R. Raj, The role of carbon in unexpected visco(an)elastic behavior of amorphous silicon oxycarbide above 1273 K. *Journal of Non-Crystalline Solids* **351** 2238-2243 (2005).

[138] A. Saha, R. Raj, D.L. Williamson, A model for the nanodomains in polymer-derived SiCO. *Journal of the American Ceramic Society* **89** 2188-2195 (2006).

[139] S.J. Widgeon, S. Sen, G. Mera, E. Ionescu, R. Riedel, A. Navrotsky, Si-29 and C-13 Solid-State NMR Spectroscopic Study of Nanometer-Scale Structure and Mass Fractal Characteristics of Amorphous Polymer Derived Silicon Oxycarbide Ceramics. *Chemistry of Materials* **22** 6221-6228 (2010).

[140] R. Riedel, G. Mera, R. Hauser, A. Klonczynski, Silicon-based polymer-derived ceramics: Synthesis properties and applications - A review. *Journal of the Ceramic*

Society of Japan **114** 425-444 (2006).

[141] G. Mera, R. Riedel, F. Poli, K. Mueller, Carbon-rich SiCN ceramics derived from phenyl-containing poly(silylcarbodiimides). *Journal of the European Ceramic Society* **29** 2873-2883 (2009).

[142] R.M. Morcos, G. Mera, A. Navrotsky, T. Varga, R. Riedel, F. Poli, K. Mueller, Enthalpy of Formation of Carbon-Rich Polymer-Derived Amorphous SiCN Ceramics. *Journal of the American Ceramic Society* **91** 3349-3354 (2008).

[143] R. Pena-Alonso, G. Mariotto, C. Gervais, F. Babonneau, G.D. Soraru, New insights on the high-temperature nanostructure evolution of SiOC and B-doped SiBOC polymer-derived glasses. *Chemistry of Materials* **19** 5694-5702 (2007).

[144] Q. Wen, Y. Xu, B. Xu, C. Fasel, O. Guillon, G. Buntkowsky, Z. Yu, R. Riedel, E. Ionescu, Single-source-precursor synthesis of dense SiC/HfCxN1-x-based ultrahigh-temperature ceramic nanocomposites. *Nanoscale* **6** 13678-13689 (2014).

[145] D. Ahn, R. Raj, Thermodynamic measurements pertaining to the hysteretic intercalation of lithium in polymer-derived silicon oxycarbide. *Journal of Power Sources* **195** 3900-3906 (2010).

[146] A.M. Wilson, J.N. Reimers, E.W. Fuller, J.R. Dahn, LITHIUM INSERTION IN PYROLYZED SILOXANE POLYMERS. *Solid State Ionics* **74** 249-254 (1994).

[147] W.B. Xing, A.M. Wilson, K. Eguchi, G. Zank, J.R. Dahn, Pyrolyzed polysiloxanes for use as anode materials in lithium-ion batteries. *Journal of the Electrochemical Society* **144** 2410-2416 (1997).

[148] D. Ahn, R. Raj, Cyclic stability and C-rate performance of amorphous silicon and carbon based anodes for electrochemical storage of lithium. *Journal of Power Sources* **196** 2179-2186 (2011).

[149] P.E. Sanchez-Jimenez, R. Raj, Lithium Insertion in Polymer-Derived Silicon Oxycarbide Ceramics. *Journal of the American Ceramic Society* **93** 1127-1135 (2010).

[150] H. Fukui, Y. Harimoto, M. Akasaka, K. Eguchi, Lithium Species in Electrochemically Lithiated and Delithiated Silicon Oxycarbides. *Acs Applied Materials & Interfaces* **6** 12827-12836 (2014).

[151] M. Graczyk-Zajac, L. Toma, C. Fasel, R. Riedel, Carbon-rich SiOC anodes for lithium-ion batteries: Part I. Influence of material UV-pre-treatment on high power properties. *Solid State Ionics* **225** 522-526 (2012).

[152] M. Wilamowska, V.S. Pradeep, M. Graczyk-Zajac, R. Riedel, G.D. Sorarù, Tailoring of SiOC composition as a way to better performing anodes for Li-ion batteries. *Solid State*

Ionics **260** 94-100 (2014).

[153] H. Fukui, H. Ohsuka, T. Hino, K. Kanamura, A Si-O-C Composite Anode: High Capability and Proposed Mechanism of Lithium Storage Associated with Microstructural Characteristics. *Acs Applied Materials & Interfaces* **2** 998-1008 (2010).

[154] M. Haaks, J. Kaspar, A. Franz, M. Graczyk-Zajac, R. Riedel, M. Vogel, Li-7 NMR studies of lithium ion dynamics in polymer-derived silicon oxycarbide ceramics. *Solid State Ionics* **287** 28-35 (2016).

[155] J. Kaspar, M. Graczyk-Zajac, R. Riedel, Lithium insertion into carbon-rich SiOC ceramics: Influence of pyrolysis temperature on electrochemical properties. *Journal of Power Sources* **244** 450-455 (2013).

[156] P. Dibandjo, M. Graczyk-Zajac, R. Riedel, V.S. Pradeep, G.D. Soraru, Lithium insertion into dense and porous carbon-rich polymer-derived SiOC ceramics. *Journal of the European Ceramic Society* **32** 2495-2503 (2012).

[157] V.S. Pradeep, M. Graczyk-Zajac, M. Wilamowska, R. Riedel, G.D. Soraru, Influence of pyrolysis atmosphere on the lithium storage properties of carbon-rich polymer derived SiOC ceramic anodes. *Solid State Ionics* **262** 22-24 (2014).

[158] B. Dong, Y. Han, T. Wang, Z. Lei, Y. Chen, F. Wang, H. Abadikhah, S.A. Khan, L. Hao, X. Xu, R. Cao, L. Yin, S. Agathopoulos, Hard SiOC Microbeads as a High-Performance Lithium-Ion Battery Anode. *Acs Applied Energy Materials* **3** 10183-10191 (2020).

[159] M. Ma, H. Wang, X. Li, K. Peng, L. Xiong, X. Du, Free-standing SiOC/nitrogen-doped carbon fibers with highly capacitive Li storage. *Journal of the European Ceramic Society* **40** 5238-5246 (2020).

[160] H. Lim, H. Kim, S.-O. Kim, K.J. Kim, W. Choi, Novel approach for controlling free-carbon domain in silicone oil-derived silicon oxycarbide (SiOC) as an anode material in secondary batteries. *Chemical Engineering Journal* **404** 126581 (2021).

[161] J. Kaspar, M. Graczyk-Zajac, S. Lauterbach, H.-J. Kleebe, R. Riedel, Silicon oxycarbide/nano-silicon composite anodes for Li-ion batteries: Considerable influence of nano-crystalline vs. nano-amorphous silicon embedment on the electrochemical properties. *Journal of Power Sources* **269** 164-172 (2014).

[162] J. Kaspar, C. Terzioglu, E. Ionescu, M. Graczyk-Zajac, S. Hapis, H.-J. Kleebe, R. Riedel, Stable SiOC/Sn Nanocomposite Anodes for Lithium-Ion Batteries with Outstanding Cycling Stability. *Advanced Functional Materials* **24** 4097-4104 (2014).

[163] J.R.D. G.A. Zank, A.M. Wilson, and W. Xing, Electrodes for Lithium Ion Batteries Using Polysilazanes Ceramic with Lithium. *U.S. Patent* **5631106(A)** (20 May 1997).

[164] V. Liebau-Kunzmann, C. Fasel, R. Kolb, R. Riedel, Lithium containing silazanes as precursors for SiCN : Li ceramics - A potential material for electrochemical applications. *Journal of the European Ceramic Society* **26** 3897-3901 (2006).

[165] D. Su, Y.-L. Li, Y. Feng, J. Jin, Electrochemical Properties of Polymer-Derived SiCN Materials as the Anode in Lithium Ion Batteries. *Journal of the American Ceramic Society* **92** 2962-2968 (2009).

[166] M. Graczyk-Zajac, G. Mera, J. Kaspar, R. Riedel, Electrochemical studies of carbon-rich polymer-derived SiCN ceramics as anode materials for lithium-ion batteries. *Journal of the European Ceramic Society* **30** 3235-3243 (2010).

[167] J. Kaspar, G. Mera, A.P. Nowak, M. Graczyk-Zajac, R. Riedel, Electrochemical study of lithium insertion into carbon-rich polymer-derived silicon carbonitride ceramics. *Electrochimica Acta* **56** 174-182 (2010).

[168] L.M. Reinold, M. Graczyk-Zajac, Y. Gao, G. Mera, R. Riedel, Carbon-rich SiCN ceramics as high capacity/high stability anode material for lithium-ion batteries. *Journal of Power Sources* **236** 224-229 (2013).

[169] G. Liu, J. Kaspar, L.M. Reinold, M. Graczyk-Zajac, R. Riedel, Electrochemical performance of DVB-modified SiOC and SiCN polymer-derived negative electrodes for lithium-ion batteries. *Electrochimica Acta* **106** 101-108 (2013).

[170] S.-H. Baek, L.M. Reinold, M. Graczyk-Zajac, R. Riedel, F. Hammerath, B. Büchner, H.-J. Grafe, Lithium dynamics in carbon-rich polymer-derived SiCN ceramics probed by nuclear magnetic resonance. *Journal of Power Sources* **253** 342-348 (2014).

[171] M. Graczyk-Zajac, M. Wimmer, Y. Xu, G. Buntkowsky, C. Neumann, R. Riedel, Lithium intercalation into disordered carbon/SiCN composite. Part 2: Raman spectroscopy and Li-7 MAS NMR investigation of lithium storage sites. *Journal of Solid State Electrochemistry* **21** 47-55 (2017).

[172] M. Graczyk-Zajac, M. Wimmer, C. Neumann, R. Riedel, Lithium intercalation into SiCN/disordered carbon composite. Part 1: influence of initial carbon porosity on cycling performance/capacity. *Journal of Solid State Electrochemistry* **19** 2763-2769 (2015).

[173] M. Storch, D. Vrankovic, M. Graczyk-Zajac, R. Riedel, The influence of pyrolysis temperature on the electrochemical behavior of porous carbon-rich SiCN polymer-derived ceramics. *Solid State Ionics* **315** 59-64 (2018).

[174] M. Graczyk-Zajac, L.M. Reinold, J. Kaspar, P.V.W. Sasikumar, G.-D. Soraru, R. Riedel, New Insights into Understanding Irreversible and Reversible Lithium Storage within

SiOC and SiCN Ceramics. *Nanomaterials* **5** 233-245 (2015).

[175] R. Fang, Y. Xia, C. Liang, X. He, H. Huang, Y. Gan, J. Zhang, X. Tao, W. Zhang, Supercritical CO2-assisted synthesis of 3D porous SiOC/Se cathode for ultrahigh areal capacity and long cycle life Li–Se batteries. *Journal of Materials Chemistry A* **6** 24773-24782 (2018).

[176] J. Kaspar, M. Storch, C. Schitco, R. Riedel, M. Graczyk-Zajac, SiOC(N)/Hard Carbon Composite Anodes for Na-Ion Batteries: Influence of Morphology on the Electrochemical Properties. *Journal of The Electrochemical Society* **163** A156-A162 (2015).

[177] C. Chandra, J. Kim, Silicon oxycarbide produced from silicone oil for high-performance anode material in sodium ion batteries. *Chemical Engineering Journal* **338** 126-136 (2018).

[178] Z. Sang, D. Su, J. Wang, Y. Liu, H. Ji, Bi-continuous nanoporous carbon sphere derived from SiOC as high-performance anodes for PIBs. *Chemical Engineering Journal* **381** 122677 (2020).

[179] Poonam, K. Sharma, A. Arora, S.K. Tripathi, Review of supercapacitors: Materials and devices. *Journal of Energy Storage* **21** 801-825 (2019).

[180] L.L. Zhang, X.S. Zhao, Carbon-based materials as supercapacitor electrodes. *Chemical Society Reviews* **38** 2520-2531 (2009).

[181] M. Halim, G. Liu, R.E.A. Ardhi, C. Hudaya, O. Wijaya, S.-H. Lee, A.Y. Kim, J.K. Lee, Pseudocapacitive Characteristics of Low-Carbon Silicon Oxycarbide for Lithium-Ion Capacitors. *Acs Applied Materials & Interfaces* **9** 20566-20576 (2017).

[182] M.A. Abass, A.A. Syed, C. Gervais, G. Singh, Synthesis and electrochemical performance of a polymer-derived silicon oxycarbide/boron nitride nanotube composite. *Rsc Advances* **7** 21576-21584 (2017).

[183] M. Kim, I. Oh, J. Kim, Influence of surface oxygen functional group on the electrochemical behavior of porous silicon carbide based supercapacitor electrode. *Electrochimica Acta* **196** 357-368 (2016).

[184] L. David, K.M. Shareef, M.A. Abass, G. Singh, Three-dimensional polymer-derived ceramic/graphene paper as a Li-ion battery and supercapacitor electrode. *Rsc Advances* **6** 53894-53902 (2016).

[185] J.J. Moyano, J. Mosa, M. Aparicio, D. Perez-Coll, M. Belmonte, P. Miranzo, M.I. Osendi, Strong and light cellular silicon carbonitride - Reduced graphene oxide material with enhanced electrical conductivity and capacitive response. *Additive Manufacturing*

30 100849 (2019).

[186] F. Qu, M. Graczyk-Zajac, D. Vrankovic, N. Chai, Z. Yu, R. Riedel, Effect of morphology of C-rich silicon carbonitride ceramic on electrochemical properties of sulfur cathode for Li-S battery. *Electrochimica Acta* **384** 138265 (2021).

[187] F. Qu, Z. Yu, M. Krol, N. Chai, R. Riedel, M. Graczyk-Zajac, Electrochemical Performance of Carbon-Rich Silicon Carbonitride Ceramic as Support for Sulfur Cathode in Lithium Sulfur Battery. *Nanomaterials* **12** 1283 (2022).

[188] A. Zambotti, F. Qu, G. Costa, M. Graczyk-Zajac, G.D. Sorarù, Polymer-Derived Ceramic Aerogels to Immobilize Sulfur for Li-S Batteries. *Energy Technology* **11** 2300488 (2023).

[189] Vrankovic, D.; Storch, M.; Schitco, C.; Graczyk-Zajac, M.; Riedel, R. Verfahren zum Herstellen poröser Keramiken und eines porösen Keramikprodukts; Patent Application. 2018. DE 102016116732.0.

[190] A. Kawase, S. Shirai, Y. Yamoto, R. Arakawa, T. Takata, Electrochemical reactions of lithium-sulfur batteries: an analytical study using the organic conversion technique. *Phys Chem Chem Phys* **16** 9344-9350 (2014).

[191] Z. Sun, J. Zhang, L. Yin, G. Hu, R. Fang, H.M. Cheng, F. Li, Conductive porous vanadium nitride/graphene composite as chemical anchor of polysulfides for lithium-sulfur batteries. *Nat Commun* **8** 14627 (2017).

[192] A. Mentbayeva, A. Belgibayeva, N. Umirov, Y. Zhang, I. Taniguchi, I. Kurmanbayeva, Z. Bakenov, High performance freestanding composite cathode for lithium-sulfur batteries. *Electrochimica Acta* **217** 242-248 (2016).

[193] D. Vrankovic, L.M. Reinold, R. Riedel, M. Graczyk-Zajac, Void-shell silicon/carbon/SiCN nanostructures: toward stable silicon-based electrodes. *Journal of Materials Science* **51** 6051-6061 (2016).

[194] Y. Qiu, W. Li, W. Zhao, G. Li, Y. Hou, M. Liu, L. Zhou, F. Ye, H. Li, Z. Wei, S. Yang, W. Duan, Y. Ye, J. Guo, Y. Zhang, High-rate, ultralong cycle-life lithium/sulfur batteries enabled by nitrogen-doped graphene. *Nano Lett* **14** 4821-4827 (2014).

[195] S. Xin, L. Gu, N.H. Zhao, Y.X. Yin, L.J. Zhou, Y.G. Guo, L.J. Wan, Smaller sulfur molecules promise better lithium-sulfur batteries. *J Am Chem Soc* **134** 18510−18513 (2012).

[196] Z. Li, Y. Jiang, L. Yuan, Z. Yi, C. Wu, Y. Liu, P. Strasser, Y. Huang, A Highly Ordered Meso@Microporous Carbon-Supported Sulfur@Smaller Sulfur Core-Shell Structured Cathode for Li-S Batteries. *Acs Nano* **8** 9295-9303 (2014).

[197] X. Ji, S. Evers, R. Black, L.F. Nazar, Stabilizing lithium-sulphur cathodes using polysulphide reservoirs. *Nat Commun* **2** 325 (2011).

[198] J. Song, M.L. Gordin, T. Xu, S. Chen, Z. Yu, H. Sohn, J. Lu, Y. Ren, Y. Duan, D. Wang, Strong lithium polysulfide chemisorption on electroactive sites of nitrogen-doped carbon composites for high-performance lithium-sulfur battery cathodes. *Angew Chem Int Ed Engl* **54** 4325-4329 (2015).

[199] U. Gulzar, T. Li, X. Bai, M. Colombo, A. Ansaldo, S. Marras, M. Prato, S. Goriparti, C. Capiglia, R. Proietti Zaccaria, Nitrogen-Doped Single-Walled Carbon Nanohorns as a Cost-Effective Carbon Host toward High-Performance Lithium-Sulfur Batteries. *ACS Appl Mater Interfaces* **10** 5551-5559 (2018).

[200] C. Huang, C. Chen, X. Ye, W. Ye, J. Hu, C. Xu, X. Qiu, Stable colloidal boron nitride nanosheet dispersion and its potential application in catalysis. *Journal of Materials Chemistry A* **1** 12192-12197 (2013).

[201] Y. Feng, S. Dou, Y. Wei, Y. Zhang, X. Song, X. Li, V.S. Battaglia, Preparation and Capacity-Fading Investigation of Polymer-Derived Silicon Carbonitride Anode for Lithium-Ion Battery. *Acs Omega* **2** 8075-8085 (2017).

[202] J. Xiong, L. Yang, Y. Chao, J. Pang, M. Zhang, W. Zhu, H. Li, Boron Nitride Mesoporous Nanowires with Doped Oxygen Atoms for the Remarkable Adsorption Desulfurization Performance from Fuels. *ACS Sustainable Chemistry & Engineering* **4** 4457-4464 (2016).

[203] G. Kaur, S. Kainth, R. Kumar, P. Sharma, O.P. Pandey, Reaction kinetics during non-isothermal solid-state synthesis of boron trioxide via boric acid dehydration. *Reaction Kinetics, Mechanisms and Catalysis* **134** 347-359 (2021).

[204] S. Aghili, M. Panjepour, M. Meratian, Kinetic analysis of formation of boron trioxide from thermal decomposition of boric acid under non-isothermal conditions. *Journal of Thermal Analysis and Calorimetry* **131** 2443-2455 (2018).

[205] M. Koebel, E.O. Strutz, Thermal and Hydrolytic Decomposition of Urea for Automotive Selective Catalytic Reduction Systems: Thermochemical and Practical Aspects. *Industrial & Engineering Chemistry Research* **42** 2093-2100 (2003).

[206] H. Hiller, R. Reimert, H.-M. Stönner, in *Ullmann's Encyclopedia of Industrial Chemistry*. (Wiley-VCH, Weinheim, 2011).

[207] D.R. Lide, in *CRC Handbook of Chemistry and Physics, 90th Edition*. (Taylor & Francis, 2009).

[208] S. Balcı, N.A. Sezgi, E. Eren, Boron Oxide Production Kinetics Using Boric Acid as

Raw Material. *Industrial & Engineering Chemistry Research* **51** 11091-11096 (2012).

[209] S. Rudolph, Boron Nitride. *American Ceramic Society Bulletin* **73** 89-90 (1994).

[210] K. Yamamoto, Y. Koga, S. Fujiwara, XPS studies of amorphous SiCN thin films prepared by nitrogen ion-assisted pulsed-laser deposition of SiC target. *Diamond and Related Materials* **10** 1921-1926 (2001).

[211] D. Schild, S. Ulrich, J. Ye, M. Stüber, XPS investigations of thick, oxygen-containing cubic boron nitride coatings. *Solid State Sciences* **12** 1903-1906 (2010).

[212] S. Fu, Q. Fang, A. Li, Z. Li, J. Han, X. Dang, W. Han, Accurate characterization of full pore size distribution of tight sandstones by low-temperature nitrogen gas adsorption and high-pressure mercury intrusion combination method. **9** 80-100 (2021).

[213] M. Melzi d'Eril, A. Zambotti, M. Graczyk-Zajac, E. Ionescu, G.D. Sorarù, R. Riedel, Effect of ultra-fast pyrolysis on polymer-derived SiOC aerogels and their application as anodes for Na-ion batteries. *Open Ceramics* **14** 100354 (2023).

[214] M. Thommes, K. Kaneko, A.V. Neimark, J.P. Olivier, F. Rodriguez-Reinoso, J. Rouquerol, K.S.W. Sing, Physisorption of gases, with special reference to the evaluation of surface area and pore size distribution (IUPAC Technical Report). **87** 1051-1069 (2015).

[215] U. Gulzar, T. Li, X. Bai, M. Colombo, A. Ansaldo, S. Marras, M. Prato, S. Goriparti, C. Capiglia, R. Proietti Zaccaria, Nitrogen-Doped Single-Walled Carbon Nanohorns as a Cost-Effective Carbon Host toward High-Performance Lithium–Sulfur Batteries. *ACS Applied Materials & Interfaces* **10** 5551-5559 (2018).

[216] R. Fang, K. Chen, L. Yin, Z. Sun, F. Li, H.-M. Cheng, The Regulating Role of Carbon Nanotubes and Graphene in Lithium-Ion and Lithium–Sulfur Batteries. *Advanced Materials* **31** 1800863 (2019).

[217] J. Lu, J. Hu, H. Zhong, Y. Ren, L. Zhang, Synthesis of silicon oxycarbonitride nanosphere as cathode host for lithium–sulfur batteries. *Journal of Alloys and Compounds* **860** 157903 (2021).

[218] J. Wang, W. Wang, H. Li, T. Tan, X. Wang, Y. Zhao, Carbon nanotubes/SiC prepared by catalytic chemical vapor deposition as scaffold for improved lithium-sulfur batteries. *Journal of Nanoparticle Research* **21** 113 (2019).

[219] S. Eun Wang, M. Ji Kim, J.-S. Park, J. Woong Lee, D. Woong Yoon, Y. Kim, J. Hyun Kim, Y. Chan Kang, D. Soo Jung, Silicon oxycarbide-derived hierarchical porous carbon nanoparticles with tunable pore structure for lithium-sulfur batteries. *Chemical Engineering Journal* **465** 143035 (2023).

[220] M.M. Amaral, S.B. Mujib, E.A. Santos, J. Ribeiro, H. Zanin, G. Singh, A sulfur host based on silicon oxycarbide for advanced lithium-sulfur batteries. *Journal of Energy Storage* **72** 108388 (2023).

[221] Y. Zhao, W. Wu, J. Li, Z. Xu, L. Guan, Encapsulating MWNTs into Hollow Porous Carbon Nanotubes: A Tube-in-Tube Carbon Nanostructure for High-Performance Lithium-Sulfur Batteries. **26** 5113-5118 (2014).

[222] Y. Qiu, W. Li, W. Zhao, G. Li, Y. Hou, M. Liu, L. Zhou, F. Ye, H. Li, Z. Wei, S. Yang, W. Duan, Y. Ye, J. Guo, Y. Zhang, High-Rate, Ultralong Cycle-Life Lithium/Sulfur Batteries Enabled by Nitrogen-Doped Graphene. *Nano Letters* **14** 4821-4827 (2014).

[223] S. Xin, L. Gu, N.-H. Zhao, Y.-X. Yin, L.-J. Zhou, Y.-G. Guo, L.-J. Wan, Smaller Sulfur Molecules Promise Better Lithium–Sulfur Batteries. *Journal of the American Chemical Society* **134** 18510-18513 (2012).

[224] Z. Li, Y. Jiang, L. Yuan, Z. Yi, C. Wu, Y. Liu, P. Strasser, Y. Huang, A Highly Ordered Meso@Microporous Carbon-Supported Sulfur@Smaller Sulfur Core–Shell Structured Cathode for Li–S Batteries. *ACS Nano* **8** 9295-9303 (2014).

I. Curriculum Vitae

PERSONAL DATA

Name	Fangmu Qu
Date of Birth	14.12.1990
Nationality	China

EDUCATION

09/2019-05/2024	Ph.D. Candidate in Materials Science
	Technical University of Darmstadt, Darmstadt, Germany
09/2015-11/2018	M.Sc. in Chemical Engineering
	Chinese Academy of Sciences, Beijing, China
09/2011-06/2015	B. Eng. In Chemical Engineering and Technology
	Nanjing Tech University, Nanjing, China

EXPERIENCE

09/2019-05/2024	Carbon-Rich SiCN/SiOC Ceramics as Sulfur Cathode Supports in Lithium-Sulfur Batteries
09/2017-11/2018	Carbon-coated nanoparticle-assembled Si microspheres as anode for lithium-ion battery
07/2017-08/2017	Summer School in Bar-Ilan University in Israel
09/2015-06/2017	Carbon-coated Si particles with self-supported Si nanowires as anode for lithium-ion battery
11/2014-06/2015	Synthesis and Properties of HM/MCM-48 Composite Molecular Sieve
05/2013-06/2013	Worked as an intern in Celanese and Sinopec
07/2012-09/2012	Nanjing Tech University's state key laboratory of chemical and material innovation fund and experiment contest

II. Publications

Statement of Personal Contribution

The personal contribution of the author herself to the following research articles is listed.

(1) **F. Qu**, M. Graczyk-Zajac*, D. Vrankovic, N. Chai, Z. Yu*, R. Riedel, Effect of morphology of C-rich silicon carbonitride ceramic on electrochemical properties of sulfur cathode for Li-S battery. *Electrochimica Acta* **384** 138265 (2021). DOI: 10.1016/j.electacta.2021.138265

The idea behind this publication originated in the discussion of Fangmu Qu, Dr. Magdalena Graczyk-Zajac, Dr. Dragoljub Vrankovic and, Prof. Zhaoju Yu and Prof. Ralf Riedel. The methodology was designed by Fangmu Qu under the supervision of Dr. Magdalena Graczyk-Zajac, Prof. Zhaoju Yu and Prof. Ralf Riedel. The preparation and characterization of the investigated samples were done by Fangmu Qu. All data were analyzed and visualized as figures or tables by Fangmu Qu. The manuscript was written by Fangmu Qu. The rest of the authors revised and approved the manuscript before publication.

(2) **F. Qu***, Z. Yu*, M. Krol, N. Chai, R. Riedel, M. Graczyk-Zajac, Electrochemical Performance of Carbon-Rich Silicon Carbonitride Ceramic as Support for Sulfur Cathode in Lithium Sulfur Battery. *Nanomaterials* **12** 1283 (2022). DOI: 10.3390/nano12081283

The idea behind this publication originated in the discussion of Fangmu Qu, Dr. Magdalena Graczyk-Zajac, Prof. Zhaoju Yu and Prof. Ralf Riedel. The methodology was designed by Fangmu Qu under the supervision of Dr. Magdalena Graczyk-Zajac, Prof. Zhaoju Yu and Prof. Ralf Riedel. The preparation and characterization of the investigated samples were done by Fangmu Qu. All data were analyzed and visualized as figures or tables by Fangmu Qu. The manuscript was written by Fangmu Qu. The rest of the authors revised and approved the manuscript before publication.

(3) Q. Wen*[&], **F. Qu**[&], Z. Yu*, M. Graczyk-Zajac, X. Xiong, R. Riedel, Si-based polymer-derived ceramics for energy conversion and storage. *Journal of Advanced Ceramics* **11** 197-246 (2022). DOI: 10.1007/s40145-021-0562-2

The idea behind this publication originated in the discussion of Qingbo Wen, Fangmu Qu, Dr. Magdalena Graczyk-Zajac, Prof. Zhaoju Yu and Prof. Ralf Riedel. The methodology was designed by Qingbo Wen and by Fangmu Qu under the supervision of Dr. Magdalena Graczyk-Zajac, Prof. Zhaoju Yu and Prof. Ralf Riedel. The manuscript was written by Qingbo Wen and Fangmu Qu. The rest of the authors revised and approved the manuscript before publication.

(4) A. Zambotti, **F. Qu***, G. Costa, M. Graczyk-Zajac, G.D. Sorarù, Polymer-Derived Ceramic Aerogels to Immobilize Sulfur for Li-S Batteries. *Energy Technology* **11** 2300488 (2023). DOI: 10.1002/ente.202300488

The idea behind this publication originated in the discussion of Andrea Zambotti, Giacomo Costa, Prof. Gian Domenico Sorarù, Fangmu Qu, and Dr. Magdalena Graczyk-Zajac. The methodology was designed by Andrea Zambotti, Giacomo Costa under the supervision of Prof. Gian Domenico Sorarù; and by Fangmu Qu under the supervision of Dr. Magdalena Graczyk-Zajac. The preparation and characterization of the investigated samples were done by Andrea Zambotti, Giacomo Costa and Fangmu Qu. All data were analyzed and visualized as figures or tables by Andrea Zambotti, Giacomo Costa and Fangmu Qu. The manuscript was written by Andrea Zambotti and Fangmu Qu. The rest of the authors revised and approved the manuscript before publication.

(5) **F. Qu***, Z. Yu*, M. Widenmeyer, C. Tian, R. Yan, H. Tian, A. Kempf, D.M. De Carolis, J.P. Hofmann, A. Weidenkaff, R. Riedel, M. Graczyk-Zajac, In-situ formed porous silicon carbonitride/boron nitride composites to boost cathode performance in lithium sulfur batteries. *Journal of Alloys and Compounds* **984** 174021 (2024). DOI: 10.1016/j.jallcom.2024.174021

The idea behind this publication originated in the discussion of Fangmu Qu, Dr. Magdalena Graczyk-Zajac. The methodology was designed by Fangmu Qu under the supervision of Dr. Magdalena Graczyk-Zajac, Prof. Zhaoju Yu and Prof. Ralf Riedel. The preparation and characterization of the investigated samples were performed by Fangmu Qu, Marc Widenmeyer, Chuanmu Tian, Ruijuan Yan and Honghong Tian. All data were analyzed and visualized as figures or tables by Fangmu Qu. The manuscript was written by Fangmu Qu. The rest of the authors revised and approved the manuscript before publication.

Effect of morphology of C-rich silicon carbonitride ceramic on electrochemical properties of sulfur cathode for Li-S battery

Fangmu Qu[a], Magdalena Graczyk-Zajac[a,c,*], Dragoljub Vrankovic[a], Nan Chai[a], Zhaoju Yu[b,d,*], Ralf Riedel[a]

[a] Institut für Materialwissenschaft, Technische Universität Darmstadt, Otto-Berndt-Straße 3, Darmstadt D-64287, Germany
[b] College of Materials, Key Laboratory of High Performance Ceramic Fibers, Ministry of Education, Xiamen University, Xiamen 361005, China
[c] EnBW Energie Baden-Württemberg AG, Durlacher Allee 93, Karlsruhe 76131, Germany
[d] College of Materials, Fujian Key Laboratory of Advanced Materials, Xiamen University, Xiamen 361005, China

ARTICLE INFO

ABSTRACT

Porous conducting materials represent a promising support for the immobilization of sulfur in the cathode of lithium–sulfur (Li-S) batteries. Herein, we provide an easy and scalable procedure for the preparation of such cathodes. This strategy consists of an infiltration of sulfur under solvothermal conditions at 155 °C into pores of carbon-rich silicon carbonitride (C-rich SiCN). Porous polymer-derived SiCN ceramics possess a unique combination of high electronic conductivity and robust, stress accommodating mechanical properties. The impact of the initial porosity and elemental composition of SiCN ceramics on the electrochemical performance of SiCN-S composites is addressed in this work. It is shown that material pyrolyzed at 1000 °C revealing a mesoporous character in line with the presence of a free carbon phase dispersed in SiCN demonstrates the best electrochemical stability and the highest capacity (more than 310 mAh/g over 40 cycles) at a high sulphur content of 66 wt.%.

1. Introduction

Advances in lithium-ion battery (LIB) technology have improved living conditions around the globe [1,2]. However, there are increasing concerns regarding the sustainability and criticality of materials (e.g. cobalt) for LIB [3–5]. Lithium-sulfur (Li-S) secondary battery is one of promising candidates for future's commercial applications due to its superior energy density (2600 Wh/kg) as well as abundant reserves and low cost of sulfur [6–8]. However, low conductivity (5×10^{-28} S/m) of sulfur, "shuttle effect" of soluble polysulfides and volume expansion of electrode materials during lithiation/delithiation processes result in a fast fading of specific capacity and low coulombic efficiency and seriously hinder a practical application of Li-S battery [9–12].

So far, remarkable works have been realized to solve above mentioned obstacles of Li-S battery [13–17]. Dispersing sulfur in an electrically conducting matrix is one of considered routes [18,19]. Therefore, conductive porous carbons are widely studied as sulfur-supporting matrices [20–23]. Well-engineered porous car-

bon framework significantly decreases electrode resistance, improves sulfur retention and provides enough transfer paths for lithium ions [24,25]. Encapsulating sulfur into hierarchically porous carbon frameworks significantly enhances the cycling stability and coulombic efficiency of Li-S battery due to the following reasons: (1) Interconnected porous carbon skeleton provides a good electrical contact between sulfur and carbon [26]; (2) Adsorption and blocking ability of high specific area and high porosity of porous carbon effectively capture polysulfides, thus weakening a "shuttle effect" [25,27]; (3) Interspace of porous carbon provides enough space for sulfur loading and accommodate the volume expansion of sulfur to a certain degree during lithiation/delithiation processes [28]; (4). Steady lithium ions supply is achieved by interconnected passageways [17,29]. Except traditional carbons, graphene [30,31], carbon nanotubes [32] and carbon fibers [33–35], some biomass-derived porous carbons from goat hair and rice are also investigated as lower cost and more environmentally friendly for future's applications of Li-S battery [36,37].

Nevertheless, the design of novel porous matrices effectively incorporating polysulfides still remains a challenge. Flexible and robust matrices are essential to ensure the encapsulation of the lithiation products Li_2S/Li_2S_2 simultaneously with the accommodation of the stresses due to the large volume change of ~80%.

---

* Corresponding author.
E-mail addresses: graczyk@materials.tu-darmstadt.de, m.graczyk-zajac@enbw.com (M. Graczyk-Zajac), zhaojuyu@xmu.edu.cn (Z. Yu).

Though the porous carbons are soft and well conductive matrices, they do not exhibit enough robustness to accommodate the stress developed during the large volume changes. Therefore, electrode structure could be easily destroyed by volume changes, resulting in fast fading of capacity and low coulombic efficiency. It has been recently demonstrated that the presence of nitrogen in a S-supporting matrix enhances the capability of capturing soluble polysulfides during charge/discharge processes [38–41]. Zhao et al. reported on sulfur/nitrogen-doped carbon nanotubes exhibiting 1267 mAh/g of initial discharge capacity and 807 mAh/g reversible capacity after 100 cycles [32]. Sun et al. used porous vanadium nitride/graphene composite as cathode for Li-S batteries. This material showed 85% capacity retention after 100 cycles under 0.2 C rate [42]. Above mentioned studies reveal that the presence of nitrogen in the cathode materials obviously anchors soluble polysulfides and provides additional electrons for conduction, resulting in enhanced cycling performance. Moreover, although many investigations proved that nitrogen-containing carbon matrices such as graphene or carbon nanotubes can further improve the electrochemical performance of the cathode. This feature makes the sulfur supports more expensive and their production difficult to be upscaled and, thus, not suitable for commercial applications. Our former works evidenced that polymer derived ceramics (PDCs) possess a unique combination of an excellent electronic conductivity [43,44] and a robust, stress accommodating mechanical properties [45–48]. Based on theoretical calculations, studies performed by Li and Zhao as well as by Wang et al. indicate a strong confinement of SiC for polysulfide due to Si-S interaction [49,50]. Furthermore, the presence of nitrogen in the ceramic has been recently revealed advantageous for hindering polysulfides shuttle. Namely, a strong lithium polysulfide chemisorption has been found on nitrogen-doped porous carbon Li-S battery cathodes [38]. In addition, the synthesis of SiCN ceramic matrix is a low-cost process and can be easily upscaled. Hence, porous C-rich SiCN ceramics represent a promising stabilizing matrix for the sulfur cathode.

Within this work, we aim at light-weight, electronically conductive and cheap silicon-based ceramic supports with a tailored porosity for the sulfur cathode of the Li-S battery. For this purpose, we synthetize carbon-rich SiCN ceramics with tailored morphology under different pyrolysis temperatures using a procedure patented by our team [51]. The synthesized materials reveal the presence of micro, meso, and macropores, which distribution depends on the pyrolysis temperature. In order to uniformly fill the pores with sulfur, we apply melting-diffusion procedure under pressure. Finally, we characterize the composite SiCN-S electrodes and determine the impact of the initial ceramic morphology and composition on the electrochemical properties of the obtained SiCN-S composite.

2. Experimental

2.1. Synthesis of carbon-rich SiCN ceramics with tailored morphology

Schlenk techniques were used to perform the reaction. Firstly, 100 g of perhydropolysilazane (PHPS) dispersions and 65 g of divinylbenzene (DVB) were mixed by magnetic stirrer under argon. Then, 0.2 mL of platinum (0)−1,3-divinyl-1,1,3,3-tetramethyldisiloxane complex used as catalyst was dropped into the mixture. Subsequently, above cross-link reaction was kept at 120 °C for 6 h under reflux till all mixture becoming white solid. The resulting white solid precursor was transferred to Schlenk tube for following pyrolysis under argon flow at 1000 °C. Afterwards, some of obtained production of pyrolysis were further heated at 1200 , 1400 and 1600 °C, respectively. At last, carbon-rich SiCN ceramics named SiCN-1000,SiCN-1200,SiCN-1400,SiCN-1600 with tailored morphology were obtained.

2.2. Synthesis of SiCN-S composites

The synthesized carbon-rich SiCN ceramics were firstly mixed with S by ratio 1:2 (66.6 wt% of sulfur) in ball milling machine for 20 min, respectively. Secondly, mixtures were transferred into Teflon inlet of autoclave and then the autoclaves were sealed. All autoclaves were then put in oven at 155 °C for 24 h. Finally, composites were ground in mortar and SiCN-S-1000,SiCN-S-1200,SiCN-S-1400,SiCN-S-1600 four different samples were obtained.

2.3. Characterization of materials

Micro-Raman spectra of the powder samples were recorded by using a micro-Raman spectrometer Horiba HR800 (Horiba, Japan) using an Ar-Ion laser of wavelength 514.5 nm and a Raman shift range of 0–4000 cm^{-1}. For all samples the filters and measuring parameters were kept constant. Nitrogen (N_2) adsorption was performed at 77 K using an Autosorb-3B (Quantachrome Instruments, USA). The samples were preheated at 100 °C for 24 h under vacuum before the measurements. The N_2 isotherm at 77 K was used to calculate the specific surface area (SSA) from the linear BET (Brunauer–Emmett–Teller) plots over the relative pressure range of $0.05 < p/p_o < 0.3$. The total pore volume (V_t) was determined from the amount of vapor adsorbed at a relative pressure $p/p_o \approx 1$ [52]. X-ray powder diffraction was performed on the as prepared powders using a STOE STADIP (STOE, Germany) equipped with monochromatic Mo-K$_\alpha$ radiation in flat-sample transmission geometry in the 2θ range of 5°–45° Hot-gas extraction (Leco-200 carbon analyzer, USA) was performed to analyze the total carbon content in SiCN samples. It amounts 50 –52 wt.% in 1000 and 1200 °C samples, respectively and increases to 59 wt.% for 1600 °C due to the carbothermal reduction leading to the loss of nitrogen, $Si_3N_4 + 3C \rightarrow 3SiC + 2N_2$ [53].

2.4. Electrochemical measurement

Electrochemical performance was analysed using Galvanostatic Cycling with Potential Limitation on VMP-multipotentiostat (Biologic Science Instruments, France) and controlled constant temperature of 25 °C. Cells were cycled by galvanostatic cycling with potential limitation (GCPL) in a potential range of 1.2– 3.6 V with a current of 83.5 mA/g. The scan rate of the cyclic voltammogram is 0.02 mV/s. For electrodes fabrication, 85 wt% SiCN-S composite as active material, 10 wt% polyvinylidenflouride (PVDF) as binder and 5 wt% carbon black (Super P, Timcal Ltd, Switzerland) as conduction additive were mixed with N-Methyl-2-pyrrolidone (NMP, BASF, Germany) to form slurry. Then the slurry was pasted onto an aluminum foil by a doctor blade and then dried at 40 °C in oven for 24 h until NMP was completely evaporated. After cutting and then drying in a Buchi (Labortechnik AG, Germany) for 24 h, electrodes with 10 mm of diameter were obtained. Afterwards, Swagelok cells were assembled in an argon-filled glovebox without air contact. lithium foil (0.75 mm thickness, Alfa Aesar, Germany) was used as the counter and QMA (Whatmann, UK) as separator. Electrolyte contained 1 M lithium bis(trifluoromethanesulfonyl)imide (LiTFSI) dissolved in a mixture of 1,3-dioxolane (DOL) and dimethoxymethane (DME) with volume ratio 1:1. Besides, 0.1 M of LiNO$_3$ was added into the electrolyte to alleviate the shuttle effect.

3. Results and discussion

3.1. X-Ray diffraction

Fig. 1 presents the X-Ray diffraction (XRD) patterns of the SiCN ceramics and SiCN-S composites, respectively. In Fig. 1a, there are
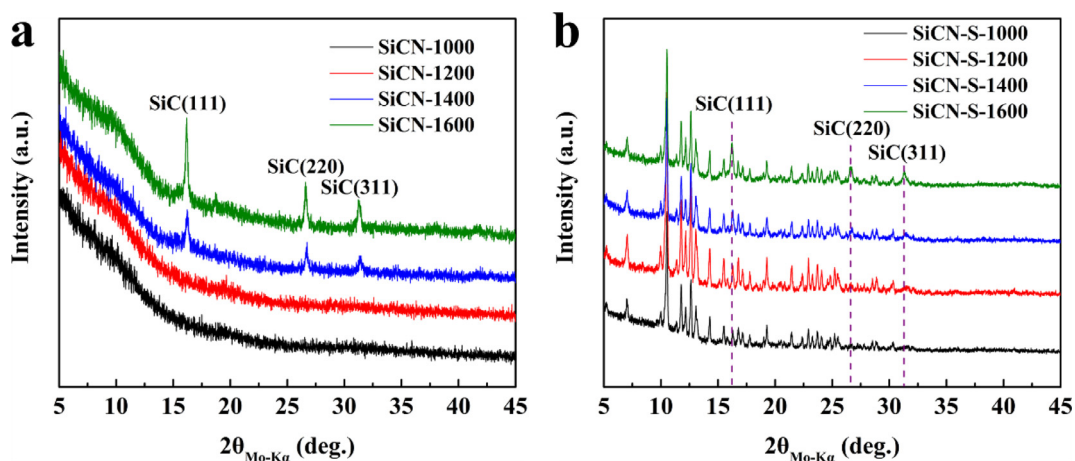
Fig. 1.. XRD patterns of SiCN ceramics (a) and SiCN-S composites (b) with different thermal treatment temperatures.

Table 1.
Porous characteristics, I (A_D)/ I (A_G) ratio and crystallite size (L_a) of SiCN-1000, SiCN-1200, SiCN-1400 and SiCN-1600. (Gaussian type curve fitting applied).

Sample	SiCN-1000	SiCN-1200	SiCN-1400	SiCN-1600
SSA (m^2/g)	72	94	318	383
V_t (cm^3/g)	0.36	0.49	0.65	0.73
Isotherm Type	IV	IV	I	I
APD (nm)	20.2	21.2	8.2	7.6
I (A_D) / I (A_G) ratio	2.19	1.96	1.62	1.51
L_a (nm)	7.67	8.57	10.39	11.13

no reflexes originating from for SiCN-1000 and SiCN-1200. It reveals the amorphous character of the ceramics. For SiCN-1400 and SiCN-1600, three reflexes attributed to three planes of crystalline SiC (JCPDS NO. 29–1129) appeared at 16.21°, 26.61° and 31.32°, corresponding to (111), (220), (311) planes, respectively. With a higher pyrolysis temperature, the reflexes become sharper and better resolved signifying increasing crystallinity. Blending with sulfur introduces the reflexes of crystalline sulfur to the pattern, as shown in Fig. 1b.

3.2. Nitrogen adsorption

Specific surface area (SSA) and pore size distribution were analyzed by means of N_2 adsorption-desorption measurement. Fig. 2a shows nitrogen adsorption-desorption isotherms of all investigated SiCN ceramics. A mesoporous character of all measured materials is confirmed by a hysteresis loop at $P/P_0 \approx 0.5$, originating a capillary condensation of nitrogen in mesopores. SSA, total pore volume (V_t) and isotherm type of SiCN-1000, SiCN-1200, SiCN-1400 and SiCN-1600 are listed in Table 1. The increase of SSA and V_t from 1000 to 1600 °C is related to the formation of SiC due to the reaction of the free carbon phase with the Si_3N_4. This reason is a carbothermal reduction, $Si_3N_4 + 3C \rightarrow 3SiC + 2 N_2$, resulting in a release of nitrogen leading to an additional microporosity [53]. Type I isotherm registered for SiCN-1400 and SiCN-1600 confirms these findings. Fig. 2b presents pore size distribution of all SiCN ceramics. Amount of mesopores with a pore size of 3 ,4 nm increase significantly with the rise of pyrolysis temperature. Average pore diameter (APD) of SiCN-1000, SiCN-1200, SiCN-1400 and SiCN-1600 are showed in Table 1. It also indicates that under 1400–1600 °C, pore size becomes smaller compared with the samples under 1000–1200 °C.
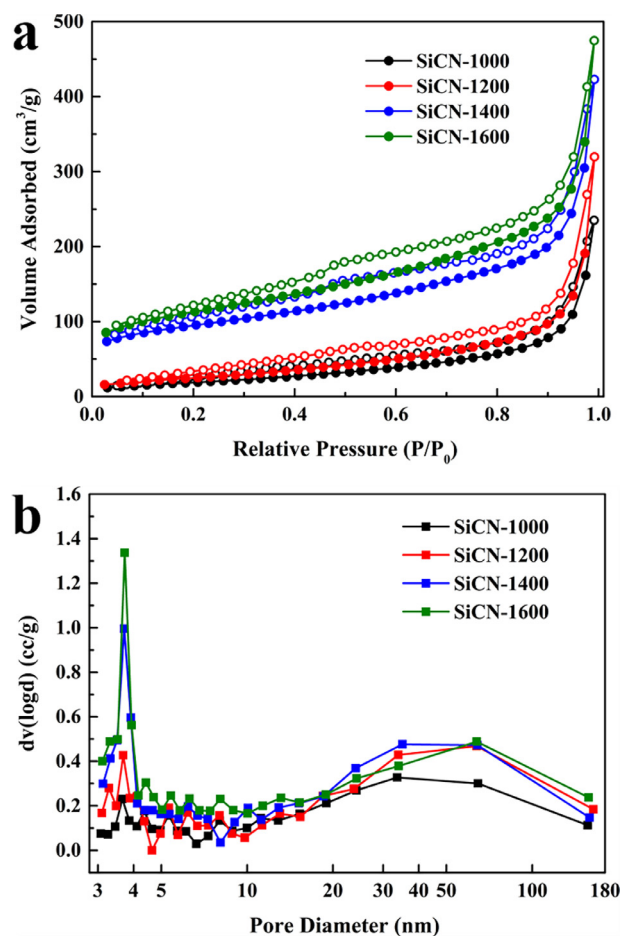
Fig. 2.. Nitrogen adsorption-desorption isotherms (a) and pore size distribution (b) of SiCN ceramics.

3.3. Raman spectroscopy

The microstructure of SiCN ceramics, pristine and after blending with sulfur has been analyzed using Micro-Raman spectroscopy. Fig. 3a shows overall measurement data recorded for the ceramics pyrolyzed at temperatures from 1000 to 1600 °C. SiCN materials reveal carbon-characteristic D and G bands at around 1346–1585 cm^{-1}, respectively. The D band is associated with disordered sp^2-
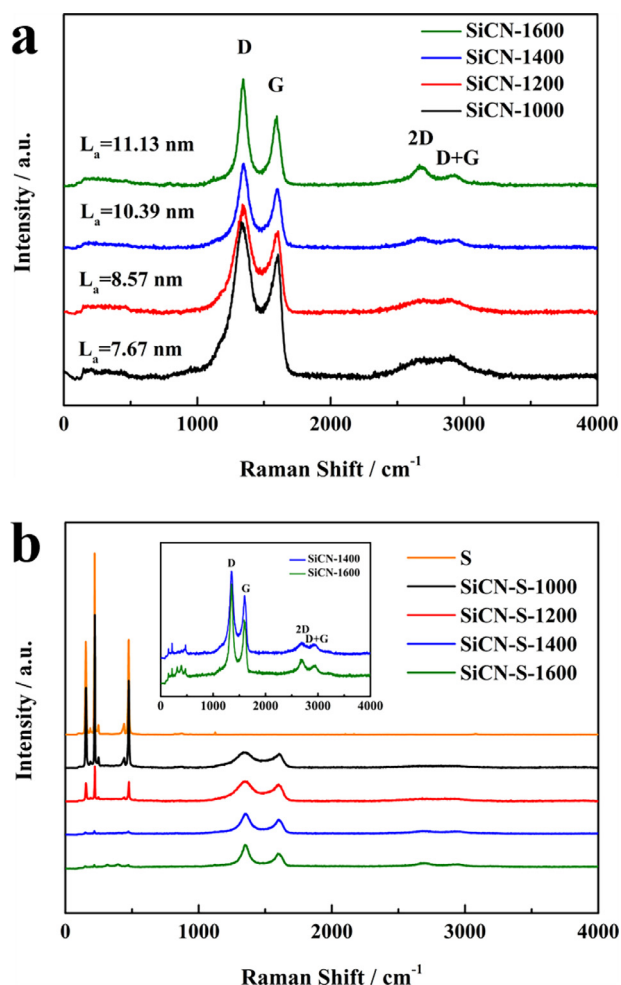
Fig. 3. Raman spectra of all SiCN ceramics (a) and all SiCN-S composites (b).

Fig. 4. Discharge curve (lithiation) of SiCN-S-1000, SiCN-S-1200, SiCN-S-1400 and SiCN-S-1600 (a); charge curve (delithiation) of SiCN-S-1000, SiCN-S-1200, SiCN-S-1400 and SiCN-S-1600 (b).

hybridized carbon structure while the presence of G band originates from the stretching of C–C in carbon materials with an ideal graphitic lattice. In all cases, the integral intensity of the D band is higher than that of the G band, indicating that the carbon in SiCN matrix is highly disordered. The curve types were adopted from extensive studies of Sadezky et al. [54]. The results of the fitting are gathered in Table 1. It is found that with increasing of the pyrolysis temperature, I (A_D) / I (A_G), the intensity ratio of D band and G band decreases but the intensity of 2D band at 2685 cm^{-1} and D+G band at 2925 cm^{-1} increases. A crystallite sizes (L_a) has been calculated using Eq. (1) elaborated by Cancado et al. [55]. L_a increases from 7.67 to 11.13 find the row from SiCN-1000 to SiCN-1600, respectively (compare Table 1). This indicates the increase of graphitic order in the free carbon phase with increasing pyrolysis temperature. Fig. 3b presents the Raman spectra of all SiCN-S composites. Besides the overtones of carbon phase, characteristic peaks of sulfur (153.67 , 219.52 and 475.11cm^{-1}) are present in each sample. However, as the pyrolysis temperature rises, the intensity of sulfur peaks becomes weaker. It signifies that in case of high temperature samples SiCN-1400 and SiCN-1600, less sulfur is present close to the surface but rather it is embedded in the interspace volume of porous SiCN (compare BET results).

$$L_a(\text{nm}) = \left(2.4 \times 10^{-10}\right) \lambda^4 \left(\frac{I(A_D)}{I(A_G)}\right)^{-1} \qquad (1)$$

3.4. Galvanostatic charge/discharge measurements

Fig. 4a and 4b presents the initial lithiation/delithiation curves of all investigated SiCN-S composites. During the first sulfur lithiation, there are two distinctive voltage plateaus at around 2.4 and 2.0 V, whereas the slope between them can be considered as a transition state [56]. This represents the conversion of sulfur from S_8 to higher order soluble Li_2S_x ($4<x<8$) and subsequent conversion to solid-state Li_2S_2 and Li_2S and has been addressed in details [56]. The initial lithiation capacities of SiCN-S-1000, SiCN-S-1200, SiCN-S-1400 and SiCN-S-1600 amount 722, 928, 730 and 851 mAh/g, respectively. The best initial columbic efficiencies (closest to 100%) are found for SiCN-S-1200 and SiCN-S-1600, for these materials the higher voltage plateau related to shuttling effect [14,57] is less pronounced.

For samples with efficiencies over 100% the short plateau at around 2.3–2.4 V corresponding to the shuttle phenomenon is clearly visible. The voltage for the first plateau varies for the composites (2.35 for SiCN-S-1000, 2.37 V for others). For the second plateau the potential values are almost identical (2.08 V), however the transition to the following slope is "smooth" for 1000 and 1200 °C materials, and a very abrupt for SiCN-1400 and SiCN-1600. The last one is typical and comparable to the transitions observed for microporous carbonaceous materials in the literatures [7,13,19,58].
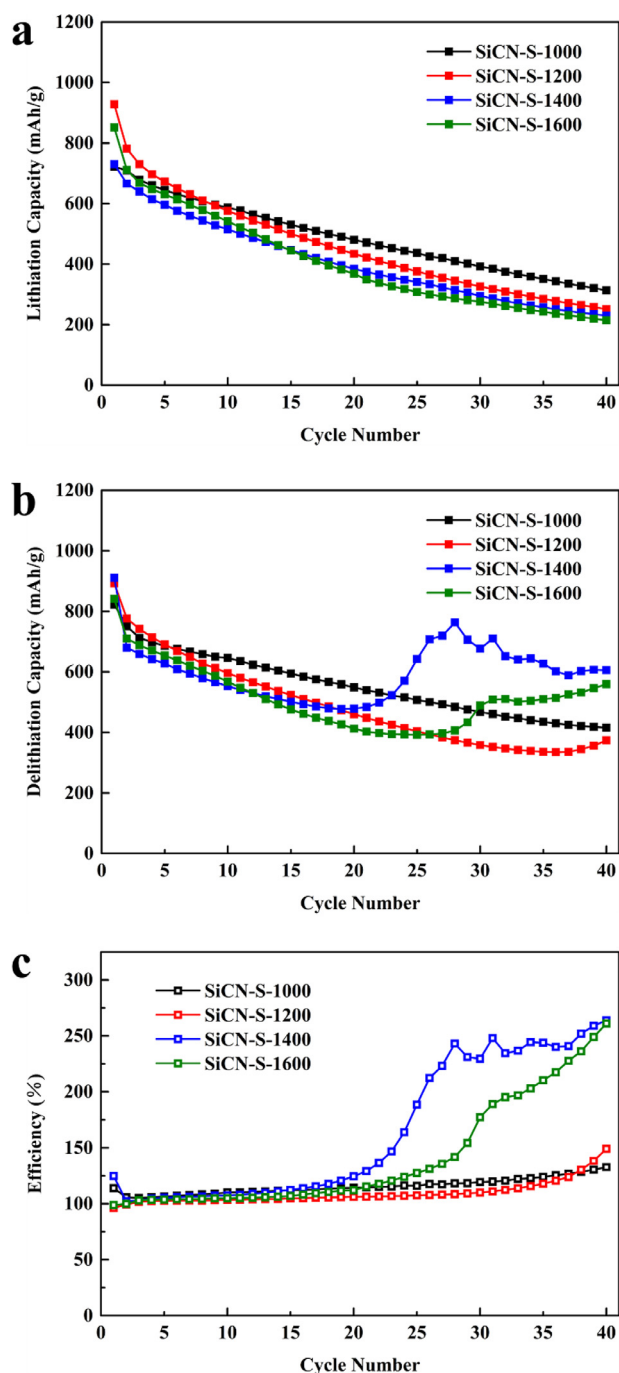
Fig. 5.. Cycling performance of SiCN-S-1000, SiCN-S-1200, SiCN-S-1400 and SiCN-S-1600. Lithiation capacity (a), delithiation capacity (b) and columbic efficiency (c).

3.5. Extended cycling performance

Lithiation/delithiation specific capacity and corresponding coulombic efficiency of SiCN-S-1000, SiCN-S-1200, SiCN-S-1400 and SiCN-S-1600 are showed in Fig. 5a, 5b and 5c, respectively. The initial discharge capacity, coulombic efficiency, reversible capacity after 40 cycles and capacity retention of all samples are listed in Table 2. In the beginning of the cycling, SiCN-S-1200 shows the highest initial discharge specific capacity while SiCN-S-1000 reveals the lowest initial discharge specific capacity. However, SiCN-S-1000 exhibits the slowest discharge capacity fading and its discharge capacity exceeds SiCN-S-1200 after 8 cycles. As for SiCN-S-1400 and SiCN-S-1600, before 12th cycle, capacity reten-

tion of SiCN-S-1600 is a little bit better than that of SiCN-S-1400 but still worse than SiCN-S-1000 and SiCN-S-1200. Over ca. 20th cycle, the efficiency of both SiCN-S-1400 and SiCN-S-1600 dramatically increases. The reason of this phenomenon is due to an increasing degree of shuttling effect, please see Fig. 5(a,b) which shows the corresponding extended lithiation and delithiation of all investigated samples. In case of SiCN-1400 and SiCN-1600, the long-chain polysulfides migrate to Li anode, are chemically oxidized, migrate back and are further oxidized to a long-chain polysulfide, corresponding to a long charge (delithiation) process and efficiency losses.

The shuttling phenomenon still does not appear visibly in the potential/capacity transient of SiCN-S-1000, while it is present to a high extend in SiCN-S-1400 and SiCN-S-1600 and to a certain level in E vs Q curves of 1200 °C material. In case of porous carbon supports for sulfur cathode, Li_2S_x trapping relies on the physical adsorption of Li_2S_x on carbon and consequently has only a weak effect on polysulfide diffusion. Some nonconductive adsorbents such as oxides have a better ability to trap [59]. However, they are usually non-conductive and their use leads to ohmic polarization. Moreover, there is no electron transfer from these non-conductive absorbents, which prevents electrochemical redox processes. Polysulfides must desorb and travel to the surface of the conductive host, what results in low reaction rates and might also lead to the permanent loss of active material if Li_2S_x too strongly adsorbed. In contrast, the N-doped carbon material enables direct and easy redox reactions of adsorbed polysulfides while showing even stronger adsorption [38]. This finding allows us to rationalize the electrochemical properties of SiCN-S composites. Their electrochemical stabilities/capacities decrease with increasing pyrolysis temperature of the SiCN host. Although Raman Spectroscopy measurements demonstrate better embedding of sulfur in those materials, a shuttling effect is strongly pronounced after ca. 20th cycle. A more stable electrochemical performance is found for SiCN-S-1000 and SiCN-S-1200 composites. Both SiCN-S-1400 and SiCN-S-1600 undergo the carbothermal reduction which is accompanied by nitrogen release (for details, please see the discussion of XRD results). Moreover, in consequence of SiC crystallization, the integrity of SiCN ceramic is broken down leading to a phase-separated, nitrogen-poor system consisting in a partially ordered carbon and crystalline SiC. These compositional and microstructural features affect the ability to stabilize sulfur cathode. Thus, the low temperature samples, consisting of free carbon phase uniformly dispersed in SiCN matrix reveal much better electrochemical properties. After 40 cycles, sample SiCN-S-1000 exhibits the highest lithiation capacity retention. The capability of the SiCN ceramic to stabilize the sulfur cathode decreases with increasing synthesis temperature.

3.6. Cyclic voltammperometry

Cyclic voltammograms allow to get closer insight to the redox reaction. As shown in Fig. 6a, during the first cycle, the first cathodic peak appears at 2.33–2.35 V corresponding to the conversion of S_8 to higher order polysulfides (Li_2S_x, $4<x<8$). The second cathodic peak appears at 2.04–2.05 V and corresponds to the further reduction of polysulfides to insoluble Li_2S_2 and Li_2S [58]. During oxidation process, a main anodic peak appears at 2.43–2.46 V, attributed to the conversion of lithium sulfide to S_8. It originates from the overlap of two peaks corresponding to oxidation of the species reduced within two cathodic peaks. The splitting into two anodic peaks is better visible during the 5th cycle, as shown in Fig. 6b. Both oxidation and reduction peaks are very sharp. It signifies less ohmic losses, namely that the ceramic matrix fulfills their role to provide sufficient electronic/ionic conductivity to embedded sulfur [19,60]. After 5 cycles, although intensity of all peaks

Table 2.
Electrochemical parameters of all samples.

Samples	Initial Discharge Capacity (mAh/g)	Reversible Capacity after 40th Cycle (mAh/g)	Initial Coulombic Efficiency (%)	Capacity Retention (%)
SiCN-S-1000	722	313	114	43
SiCN-S-1200	928	251	96	27
SiCN-S-1400	730	230	125	32
SiCN-S-1600	851	214	99	25

Fig. 6. Cyclic voltammograms of SiCN-S-1000, SiCN-S-1200, SiCN-S-1400, SiCN-S-1600 at a scan rate of 0.02 mV/s. The first cycle (a) and the fifth cycle (b).

decreases, SiCN-S-1000 still maintains a highest intensity of anodic peak, indicating a good reversibility during cycling.

Summarizing, SiCN ceramic matrix pyrolyzed under 1000–1200 °C exhibit better electrochemical performance compared with other temperatures. We rationalize the enhanced electrochemical properties of SiCN-S-1000 as follows: (1) presence of amorphous, highly defective free carbon dispersed in SiCN matrix provides highly conductive room for sulfur infiltration, (2) carbothermal reduction occurring at higher temperature leads to a separation of free carbon and ceramic phases, namely it results in separated free, less disordered carbon and SiC [61–63]. Here, the conductivity is provided by a free carbon phase exclusively, this phase however is not able to provide the robustness, leading to enhanced shuttling effect after 20 cycles; and (3) the presence of nitrogen at lower temperature materials appears to be of advantage for polysulfides stabilization. The presence of nitrogen in the cathode material can suppress migration of soluble polysulfides during cycling, resulting in a weakened shuttling effect and enhanced cycling stability [38]. It signifies, that the microporous morphology of the sulfur support

might be of advantage for the cathode stabilization, but it is not a necessary condition since other properties might play a crucial role. The high efficiency of the low temperature pyrolyzed ceramics is owing to both the advantageous role of mesoporous ceramic matrix containing nitrogen and the $LiNO_3$ electrolyte additive since $LiNO_3$ is known to promote the formation of a stable protective film on the lithium anode [64].

4. Conclusions

Porous C-rich SiCN ceramics with tailored morphology were synthesized under different pyrolysis temperatures. Sulfur has been infiltrated into the porous morphology using a melting-diffusion procedure under pressure. The resulting SiCN-S composites have been characterized as a sulfur host for Li–S batteries. Their electrochemical performance has been analyzed and discussed with respect to the initial microstructure and composition of the SiCN ceramic. It has been shown that SiCN-S-1000 composite demonstrates better electrochemical stability and higher capacity (more than 310 mAh/g over 40 cycles) at a high sulfur content of 66 wt.% than the cathode materials with ceramics sintered at higher temperatures. These findings are rationalized as a consequence of the microstructural integrity of the low temperature sintered materials in line with an advantage of a higher nitrogen content. Furthermore, this work provides an inexpensive and scalable route of sulfur infiltration which allows for further enhancement of the electrochemical properties of Li–S batteries.

Declaration of Competing Interest

The authors declare that they have no known competing financial interests or personal relationships that could have appeared to influence the work reported in this paper.

Credit authorship contribution statement

Fangmu Qu: Conceptualization, Methodology, Data curation, Writing - original draft, Funding acquisition. **Magdalena Graczyk-Zajac:** Supervision, Conceptualization, Methodology, Writing - review & editing. **Dragoljub Vrankovic:** Conceptualization, Supervision. **Nan Chai:** Data curation, Supervision. **Zhaoju Yu:** Supervision, Writing - review & editing, Funding acquisition. **Ralf Riedel:** Supervision, Writing - review & editing, Funding acquisition.

Acknowledgments

References

[1] J.M. Tarascon, M. Armand, Issues and challenges facing rechargeable lithium batteries, Nature 414 (2001) 359–367.
[2] M. Li, J. Lu, Z. Chen, K. Amine, 30 Years of lithium-ion batteries, Adv. Mater. 30 (2018) 1800561.
[3] J.W. Choi, D. Aurbach, Promise and reality of post-lithium-ion batteries with high energy densities, Nat. Rev. Mater. 1 (2016) 160013.

[4] Y. Liu, Y. Zhu, Y. Cui, Challenges and opportunities towards fast-charging battery materials, Nat. Energy 4 (2019) 540–550.

[5] T. Kim, W. Song, D.-.Y. Son, L.K. Ono, Y. Qi, Lithium-ion batteries: outlook on present, future, and hybridized technologies, J. Mater. Chem. A 7 (2019) 2942–2964.

[6] B. Scrosati, J. Garche, Lithium batteries: status, prospects and future, J. Power Sources 195 (2010) 2419–2430.

[7] A. Manthiram, Y. Fu, S.H. Chung, C. Zu, Y.S. Su, Rechargeable lithium-sulfur batteries, Chem. Rev. 114 (2014) 11751–11787.

[8] R. Fang, S. Zhao, Z. Sun, D.W. Wang, H.M. Cheng, F. Li, More reliable lithium-sulfur batteries: status, solutions and prospects, Adv. Mater. 29 (2017) 1606823.

[9] Y.X. Yin, S. Xin, Y.G. Guo, L.J. Wan, Lithium-sulfur batteries: electrochemistry, materials, and prospects, Angew. Chem. Int. Ed. Engl. 52 (2013) 13186–13200.

[10] A. Manthiram, Y. Fu, Y.-.S. Su, Challenges and prospects of lithium-sulfur batteries, Acc. Chem. Res. 46 (2013) 1125–1134.

[11] H.-.J. Peng, J.-.Q. Huang, X.-.B. Cheng, Q. Zhang, Review on high-loading and high-energy lithium-sulfur batteries, Adv. Energy Mater. 7 (2017) 1700260.

[12] H. Yuan, H.-.J. Peng, B.-.Q. Li, J. Xie, L. Kong, M. Zhao, X. Chen, J.-.Q. Huang, Q. Zhang, Conductive and catalytic triple-phase interfaces enabling uniform nucleation in high-rate lithium-sulfur batteries, Adv. Energy Mater. 9 (2019) 1802768.

[13] S. Xin, L. Gu, N.H. Zhao, Y.X. Yin, L.J. Zhou, Y.G. Guo, L.J. Wan, Smaller sulfur molecules promise better lithium-sulfur batteries, J. Am. Chem. Soc. 134 (2012) 18510–18513.

[14] N. Ding, L. Zhou, C. Zhou, D. Geng, J. Yang, S.W. Chien, Z. Liu, M.F. Ng, A. Yu, T.S. Hor, M.B. Sullivan, Y. Zong, Building better lithium-sulfur batteries: from LiNO₃ to solid oxide catalyst, Sci. Rep. 6 (2016) 33154.

[15] A. Bhargav, J. He, A. Gupta, A. Manthiram, Lithium-sulfur batteries: attaining the critical metrics, Joule 4 (2020) 285–291.

[16] Z. Du, X. Chen, W. Hu, C. Chuang, S. Xie, A. Hu, W. Yan, X. Kong, X. Wu, H. Ji, L.J. Wan, Cobalt in nitrogen-doped graphene as single-atom catalyst for high-sulfur content lithium-sulfur batteries, J. Am. Chem. Soc. 141 (2019) 3977–3985.

[17] P. Shi, T. Li, R. Zhang, X. Shen, X.B. Cheng, R. Xu, J.Q. Huang, X.R. Chen, H. Liu, Q. Zhang, Lithiophilic LiC₆ layers on carbon hosts enabling stable Li metal anode in working batteries, Adv. Mater. 31 (2019) 1807131.

[18] B. Zhang, X. Qin, G.R. Li, X.P. Gao, Enhancement of long stability of sulfur cathode by encapsulating sulfur into micropores of carbon spheres, Energy Environ. Sci. 3 (2010) 1531–1537.

[19] Y. Qiu, W. Li, W. Zhao, G. Li, Y. Hou, M. Liu, L. Zhou, F. Ye, H. Li, Z. Wei, S. Yang, W. Duan, Y. Ye, J. Guo, Y. Zhang, High-rate, ultralong cycle-life lithium/sulfur batteries enabled by nitrogen-doped graphene, Nano Lett. 14 (2014) 4821–4827.

[20] Y. Zhao, W. Wu, J. Li, Z. Xu, L. Guan, Encapsulating MWNTs into hollow porous carbon nanotubes: a tube-in-tube carbon nanostructure for high-performance lithium-sulfur batteries, Adv. Mater. 26 (2014) 5113–5118.

[21] D. Gueon, J.T. Hwang, S.B. Yang, E. Cho, K. Sohn, D.K. Yang, J.H. Moon, Spherical macroporous carbon nanotube particles with ultrahigh sulfur loading for lithium-sulfur battery cathodes, ACS Nano 12 (2018) 226–233.

[22] A. Abdul Razzaq, Y. Yao, R. Shah, P. Qi, L. Miao, M. Chen, X. Zhao, Y. Peng, Z. Deng, High-performance lithium sulfur batteries enabled by a synergy between sulfur and carbon nanotubes, Energy Storage Mater. 16 (2019) 194–202.

[23] M. Chen, Z. Su, Y. Liu, Y. Pan, Y. Zhang, M. Hu, Q. Ma, Q. Zhou, D. Long, Self-propelled nanoemulsion assembly of organosilane to the synthesis of high-surface-area hollow carbon spheres for enhanced energy storage, Chem. Eng. J. 400 (2020) 124973.

[24] J. Hou, X. Tu, X. Wu, M. Shen, X. Wang, C. Wang, C. Cao, H. Pang, G. Wang, Remarkable cycling durability of lithium-sulfur batteries with interconnected mesoporous hollow carbon nanospheres as high sulfur content host, Chem. Eng. J. 401 (2020) 126141.

[25] M.A. Pope, I.A. Aksay, Structural design of cathodes for Li-S batteries, Adv. Energy Mater. 5 (2015) 1500124.

[26] X. Wen, K. Xiang, Y. Zhu, L. Xiao, H. Liao, W. Chen, X. Chen, H. Chen, 3D hierarchical nitrogen-doped graphene/CNTs microspheres as a sulfur host for high-performance lithium-sulfur batteries, J. Alloy. Compd. 815 (2020) 152350.

[27] L. Peng, Z. Fang, Y. Zhu, C. Yan, G. Yu, Holey 2D nanomaterials for electrochemical energy storage, Adv. Energy Mater. 8 (2018) 1702179.

[28] Y. Wang, R. Zhang, Y.C. Pang, X. Chen, J. Lang, J. Xu, C. Xiao, H. Li, K. Xi, S. Ding, Carbon@titanium nitride dual shell nanospheres as multi-functional hosts for lithium sulfur batteries, Energy Storage Mater. 16 (2019) 228–235.

[29] Z.-.L. Xu, J.-.K. Kim, K. Kang, Carbon nanomaterials for advanced lithium sulfur batteries, Nano Today 19 (2018) 84–107.

[30] J. Cao, C. Chen, Q. Zhao, N. Zhang, Q. Lu, X. Wang, Z. Niu, J. Chen, A flexible nanostructured paper of a reduced graphene oxide-sulfur composite for high-performance lithium-sulfur batteries with unconventional configurations, Adv. Mater. 28 (2016) 9629–9636.

[31] J. Jin, Z. Wen, G. Ma, Y. Lu, Y. Cui, M. Wu, X. Liang, X. Wu, Flexible self-supporting graphene–sulfur paper for lithium sulfur batteries, RSC Adv. 3 (2013) 2558–2560.

[32] Y. Zhao, F. Yin, Y. Zhang, C. Zhang, A. Mentbayeva, N. Umirov, H. Xie, Z. Bakenov, A free-standing sulfur/nitrogen-doped carbon nanotube electrode for high-performance lithium/sulfur batteries, Nanoscale Res. Lett. 10 (2015) 450.

[33] Z. Li, J.T. Zhang, Y.M. Chen, J. Li, X.W. Lou, Pie-like electrode design for high-energy density lithium-sulfur batteries, Nat. Commun. 6 (2015) 8850.

[34] A. Mentbayeva, A. Belgibayeva, N. Umirov, Y. Zhang, I. Taniguchi, I. Kurmanbayeva, Z. Bakenov, High performance freestanding composite cathode for lithium-sulfur batteries, Electrochim. Acta 217 (2016) 242–248.

[35] X. Song, S. Wang, Y. Bao, G. Liu, W. Sun, L.-.X. Ding, H. Liu, H. Wang, A high strength, free-standing cathode constructed by regulating graphitization and the pore structure in nitrogen-doped carbon nanofibers for flexible lithium–sulfur batteries, J. Mater. Chem. A 5 (2017) 6832–6839.

[36] Y. Zhong, X. Xia, S. Deng, J. Zhan, R. Fang, Y. Xia, X. Wang, Q. Zhang, J. Tu, Popcorn inspired porous macrocellular carbon: rapid puffing fabrication from rice and its applications in lithium-sulfur batteries, Adv. Energy Mater. 8 (2018) 1701110.

[37] R. Zhang, X. Chen, X. Shen, X.-.Q. Zhang, X.-.R. Chen, X.-.B. Cheng, C. Yan, C.-.Z. Zhao, Q. Zhang, Coralloid carbon fiber-based composite lithium anode for robust lithium metal batteries, Joule 2 (2018) 764–777.

[38] J. Song, M.L. Gordin, T. Xu, S. Chen, Z. Yu, H. Sohn, J. Lu, Y. Ren, Y. Duan, D. Wang, Strong lithium polysulfide chemisorption on electroactive sites of nitrogen-doped carbon composites for high-performance lithium-sulfur battery cathodes, Angew. Chem. Int. Ed. Engl. 54 (2015) 4325–4329.

[39] Q. Pang, L.F. Nazar, Long-life and high-areal-capacity Li-S batteries enabled by a light-weight polar host with intrinsic polysulfide adsorption, ACS Nano 10 (2016) 4111–4118.

[40] T. Zhou, W. Lv, J. Li, G. Zhou, Y. Zhao, S. Fan, B. Liu, B. Li, F. Kang, Q.-.H. Yang, Twinborn TiO₂–TiN heterostructures enabling smooth trapping–diffusion–conversion of polysulfides towards ultralong life lithium–sulfur batteries, Energy Environ. Sci. 10 (2017) 1694–1703.

[41] L. Qu, P. Liu, P. Zhang, T. Wang, Y. Yi, P. Yang, X. Tian, M. Li, B. Yang, Carbon–nanotube/sulfur cathode with in-situ assembled Si₃N₄/graphene interlayer for high-rate and long cycling-life lithium-sulfur batteries, Electrochim. Acta 296 (2019) 155–164.

[42] Z. Sun, J. Zhang, L. Yin, G. Hu, R. Fang, H.M. Cheng, F. Li, Conductive porous vanadium nitride/graphene composite as chemical anchor of polysulfides for lithium-sulfur batteries, Nat. Commun. 8 (2017) 14627.

[43] J. Kaspar, M. Graczyk-Zajac, S. Choudhury, R. Riedel, Impact of the electrical conductivity on the lithium capacity of polymer-derived silicon oxycarbide (SiOC) ceramics, Electrochim. Acta 216 (2016) 196–202.

[44] M. Graczyk-Zajac, D. Vrankovic, P. Waleska, C. Hess, P.V. Sasikumar, S. Lauterbach, H.-.J. Kleebe, G.D. Sorarù, The Li-storage capacity of SiOC glasses with and without mixed silicon oxycarbide bonds, J Mater. Chem. A 6 (2018) 93–103.

[45] D. Vrankovic, M. Graczyk-Zajac, C. Kalcher, J. Rohrer, M. Becker, C. Stabler, G. Trykowski, K. Albe, R. Riedel, Highly porous silicon embedded in a ceramic matrix: a stable high-capacity electrode for Li-Ion Batteries, ACS Nano 11 (2017) 11409–11416.

[46] P. Stein, D. Vrankovic, M. Graczyk-Zajac, R. Riedel, B.-.X. Xu, A model for diffusion and immobilization of lithium in SiOC nanocomposite anodes, JOM 69 (2017) 1524–1531.

[47] J. Kaspar, C. Terzioglu, E. Ionescu, M. Graczyk-Zajac, S. Hapis, H.-.J. Kleebe, R. Riedel, Stable SiOC/Sn nanocomposite anodes for lithium-ion batteries with outstanding cycling stability, Adv. Funct. Mater. 24 (2014) 4097–4104.

[48] J. Kaspar, M. Graczyk-Zajac, R. Riedel, Determination of the chemical diffusion coefficient of Li-ions in carbon-rich silicon oxycarbide anodes by electro-analytical methods, Electrochim. Acta 115 (2014) 665–670.

[49] F. Li, J. Zhao, Three dimensional porous SiC for lithium polysulfide trapping, Phys. Chem. Chem. Phys. 20 (2018) 4005–4011.

[50] J. Wang, W. Wang, H. Li, T. Tan, X. Wang, Y. Zhao, Carbon nanotubes/SiC prepared by catalytic chemical vapor deposition as scaffold for improved lithium–sulfur batteries, J. Nanoparticle Res. 21 (2019) 113.

[51] D. Vrankovic, M. Storch, C. Schitco, M. Graczyk-Zajac, R. Riedel, Verfahren Zum Herstellen poröser Keramiken und Eines Porösen Keramikprodukts, 2018 Patent Application.DE 102016116732.0..

[52] K.S.W. Sing, D.H. Everett, R.A.W. Haul, L. Moscou, R.A. Pierotti, J. Rouquerol, T. Siemieniewska, Reporting physisorption data for gas solid systems with special reference to the determination of surface-area and porosity (recommendations 1984), Pure Appl. Chem. 57 (1985) 603–619.

[53] M. Storch, D. Vrankovic, M. Graczyk-Zajac, R. Riedel, The influence of pyrolysis temperature on the electrochemical behavior of porous carbon-rich SiCN polymer-derived ceramics, Solid State Ion. 315 (2018) 59–64.

[54] A. Sadezky, H. Muckenhuber, H. Grothe, R. Niessner, U. Pöschl, Raman microspectroscopy of soot and related carbonaceous materials: spectral analysis and structural information, Carbon 43 (2005) 1731–1742.

[55] L.G. Cançado, K. Takai, T. Enoki, M. Endo, Y.A. Kim, H. Mizusaki, A. Jorio, L.N. Coelho, R. Magalhães-Paniago, M.A. Pimenta, General equation for the determination of the crystallite size Lₐ of nanographite by Raman spectroscopy, Appl. Phys. Lett. 88 (2006) 163106.

[56] A. Kawase, S. Shirai, Y. Yamoto, R. Arakawa, T. Takata, Electrochemical reactions of lithium-sulfur batteries: an analytical study using the organic conversion technique, Phys. Chem. Chem. Phys. 16 (2014) 9344–9350.

[57] Y.-.J. Choi, Y.-.D. Chung, C.-.Y. Baek, K.-.W. Kim, H.-.J. Ahn, J.-.H. Ahn, Effects of carbon coating on the electrochemical properties of sulfur cathode for lithium/sulfur cell, J. Power Sources 184 (2008) 548–552.

[58] Z. Li, Y. Jiang, L. Yuan, Z. Yi, C. Wu, Y. Liu, P. Strasser, Y. Huang, A highly ordered Meso@Microporous carbon-supported Sulfur@Smaller sulfur core-shell structured cathode for Li-S batteries, ACS Nano 8 (2014) 9295–9303.

[59] X. Ji, S. Evers, R. Black, L.F. Nazar, Stabilizing lithium-sulphur cathodes using polysulphide reservoirs, Nat. Commun. 2 (2011) 325.

[60] U. Gulzar, T. Li, X. Bai, M. Colombo, A. Ansaldo, S. Marras, M. Prato, S. Goriparti, C. Capiglia, R.Proietti Zaccaria, Nitrogen-doped single-walled carbon nanohorns as a cost-effective carbon host toward high-performance lithium-sulfur batteries, ACS Appl. Mater. Interfaces 10 (2018) 5551–5559.

[61] J. Kaspar, M. Graczyk-Zajac, R. Riedel, Lithium insertion into carbon-rich SiOC ceramics: influence of pyrolysis temperature on electrochemical properties, J. Power Sources 244 (2013) 450–455.

[62] V.S. Pradeep, M. Graczyk-Zajac, R. Riedel, G.D. Soraru, New insights in to the lithium storage mechanism in polymer derived SiOC anode materials, Electrochim. Acta 119 (2014) 78–85.

[63] M. Graczyk-Zajac, M. Wimmer, Y. Xu, G. Buntkowsky, C. Neumann, R. Riedel, Lithium intercalation into disordered carbon/SiCN composite. Part 2: raman spectroscopy and ^{7}Li MAS NMR investigation of lithium storage sites, J. Solid State Electrochem. 21 (2016) 47–55.

[64] S.S. Zhang, A new finding on the role of $LiNO_3$ in lithium-sulfur battery, J. Power Sources 322 (2016) 99–105.

Article

Electrochemical Performance of Carbon-Rich Silicon Carbonitride Ceramic as Support for Sulfur Cathode in Lithium Sulfur Battery

Fangmu Qu [1,*], Zhaoju Yu [2,3,*], Monika Krol [1,†], Nan Chai [1], Ralf Riedel [1] and Magdalena Graczyk-Zajac [1,4]

[1] Institut für Materialwissenschaft, Technische Universität Darmstadt, Otto-Berndt-Straße 3, 64287 Darmstadt, Germany; m.graczyk-zajac@enbw.com (M.G.-Z.); monika.krol@aalto.fi (M.K.); n.chai@materials.tu-darmstadt.de (N.C.); riedel@materials.tu-darmstadt.de (R.R.)

[2] Key Laboratory of High-Performance Ceramic Fibers, Ministry of Education, College of Materials, Xiamen University, Xiamen 361005, China

[3] Fujian Key Laboratory of Advanced Materials, College of Materials, Xiamen University, Xiamen 361005, China

[4] EnBW Energie Baden-Württemberg AG, Durlacher Allee 93, 76131 Karlsruhe, Germany

* Correspondence: fangmu.qu@stud.tu-darmstadt.de (F.Q.); zhaojuyu@xmu.edu.cn (Z.Y.)

† Present address: Applied Physics, Aalto University, FI-00076 Aalto, Finland.

Abstract: As a promising matrix material for anchoring sulfur in the cathode for lithium-sulfur (Li-S) batteries, porous conducting supports have gained much attention. In this work, sulfur-containing C-rich SiCN composites are processed from silicon carbonitride (SiCN) ceramics, synthesized at temperatures from 800 to 1100 °C. To embed sulfur in the porous SiCN matrix, an easy and scalable procedure, denoted as melting-diffusion method, is applied. Accordingly, sulfur is infiltrated under solvothermal conditions at 155 °C into pores of carbon-rich silicon carbonitride (C-rich SiCN). The impact of the initial porosity and microstructure of the SiCN ceramics on the electrochemical performance of the synthesized SiCN-sulfur (SiCN-S) composites is analysed and discussed. A combination of the mesoporous character of SiCN and presence of a disordered free carbon phase makes the electrochemical performance of the SiCN matrix obtained at 900 °C superior to that of SiCN synthesized at lower and higher temperatures. A capacity value of more than 195 mAh/g over 50 cycles at a high sulfur content of 66 wt.% is achieved.

Keywords: SiCN ceramic matrix; disordered carbon; porous structure; sulfur cathode

1. Introduction

The rapidly growing technological development of the modern world relies on the increasing demand for the allocation of energy, in the form of electrical power. While renewable energies are continuously growing worldwide, fossil fuels still show an increasing consumption associated with the production of high levels of carbon dioxide and other greenhouse gasses, which are responsible for our climate change [1]. In order to significantly reduce the usage of fossil fuels and, at the same time, increase the production of electrical power, renewable energies have to be further developed in the near future. One of the most sustainable solutions is using renewable green sources based on wind, water, or solar energy, which are clean and do not emit as much greenhouse gasses. However, renewable sources are intermittent and require efficient energy storage systems to become a valid competitor of fossil fuels. Electrochemical energy storage systems such as the Li-ion battery (LIB) represent the most promising technology to fill the gap between energy production and utilization securing energy supply. However, there are increasing concerns regarding the sustainability and criticality of materials used in LIBs, such as cobalt-containing cathode materials [2]. One of the most promising alternative Li-ion-based battery systems is the lithium-sulfur technology. Sulfur is abundant and cheap—it is considered waste by industries. Additionally, Li-S with pristine sulfur cathode yields superior high theoretical

capacity (1672 mAh/g) and gravimetric energy (2500 Wh/kg) [3]. Nevertheless, the electrically insulating nature of sulfur and lithium sulfide, its poor cycling performance, due to the high polysulfides solubility and large volume (80%) changes during the redox reaction, impede the use of sulfur as cathode material. Thus, designing a highly efficient Li-sulfur system still remains a challenge.

For tackling above issues, various strategies have been suggested. Providing skeleton materials with porous structure to reduce the "shuttle effect" and volume expansion of sulfur, as well as incorporating conductive materials to increase the electrical conductivity, are the main methods for enhancing the electrochemistry performance of lithium-sulfur batteries (LSB) [4–7]. In the past decade, nanomaterials, such as graphene, carbon nanotubes, porous carbon, and SiC, as well as nitrogen-doped carbonaceous materials, are widely investigated as skeleton and conductive materials for Li-S batteries, and they indeed lead to an improvement of the electrochemical performance of the sulfur cathode [8–17]. However, most of the applied nanomaterials are expensive in production; therefore, their practical large-scale commercialization is hard to achieve. For normal porous carbon materials, their soft structure is not enough to hamper the volume expansion during the battery cycling process. Thus, there is still a big demand for the development of an advanced host material, which is not only mechanically flexible and robust, but also shows enhanced conductivity and can be produced at low costs.

C-rich polymer derived ceramics (PDCs) are remarkable materials, due to their robust architecture, suitable to restrain volume changes and tunable electrical conductivity providing pathways for electrons and ions [18–22]. In addition, their porous property makes it possible to load sulfur and to realize physical adsorption barrier for polysulfides to hamper the "shuttle effect" [23–26]. Our previous work showed that porous C-rich SiCN ceramics pyrolyzed at temperatures between 1000 °C and 1600 °C can stabilize the electrochemical behaviour of sulfur [27]. It has been also demonstrated that the morphology of C-rich SiCN ceramics significantly affects the electrochemical performance of the S/SiCN composites and nitrogen contained in the ceramic matrix has a stabilizing effect for the electrochemical performance. Our former study [28,29] also showed that the microstructure of SiCN ceramics processed at temperatures lower than 1000 °C significantly differs from those prepared at higher temperatures. Thus, in this work, we further investigate the electrochemical stability of SiCN-S composites containing C-rich SiCN ceramics pyrolyzed at temperatures below 1000 °C in more detail. The C-rich SiCN-S composites are synthesized using a scalable melting-diffusion method [27]. After the melting-diffusion procedure, sulfur is introduced and embedded into the C-rich SiCN ceramic. The obtained SiCN-S composites are characterized by XRD, scanning electron microscopy, Raman spectroscopy, and N_2 adsorption, followed by their electrochemical performance evaluation.

2. Experimental

2.1. Synthesis of C-Rich SiCN Ceramics

Cross-linking reactions of commercial perhydropolysilazane (PHPS, DURAZANE 2250, Merck Performance Materials GmbH, Wiesbaden, Germany) with divinylbenzene (DVB, 80%, mixture of isomers, Sigma-Aldrich, Burlington, MA, USA) in Di-n-butylether (DBE, Merck Performance Materials GmbH, Wiesbaden, Germany) as the solvent and catalyzed by platinum (0)-1,3-divinyl-1,1,3,3-tetramethyldisiloxane complex solution (~Pt 2% in xylene, Sigma-Aldrich, Burlington, MA, USA) were performed via the same method, as described in our previous work—reference [27]. The obtained colorless solid precursors were then pyrolyzed in a Schlenk tube under argon flow at 800 °C, 900 °C, and 1100 °C. Finally, the C-rich SiCN ceramic matrices were denoted as SiCN-800, SiCN-900, and SiCN-1100. The schematic diagram of the preparation of the C-rich SiCN-S composite is shown in Scheme 1.
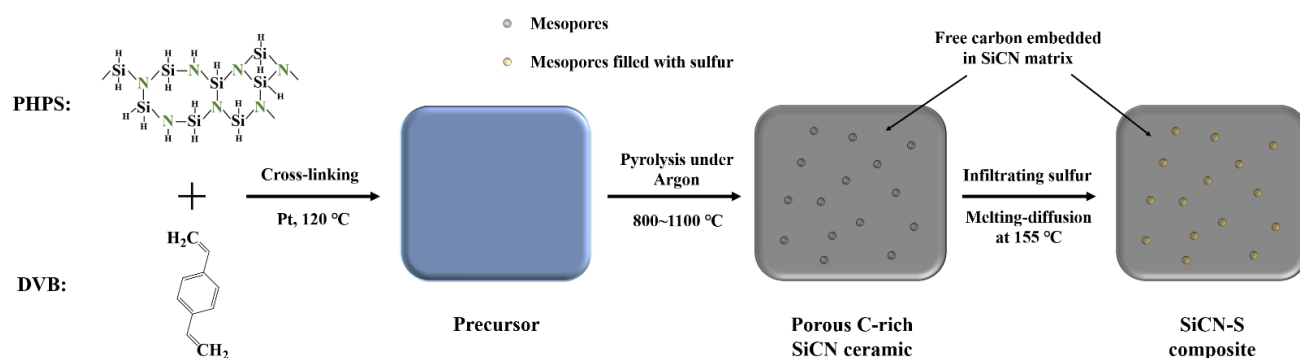
Scheme 1. Preparation of the C-rich SiCN-S composite.

2.2. Fabrication of SiCN-S Composites

Firstly, sulfur (Sigma-Aldrich, Burlington, MA, USA) and the obtained C-rich SiCN ceramic matrices were mixed via ball milling for 20 min, with a mass ratio of 2:1 (66.6 wt% of sulfur). Secondly, the obtained mixtures were heated to 155 °C in an autoclave, with Teflon inlet, for 24 h. Finally, the obtained samples (SiCN-S-800, SiCN-S-900, and SiCN-S-1100) were powderized by grounding them in a mortar.

2.3. Characterization of the Samples

Crystalline phases of the samples were measured by high power x-ray diffraction (STOE STADIP, Darmstadt, Germany) with monochromatic Mo-K$_\alpha$ radiation at a 2θ range of 5° to 45°. Specific surface area and pore size distribution of the C-rich SiCN ceramics were determined by N$_2$ adsorption and desorption measurements at 77 K (Quantachrome Autosorb-3B, Boynton Beach, FL, USA). Raman spectra were detected via a micro-Raman spectrometer (Horiba HR800, Kyoto, Japan) with an Ar-ion laser with the wavelength 514.5 nm between a scan window of 0 cm^{-1} to 4000 cm^{-1}. All filters and parameters were kept constant for measurements. Morphology images and elemental mapping analysis of the samples were performed by scanning electron microscopy on a Philips XL30 FEG (Koninklijke Philips N.V., Amsterdam, Netherlands).

2.4. Electrochemical Measurement

Galvanostatic Cycling was performed by using a VMP-multipotentiostat (Biologic Science Instruments, Seyssinet-Pariset, France), at a controlled constant temperature of 25 °C. All cells were tested in a voltage window between 1.2 and 3.6 V under a constant current density of 83.5 mA/g. Cyclic Voltammogram was recorded at a scan rate of 0.02 mV/s. For electrodes fabrication, SiCN-S composites, polyvinylidenflouride (PVDF, Sigma-Aldrich, Burlington, MA, USA), and carbon black (Super P, Timcal Ltd., Bodio, Switzerland), with a mass ratio of 85 wt%, 10 wt%, and 5 wt%, were mixed in N-Methyl-2-pyrrolidone (NMP, BASF, Ludwigshafen, Germany) to form a slurry. A doctor blade was used to paint an aluminum foil with the obtained slurry. The coated aluminum foil was dried at 40 °C for 24 h to evaporate the solvent. After cutting, the samples were further dried for 24 h in a Buchi furnace (Labortechnik AG, Essen, Germany). Finally, nummular electrode slices with 10 mm in diameter were obtained. All electrodes were assembled in Swagelok cells, under argon, in a glovebox. Lithium foil (0.75 mm thickness, Alfa Aesar GmbH & Co KG, Karlsruher, Germany) was used as counter electrode and QMA (Whatman, Maidstone, UK) was used as separator; 1,3-dioxolane (DOL, Sigma-Aldrich, Burlington, MA, USA) and dimethoxymethane (DME, Sigma-Aldrich, Burlington, MA, USA) (volume ratio: 1:1), with 1 M lithium bis(trifluoromethanesulfonyl)imide (LiTFSI, Sigma-Aldrich, Burlington, MA, USA), were used as electrolyte (containing 0.1 M LiNO$_3$ for alleviating the "shuttle effect").

3. Results and Discussion

3.1. X-ray Diffraction

The XRD patterns of C-rich SiCN ceramics and SiCN-S composites are shown in Figure 1. The diffractograms shown in Figure 1a reveal a characteristic amorphous structure of the synthesized SiCN ceramics at all temperatures, indicating that no crystallization occurs in the pyrolysis temperature range between 800 °C and 1100 °C. Figure 1b presents the diffraction patterns, after introducing sulfur into the SiCN ceramic matrix via solvothermal treatment in an autoclave. All the diffraction lines are associated with crystallized sulfur (S_8, reference card number: [01-085-0799]).
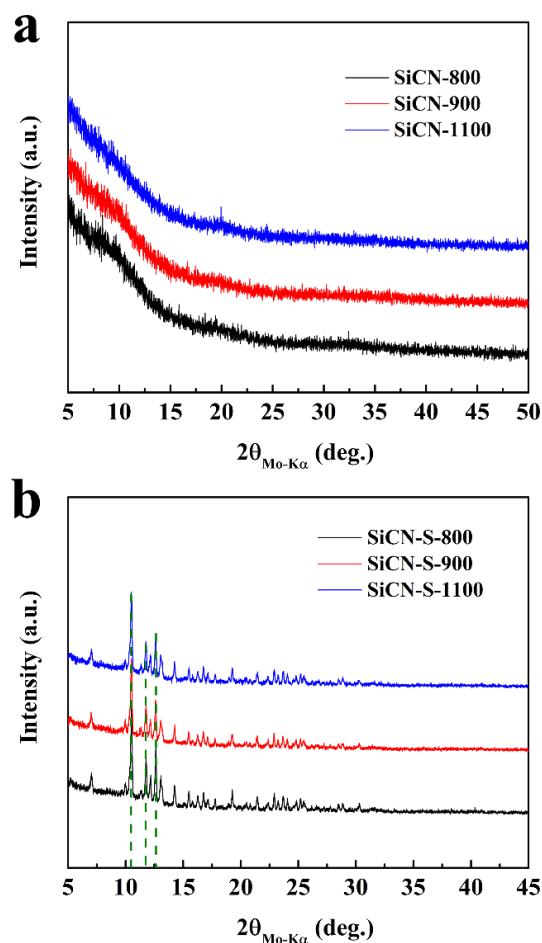
Figure 1. XRD patterns of (**a**) C-rich SiCN ceramics and (**b**) SiCN-S composites processed at different pyrolysis temperatures. The green dotted line in Figure 1b represents the position of the characteristic peaks of S_8.

3.2. N_2 Adsorption-Desorption Measurements

Nitrogen adsorption-desorption measurement was performed to determine the specific surface area (SSA) and to provide insights into the pore size and distribution. The N_2 adsorption-desorption isotherms are depicted in Figure 2a. A hysteresis loop is observed at $P/P_0 \approx 0.5$, due to capillary condensation of nitrogen in mesopores, especially for the sample SiCN-S-800 [30]. It indicates that all samples exhibit mesoporous character. Detailed SSA data and pore structure parameters, such as total pore volume (Vt) and isotherm type and average pore diameter (APD), are listed in Table 1. All the isotherms are described by type IV behavior, which is characteristic for materials containing mesopores [31]. From 800 °C to 900 °C, SSA and V_t of SiCN ceramics decrease with increasing pore size (corresponding to the value of APD). Due to equipment precision, larger mesopores could not be detected by a BET approach. With further increasing of the pyrolysis temperature to

1100 °C in argon, V_t and APD turn to increase, but there is no obvious change in SSA. The change in APD indicates a reduced the presence of bigger pores in the sample pyrolyzed at 1100 °C. The pore size distribution of all ceramic samples is presented in Figure 2b. With increasing pyrolysis temperature, the amount of mesopores in the range between 3 and 4 nm decreases.
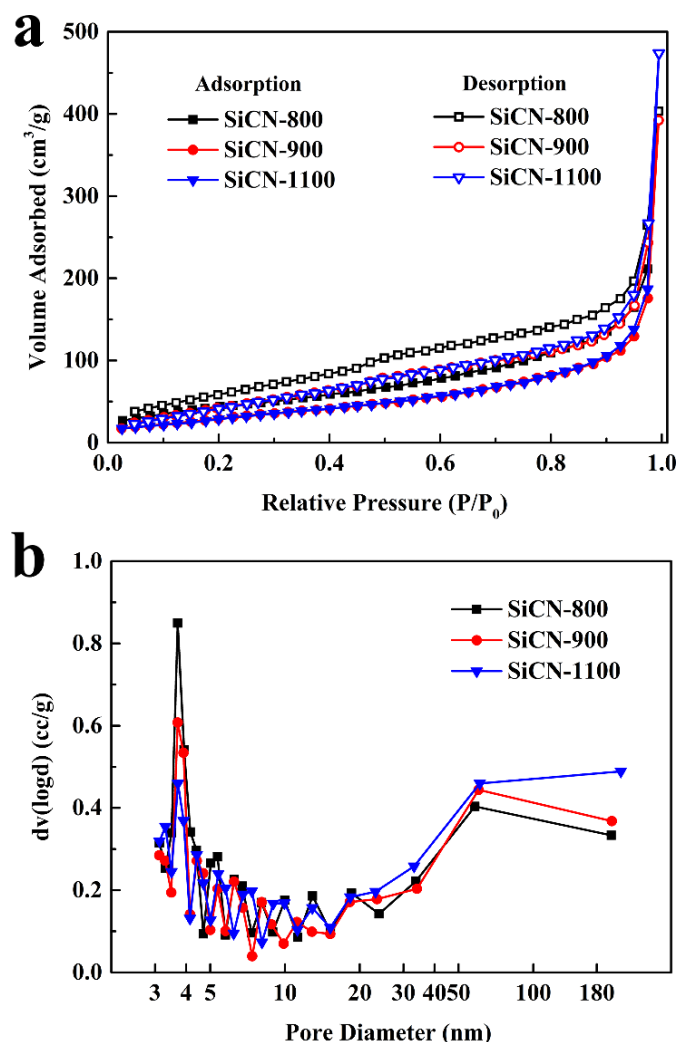
Figure 2. N_2 adsorption-desorption isotherms (**a**) and pore diameter distribution (**b**) of C-rich SiCN ceramic matrix.

Table 1. Pore structure parameters analyzed by BET and characterization of the developed free carbon measured by Raman spectroscopy. Specific surface area (SSA), total pore volume (V_t), average pore diameter (APD), intensity ratio of $I (A_D)/ I (A_G)$, and crystallite size (L_a) of samples SiCN-800, SiCN-900, and SiCN-1100 (Gaussian-type curve fitting applied [32]).

Sample	SiCN-800	SiCN-900	SiCN-1100
SSA (m^2/g)	162	116	115
V_t (cm^3/g)	0.62	0.61	0.73
Isotherm Type	IV	IV	IV
APD (nm)	15.46	20.94	25.5
$I (A_D)/I (A_G)$ ratio	2.68	2.67	2.47
L_a (nm)	6.28	6.29	6.81

3.3. Raman Spectroscopy

Figure 3 presents the Raman spectra of our SiCN ceramics without and with sulfur. All samples show characteristic D band and G band peaks of carbon at around 1345 cm^{-1} and 1583 cm^{-1}, as well as a broad peak between 2500 cm^{-1} and 3000 cm^{-1}, corresponding to the 2D and D + G band of carbon, respectively. The sulfur-free SiCN ceramics show decreased ratio of I (A$_D$)/I (A$_G$) and increased crystallite size (L$_a$), with increasing pyrolysis temperature (Figure 3a and Table 1) [27]. The I (A$_D$)/I (A$_G$) ratio of all samples indicate that the carbon inside the SiCN ceramics exhibits amorphous structure originating from disordered sp^2-hybridized carbon. After introducing sulfur into the SiCN ceramics, characteristic bands of sulfur are also detected in the Raman spectra besides that of the D, G, 2D, and D + G bands of carbon (Figure 3b).
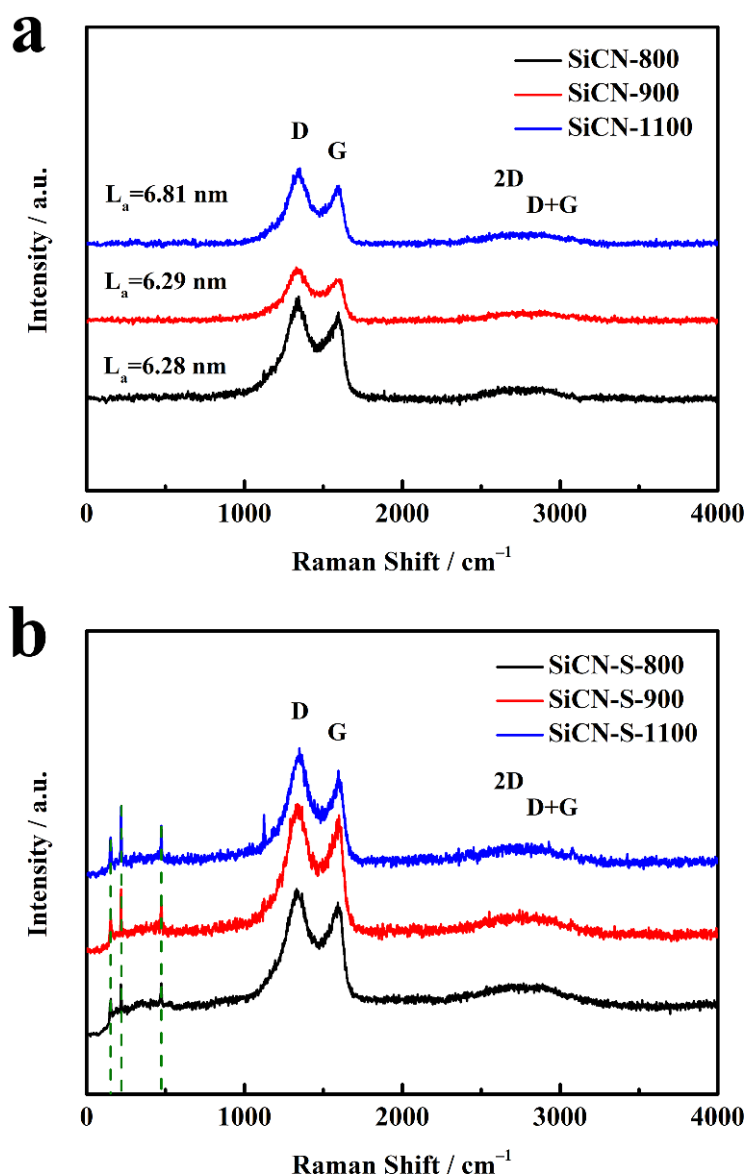
Figure 3. Raman spectra of C-rich SiCN ceramic matrices (**a**) and SiCN-S composites (**b**). The green dotted line in Figure 3b represents the position of the characteristic bands of S$_8$.

3.4. Scanning Electron Microscopy Measurements

Figure 4 presents the morphologies and elemental mapping results of all SiCN-S composites, as measured by scanning electron microscopy (SEM) and energy dispersive spectroscopy (EDS). The synthesized SiCN-S composite particles exhibit a size between

20–30 μm and a rough surface morphology. The EDS results show that sulfur is uniformly distributed in the SiCN material. This result clearly shows that the autoclave technique applied to load sulfur in SiCN is highly efficient and allows for uniform embedding of sulfur into the porous structure of the SiCN matrix.
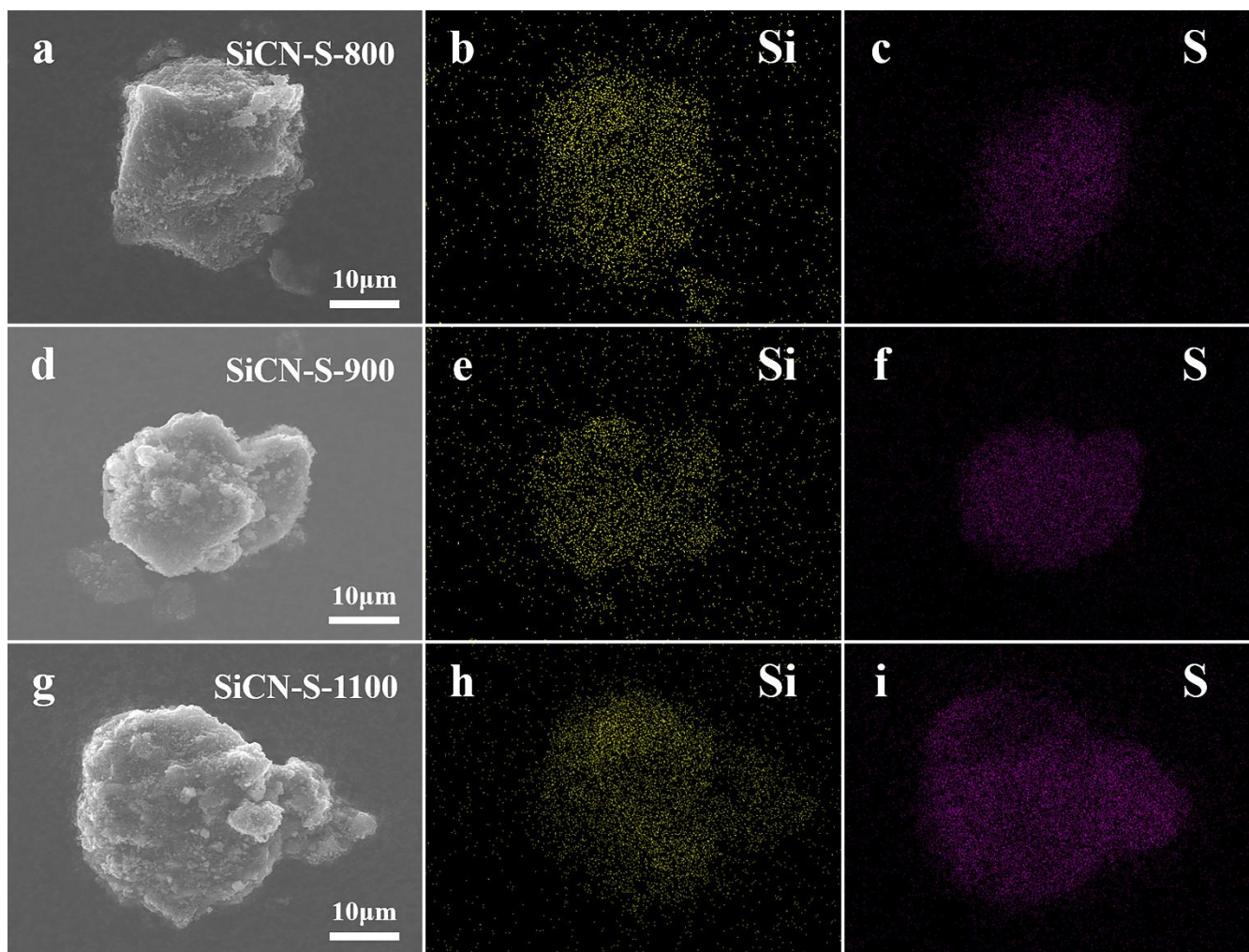
Figure 4. SEM images and EDS elemental mapping of SiCN-S-800 (**a–c**), SiCN-S-900 (**d–f**), SiCN-S-1100 (**g–i**). Yellow represents Si, purple represents S.

3.5. Galvanostatic Charge/Discharge Measurements

Initial lithiation/delithiation curves of the SiCN-S composites are shown in Figure 5. Two typical lithiation voltage plateaus of sulfur are clearly visible at around 2.4 and 2.0 V during the lithiation process. This behavior is related to the reaction of S_8 with Li to form soluble polysulfides Li_2S_x ($4 \leq x \leq 8$) and solid Li_2S_2 and Li_2S [6,15,33]. The relevant reaction equations are as follows [34]:

$$S_8 + 2e^- + 2Li^+ \longrightarrow Li_2S_8 \tag{1}$$

$$Li_2S_8 + 2e^- + 2Li^+ \longrightarrow 2Li_2S_4 \tag{2}$$

$$2Li_2S_4 + 4e^- + 4Li^+ \longrightarrow 4Li_2S_2 \tag{3}$$

$$4Li_2S_2 + 8e^- + 8Li^+ \longrightarrow 8Li_2S \tag{4}$$
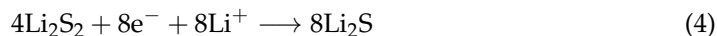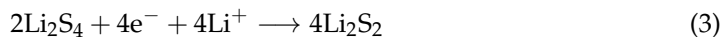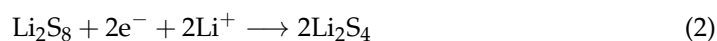
Nevertheless, the two voltage plateaus of SiCN-S-800 (2.33 and 2.03 V) reveal a hysteresis, compared with other two composites (2.36 and 2.06 V), relating to a higher polariza-

tion [35,36]. This phenomenon is also seen in the delithiation curves (2.35 V of SiCN-S-800 vs. 2.23 V of SiCN-S-900 and SiCN-S-1100), which is discussed in terms of sample SiCN-S-800, which has the lowest degree of graphitization among all composites based on the Raman results. This, in turn, results in the lowest conductivity of the free carbon phase in sample SiCN-S-800 [37]. Initial lithiation capacities and corresponding columbic efficiencies of all SiCN-S composites are listed in Table 2. The initial lithiation capacity decreases from sample SiCN-S-800 to sample SiCN-S-900 and then increases in sample SiCN-S-1100. This behavior is explained by the amount of accessible sulfur embedded in the ceramic matrix, which decreases from SiCN-S-800 to SiCN-S-900 with decreasing SSA of the ceramic matrix. With increasing pyrolysis temperature, the degree of graphitization increases, resulting in an enhanced electrical conductivity of the SiCN matrix and, hence, higher initial lithiation capacity of the sulfur. All composites exhibit around 85% of initial coulombic efficiency, which indicates that the characteristic "shuttle effect" is less pronounced in all samples in the beginning of cycling.
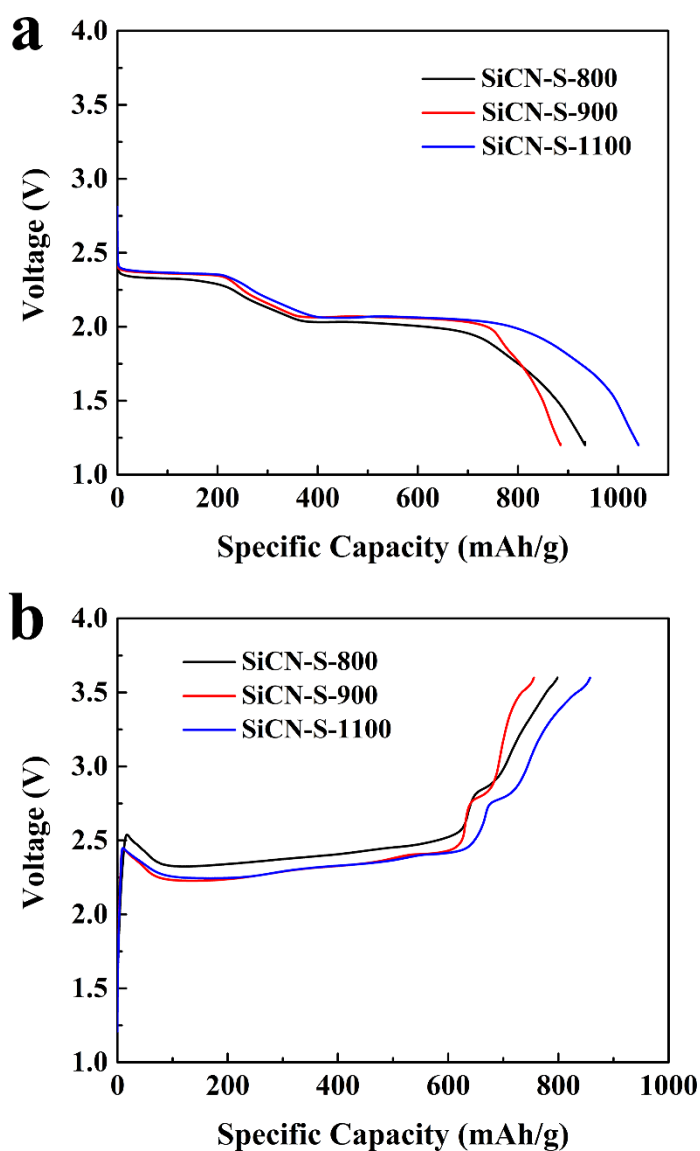
Figure 5. Lithiation curve of samples SiCN-S-800, SiCN-S-900, and SiCN-S-1100 (**a**); delithiation curve of samples SiCN-S-800, SiCN-S-900, and SiCN-S-1100 (**b**).

Table 2. Electrochemical parameters of the sulfurized SiCN samples.

Samples	Initial Lithiation Capacity (mAh/g)	Reversible Capacity after 50 Cycle (mAh/g)	Initial Coulombic Efficiency (%)	Capacity Retention (%)
SiCN-S-800	934	158	85	17
SiCN-S-900	885	195	85	22
SiCN-S-1100	1040	118	82	11

3.6. Cyclic Voltammperometry

To follow the redox reactions in the investigated system in more detail, cyclic voltammperometry measurements have been performed and are shown in Figure 6. For the initial cycle of all composites, the curves present two cathodic peaks related to the lithiation of S_8 to higher order soluble polysulfides (Li_2S_x ($4 \leq x \leq 8$)) and, finally, to solid Li_2S_2 and Li_2S, as well as one anodic peak due to the conversion of polysulfides back to elemental sulfur S_8. It is worth noting that the cathodic peak appears at higher potential position also with higher intensity for the SiCN-S composites pyrolyzed at 1100 °C. This feature, again, indicates that the electrical conductivity of the C-rich SiCN matrix increases, leading to a higher sulfur capacity. Besides, there is a significant increase of the distance between the cathodic and the anodic peak for the sample SiCN-S-800 during the first CV cycle. The cathodic peaks are found at 2.30 and 1.99 V, whereas for the SiCN-S-900 and SiCN-S-1100 composites they are located at 2.33 and 2.03 V, respectively. The anodic peaks of the samples SiCN-S-800 and SiCN-S-900 are at around 2.47 V, whereas for SiCN-S-1100 the anodic peak is shifted to 2.44 V. This feature is caused by the higher ohmic resistance in the case of the samples synthesized at lower temperature [35,38,39]. Additionally, it is not more visible, in case of SiCN-S-900, meaning that, in this case, a degree of graphitization of the free carbon phase is enough to provide a sufficient electrical conductivity. After the fifth cycle, the ohmic resistance of SiCN-S-800 and SiCN-S-900 is still a bit higher than that of SiCN-S-1100, but much lower than for the initial cycle. Both cathodic and anodic peak intensity of the samples SiCN-S-1100 decrease compared with the samples SiCN-S-800 and SiCN-S-900. This behavior reveals that the cyclic stability of the electrode material is significantly decreased when the pyrolysis temperature is beyond 900 °C.

3.7. Extended Cycling Performance

Figure 7a–c represents the lithiation/delithiation specific capacity and corresponding coulombic efficiency of all SiCN-S composites. Besides the initial lithiation capacity, the reversible capacity after 50 cycles, the coulombic efficiency and capacity retention of all SiCN-S composites are listed in Table 2. As shown in Figure 7a,b, both the lithiation and delithiation capacity of the sample SiCN-S-900 are the lowest in the first four cycles. Nevertheless, after the fourth cycle, its specific capacity surpasses that of the sample SiCN-S-1100. After 12 cycles, the sample SiCN-S-900 even surpasses that of the SiCN-S-800 and remains the highest capacity until the 50th cycle. The lowest performance is registered for the sample SiCN-S-1100. In the end, after 50 cycles, the sample SiCN-S-900 exhibits the highest lithiation retention of 22%. The enhancement of the electrochemical performance of sample SiCN-S-900, in comparison to that of SiCN-S-800, is mainly due to the enhanced conductivity resulted from the increasing of the degree of graphitization of the free carbon. Although the SSA of the sample SiCN-900 is lower, its total pore volume V_t changed little, in comparison with the sample SiCN-800, and it reveals more mesopores, in comparison to SiCN-1100 (results of BET). The presence of mesopores is of advantage for stabilization of sulfur electrochemical behavior [27,40,41], which can explain the best electrochemical performance of SiCN-S-900 among measured samples. Even though SiCN-S-1100 contains more organized free carbon phase and thus reveals higher electronic conductivity, SiCN-S-900 outperforms it in prolonged cycles stability. It is known that the "shuttle effect" originating from the diffusion of soluble polysulfides usually leads to a coulombic efficiency higher than 100% [11,33,42]. This phenomenon was also discussed in our previous work.

During delithiation process, the long-chain soluble polysulfides pass through the membrane and migrate to Li anode, redox reaction happens, and short chain polysulfides are formed; then, the short-chain polysulfides migrate back and are re-oxidized to long-chain polysulfides, resulting in long delithiation process and excessive coulombic efficiency over 100% [27]. Hence, the level of coulombic efficiency can reflect the degree of the "shuttle effect". While, in addition to the remarkable initial coulombic efficiency of all SiCN-S composites, in the first 14 cycles, all samples keep the state where the coulombic efficiency is not growing rapidly (lower than 110%). In the subsequent cycles up to the 50th cycle, all samples except SiCN-S-900 exhibit a coulombic efficiency around 110%. This finding in turn demonstrates that that the lowest extent of a "shuttle effect" is observed for SiCN-S-800 and SiCN-S-1100. As for the sample SiCN-S-900, its coulombic efficiency, growing from 110% to 130%, is a sign of a progressing polysulfides diffusion ("shuttle effect"), visible also in an excessive anodic polarization of the cyclic voltammetry curve shown in Figure 6b.
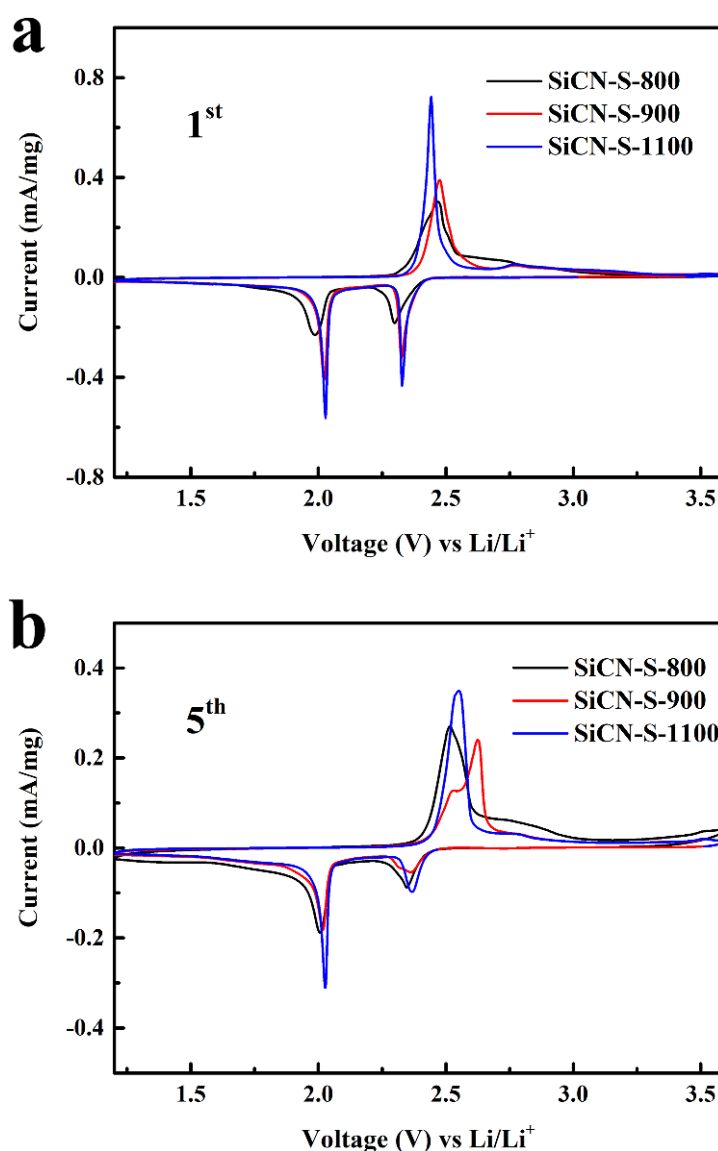
Figure 6. Cyclic voltammograms of samples SiCN-S-800, SiCN-S-900, and SiCN-S-1100 at a scan rate of 0.02 mV/s. The first cycle (**a**) and the fifth cycle (**b**).
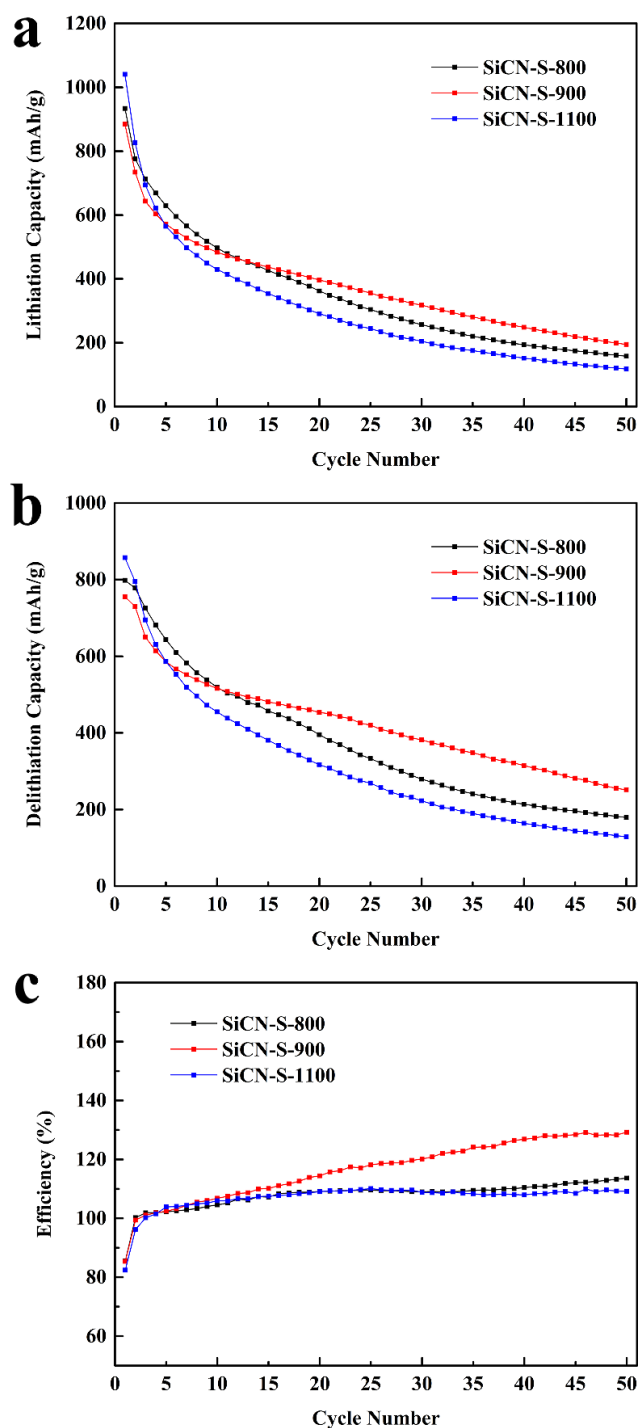
Figure 7. Cycling performance of samples SiCN-S-800, SiCN-S-900, and SiCN-S-1100. Lithiation capacity (**a**), delithiation capacity (**b**), and columbic efficiency (**c**).

In our former study, the sample SiCN-S-1000 (pyrolyzed at 1000 °C) was identified as the sample with the most promising electrochemical behavior [27]. The screening of this low pyrolysis temperature region, performed in this work, allowed us to find out the tendency in electrochemical behavior. SiCN-S-900 composite electrode demonstrates a similar electrochemical stability to SiCN-S-1000. Both materials contain amorphous, defective free carbon, organized enough to provide a sufficient electrical conductivity, and dispersed in the SiCN matrix, with significant amount of mesoporous present in their microstructure, thus providing a stabilizing host for sulfur infiltration. At higher pyrolysis

temperature, more ordered free carbon phase is present, however a pore diameter increase, resulting in lower capacity retention. At lower pyrolysis temperatures, the conductivity is provided by a free carbon phase exclusively, this phase however is not able to provide the robustness, leading to enhanced shuttling effect after 20 cycles. The presence of nitrogen in the electrode materials produced at lower pyrolysis temperature appears to be of advantage for polysulfides stabilization [43]. Therefore, a trade-off between the choice of the pyrolysis temperature and the effects of it on conductivity, capacity, and cycling stability should always be considered carefully. In addition, the mesoporous morphology of the SiCN sulfur support is beneficial for the cathode stabilization, but it is not a necessary condition, since other properties, such as SSA, degree of graphitization, etc., play a crucial role.

4. Conclusions

A series of C-rich SiCN ceramics, pyrolyzed at temperatures $\leq 1100\ ^{\circ}C$, were synthesized to investigate the effect of the corresponding change of microstructure on the electrochemical performance, when used as cathode material in a Li-S battery. The melting-diffusion method has been applied for sulfur infiltration into the SiCN ceramic matrices. The resulting SiCN-S composites have been characterized as a sulfur host for Li-S batteries. Their electrochemical performance has been analyzed, with respect to the initial microstructure and composition of the SiCN ceramic. The results indicate that the composite electrode, comprised of the SiCN matrix synthesized at 900 °C (sample SiCN-S-900), possesses enhanced electrochemical stability and higher capacity (more than 195 mAh/g over 50 cycles) at a high sulfur content of 66 wt.% than that of the cathode materials containing SiCN ceramics produced at lower and higher temperatures. The superior electrochemical performance of sample SiCN-S-900 is attributed to the microstructural integrity of the electrode produced at lower temperature, in line with higher composite conductivity.

References

1. Mardani, A.; Streimikiene, D.; Cavallaro, F.; Loganathan, N.; Khoshnoudi, M. Carbon dioxide (CO2) emissions and economic growth: A systematic review of two decades of research from 1995 to 2017. *Sci. Total Environ.* **2019**, *649*, 31–49. [CrossRef] [PubMed]
2. Kim, T.; Song, W.; Son, D.-Y.; Ono, L.K.; Qi, Y. Lithium-ion batteries: Outlook on present, future, and hybridized technologies. *J. Mater. Chem. A* **2019**, *7*, 2942–2964. [CrossRef]
3. Manthiram, A.; Fu, Y.; Chung, S.-H.; Zu, C.; Su, Y.-S. Rechargeable Lithium-Sulfur Batteries. *Chem. Rev.* **2014**, *114*, 11751–11787. [CrossRef]
4. Hou, J.; Tu, X.; Wu, X.; Shen, M.; Wang, X.; Wang, C.; Cao, C.; Pang, H.; Wang, G. Remarkable cycling durability of lithium-sulfur batteries with interconnected mesoporous hollow carbon nanospheres as high sulfur content host. *Chem. Eng. J.* **2020**, *401*, 126141. [CrossRef]
5. Xu, Z.-L.; Kim, J.-K.; Kang, K. Carbon nanomaterials for advanced lithium sulfur batteries. *Nano Today* **2018**, *19*, 84–107. [CrossRef]

6. Peng, H.-J.; Huang, J.-Q.; Cheng, X.-B.; Zhang, Q. Review on High-Loading and High-Energy Lithium-Sulfur Batteries. *Adv. Energy Mater.* **2017**, *7*, 1700260. [CrossRef]

7. Song, Y.; Sun, Z.; Fan, Z.; Cai, W.; Shao, Y.; Sheng, G.; Wang, M.; Song, L.; Liu, Z.; Zhang, Q.; et al. Rational design of porous nitrogen-doped Ti3C2 MXene as a multifunctional electrocatalyst for Li-S chemistry. *Nano Energy* **2020**, *70*, 104555. [CrossRef]

8. Yang, Y.; Zheng, G.; Cui, Y. Nanostructured sulfur cathodes. *Chem. Soc. Rev.* **2013**, *42*, 3018–3032. [CrossRef]

9. Wen, X.; Xiang, K.; Zhu, Y.; Xiao, L.; Liao, H.; Chen, W.; Chen, X.; Chen, H. 3D hierarchical nitrogen-doped graphene/CNTs microspheres as a sulfur host for high-performance lithium-sulfur batteries. *J. Alloy. Compd.* **2020**, *815*, 152350. [CrossRef]

10. Wang, Y.; Zhang, R.; Pang, Y.-c.; Chen, X.; Lang, J.; Xu, J.; Xiao, C.; Li, H.; Xi, K.; Ding, S. Carbon@titanium nitride dual shell nanospheres as multi-functional hosts for lithium sulfur batteries. *Energy Storage Mater.* **2019**, *16*, 228–235. [CrossRef]

11. Xin, S.; Gu, L.; Zhao, N.H.; Yin, Y.X.; Zhou, L.J.; Guo, Y.G.; Wan, L.J. Smaller sulfur molecules promise better lithium-sulfur batteries. *J. Am. Chem. Soc.* **2012**, *134*, 18510–18513. [CrossRef] [PubMed]

12. Ren, J.; Zhou, Y.; Wu, H.; Xie, F.; Xu, C.; Lin, D. Sulfur-encapsulated in heteroatom-doped hierarchical porous carbon derived from goat hair for high performance lithium-sulfur batteries. *J. Energy Chem.* **2019**, *30*, 121–131. [CrossRef]

13. Du, Z.; Chen, X.; Hu, W.; Chuang, C.; Xie, S.; Hu, A.; Yan, W.; Kong, X.; Wu, X.; Ji, H.; et al. Cobalt in Nitrogen-Doped Graphene as Single-Atom Catalyst for High-Sulfur Content Lithium-Sulfur Batteries. *J. Am. Chem. Soc.* **2019**, *141*, 3977–3985. [CrossRef] [PubMed]

14. Li, Z.; Jiang, Y.; Yuan, L.; Yi, Z.; Wu, C.; Liu, Y.; Strasser, P.; Huang, Y. A Highly Ordered Meso@Microporous Carbon-Supported Sulfur@Smaller Sulfur Core-Shell Structured Cathode for Li-S Batteries. *ACS Nano* **2014**, *8*, 9295–9303. [CrossRef]

15. Fang, R.; Chen, K.; Yin, L.; Sun, Z.; Li, F.; Cheng, H.M. The Regulating Role of Carbon Nanotubes and Graphene in Lithium-Ion and Lithium-Sulfur Batteries. *Adv. Mater* **2019**, *31*, e1800863. [CrossRef]

16. Li, F.; Zhao, J. Three dimensional porous SiC for lithium polysulfide trapping. *Phys. Chem. Chem. Phys.* **2018**, *20*, 4005–4011. [CrossRef]

17. Wang, J.; Wang, W.; Li, H.; Tan, T.; Wang, X.; Zhao, Y. Carbon nanotubes/SiC prepared by catalytic chemical vapor deposition as scaffold for improved lithium-sulfur batteries. *J. Nanoparticle Res.* **2019**, *21*, 113. [CrossRef]

18. Graczyk-Zajac, M.; Reinold, L.M.; Kaspar, J.; Sasikumar, P.V.; Soraru, G.D.; Riedel, R. New Insights into Understanding Irreversible and Reversible Lithium Storage within SiOC and SiCN Ceramics. *Nanomaterials* **2015**, *5*, 233–245. [CrossRef]

19. Graczyk-Zajac, M.; Fasel, C.; Riedel, R. Polymer-derived-SiCN ceramic/graphite composite as anode material with enhanced rate capability for lithium ion batteries. *J. Power Sources* **2011**, *196*, 6412–6418. [CrossRef]

20. Reinold, L.M.; Graczyk-Zajac, M.; Gao, Y.; Mera, G.; Riedel, R. Carbon-rich SiCN ceramics as high capacity/high stability anode material for lithium-ion batteries. *J. Power Sources* **2013**, *236*, 224–229. [CrossRef]

21. Graczyk-Zajac, M.; Vrankovic, D.; Waleska, P.; Hess, C.; Sasikumar, P.V.; Lauterbach, S.; Kleebe, H.-J.; Sorarù, G.D. The Li-storage capacity of SiOC glasses with and without mixed silicon oxycarbide bonds. *J. Mater. Chem. A* **2018**, *6*, 93–103. [CrossRef]

22. Stein, P.; Vrankovic, D.; Graczyk-Zajac, M.; Riedel, R.; Xu, B.-X. A Model for Diffusion and Immobilization of Lithium in SiOC Nanocomposite Anodes. *JOM* **2017**, *69*, 1524–1531. [CrossRef]

23. Vrankovic, D.; Graczyk-Zajac, M.; Kalcher, C.; Rohrer, J.; Becker, M.; Stabler, C.; Trykowski, G.; Albe, K.; Riedel, R. Highly Porous Silicon Embedded in a Ceramic Matrix: A Stable High-Capacity Electrode for Li-Ion Batteries. *ACS Nano* **2017**, *11*, 11409–11416. [CrossRef] [PubMed]

24. Gulzar, U.; Li, T.; Bai, X.; Colombo, M.; Ansaldo, A.; Marras, S.; Prato, M.; Goriparti, S.; Capiglia, C.; Proietti Zaccaria, R. Nitrogen-Doped Single-Walled Carbon Nanohorns as a Cost-Effective Carbon Host toward High-Performance Lithium-Sulfur Batteries. *ACS Appl. Mater Interfaces* **2018**, *10*, 5551–5559. [CrossRef]

25. Gueon, D.; Hwang, J.T.; Yang, S.B.; Cho, E.; Sohn, K.; Yang, D.K.; Moon, J.H. Spherical Macroporous Carbon Nanotube Particles with Ultrahigh Sulfur Loading for Lithium-Sulfur Battery Cathodes. *ACS Nano* **2018**, *12*, 226–233. [CrossRef]

26. Pradeep, V.S.; Ayana, D.G.; Graczyk-Zajac, M.; Soraru, G.D.; Riedel, R. High Rate Capability of SiOC Ceramic Aerogels with Tailored Porosity as Anode Materials for Li-ion Batteries. *Electrochim. Acta* **2015**, *157*, 41–45. [CrossRef]

27. Qu, F.; Graczyk-Zajac, M.; Vrankovic, D.; Chai, N.; Yu, Z.; Riedel, R. Effect of morphology of C-rich silicon carbonitride ceramic on electrochemical properties of sulfur cathode for Li-S battery. *Electrochim. Acta* **2021**, *384*, 138265. [CrossRef]

28. Reinold, L.M.; Yamada, Y.; Graczyk-Zajac, M.; Munakata, H.; Kanamura, K.; Riedel, R. The influence of the pyrolysis temperature on the electrochemical behavior of carbon-rich SiCN polymer-derived ceramics as anode materials in lithium-ion batteries. *J. Power Sources* **2015**, *282*, 409–415. [CrossRef]

29. Storch, M.; Vrankovic, D.; Graczyk-Zajac, M.; Riedel, R. The influence of pyrolysis temperature on the electrochemical behavior of porous carbon-rich SiCN polymer-derived ceramics. *Solid State Ion.* **2018**, *315*, 59–64. [CrossRef]

30. Sing, K.S.W.; Everett, D.H.; Haul, R.A.W.; Moscou, L.; Pierotti, R.A.; Rouquerol, J.; Siemieniewska, T. REPORTING PHYSISORPTION DATA FOR GAS SOLID SYSTEMS WITH SPECIAL REFERENCE TO THE DETERMINATION OF SURFACE-AREA AND POROSITY (RECOMMENDATIONS 1984). *Pure Appl. Chem.* **1985**, *57*, 603–619. [CrossRef]

31. Klobes, P.; Munro, R.G. Porosity and Specific Surface Area Measurements for Solid Materials. *Natl. Inst. Stand. Technol. Spec. Publ.* **2006**, *960*, 17.

32. Sadezky, A.; Muckenhuber, H.; Grothe, H.; Niessner, R.; Pöschl, U. Raman microspectroscopy of soot and related carbonaceous materials: Spectral analysis and structural information. *Carbon* **2005**, *43*, 1731–1742. [CrossRef]

33. Cheon, S.E.; Ko, K.S.; Cho, J.H.; Kim, S.W.; Chin, E.Y.; Kim, H.T. Rechargeable lithium sulfur battery—I. Structural change of sulfur cathode during discharge and charge. *J. Electrochem. Soc.* **2003**, *150*, A796–A799. [CrossRef]

34. Amine, K.; Kanno, R.; Tzeng, Y. Rechargeable lithium batteries and beyond: Progress, challenges, and future directions. *MRS Bull.* **2014**, *39*, 395–401. [CrossRef]

35. Sun, Z.; Zhang, J.; Yin, L.; Hu, G.; Fang, R.; Cheng, H.M.; Li, F. Conductive porous vanadium nitride/graphene composite as chemical anchor of polysulfides for lithium-sulfur batteries. *Nat. Commun.* **2017**, *8*, 14627. [CrossRef]

36. Mentbayeva, A.; Belgibayeva, A.; Umirov, N.; Zhang, Y.; Taniguchi, I.; Kurmanbayeva, I.; Bakenov, Z. High performance freestanding composite cathode for lithium-sulfur batteries. *Electrochim. Acta* **2016**, *217*, 242–248. [CrossRef]

37. Vrankovic, D.; Reinold, L.M.; Riedel, R.; Graczyk-Zajac, M. Void-shell silicon/carbon/SiCN nanostructures: Toward stable silicon-based electrodes. *J. Mater. Sci.* **2016**, *51*, 6051–6061. [CrossRef]

38. Abdul Razzaq, A.; Yao, Y.; Shah, R.; Qi, P.; Miao, L.; Chen, M.; Zhao, X.; Peng, Y.; Deng, Z. High-performance lithium sulfur batteries enabled by a synergy between sulfur and carbon nanotubes. *Energy Storage Mater.* **2019**, *16*, 194–202. [CrossRef]

39. Zhou, T.; Lv, W.; Li, J.; Zhou, G.; Zhao, Y.; Fan, S.; Liu, B.; Li, B.; Kang, F.; Yang, Q.-H. Twinborn TiO2-TiN heterostructures enabling smooth trapping-diffusion-conversion of polysulfides towards ultralong life lithium-sulfur batteries. *Energy Environ. Sci.* **2017**, *10*, 1694–1703. [CrossRef]

40. Liu, M.; Liu, Y.; Yan, Y.; Wang, F.; Liu, J.; Liu, T. A highly conductive carbon-sulfur film with interconnected mesopores as an advanced cathode for lithium-sulfur batteries. *Chem. Commun.* **2017**, *53*, 9097–9100. [CrossRef]

41. Lee, J.T.; Zhao, Y.; Thieme, S.; Kim, H.; Oschatz, M.; Borchardt, L.; Magasinski, A.; Cho, W.-I.; Kaskel, S.; Yushin, G. Sulfur-Infiltrated Micro- and Mesoporous Silicon Carbide-Derived Carbon Cathode for High-Performance Lithium Sulfur Batteries. *Adv. Mater.* **2013**, *25*, 4573–4579. [CrossRef] [PubMed]

42. Cheon, S.E.; Ko, K.S.; Cho, J.H.; Kim, S.W.; Chin, E.Y.; Kim, H.T. Rechargeable lithium sulfur battery—II. Rate capability and cycle characteristics. *J. Electrochem. Soc.* **2003**, *150*, A800–A805. [CrossRef]

43. Song, J.; Gordin, M.L.; Xu, T.; Chen, S.; Yu, Z.; Sohn, H.; Lu, J.; Ren, Y.; Duan, Y.; Wang, D. Strong lithium polysulfide chemisorption on electroactive sites of nitrogen-doped carbon composites for high-performance lithium-sulfur battery cathodes. *Angew. Chem. Int. Ed. Engl.* **2015**, *54*, 4325–4329. [CrossRef] [PubMed]

Review

Si-based polymer-derived ceramics for energy conversion and storage

Qingbo WEN^{a,†}, Fangmu QU^{c,†}, Zhaoju YU^{b,*},
Magdalena GRACZYK-ZAJAC^{c,d,*}, Xiang XIONG^{a}, Ralf RIEDEL^{c}

^{a}*State Key Laboratory of Powder Metallurgy, Central South University, Changsha 410083, China*
^{b}*College of Materials, Key Laboratory of High-Performance Ceramic Fibers (Xiamen University),
Ministry of Education, Xiamen 361005, China*
^{c}*Technische Universität Darmstadt, Institut für Materialwissenschaft, Otto-Berndt-Straße 3,
D-64287, Darmstadt, Germany*
^{d}*EnBW Energie Baden-Württemberg AG, Durlacher Allee 93, 76131 Karlsruhe, Germany*

© The Author(s) 2021.

Abstract: Since the 1960s, a new class of Si-based advanced ceramics called polymer-derived ceramics (PDCs) has been widely reported because of their unique capabilities to produce various ceramic materials (e.g., ceramic fibers, ceramic matrix composites, foams, films, and coatings) and their versatile applications. Particularly, due to their promising structural and functional properties for energy conversion and storage, the applications of PDCs in these fields have attracted much attention in recent years. This review highlights the recent progress in the PDC field with the focus on energy conversion and storage applications. Firstly, a brief introduction of the Si-based polymer-derived ceramics in terms of synthesis, processing, and microstructure characterization is provided, followed by a summary of PDCs used in energy conversion systems (mainly in gas turbine engines), including fundamentals and material issues, ceramic matrix composites, ceramic fibers, thermal and environmental barrier coatings, as well as high-temperature sensors. Subsequently, applications of PDCs in the field of energy storage are reviewed with a strong focus on anode materials for lithium and sodium ion batteries. The possible applications of the PDCs in Li–S batteries, supercapacitors, and fuel cells are discussed as well. Finally, a summary of the reported applications and perspectives for future research with PDCs are presented.

Keywords: polymer-derived ceramics (PDCs); high-temperature resistance; structural properties; electrochemical properties; microstructure

1 Introduction

In the modern society, energy is necessary for almost

every activity of our life from household tasks, transportation, and entertainment, to architecture, agriculture, and manufacturing [1]. Because of a global development of human beings' society, energy use and production is predicted to increase by 60% from 2010 to 2040 [1,2]. The first law of thermodynamics states that energy can be neither created nor destroyed but only converted from one form to another. Therefore,

---

† Qingbo Wen and Fangmu Qu contributed equally to this work.
* Corresponding authors.
E-mail: Z. Yu, zhaojuyu@xmu.edu.cn;
    M. Graczyk-Zajac, m.graczyk-zajac@enbw.com

strictly speaking, energy production (e.g., power generation and solar energy harvesting) is energy conversion. The traditional energy conversion systems (e.g., steam turbine engines, gas/combustion turbine engines) mainly use fossil fuels as energy sources, which however leads to serious pollutant emissions and global warming. Thus, in recent years, clean and sustainable energy conversion systems have been widely developed, such as hydroelectric power generators, wind turbine generators (wind mills), solar cells, and fuel cells. It is well known that the power plants using steam and/or gas turbine engines can be operated continuously and therefore can be well integrated into the electric grids. However, for most of the sustainable energy conversion systems, the intermittency feature strongly limits their integration into the electric grids and large-scale applications. In order to solve this problem, energy storage systems, such as novel secondary batteries and super capacitors with long life and high charge/discharge efficiency, are urgently demanded.

In the last 100 years, energy conversion and storage systems have experienced a large revolution with the development of materials which possess dramatically improved structural and functional properties. One good example is the increasing application of advanced ceramics despite that most of the time, these "hidden champions" cannot be seen by the end users and consumers [1]. Advanced ceramics (e.g., SiC, Si_3N_4) is a class of inorganic and nonmetallic polycrystalline materials, which provide a good combination of high strength, high hardness, outstanding oxidation resistance, as well as excellent thermal stability and chemical durability. Importantly, their properties and performance

can be tailored and optimized via modifying the chemical/phase compositions and microstructure. Therefore, advanced ceramics have been broadly used in energy conversion and storage devices [1].

In the early 1960s, a new class of advanced ceramics produced via pyrolysis of organosilicon polymers has been developed, namely polymer-derived ceramics (PDCs) [3,4]. Because of their unique capabilities to produce ceramic fibers [5,6], films/coatings [7–10], foams [11], nanocomposites [12–15], ceramic matrix composites (CMCs) [16–19] and for additive manufacturing [20,21], PDCs have been extensively investigated for more than 50 years and have received increasing attention in recent years [5,22–37]. Generally, the preparation of silicon-based PDCs requires 3 steps: (1) synthesis of Si-containing preceramic polymers; (2) shaping and crosslinking (100–400 ℃); (3) polymer-to-ceramic transformation (400–1400 ℃) [35,38]. After polymer-to-ceramic transformation, the PDCs are generally amorphous. When annealed at higher temperatures ($\geqslant$ 1400 ℃), they will transform into (poly)crystalline ceramics. The general temperature range for processing of PDCs is shown in Fig. 1.

It has been widely reported that the chemical and phase composition as well as microstructure of the PDCs are strongly determined by the molecular structure of the preceramic polymer [41–47]. The molecular structure design and polymer-to-ceramic transformation enable facile fabrication of Si-based ternary (e.g., SiOC [48–52], SiCN [53–57], SiHfC [12], SiTaC [58]), quaternary (e.g., SiCNO [59–62], SiBCO [63–65], SiAlCO [66–69], SiAlCN [70–73], SiBCN [31,74–77],
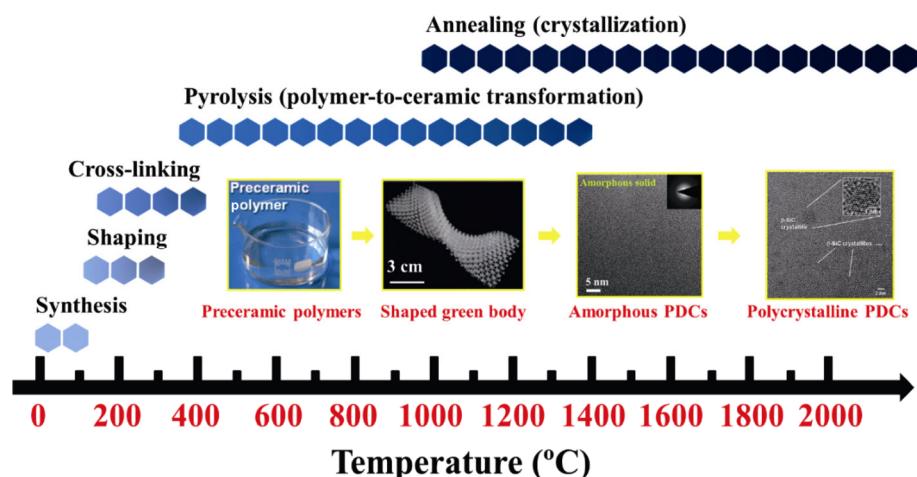
Fig. 1 General processes involved in the producing of polymer-derived ceramics. Reproduced with permission from Ref. [36], © Elsevier Ltd. 2019; Ref. [39], © Acta Materialia Inc. 2017; Ref. [40], © Elsevier Ltd. 2016.

SiHfTaC [78]), as well as pentanary (e.g., SiHfCNO [79,80], SiHfBCN [81–84]) ceramics, which are difficult to produce using other methods [35,36,85]. Owing to their tunable structures/compositions, excellent high-temperature stabilities as well as their capabilities for being shaped via various processing techniques (e.g., fiber drawing [5,25,86,87], dip- or spin-coating [9,88–91], freeze casting [50,92–94], additive manufacturing (3D printing) [20,21,95–98], and warm pressing [32,99–102]), PDCs can be conveniently used in plenty of technological key fields, such as high-temperature structural applications (e.g., thermal/environmental barrier coatings [9,103–105]), ceramic matrix composites [19,82,106,107], joining/ adhesive materials [108,109], anode materials used in lithium/sodium ion batteries [110–117], porous electrode used for supercapacitors [118–120], electromagnetic absorbing and shielding applications [121–125], micro-electromechanical systems (MEMS) [126–131], photoluminescent applications [132–135], tribological applications (e.g., brakes for motorbikes) [136–140], sensing materials [141–144], and biomedical components [145–147]. Detailed information with respect to the application of PDCs can be found in various review articles and books [30,35,127,148–154].

As mentioned above, advanced technologies for energy conversion and storage become increasingly important for our daily life and for the future of human beings. Therefore, the applications of PDCs in energy conversion and storage have attracted much attention in recent years as well [110–115]. However, no review articles regarding the applications of PDCs in the areas of energy conversion and storage have been published. Therefore, this review will focus on recent progress of PDCs in energy conversion and storage applications in order to provide a comprehensive summary of the PDCs used in this field and to facilitate their further development. Firstly, synthesis of the preceramic polymers, polymer-to-ceramic transformation, and microstructure characterization of the silicon-based PDCs will be briefly introduced. Then, applications of PDCs in energy conversion and energy storage will be systematically summarized. The correlation between the microstructure and associated properties will be comprehensively highlighted in this part as well. Finally, the perspectives of PDCs in the field of energy conversion and storage will be discussed. Actually, a few Si-free PDCs have also been reported in the last few years, such as the polymer-derived BCN

[155–157], BN [158–162], ZrO_2 [163], as well as transition metal nitrides [164–166], carbides [167–172], and borides [173–175]. In order to be more exalted, the present review mainly focuses on Si-based PDCs.

2 Si-based polymer-derived ceramics

2.1 Synthesis of preceramic polymers

Polymer-derived ceramics mean that the ceramics are produced from polymers, which differentiates them from those fabricated via the traditional powder technological route. However, not all polymers can be used as preceramic precursors. Typically, they are thermosetting polymers and should meet some requirements for practical applications: (1) high molecular weight with low volatilization during pyrolysis; (2) no uncontrolled polymerization (e.g., gelation or crosslinking) for storage; (3) good solubility or suitable rheological properties for shaping; (4) presence of functional groups for further reaction or modification; (5) defined molecular structure for the synthesis of stoichiometric ceramic compositions (e.g., SiC, Si_3N_4) [38,85].

In the last 50 years, numbers of Si-based preceramic polymers with different molecular structures have been synthesized [35]. As shown in Fig. 2, organochlorosilanes are always used as the starting materials to synthesize different silicon-based polymers. For instance, the polycarbosilanes, polysiloxanes, and polysilazanes are synthesized via reactions of organochlorosilanes with Na/K, water, and ammonia, respectively. Poly(silylcarbodiimides) are synthesized via reactions between organochlorosilanes and bis(trimethylsilyl)carbodiimide. For the well-known SiBCN ceramics, at least two different approaches can be used (i.e., starting from monomers or chemical modification of polysilazanes or poly(silylcarbodiimides)) to synthesize the preceramic polymers (i.e., polyborosilazane or polyborosilylcarbodiimide). The chemical modification basically relies on hydroboration reactions between B–H groups of the modifiers (e.g., $BH_3 \cdot SMe_2$) and unsaturated carbon bonds of the hydrocarbon side group (e.g., vinyl or allyl groups) as well as on dehydrocoupling reactions between B–H and N–H bonds on the backbone of the polymers [31,176–179]. For more detailed synthesis routes, please refer to previously reported review articles [35,85,179–185].
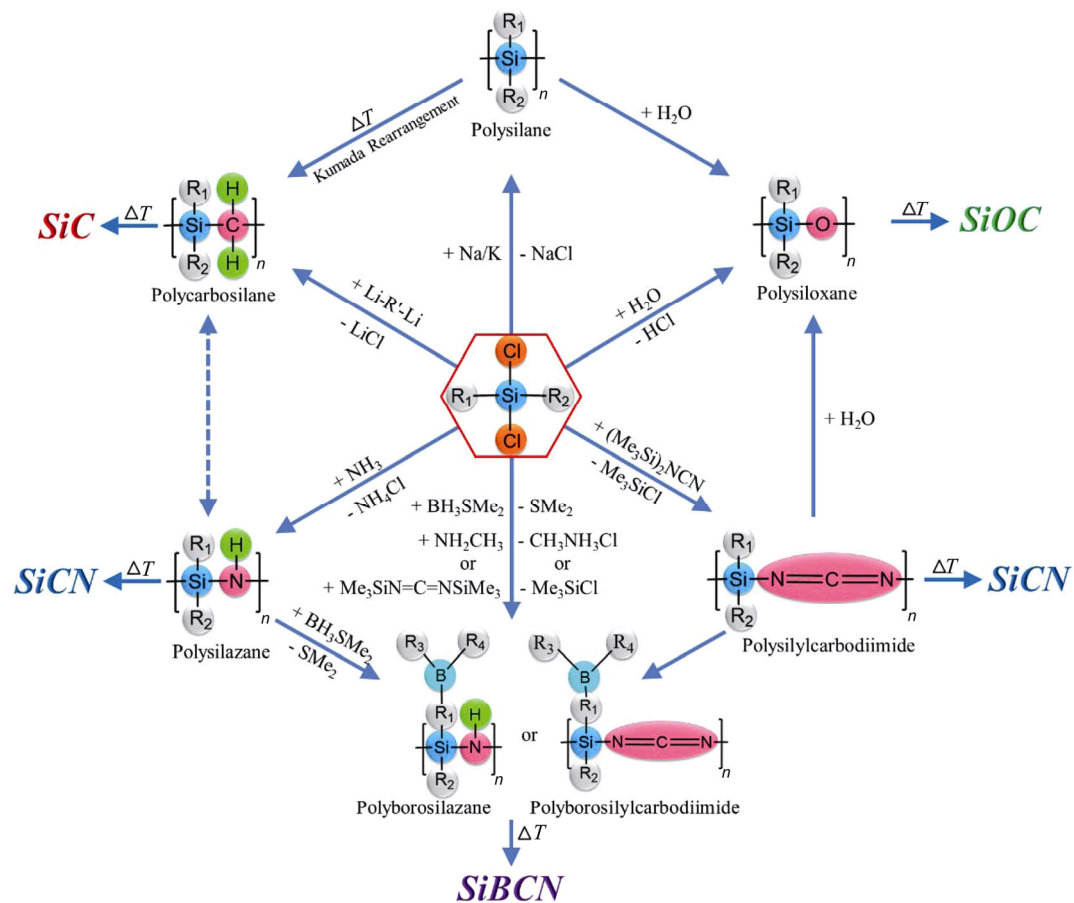
Fig. 2 Synthetic routes for typical Si-based polymers and associated ceramics from organochlorosilanes. R_1–R_4 represent organic groups or hydrogen attached to silicon of the polymer backbone. Reproduced with permission from Ref. [36], © Elsevier Ltd. 2019.

2. 2 Crosslinking

Before transformation into ceramics, there is an important step, in which the preceramic polymers are converted into infusible organic/inorganic materials, namely crosslinking. This is a crucial step because it not only retains the shape of the precursors but also increases the ceramic yield due to the formation of a continuous network within the infusible precursors [186,187]. Based on molecular structure of the polymers and requirements of the resultant ceramics, different initiation mechanisms of the crosslinking process can be utilized [35]. Thermal crosslinking is usually employed (200–400 ℃) when the chemical and phase compositions of final ceramics must be controlled. This is because, under this condition, no additional elements are introduced. The thermal crosslinking capability comes from the condensation or addition reactions which occur between the functional groups on the preceramic polymers (e.g., Si–OH, Si–H,

N–H, and allyl/vinyl substituents) [35,183]. As reported, during the thermal crosslinking process, four major reactions are generally involved, namely, polymerization (e.g., vinyl or allyl groups), hydrosilylation (e.g., Si–H/vinyl groups), transamination (i.e., evolution of amines, ammonia, or oligomeric silazanes), and dehydrocoupling (e.g., Si–H/Si–H or Si–H/N–H groups) [12,36,81,99,183,188–190]. As a function of temperature, the reaction activities are in the order of hydrosilylation > dehydrocoupling > transamination > vinyl group polymerization [188]. Furthermore, in order to reduce the crosslinking temperature, some catalysts (e.g., dicumyl peroxide, transition metal ions) can be used [12,131,191]. Moreover, the crosslinking activity can be also initiated using other methods, such as oxygen [6,25,192–196], electron-beam [150,196–198], UV light [126,199–202], laser beam (3D printing) [21,203–211], or other reactive gases (e.g., NH3, NO2) [212–215], reactive plasma (based on NH3, CH4, O2, SiH4, or BH3 gas)

[216,217], or even via highly alkaline solutions [218]. Most of these methods are able to start the crosslinking behavior at room temperature.

2. 3   Polymer-to-ceramic transformation

After crosslinking, the next step of the synthesis of PDCs is the polymer-to-ceramic transformation, i.e., ceramization. The ceramization process occurs during pyrolysis at temperatures from 400 to 1400 ℃ (Fig. 1) [38]. As shown in Fig. 2, after ceramization, the poly(organosiloxanes), poly(organocarbosilanes), poly(organoborosilazane), as well as poly(organosilazanes)/ poly(organosilylcarbodiimides) are transformed into amorphous SiOC, SiC, SiBCN, and SiCN ceramics, respectively. During polymer-to-ceramic transformation, different atmospheres, inert or reactive gases, are used. Interestingly, the atmosphere strongly affects the ceramic yield as well as the chemical/phase composition of the resultant ceramics [35]. For example, in PDCs, free carbon always exists in the ceramic matrix because of the presence of hydrocarbon groups on the polymers [36]. It is hard to avoid free carbon in PDCs if using argon or nitrogen as protective gas, whereas free carbon can be reduced or even completely removed when pyrolysis is performed in H_2 [40,219–221]. Moreover, in addition to the generally used pyrolysis method [35], the ceramization process can be achieved through rapid thermal annealing [222], plasma spraying [223], laser pyrolysis [224–229], flash pyrolysis [230], microwave pyrolysis [231,232], and ion irradiation [233–237]. The ion irradiation is a nonthermal ceramization process which occurs by elimination of hydrogen atoms via cleavage of C–H bonds [235,236,238–240].

2. 4   Microstructure

The microstructure of PDCs has been comprehensively characterized by using various techniques that can provide the average/integral information of the microstructures (e.g., X-ray diffraction (XRD), small-angle X-ray scattering (SAXS), magic-angle spinning nuclear magnetic resonance (MAS-NMR), Fourier transform infrared spectroscopy (FT-IR), Raman spectroscopy and small-angle neutron scattering (SANS)) or local information at the nanometer scale (e.g., scanning electron microscopy (SEM), transmission electron microscopy (TEM), electron energy loss spectroscopy (EELS), and energy-filtered transmission

electron microscopy (EF-TEM)) [35,36]. Furthermore, theoretical simulations have also been employed to investigate the microstructures of PDCs [241–246] and numbers of modes have been developed to understand the relationship between microstructure and properties [54,241,243,247].

Silicon oxycarbide (SiOC) and silicon carbonitride (SiCN) are two typical polymer-derived ceramics which possess unique microstructures hard to be observed in other ceramic materials [54]. The SiOC is generally amorphous with Si atoms tetrahedrally coordinated by O and C atoms [49,54,248,249]. Thus, within the SiOC ceramics, SiC_4, SiC_3O, SiC_2O_2, and SiO_4 tetrahedral units with "Si–O/–C" mixed bonds can be clearly detected [54,250]. A classic model (see Model 1 in Fig. 3) for the microstructure of the SiOC ceramics has been proposed in 2005 [251,252]. According to this model, the SiOC ceramic is constructed by three constituents: (1) the clusters of silica tetrahedra that form the heart of the nanodomains; (2) the graphene cage-like network that encases the silica nanodomains, and (3) the monolayer of SiC_xO_{4-x} mixed bonds ($0 \leqslant x \leqslant 4$) that interconnect the silica nanodomains with the graphene network. This model is consistent with the experimentally determined data including MAS-NMR and SAXS results as well as the mechanical properties (e.g., unique viscoelastic behavior and high creep resistance) of the SiOC ceramics.

In addition, another model (see Model 2 in Fig. 3) with two continuous interpenetrating phases (i.e., silica-rich phase and free carbon) and a carbon-rich SiO_xC_{4-x} interface (Fig. 3(b)) was also proposed [36]. However, according to the experimental results, Model 2 was ruled out in Saha *et al.*'s work because it cannot interpret the unique creep and viscoelastic behavior of the SiOC ceramics [251,252]. Interestingly, based on the high-resolution ^{29}Si NMR spin–lattice relaxation studies, Widgeon *et al*. found that the SiOC ceramics consist of a continuous mass fractal backbone of corner-shared SiC_xO_{4-x} tetrahedral units with "voids" occupied by free carbon nanodomains. Obviously, this is more consistent with Model 2 (Fig. 3(b)) [36,250]. In this model, the oxygen-rich SiC_xO_{4-x} units (i.e., $x < 2$) locate at the interior of the backbone with a mass fractal dimension of ~2.5, and the carbon-rich units (i.e., $x \geqslant 2$) occupy the interface between the backbone and the free carbon nanodomains with a slightly lower dimensionality (2.1–2.3) [250,253]. Moreover, for the carbon-rich SiOC ceramics, the
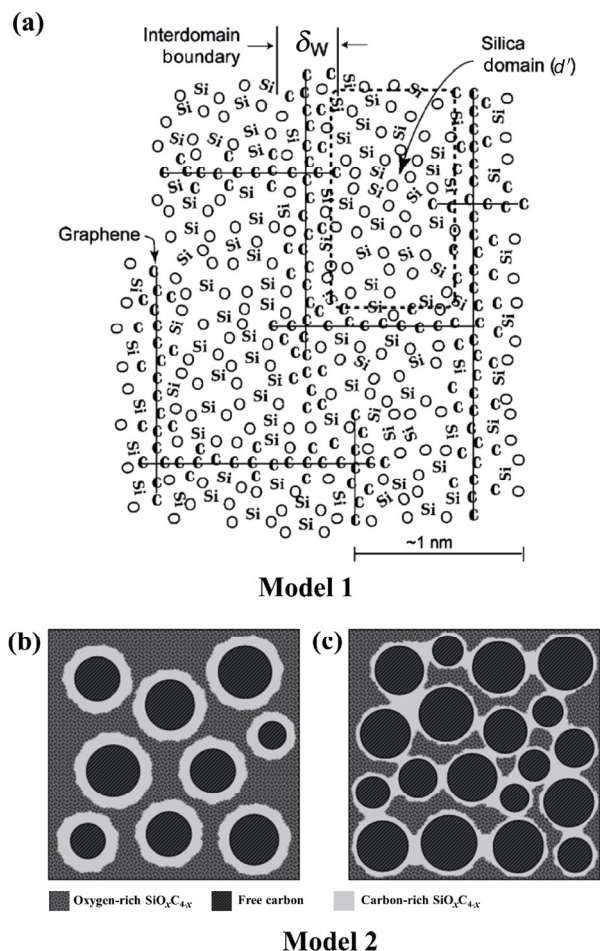
Fig. 3 Two proposed models illustrating the microstructure of polymer-derived SiOC ceramics: (a) a classic model illustrating a microstructure with clusters of silica tetrahedra, monolayer of SiC_xO_{4-x} mixed bonds and graphene cage-like network that encases the silica nanodomains; (b) Model 2 with isolated carbon-rich SiO_xC_{4-x} interface and (c) Model 2 with interconnected carbon-rich SiO_xC_{4-x} interface in carbon rich SiOC ceramics. Reproduced with permission from Ref. [36], © Elsevier Ltd. 2019.

carbon-rich SiO_xC_{4-x} interface can be interpenetrated as well, which can be illustrated by Model 2 (right) (Fig. 3(c)) [250]. Accordingly, the microstructure of SiOC ceramics is rather complicated. It varies and strongly depends on the molecular structure and composition of the preceramic polymers.

The microstructure of amorphous SiCN ceramics is strongly determined by the molecular structures of the preceramic polymers. The main difference between amorphous SiCN ceramics is whether there are Si–C/N mixed bonds (i.e., the presence of SiC_xN_y units) in the ceramic matrix or not. Within the ceramic matrix of polysilazane-derived SiCN ceramics, the tetrahedrally coordinated Si atoms are bonded to either N or C or a

mixture of C and N (i.e., SiC_xN_y), forming SiC_4, SiN_4, or SiC_xN_y units, respectively (Fig. 4(a)) [148]. In contrast, no significant concentration of SiC_xN_{4-x} mixed bonds can be found in the polysilylcarbodiimide-derived SiCN ceramics [44,178,254,255]. As shown in Fig. 4(b), within the matrix of carbon-rich polysilylcarbodiimides-derived SiCN ceramics, three amorphous phases including Si_3N_4, SiC, and free carbon nanodomains can be characterized [44,256,257]. The thermal stabilities of the amorphous SiCN against crystallization are significantly affected by the microstructures. As reported, with an analogous C/Si ratio, the amorphous SiCN ceramics obtained from polysilylcarbodiimides crystallize at temperatures 50–100 ℃ higher than that derived from polysilazanes [35].

Furthermore, one of the most intriguing characteristics of PDCs is that, the X-ray amorphous PDCs are not strictly amorphous because they contain short-range structural features with the size ranging from 1 to 5 nm, namely nanodomains. The nanodomains are firstly discovered in the Si(B)CN ceramics and then in the SiOC ceramics via small-angle X-ray scattering (SAXS) analysis [247,252,257,258]. The nature of nanodomains was proposed to be the basis for the excellent resistance of PDCs to crystallization even at ultrahigh temperatures [241,242,252,259]. Taking the polysilazane-derived SiCN ceramics as an example, the characteristic nanodomain microstructures are schematically illustrated in Fig. 5 [260,261]. In the amorphous Si-containing phase, the silicon atoms are tetrahedrally coordinated by C or N atoms via sp^3-hybridization, forming several different nanodomains with SiC_4, SiN_4, or SiC_xN_{4-x} ($0 \leqslant x \leqslant 4$) units. Within the free carbon nanodomains, the C atoms are bonded to each other through sp^2-hybridization, forming the basic structural unit (BSU) of free carbon [148,262,263].

When the amorphous PDCs are subjected to elevated temperature conditions ($\geqslant 1400$ ℃), they will undergo further phase separation and crystallization, generally leading to the formation of ceramic (nano)composites with multiple phases [49,264–269]. In addition, the carbothermal reactions between the oxygen- or nitrogen-containing phases (e.g., SiO_xC_y, Si_3N_4) and free carbon occur significantly when the temperature exceeds 1500 ℃, leading to a mass loss of the ceramic materials, generation of new phases, and a reduce of carbon, oxygen, and nitrogen content via releasing of gaseous products (e.g., CO, SiO, or N_2) [12,78,186,269–272].
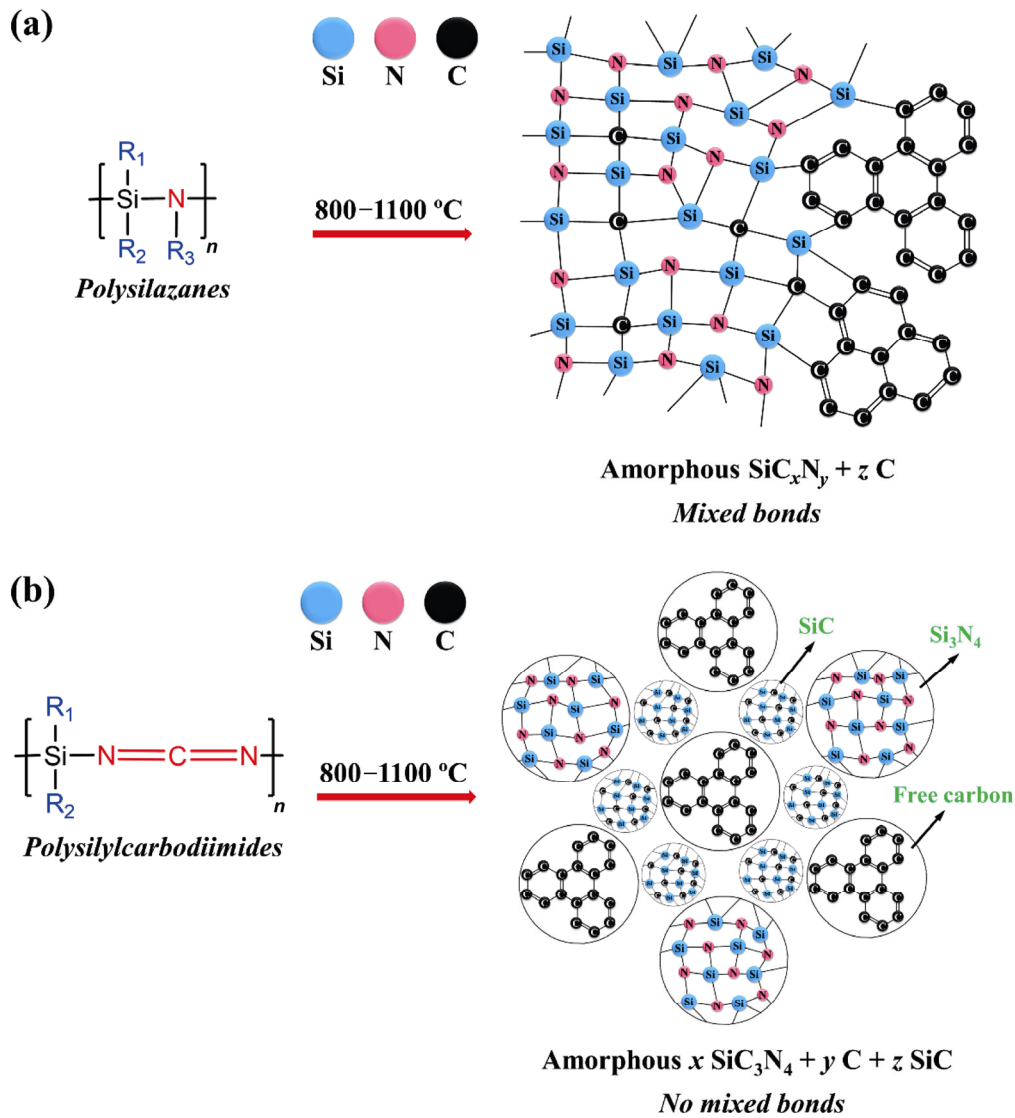
Fig. 4 Microstructure of amorphous SiCN ceramics derived from two different polymers: (a) polysilazanes, (b) polysilylcarbodiimides. Reproduced with permission from Ref. [36], © Elsevier Ltd. 2019.
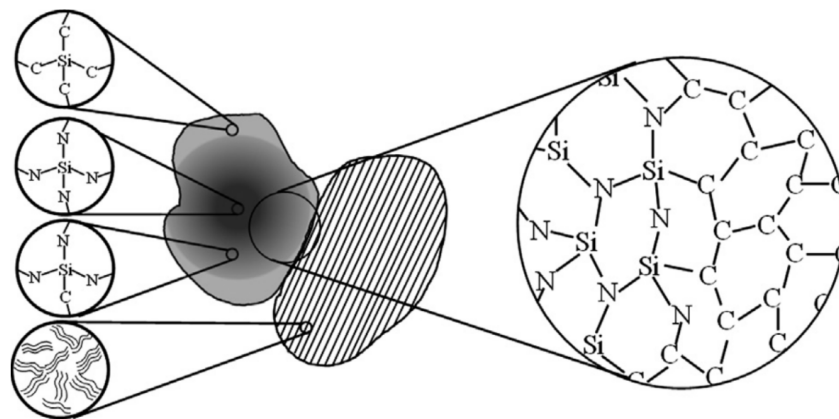
Fig. 5 Proposed nanodomain structural models for SiCN ceramics derived from polysilazane. The dark area is Si-containing phase, and the stripe area is free carbon phase. The atomic structures within these nanodomains are shown schematically in the insets. Reproduced with permission from Ref. [261], © Acta Materialia Inc. 2014.

3 Polymer-derived ceramics for energy conversion

3.1 Fundamentals and material issues

As mentioned in the introduction, several energy conversion systems (e.g., gas turbine engines, steam turbine engines, wind mills, solar cells, and fuel cells) have been developed based on different energy sources. According to the prediction, gas turbine engines will still play an important role in energy conversion at least till 2050 [1], despite that the application of renewable energy will significantly increase in the following decades. Particularly, gas turbine technology is very important for future worldwide reduction of CO_2 emissions in both power generation and aviation sectors, owing to their high efficiency and fuel flexibility [273]. The sustainable energy conversion systems (e.g., solar cells and fuel cells) have been comprehensively highlighted in several review articles and books [274–281]. Therefore, in this review, we mainly focus on the application of polymer-derived ceramics in gas turbine engines.

The gas turbine engine is a type of continuous and internal combustion engine (ICE) that burns gaseous or liquid fuel, and therefore it is also called combustion turbine engine. The gas turbine engines are mainly composed of upstream rotating gas compressors (low- and high-pressure compressors), a combustor, and downstream turbines (low- and high-pressure turbines) on the same shaft as the upstream compressors (Fig. 6(a)). Because the energy of gas turbines can be split into thrust and shaft work based on the specific purpose, they are now setting world standards in two major industrial applications, namely jet engines for the aero industry and the electric power generation. Moreover, the rotating shaft can also provide mechanical power for driving compressors/pumps and ship/train/tank propulsion [273].

For power generation sector, the gas turbine engines are becoming the main technology for conversion of fossil fuels into electricity. As reported in literature, the gas turbines were used to generate ~20% of the world's electricity, with the sales estimated at around US$17 billion in 2015 [283]. In the near future, the conventional gas- and oil-fired steam power plants will be replaced by the quite high efficient combined-cycle power plants, in which the rotary shaft of the gas turbine engine works for a electricity generator, while the exhaust heat is used in an additional steam power plant [273]. In 2018, the combined-cycle mode has been proven to exhibit high efficiency up to 63% [286].

Within the aviation sector, the gas turbines play an enormously important role in moving cargos and people around the world in a time- and energy-efficient way. As the mainstay of commercial and military aircraft propulsion, the sales of gas turbines in 2015 were estimated at US$ 39 billion globally, and it was predicted to be around US$1.07 trillion in 2028 [283]. Generally, the gas turbines used for air transport applications can be classified into three different configurations: (1) turbojet/turbofan (generally called jet engines), (2) turboprop, as well as (3) turboshaft designs [273]. Among the three configurations, jet engines are the most popular use of gas turbines owing to their excellent thrust/weight ratio [1].

As mentioned above, a further improvement in technologies and materials used in the gas turbine engines is highly demanded to improve fuel efficiency and reduce CO_2 emissions, in response to the energy crisis and climate change [284,285]. In order to find out the essential factors that affect the fuel efficiency of gas turbines, a simplified gas-turbine cycle (i.e., the so-called Brayton cycle) has been proposed (Fig. 6(b)). A thermodynamic evaluation of the Brayton cycle proves that the efficiency η of a Brayton process depends on the pressure ratio $R = P_2/P_1$ and the ratio of specific heats ($k = C_p/C_V$) at constant pressure (C_p) and constant volume (C_V):

$$\eta_{\text{Brayton}} = 1 - \frac{1}{R^{\frac{k-1}{k}}} \tag{1}$$

Obviously, higher pressure ratio is the prerequisite of higher efficiency of the gas turbines. The pressure ratio (R) can be described by

$$R = \left(\frac{T_2}{T_1}\right)^{\frac{k}{k-1}} = \left(\frac{T_3}{T_4}\right)^{\frac{k}{k-1}} \tag{2}$$

Accordingly, the increase of fuel efficiency results in the demand for higher operation temperatures [287]. The specific core power of a gas-turbine engine as a function of gas-inlet temperature is shown in Fig. 6(c) [283,284]. The increasingly improved gas-inlet temperature translates into more severe operating conditions.

In the last 100 years, plenty of advanced materials
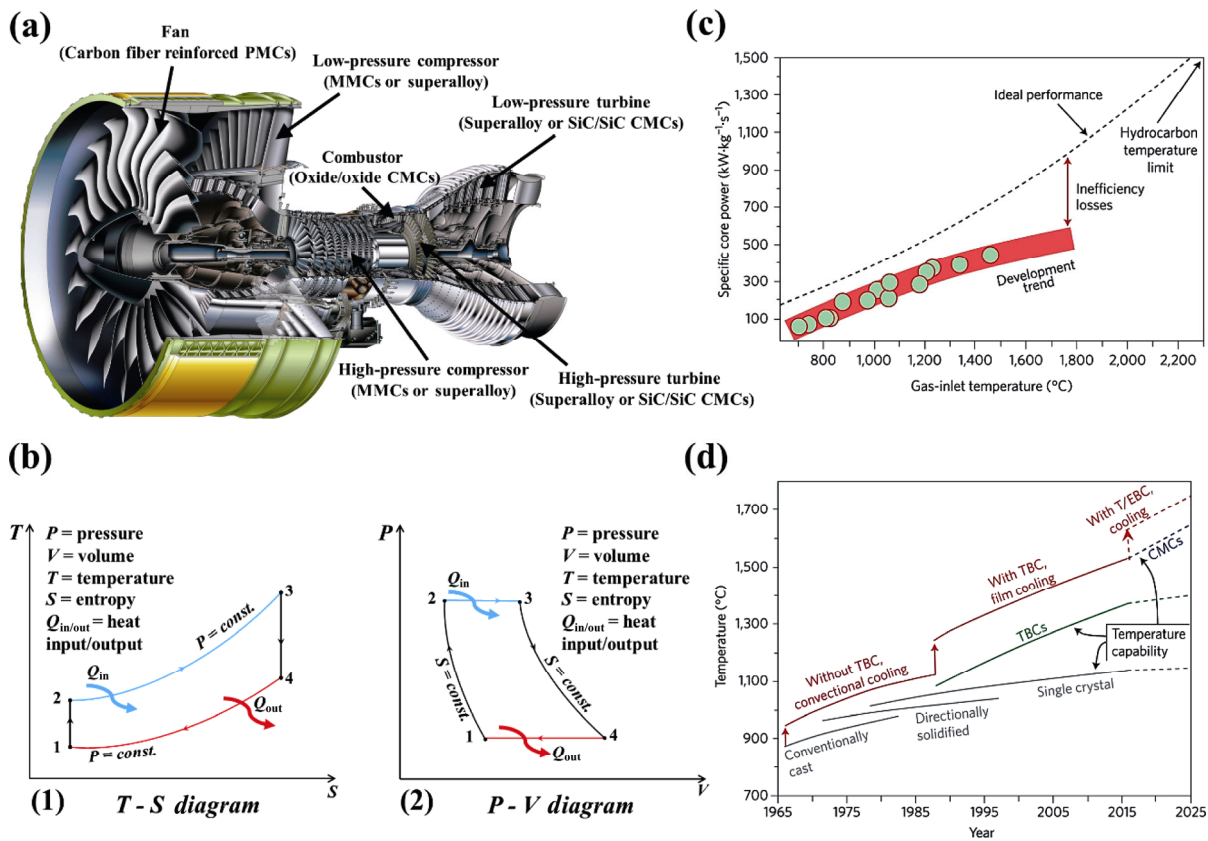
Fig. 6 (a) Cutaway view of GP7200 aircraft engine (retrieved from https://prattwhitney.com/products-and-services/products/commercial-engines/gp7200) and the potential applications of continuous fiber reinforced composites (PMCs: polymer matrix composites; MMCs: metal matrix composites; CMCs: ceramic matrix composites) [282]. (b) *T–S* (1) and *P–V* (2) diagrams of an ideal Brayton cycle. Reproduced with permission from Ref. [1], © Elsevier Ltd. 2020. (c) Specific core power of a gas-turbine engine as a function of gas-inlet temperature, and (d) progression and projection of temperature capabilities of Ni-based superalloy (grey), TBCs (green, rough estimates), CMCs (blue, rough estimates), and maximum allowable gas temperatures with cooling (red, rough estimates). Reproduced with permission from Ref. [283], © Nature Publishing Group, a division of Macmillan Publishers Limited 2016.

have been used as high-temperature structural materials at the heart of gas turbines, ranging from conventionally casted or directionally solidified high-temperature alloys to nickel-based single-crystal superalloys. Figure 6(d) shows the development of temperature capability of materials used at the heart of the gas turbine engines over the last decades. It clearly shows that high-temperature alloys and thermal barrier coatings, in conjunction with cooling systems, have played a crucial role in the development of gas turbine engines. However, the increasing severity of operating conditions with the gas-inlet temperature higher than 1800 ℃ in future turbine engines limits the menu of available materials to very few high-temperature ceramics, mainly ceramic matrix composites (CMCs) protected by environmental barrier coatings (EBCs). Polymer-derived ceramics are one of the best candidates for producing these materials [35]. The following

sections will comprehensively summarize the role of PDCs in production of ceramic matrix composites, ceramic fibers, as well as ceramic coatings.

3. 2 Ceramic matrix composites

Ceramic matrix composites (CMCs) are considered as the most promising candidates for significant enhancement of material capability with respect to (ultra)high temperature applications under harsh environmental conditions and strong mechanical load [288]. As the replacements of Ni-based superalloys in future gas turbine engines, CMCs are capable of handling the highest temperature ($\geqslant$ 1500 ℃) even without thermal barrier coatings (Fig. 6(d)) [283]. This feature is in particular of great technological importance for the development of the next-generation gas turbines for stationary and non-stationary energy conversion systems. Typically, the CMCs which have

the potential to be used for the blades of gas turbine engines in the future consist of a SiC-based ceramic matrix, a continuous SiC fiber reinforcement, and a moderately weak fiber/matrix interface (e.g., BN and C) [289,290]. Carbon fibers are also used to produce C/SiC CMCs. However, they are more suitable for hypersonic and rocket engine applications because of their relatively short lifetime caused by the poor oxidation resistance of carbon fibers [283,291]. Oxide-based ceramic matrix exhibits excellent oxidation-resistant, but the low strength and creep resistance limit their applications as the core section of the engines [283].

In addition to the excellent high-temperature strength, CMCs are inherently lightweight, with 1/3 of the weight of superalloys, resulting in a high specific strength [291]. This will enable to substantially reduce the fuel consumption and pollution associated with the operation of combustion engines, contributing to further development of environmentally friendly technologies. Moreover, compared with superalloys, the CMCs exhibit better high-temperature oxidation and creep resistance [283,291–293]. Most importantly, CMCs are damage-tolerant and notch-insensitive, which is the inherent disadvantages of monolithic ceramics [294,295]. Because of these superiorities, significant investments have been made in CMCs by the major engine manufacturers, and huge progress has been made in the last decades. For instance, the exhaust-section flaps/seals and afterburners made of CMCs have been used in military engines for years [283]. In the recent demonstration of jet engines, both stationary and rotating CMC components in the hot section have been used [283,296].

Several methods have been developed to prepare CMCs using 2D/3D fiber preforms and ceramic precursors, such as chemical vapor infiltration (CVI), polymer infiltration and pyrolysis (PIP), slurry infiltration (SI), reactive melt infiltration (RMI), or liquid silicon infiltration (LSI), as well as the hybrid of these methods [82,106,298,299]. Preceramic polymers have been used for the fabrication of CMCs in two different aspects: (1) producing ceramic fibers as reinforcement (will be discussed later) [6,150,300–303]; (2) producing the ceramic matrix via PIP process [16,17,297,304]. The procedures of PIP processing to fabricate polymer-derived CMCs are shown in Fig. 7. For producing ceramic matrix, preceramic polymers provide myriad advantages, including lower thermal
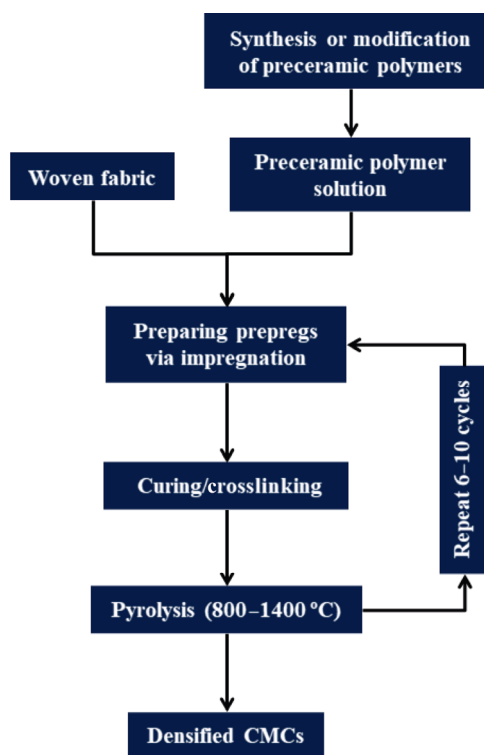
Fig. 7 Flow chart of PIP processing protocol to fabricate polymer-derived CMCs [17,83,297].

treatment temperatures (which is of significant importance for strength retention of ceramic fibers and mechanical properties of the CMCs), deeper infiltration depth, shorter cycle time, better homogeneity, no residue silicon or other metallic elements, as well as the capability for near-net-shape fabricating large and complex parts with simpler and cheaper equipments [18,19,35,305]. Importantly, preceramic polymers can be chemically modified by other elements (e.g., B, Ti, Zr, Hf) to fabricate CMCs with preferable nanostructures and ultra-high temperature resistant ceramics with improved thermal protection performance (e.g., $C_f/SiHfBCN$ and $C_f/SiHfC$) [12,83,102,306–309].

Up to now, several CMCs with different ceramic matrix have been investigated using PIP method for the purpose of structural application in hot section of gas turbine engines, such as C_f/SiC [106], $C_f/SiBCN$ [107,310–312], $C_f/SiCN$ [82,298,313], $C_f/SiHfBCN$ [82], $C_f/SiOC$ [314,315], $C_f/SiCON$ [18], $C_f/SiBOC$ [316], $SiC_f/SiCN$ [298,317], SiC_f/SiC [318,319], and $SiC_f/SiBCN$ [320]. These CMCs with polymer-derived ceramic matrix have been demonstrated to exhibit excellent structural properties which are preferable for application in gas turbine engines, such as excellent thermal stability, oxidation resistance, high-temperature

mechanical properties, as well as creep resistance [321–323]. Jones *et al.* [321] reported the mechanical properties of PIP-fabricated SiC$_f$/SiC CMCs containing two different SiC fibers (namely, CG Nicalon CMC and Hi-Nicalon CMC). As shown in Table 1, SiC$_f$/SiC CMCs exhibit excellent mechanical properties with tensile strength higher than 250 MPa at both room and high temperatures. Compared to CG Nicalon CMC, the Hi-Nicalon CMC shows enhanced tensile strength at high temperatures, which is due to the improved thermal stability of the Hi-Nicalon fibers. Moreover, the authors found out that the Hi-Nicalon CMC exhibits outstanding creep resistance at 1200 ℃, despite that the CG Nicalon CMC can only perform under moderate stress in air for extended periods at 1100 ℃ [321]. Xu *et al.* [315] prepared three-dimensional carbon-fiber reinforced SiOC (3D C$_f$/SiOC) composites through PIP processing and investigated their mechanical properties after annealing at 1300–1700 ℃. The results show that the annealing temperature played a crucial role on the mechanical properties of the C$_f$/SiOC composites. The mechanical properties of the composites vary slightly when the annealing temperature increases from 1200 ℃ (flexural strength: 308±14 MPa) to 1400 ℃ (flexural strength: 303±10 MPa). However, when the annealing temperature exceeds 1500 ℃, both the flexural strength and modulus decrease remarkably, which is due to the decomposition and volume shrinkage of SiOC matrixes caused by carbothermal reductions [315]. Tian *et al.* [324] prepared carbon-fiber reinforced SiCN CMCs (C$_f$/SiCN) via PIP processing using homemade polysilazanes (PSN-T03) as precursors and investigated their high-temperature mechanical properties at 1200–1500 ℃. Interestingly, compared with the mechanical properties at room temperature, the C$_f$/SiCN exhibits enhanced mechanical properties at 1200–1400 ℃. The tensile strength of the C$_f$/SiCN composites at room temperature and 1400 ℃ are 230 and 350 MPa, respectively, and the bending strength are measured to be 380 and 530 MPa, respectively. This behavior might be because the testing temperatures are close to the fabrication process temperature, and the internal heat stress was relieved well under the testing condition. Nevertheless, the mechanical properties of the C$_f$/SiCN composites decline rapidly at 1500 ℃ due to the carbothermic reduction of the silicon nitride phase [324]. Lee *et al.* [310] fabricated C$_f$/SiBCN CMCs using a liquid two-component Si–B–C–N precursor via PIP processing (Fig. 8(a)). The thermogravimetric

analysis (TGA) and mechanical tests show that the C$_f$/SiBCN CMCs exhibit excellent high temperature stability (Fig. 8(b)) and mechanical properties (Fig. 8(c)), respectively. The flexural strength of the as-fabricated C$_f$/SiBCN CMCs was 255 MPa, and they retained most of their strength up to 1500 ℃ (Fig. 8(c)). Moreover, the C$_f$/SiBCN exhibits excellent creep resistance. The results show that the secondary creep occurred up to 60 h at 1400 ℃ with 100 MPa pressure in argon, and the total creep strain was as low as 0.55% (Fig. 8(d)). This value is smaller than that of CMCs obtained by chemical vapor infiltration (CVI) (e.g., C$_f$/SiC 1400 ℃, 110 MPa, 60 h: ~0.75% [325] and Hi-Nicalon™ SiC$_f$/SiC 1300 ℃, 90 MPa, 30 h: ~0.7% [326]) which have been reported to offer the best high-temperature properties. Very recently, Yuan *et al.* [82] prepared a carbon fiber reinforced C$_f$/SiHfBCN CMCs via PIP approach using a Hf- and B-modified polysilazane as precursor. The results prove that incorporation of Hf and B into SiCN matrix is able to significantly enhance the hydrothermal corrosion performance of the as-prepared C$_f$/SiHfBCN CMCs.

As discussed above, taking the full advantages of the low temperature processability of preceramic polymers, the PIP approach offers solution to most of the problems associated with other processing methods (e.g., CVI, RMI) for CMCs. However, when employing this approach, one must pay much attention to each processing step, particularly the pyrolysis step. This is because, during polymer-to-ceramic transformation, the decomposition of precursor matrix inevitably leads to shrinkage of the matrix and formation of pores, voids, and micro-cracks. The evolution of gases during pyrolysis may also result in delamination of the green composite. In order to overcome this problem, the first pyrolysis step should be carried out at a slow heating rate. The ceramic matrix may react with the interphase coating/fiber during the repeated PIP process, which can deteriorate the strength of fiber reinforcement as well. In addition, the pyrolysis temperature should be carefully chosen to ensure that the reinforcing fibers do not lose its strength [297,327].

3. 3　Ceramic fibers

Ceramics fibers, acting as the strengthening and toughening component, are of crucial importance for ceramic-fiber reinforced ceramic matrix composites (CMCs) using gas turbine engines [86]. It is clearly shown in Table 1 that SiC$_f$/SiC CMCs containing
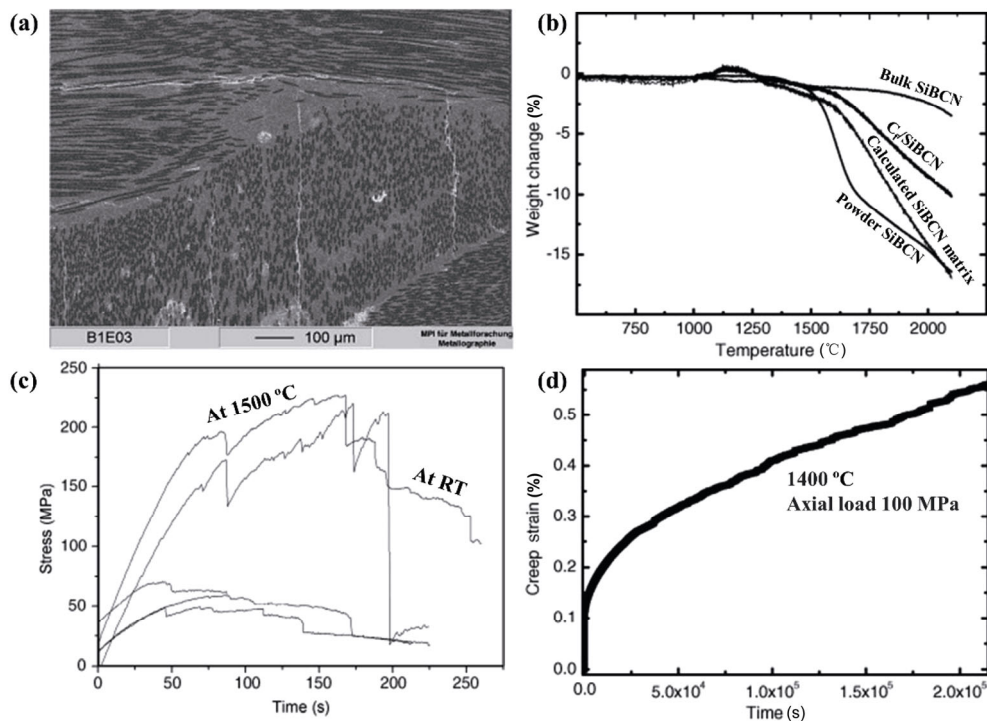
Fig. 8 (a) SEM image of cross-section of the as-prepared C$_f$/SiBCN CMCs; (b) TGA curves of bulk and powdered SiBCN, C$_f$/SiBCN composite, as well as the SiBCN matrix of the C$_f$/SiBCN composites (calculated based on a matrix content of 59.6 wt%); (c) fracture behavior of the C$_f$/SiBCN composite at room temperature (RT) and 1500 ℃; (d) creep strain curve of the as-fabricated C$_f$/SiBCN composite at 1400 ℃ in Ar atmosphere with 100 MPa axial load. Reproduced with permission from Ref. [310], © Acta Materialia Inc. 2007.

Table 1   Mechanical properties of typical SiC$_f$/SiC CMCs prepared by PIP processing [19]

Temperature (℃)	CG Nicalon CMC	Hi-Nicalon CMC
Tensile strength (MPa)		
20	250	360
1000	265	360
1200	290	347
Tensile modulus (GPa)		
20	95.2	120
1000	88.4	115
1200	85	100
Double notch shear strength (MPa)		
20	35	37
1000	26	37
1200	—	—
Compression strength (MPa)		
20	431	—
Density (g/cm^3)		
20	2.1–2.2	2.2–2.3

different SiC fibers exhibit totally different mechanical properties at both room and high temperatures. As mentioned above, the other important application of

preceramic polymers for fabrication of CMCs is producing ceramic fibers. Actually, the potential of polymer-derived ceramics (PDCs) for materials science was not recognized until people produced small-diameter ceramic fibers via spinning and pyrolysis of polyorganosilicon precursors in the 1970s [5,22–27,36]. Up to now, ceramic fibers are the most successful commercial application of PDCs. SiC fiber reinforced CMCs have been widely used in exhaust flaps, seals of jet engines and have been introduced in heat-resistant parts of the new GE LEAP jet engines for passenger planes [36,150,196].

Typical manufacturing steps and important parameters for a controllable processing of ceramic fibers from preceramic precursors are shown in Fig. 9 [86]. The viscoelasticity, melting point, and thermal stability of preceramic polymers, the curing methods, ceramic yield, as well as thermal treatment methods are critical factors for the successful fabrication of high-performance ceramic fibers. During the last 50 years, numbers of ceramic fibers have been developed via PDC route, such as SiC(O) [212], Si–Ti–C–O [328], Si–Zr–C–O [328,329], SiCN [86], SiOC [87], SiBN [330,331],
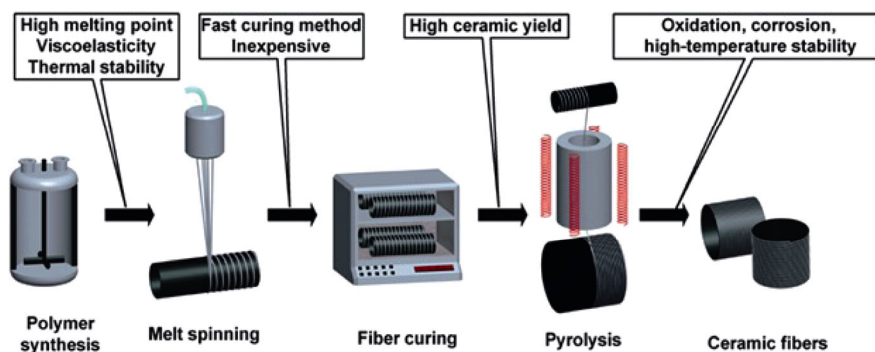
Fig. 9   Manufacturing procedures for polymer-derived ceramic fibers. Reproduced with permission from Ref. [86], © WILEY-VCH Verlag GmbH & Co. KGaA, Weinheim 2014.

SiBCN [74], SiBOC [302,332] fibers. The fracture surface of typical ceramic fibers, namely SiC fiber (Hi-Nicalon) and SiCN fiber (derived from polyorganosilazane named ABSE), is shown in Fig. 10. The chemical composition, properties, commercial availability, and price of these fibers are summarized in Table 2. So far, only a handful of ceramic fibers for use in CMCs have reached the market, and all of them are SiC-based fibers. Therefore, here we briefly introduce SiC fibers.

As reported in literature, SiC-based ceramic fibers can be classified into three generations according to their oxygen content and C/Si atomic ratio [150,196]. The first-generation fibers are Si–C–O (Nicalon) fibers and Si–Ti–C–O (Tyranno Lox M) fibers which were fabricated in the 1980s. However, the maximum working temperature of the first-generation fibers cannot be higher than 1100 ℃ because their strength starts degrading significantly at temperatures above 1300 ℃. This is due to the presence of large amount of oxygen (> 10 wt%) and free carbon (the C/Si ratio is around 1.3–1.4) within the ceramic fibers, which leads to carbothermal reaction at temperatures higher than 1300 ℃. The first-generation fibers have a very high

oxygen content because the preceramic precursor is crosslinked in air in the temperature range from 145 to 200 ℃ by forming Si–O–Si linkages (i.e., oxygen curing) [150]. The typical second-generation fibers are Hi-Nicalon SiC fibers [150]. For the second-generation fibers, the curing process has been changed into electron beam irradiation curing in helium atmosphere. As a result, the oxygen content of the fibers is significantly reduced (less than 1 wt%), leading to a dramatically enhanced high-temperature stability and strength. The strength retention temperature of these fibers was improved up to 1500 ℃. However, the creep resistance of the second-generation fibers is limited to a maximum of 1150 ℃. This can be attributed to the polycrystalline feature of the fibers which is caused by the relatively high free carbon content (the C/Si ratio is around 1.4). It should be noted that the cost of irradiation curing process is actually too expensive for commercial application of the ceramic fibers. Therefore, the oxygen curing process used for the first-generation fibers is also used for the second-generation fibers (e.g., Tyranno ZM fibers). The difference is that, in order to enhance the thermal stability, the metal element grafted to the PCS polymer was changed (i.e., the titanium
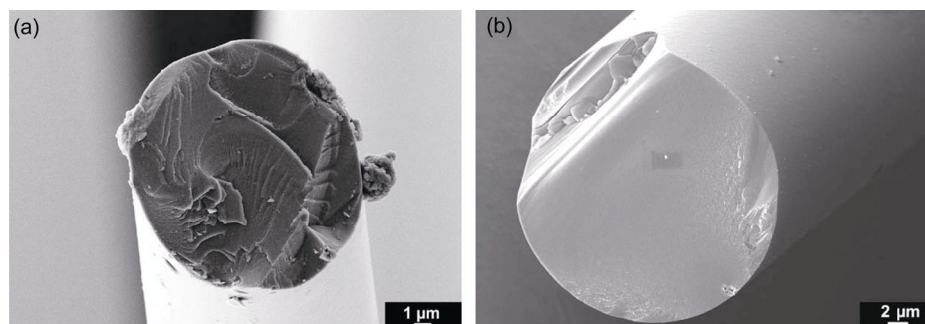
Fig. 10   Fracture surface of typical ceramic fibers derived from preceramic polymers: (a) Hi-Nicalon; (b) ABSE-derived SiCN fiber. Reproduced with permission from Ref. [86], © WILEY-VCH Verlag GmbH & Co. KGaA, Weinheim 2014.

Table 2 Chemical composition, properties, commercial availability, and approximate price of polymer-derived ceramic fibers [86,196]

Name	Si–C–O	SiC	SiC	Si–Ti–C–O	Si–Zr–C–O	SiC	SiC	SiC/BN	Si–C–O	SiC	Si–N–C–O	Si–N	Si–N–C–O	Si–B–N–C
Trade name	Nicalon NL-200	Hi-Nicalon	Hi-Nicalon Type S	Tyranno Lox M	Tyranno ZMI	Tyranno SA	Sylramic	Sylramic-iBN	UF-127	UF-HM	HPZ		SiNC-1400X	SiBN₃C
Manufacturer	Nippon Carbon (NGS Advanced Fibers)			Ube Industries			COI Ceramics (Dow Corning/NASA)		University of Florida		Dow Corning	Tonen	MATE-CH	Fraunhofer Institute
Fiber diameter (μm)	14	14	12	11	11	10/7.5	10	10	10–15		Oblong 8.4/14.4	10	12–14	8–14
Number of filaments	500	500	500	800	800	800/1600	800	800	NA	NA	NA	NA	500	NA
Tex (g/km)	210	200	195	200	200	170/190	180	NA	NA	NA	NA	NA	NA	NA
Tensile strength (GPa)	3.0	2.8	2.3	3.3	3.4	2.4	3	3	2.8–3.5	2.1–3.5	2.8	2.5	2.8	2.0–4.0
Tensile modulus (GPa)	220	270	380	180	195	380	386	400	220	NA	180	250	200	180–350
Density (g/cm³)	2.55	2.74	3.1	2.48	2.48	3.1	3.1	3.1	2.5–2.7	3.1–3.2	2.4	2.5	2.48	1.8
Grain size (nm)	2	5	100	1	2	200	100	100	5	50–300	NA	Amorphous	Amorphous	Amorphous
Thermal conductivity (W/(m·K))	2.97	7.77	24.1	1.4	2.5	65	46	>46	NA	NA	NA	NA	NA	NA
Thermal expansion (10^{-6} K⁻¹)	3.2	3.5	5.1	3.1	4	4.5	NA	NA	NA	NA	NA	NA	NA	3
Si (wt%)	56.6	62.4	69	55	56	67	67	SiC: 96	59–62	67–70	59	59.3	NA	29
C (wt%)	31.7	37.1	31	32	34	31	29	TiB₂: 3.0	38–41	30–33	10	0	NA	13
O (wt%)	11.7	0.5	0.8	11	9	<1	0.3	B₄C: 1.0	0.5–1.5	0.2	3	1.2	NA	0.8–3.4
N (wt%)	—	—	—	—	—	—	0.4	O: 0.3	—	—	28	39.5	NA	44
Ti, Zr, Al, B	NA	—	—	Ti: 2	Zr: 1	Al <2	B: 2.3; Ti: 2.1	—	B: 0–1	B: 0–3.0	—	—	—	B: 11
C/Si atomic ratio	1.31	1.39	1.05	1.37	1.44	1.08	~1.0	~1.0	1.48	1.04	NA	NA	NA	N/Si = 3
Producing temperature (°C)	1200	1300	1500	1200	1300	>1700	>1700	>1700	1000 [333]	1000 [334]	1200	1200	NA	1500
Strength retention temperature (°C)*	1100	1500	1600	1100	1300	1700	1700	1700	1500	1700	NA	NA	NA	NA
Creep resistance (°C)**	1000	1200	1400	1000	1150	1400	1300	>1400	NA	NA	NA	NA	NA	1400
Commercial availability	Available	Available	Available	Available	Available	Available	Available	Available on a limited basis	NA	NA	Available on a limited basis	NA	NA	NA
Approx. price (2013)	€2650/kg	€8000/kg	€11500/kg	€1500/kg	€2000/kg	€8000/kg	€18750/kg	NA	NA	NA	NA	NA	NA	NA

NA: not available; em dash (—): not applicable.
* Maximum strength retention temperature of the ceramic fibers after thermal exposure for a short time (1–10 h) in an inert atmosphere.
** Temperature for $m = 0.8$ in 1-h BSR (bend stress relaxation) measurement.

was replaced by zirconium). Hi-Nicalon Type S, Tyranno SA, and Sylramic TM fibers are typical third-generation SiC fibers. The chemical composition of the third-generation SiC fibers must meet two requirements: (1) with C/Si ratio near to 1 and (2) with rather low oxygen content (< 1 wt%). Furthermore, they exhibit improved thermal stability and creep resistance up to 1400 ℃ [196].

As shown in Table 2, currently, other Si-based ceramic fibers (e.g., SiCO, SiCNO, SiCN, SiBCN, and SiBOC) are not commercially available. Further studies are needed to realize their industrial application. More details of manufacture and the elemental composition of polymer-derived ceramic fibers can be found in review articles and books [86,150,152,196, 335–338].

3. 4   Thermal and environmental barrier coatings

Coating is an integral part of gas-turbine engines. It is well known that the maximum temperature in the hottest part of the gas-turbine engine (gas inlet) has been dramatically boosted to unprecedented levels (> 1500 ℃) due to the introduction of thermal barrier coatings (TBCs) on the Ni-based superalloys (Fig. 6(d)). The TBCs are thin oxide-ceramic coatings (100 μm to 1 mm in thickness) with low thermal conductivity, which allow the engine to operate at temperatures above the melting point of the superalloys [339]. The most widely used TBCs are the atmospheric plasma-sprayed 7YSZ (7 wt% yttria stabilized zirconia). However, the TBC coated superalloys are approaching their temperature-capability limit, and it is not confident for the scientists and engineers whether they will be able to achieve the > 1700 ℃ gas inlet temperature goal or not.

Within this context, the SiC-based CMCs can provide a "quantum jump" in temperature capability [340], which is able to withstand high temperatures > 1500 ℃ in dry air even without TBCs. Unfortunately, in the gas turbine engines, the high-velocity, high-pressure, and high-temperature gas stream contains ~10 vol% of water vapor [339]. Under such harsh environment conditions, the CMCs are subject to active oxidation and recession owing to the formation and volatilization of $Si(OH)_4$, leading to catastrophic degradation [71,89,283,341,342]. Accordingly, the SiC-based CMCs also need protective coatings, namely environmental barrier coatings (EBCs). Different from TBCs, the EBCs should be impervious (i.e., dense and crack-free) and have a good coefficient of thermal expansion (CTE) match with the CMCs in order to protect the CMCs from environmental degradation via blocking diffusion/ingression of oxygen/steam [340]. Of course, for the purpose of further enhancing the gas-inlet temperature of turbine engines (> 1700 ℃), the thermal stability and chemical durability of EBCs must be improved as well. In addition, the EBCs must be resistant to degradation by molten calcia–magnesia–aluminosilicate (CMAS) deposits coming from ingested dust, sand, or ash as well as exhibit mechanical robustness against fracture [340]. Considering the strict requirements, the EBCs are generally multilayered ceramics with a bond-coat, inter-layer, and top-coat [343]. Furthermore, in order to meet the requirements for application at temperatures > 1700 ℃, a thermal insulating TBC layer is needed on the top of EBCs, forming a T/EBC coating system (Fig. 11(a)).

Preparing TBCs or EBCs is another important application of polymer-derived ceramics. Taking
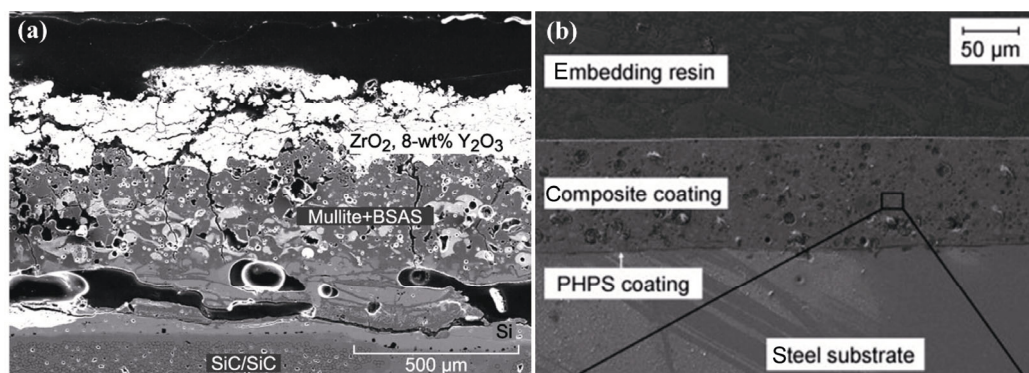
Fig. 11   (a) Typical T/EBC systems for CMCs used in gas turbine engines. Reproduced with permission from Ref. [292], © American Society of Civil Engineers 2013. (b) A polymer-derived EBC system consisting of a SiNO bond coat and a ZrO_2-filled SiCN glass/ceramic composite coat. Reproduced with permission from Ref. [9], © Elsevier Ltd. 2011.

advantage of preceramic polymers, it is very easy to prepare ceramic coatings using liquid phase deposition (e.g., dip coating, spray coating, lacquer technology, and spin coating) and subsequent pyrolysis [344]. The problems regarding thickness and isotropic shrinkage of the coatings can be solved via multiple deposition and loading active/inert fillers (Fig. 12), respectively [9,88,345]. Compared with PVD, CVD, and thermal spray methods, the PDC route possesses its superiorities including more tailorable chemical/phase compositions, lower processing temperatures (< 800 ℃), lower requirements for coating equipments and low cost [36,88]. Particularly, the low processing temperature is important for the metal substrates with relatively low melting point [88].

Several studies with respect to preparing and testing of TBCs/EBCs using PDC route have been reported in the last years [8,9,91,103–105,344–351]. For instance, Günthner *et al.* [9] developed a well adherent, dense, and crack-free environmental barrier coating system composed of a perhydropolysilazane-derived SiNO bond coat and a ZrO_2-filled polysilazane-derived glass/ceramic top coat on mild steel (Fig. 11(b)). After cyclic oxidation tests at 700 ℃, the coating system was undamaged and no oxidation occurred on the mild steel substrates [9]. Liu *et al.* [347] fabricated yttrium silicate environmental barrier coatings (EBCs) on C/SiC composites using polysiloxanes-derived ceramic process and tested their coefficient of thermal expansion (CTE) and water-vapor resistance. The results demonstrate

that the EBCs prepared from 50% Y_2O_3–50% polysiloxanes can effectively protect the C/SiC composites at 1400 ℃. In addition, Liu *et al.* [91] prepared a dense SiOC–BSAS EBC on C/SiC composites using polysiloxane mixed with barium–strontium aluminosilicate (BSAS) fillers. The results prove that the polymer-derived SiOC–BSAS coatings are able to protect the C/SiC composites well both in dry air and in water vapor. After being corroded in a gas flow with 50% H_2O and 50% O_2 at 1250 ℃, the EBC coated C/SiC composites showed slight weight loss and high residual flexural strength. Barroso *et al.* [349] developed a 50 μm thick TBC with high pull-off adhesion of 10 MPa, excellent thermal stability up to 1000 ℃, and outstanding low thermal conductivity of 0.44 W/(m·K). Within this TBC system, polysilazane (PHPS) derived Si_3N_4 was used as bond-coat, and (organo)polysilazane derived SiCN mixed with passive YSZ and active $ZrSi_2$ fillers were used as an insulating layer. The results indicate that the combination of the easy processability and geometry flexibility of PDC coatings with the use of commercially available preceramic polymers makes the developed processing route a promising candidate for the expansion of TBC applications. Hasemann *et al.* [352] prepared a SiON TBC on Mo–Si–B alloys using perhydropolysilazane as preceramic precursors and tested it cyclic oxidation resistance. The results show that the SiON coating is promising in reducing the mass loss during the initial stage of oxidation exposure at 1100 ℃. More details

	Preceramic polymer	**with passive filler**	**with active filler**	**with meltable filler**	**with sacrificial filler**
Green body					
Pyrolysis					
PDC					
Effects	High shrinkage, formation of cracks and porosity	Low shrinkage, porosity, tailored properties	Zero shrinkage possible, dense materials, new phases	Low shrinkage, sealing, densification, stress-relief	Low shrinkage, controlled porosity, strain compliance

Fig. 12 Effects of different fillers on the polymer-derived ceramic coating systems. Reproduced with permission from Ref. [88], © The Royal Society of Chemistry 2019.

regarding polymer-derived TBCs and EBCs are summarized in Table 3.

Currently, the polymer-derived TBCs and EBCs are still at the laboratory research stage, and the testing temperature is not high enough for the new generation gas turbine engine applications. More fundamental studies are needed to further improve their performance via enhancing their thermomechanical properties (e.g., hardness, creep resistance), thermal stabilities (with respect to crystallization and decomposition), and corrosion resistance against high-temperature water vapor as well as to tailor their thermal expansion coefficient and thermal conductivity.
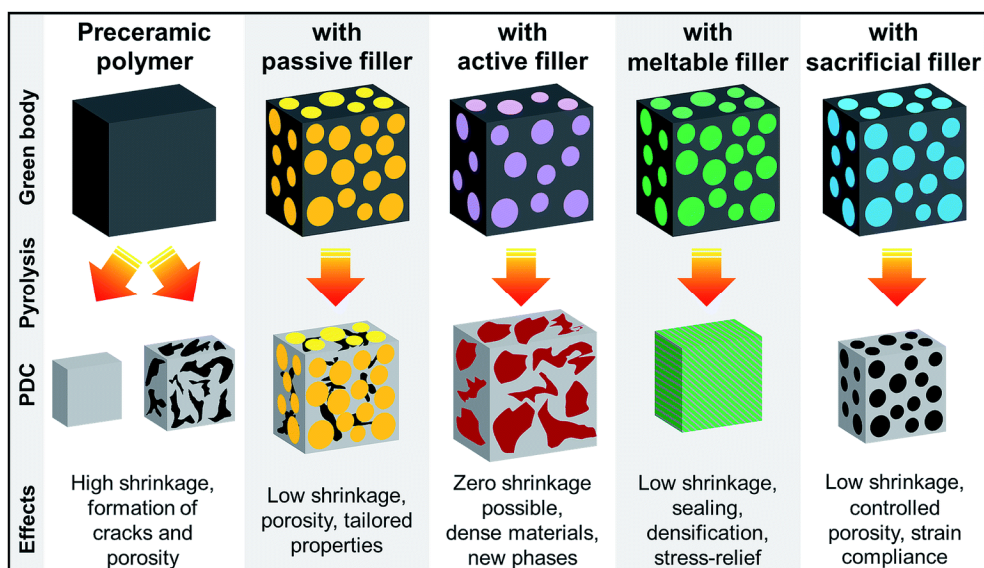
3. 5 High-temperature sensors

In situ and real-time monitoring of the temperature and dynamic pressure within the hot sections of gas turbine engines is another good way to increase their efficiency and reliability [354]. Nevertheless, currently no existing technology is able to provide online, real-time monitoring of the temperature and pressure in gas turbine engines due to the rather harsh environment. Optical-based technology is attractive due to its wireless nature. However, they lack the necessary accuracy for credible measurements and are not applicable for measurements in many important sections, such as the turbine blades, where line of sight cannot achieve [355,356]. Accordingly, new sensors

with the capability of *in situ* and real-time monitoring the temperature and pressure in gas turbine engines are highly demanded. Because of the harsh environment in gas turbine engines, the sensors should meet some strict requirements: (1) with excellent thermal stability and chemical durability at temperatures higher than 1000 ℃; (2) be wireless for accessing any section in turbine engines; (3) be small or low profile without disturbing the aerodynamic flow in turbine engines, as well as (4) with high reliability [354].

PDCs are versatile materials with both interesting structural and functional properties because of their unique microstructures [35]. One good example is the piezoresistivity (i.e., the variation of the electrical resistivity caused by an applied stress) which has been firstly reported by Zhang *et al.* in 2008 [357]. Within this work, the amorphous SiCN monoliths have been found to exhibit extremely high piezoresistive coefficients (1000–4000) along both longitudinal and transverse directions, which are much higher than that of any existing ceramic materials [357]. In recent years, the piezoresistive behavior has been found in SiCNO, SiCO, and SiAlCO ceramics as well, and the piezoresistive coefficients (also known as gauge factors) are measured to be 100–1700, 145, and 7000–16,000, respectively [60,358]. Figure 13 presents the piezoresistivity behavior of the SiCN and SiOC at room temperature. It clearly shows that the electrical resistance of the monolithic

Table 3   Summary of polymer-derived TBC or EBC systems (PT = processing temperature)

Precursor systems	Coatings	Substrates	PT (℃)	Ref.
Polysilazane	HfO_2/SiCN–ZrO_2	Si_3N_4	1000	[350]
Polyhydridomethylsiloxane	$TiSi_2$–SiOC	316 stainless	800	[8]
Perhydropolysilazane/polysilazane (Durazane 1800)	Si_3N_4/SiCN–YSZ–$ZrSi_2$	Steel SISI441	1000	[349]
Polyhydromethylsiloxane	SiOC	316 Stainless Steel (UNS S31600)	800	[105]
Polysilazane	SiCN	13CrMo4-5 (AISI A182)/X5CrNi18-10 (AISI 304)	700	[345]
Perhydropolysilazane/ABSE polycarbosilazane	Si_3N_4/SiCN	Stainless steel (AISI 304)	1000	[346]
Perhydropolysilazane	SiON	Mo–Si–B alloys	800	[352]
Polymethoxymethylsiloxane/hydroxy-terminated linear dimethylpolysiloxane	SiOC	Stainless steel (#1.4301 DIN EN 10027-2)	1000	[353]
Poly(hydridomethylsiloxane)	SiOC–$TiSi_2$	316 Stainless Steel	800	[8]
ABSE polysilazane	SiCN	Carbon fiber (Tenax HTA 5411 12k)	800	[344]
Perhydropolysilazane/KiON HTT1800	Si_3N_4/SiCN	Mild steel (13CrMo4)/stainless steel (AISI 304)	800	[9]
Polysiloxanes mixed Y_2O_3	Y_2SiO_5/$Y_2Si_2O_7$	2D C/SiC composites	1400	[347]
Polysiloxanes mixed with barium strontium aluminosilicate (BSAS)	SiOC–BSAS	C_f/SiC composite	1350	[91]

SiCN and SiOC varies as a function of applied stress. The piezoresistive effect of PDCs has been proven to be dominated by the tunneling-percolation mechanism, which is owing to the presence of graphitic free carbon within the ceramic matrix of PDCs, forming a tunneling-percolation structure. Because of this unique structure, the electrical resistivity of the ceramics is sensitive to the distance between the free carbon clusters [36]. The change of distance between the free carbon clusters caused by applied stress therefore leads to a significant variation in the resistivity, resulting in a high piezoresistive coefficient [60,66,101,357–360]. Importantly, the piezoresistive behavior of PDCs can be also detected at high temperatures. Terauds *et al.* [60] found that the SiCNO ceramics exhibit large piezoresistive coefficients (in the range of 600–1700) at 700–1000 ℃, and the values depend on both the stress and temperature. The extrapolated values of the gage factor at an applied stress of 1 MPa yield a value of 322 and 287 at 1400 and 1500 ℃, respectively. Based on the excellent high-temperature stability, chemical durability, and piezoresistivity, the PDCs are expected to be ideal candidates for *in situ* pressure

sensors used in gas turbine engines [60,68,358,361, 362]. For instance, Shao *et al.* [363] prepared a SiBCN ceramic pressure sensor and tested its performance using half Wheatstone bridge. The SiBCN sensor shows a giant gauge factor of 5500, and the output voltage of the packed SiBCN ceramic sensor changes monotonically and smoothly versus external pressure. The short response time, excellent repeatability, stability, sensitivity, and accuracy ensure its potential for pressure measurement at high temperature and harsh environments in gas turbine engines.

In addition to the pressure sensor based on piezoresistivity, the PDCs can also be used as *in situ* heat flux sensors [364], temperature sensors [365], and hot-wire anemometers [366] which are useful sensors for gas turbine engines. For example, Nagaiah *et al*. [364] designed a high-temperature heat flux sensor for gas turbine engines using polymer-derived SiCN ceramics. The sensor consists of two resistance temperature detectors (RTDs) made of SiAlCN, a resistive layer made of insulator-lightly doped SiCN, and electrical leads made of conductor-heavily doped SiCN (Fig. 14). This novel sensor possesses a temperature coefficient
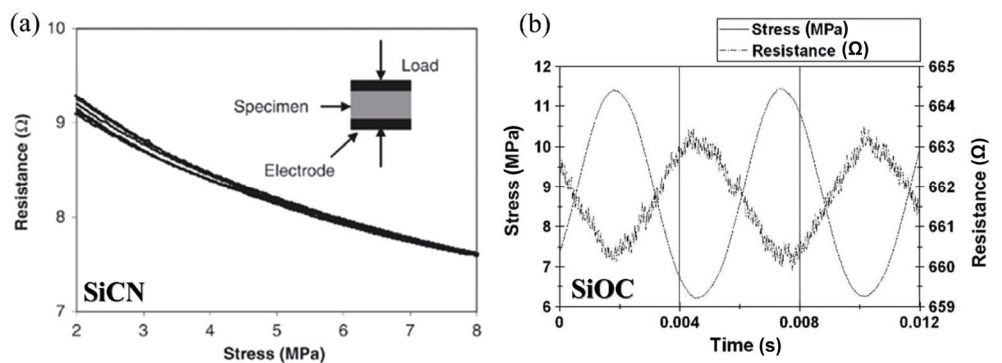
Fig. 13 Experimental proof of the piezoresistive response of (a) SiCN and (b) SiOC. Reproduced with permission from Ref. [101], © The American Ceramic Society 2011; Ref. [357], © The American Ceramic Society 2008.
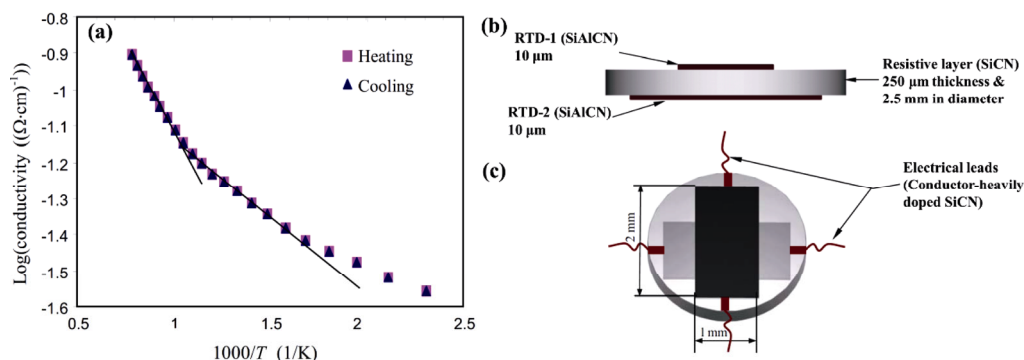
Fig. 14 (a) Electric conductivity of semiconducting SiAlCN as a function of temperature. Schematics of the proposed heat-flux sensor made of PDCs: (b) sectional view and (c) top view. Reproduced with permission from Ref. [364], © IOP Publishing Ltd. 2006.

of resistance of 4000 ppm/℃ and is found to perform quite satisfactorily at 1400 ℃ for a long time as compared to conventional heat flux sensors.

Zhao *et al.* [366] fabricated a temperature sensor using polymer-derived SiAlCN (Fig. 15(a)). The Pt wires are seamlessly embedded in the SiAlCN sensor head as electrodes (Fig. 15(b)). The results demonstrate that the resistance of the senor head decreases monotonically with surrounding temperatures. In actual experiments, the SiAlCN sensors exhibit good repeatability to both unidirectional and bidirectional temperature variations, and the measured data follow closely with the thermal couple measurements at temperatures up to 830 ℃ (Fig. 15(c)). In addition, Nagaiah *et al.* [367] developed a novel high-temperature MEMS hot-wire anemometer (HWA) for gas turbine environment using three types of PDC materials, namely SiAlCN, SiCN (lightly doped), and SiCN (heavily doped), which act as sensing elements (hot-wire), support prongs, and connecting leads, respectively. The results prove that PDC-based HWA can perform better than a conventional HWA in which the hot wire is made of tungsten or platinum–iridium.

As mentioned above, due to the harsh environment in the gas turbine engines, passive, wireless, and robust characteristics are highly desirable for sensors to survive. Therefore, Cheng *et al.* [368] fabricated a wireless pressure sensor based on a microwave evanescent-mode cavity resonator (Fig. 16(a)). The sensor is composed of a cap with a coupling aperture (Fig. 16(b)) and a cavity resonator loaded with a cylindrical post (Fig. 16(d)). On the surface of the pressure sensor cap, a patch antenna is seamlessly integrated in order to be wirelessly interrogated by the interrogation antenna (Fig. 16(c)). A PDC soft-lithography technique was developed to prepare the SiAlCN-based ceramic pressure sensor (Fig. 16(e)). The results show that the resonant frequency decreases with the increasing applied force in a quasi-linear fashion due to the reduced gap dimension, and the wireless passive pressure sensor can be used up to 800 ℃ owing to the robust PDC material and high-Q evanescent-mode resonator structure (Figs. 16(f) and 16(g)).

Moreover, Ren *et al.* [144,369] proposed a novel wireless passive temperature sensor based on the temperature-dependent dielectric behavior of PDCs. The authors found that, with the increasing of temperatures from 25 to 500 ℃, the dielectric constant and loss tangent of the SiCN sample increase from 3.707 to 3.883 and from 0.0038 to 0.0213, respectively. For the SiBCN samples, the dielectric constant and loss tangent increase from 4.817 to 5.132 and from
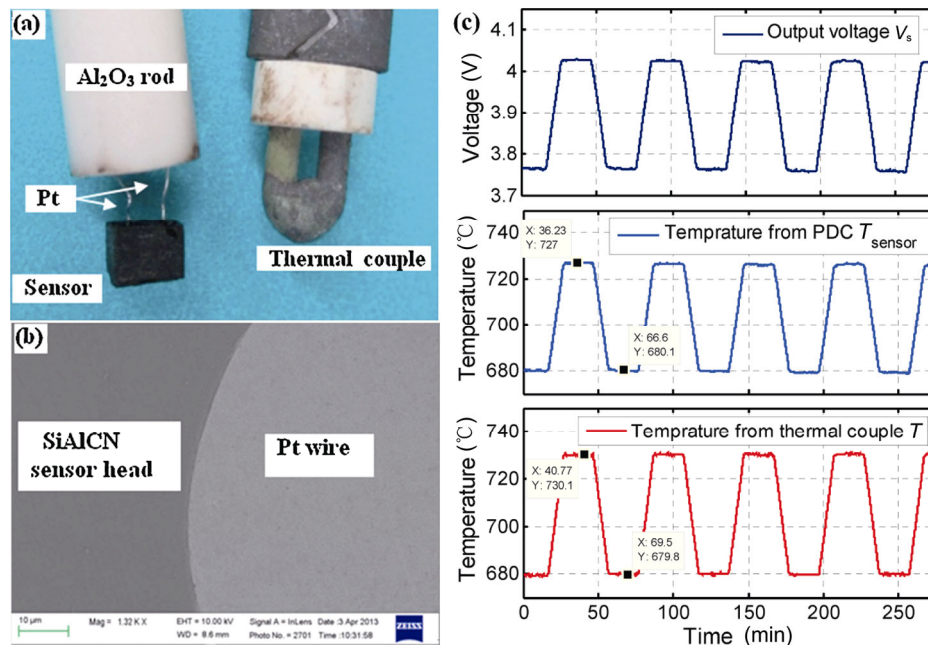
Fig. 15 (a) Photographs of a SiAlCN sensor with seamlessly embedded Pt leads (left) and a commercially available thermal couple used as reference (right); (b) SEM image showing the interface between SiAlCN and Pt leads; and (c) comparison between the temperatures measured by SiAlCN sensor and the commercial available thermal couple. Reproduced with permission from Ref. [366], © The Authors 2014.
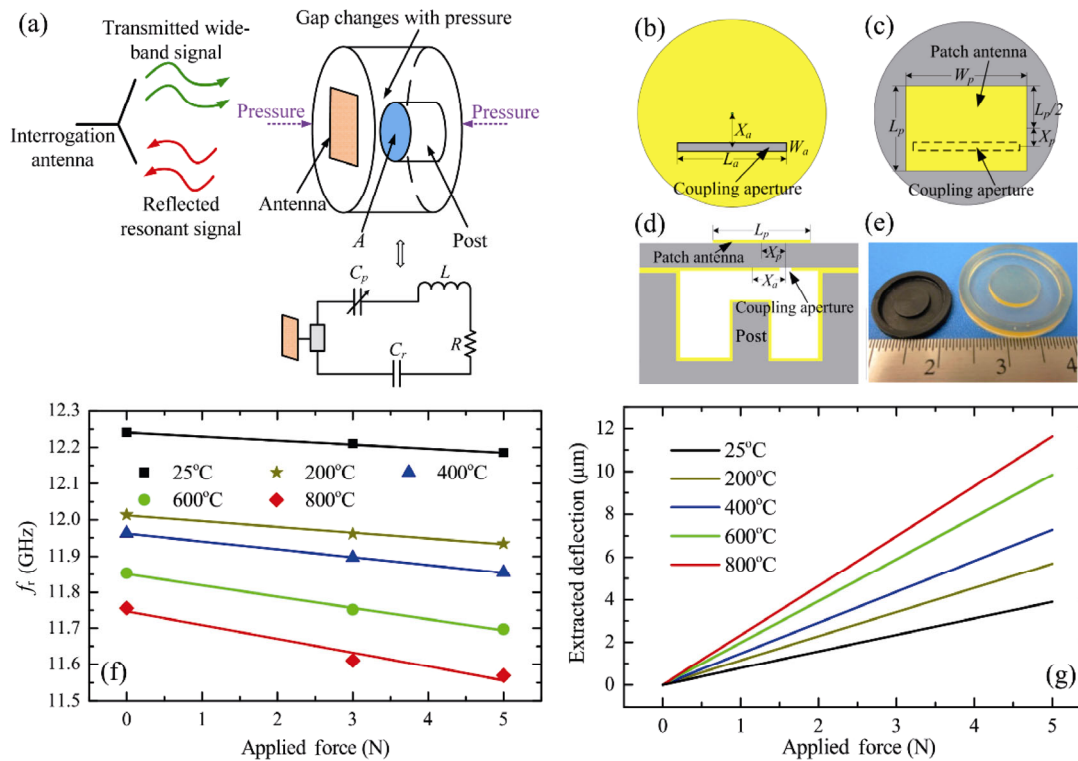
Fig. 16 (a) Schematic and circuit model of the proposed wireless pressure sensor based on an evanescent-mode cavity resonator; (b) and (c) are bottom and top views of the cap of the pressure sensor, respectively; (d) is the cut view of the patch antenna integrated pressure sensor; (e) are photographs of the polymer-derived ceramic cavity resonator before (right) and after pyrolysis (left); (f) measured resonant frequency of the polymer-derived pressure sensor as a function of the applied force at high temperatures; and (g) extracted deflection of the pressure sensor cap as a function of the applied force at high temperatures. Reproduced with permission from Ref. [368], © Elsevier B.V. 2014.

0.0020 to 0.0186, respectively, when the temperatures increase from 25 to 1000 ℃. Importantly, the experimental uncertainties for extracted the dielectric constant and loss tangent values are no more than 0.0004 and 0.0001, respectively [369]. Based on this temperature-dependent dielectric behavior, Li *et al.* [370] developed a passive wireless polymer-derived SiCN sensor consisting of a cavity radio frequency resonator and an integrated slot antenna. The authors demonstrated that the sensor signals can be wirelessly detected at distances up to 20 mm. Despite that the distance is still very short, this is a good start for wirelessly detected temperature in gas turbine engine using polymer derived ceramic sensors.

The studies regarding sensor applications of PDCs have been conducted for several years due to their unique microstructure, tailorable electric properties, excellent thermal stability, high chemical durability, and superior oxidation resistance. However, they are still under development and produced on a laboratory scale. It is really challenging to produce PDC sensors with precisely controllable electric properties which are of crucial importance for their practical applications. This is because the microstructure of PDCs varies with the variation of molecular structures and thermal treatment conditions. The shrinkage of the precursors during polymer-to-ceramic transformation leads to the formation of uncontrollable cracks and pores. Moreover, the carbothermal reduction reaction occurred in SiOC and SiCN systems at high temperature, which makes it hard to densify these ceramics. Therefore, more efforts should be made to recognize and to account for the effects of molecular structure, thermal treatment conditions, microstructure, and chemical/phase compositions on the electric properties of PDCs. A rigorous investigation of the correlations between these factors and the electric properties and performance of PDC sensors should be conducted using advanced technologies to derive a complete understanding of the origins of the high sensitivity of PDC sensors and to produce applicable PDC sensors.

4 Polymer-derived ceramics for electrochemical energy storage

With the advancement of science and technology, development of electrochemical energy storage devices does not only provide us environmentally friendly solutions for driving our world but also greatly facilitates our modern life [371–379]. Among all types of electrochemical energy storage devices, lithium-ion secondary battery becomes a star in the past 30 years. Since a first lithium-based secondary battery had been invented in 1972 until its commercialization in 1990 with $LiCoO_2$ as a positive electrode and carbon black as a negative electrode by Sony Corporation, and then until today, lithium-ion batteries have attracted a lot of attention and are nowadays widely used to power cellphones, laptops, electric vehicles, and other electric devices and in parallel have revolutionized our life [380–385]. Besides lithium-ion batteries, with the growth of application demand and the diversification of the application environment, other electrochemical energy storage and generation concepts like sodium-ion batteries [386–388], lithium sulfur batteries [389–391], supercapacitors [392–394], as well as metal–air batteries [395,396] and fuel cells [397,398] have recently gained momentum for future applications due to their respective characteristics.

All electrochemical energy storage devices are composed of electrodes, electrolytes, and separators. The performance of all those parts affects the electrochemical round-trip device efficiency. To store and release (charge/discharge) energy from a battery, three primary mobilities are involved: electronic transport in the solid state, ionic transport in the liquid and solid state, and molecular (mass) transport. The batteries used today still employ design concepts of Volta and LeClanché [401], which have been known for the last 200 years, although the electrochemical energy storage has experienced enormous transitions. The battery chemistry powering one's laptop has changed from nickel–cadmium (Ni–Cd) to nickel–metal hydride (NiMH) to lithium-ion (typically a graphitic carbon negative electrode versus a lithiated cobalt oxide positive electrode), becoming less environmentally problematic and less heavy. Lithium-ion insertion materials, proposed by Whittingham in the mid-1970s as the active agent in the positive electrode [402], added the first new strategy in decades (if not centuries) to the portfolio of battery-derived

portable power [403]. No perfect combination has been achieved in commercialized or about to be commercialized systems yet due to shortcomings such as electrode decomposition, formation/stability of solid-state electrolyte interface, side reactions, etc., resulting in capacity fading, instability, or safety issues. Thus, developing new multifunctional materials for electrodes, electrolytes, and electrochemical energy storages is imperative to overcome the mentioned issues [404–410]. A comparison of specific energy and specific power of different electrochemical energy storage systems is shown in Fig. 17.

In the past two decades, polymer-derived ceramics (PDCs) have been proved to be advantageous for electrochemical energy storage due to their unique chemical and thermodynamic stability, porosity structure, and decent electronic conductivity and robust, stress accommodating mechanical properties [35,411]. All physical and chemical properties of PDCs are tunable by controlling processing route and parameters or making chemical modification of precursor as demanded by the specific applications [148,412,413].

PDCs have been shown to exhibit an interesting potential for energy storage devices due to their remarkable electrochemical performance. Herein, the development and application of PDCs used for electrochemical energy
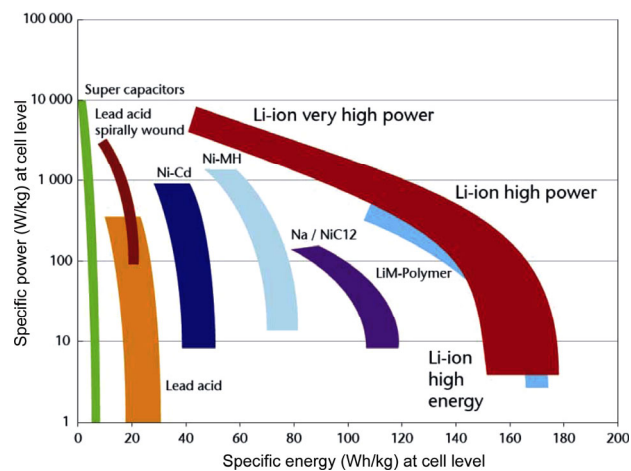
Fig. 17 Specific power versus specific energy of different electrochemical energy storage systems (note: Ni–Cd = nickel–cadmium; Ni–MH = nickel–metal-hydride; Na/NiCl2 = sodium/nickel chloride; LiM–polymer = lithium-metal–polymer; Li-ion = lithium ion; W/kg = watt per kilogram; Wh/kg = watt–hour per kilogram) (source: International Energy Agency, Technology Roadmaps: Electric and Plug-in Hybrid Electric Vehicles, 2009, p. 12. (original source: Johnson Control – SAFT 2005 and 2007)). Reproduced with permission from Ref. [399], © ICE Publishing 2012; Ref. [400].

storage including lithium-ion batteries, sodium-ion batteries, lithium sulfur batteries, metal-air batteries, and supercapacitors are highlighted and discussed.

4.1 Electrode materials in battery systems

4.1.1 Anode materials in lithium-ion batteries

Lithium-ion batteries (LIBs) are widely used in all aspects of our modern life from portable electronic devices to electric vehicles and even to military and space applications due to its high energy density, high voltage, low self-discharge, and no memory effect [414]. Currently graphite with a theoretical capacity of 372 mAh/g is used as anode in the majority of commercial lithium-ion batteries. The capacity of graphite is far from meeting the demand for high performance lithium-ion batteries [415,416]. Lithium dendrites formed during the battery charge are considered as one of the reasons of a decay of battery electrochemical performance [417–421]. The formation of solid electrolyte interphase is another aspect that might cause the capacity fading of graphite anode. It will irreversibly consume lithium ions and increase the internal impedance of electrode. Introducing stabilizers and robust electrolytes as well as temperature treatment are the effective methods to improve to a certain extent the stability of the solid electrolyte interface (SEI) and to avoid the exfoliation of graphite layer [422–428]. Silicon is a promising candidate to replace graphite due to its extraordinary high theoretical capacity of approximate 3600 mAh/g which is almost 10 times higher as compared with a graphite anode, its low discharge potential (0.5 V versus Li/Li$^+$) and abundance. Nevertheless, ~300% volume expansion of silicon during lithiation and an accompanying phase transformation causes pulverization of the material and detachment of the electrode, thus leading to a fast fading of capacity and low coulombic efficiency. Although many solutions for enhancing the electrochemical performance of Si-based anode such as nanosizing of Si and Si-conductive coating composites have been addressed, from a commercial and practical point of view, only anodes with a little fraction of elemental silicon (up to 10 wt%) present a stable electrochemical behavior [429–433].

Si-based PDCs materials namely SiOC and SiCN gained extensive attention as anode materials in LIBs since their unique temperature-dependent amorphous microstructure at relatively low pyrolysis temperatures

(up to 1100 ℃ for SiOC and up to 1300 ℃ for SiCN) under an inert or reactive atmosphere. Crystallization up to around 1300–1500 ℃ can be resisted due to the graphene-like sp^2 bonded carbon network atoms located at the boundary of tetrahedral nanodomains of silicon. This character results in an excellent chemical and thermodynamic stability, elevated electrical conductivity (6×10^{-3} S/cm), as well as robust mechanical properties. Moreover, remarkable studies have demonstrated that PDCs can reversibly accommodate Li in a potential range of 0–3 V with high electrochemical capacities up to 900 mAh/g and coulombic efficiencies over 99% [411]. All these benefits make PDCs promising candidates for anodes in LIBs. Besides, all above properties including porosity can be easily adjusted by chemical modification of the preceramic polymer and by tunable parameters during the polymer-to-ceramic transformation [179,434–436].

Polymer-derived SiOC LIB anode was firstly reported by Wilson *et al.* in 1994 [438]. This work reveals that a polymer-derived SiOC pyrolyzed from siloxane polymers can reversibly intercalate lithium ions at potentials lower than 1 V with a specific capacity of 600 mAh/g. The study of the effect of processing temperature on the cycle stability of SiOC anode demonstrates the lowest first cycle loss and
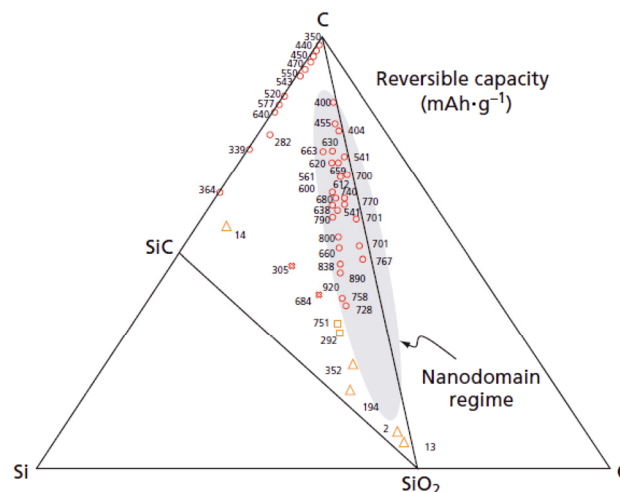

Fig. 18 SiOC compositional triangle. The numbers indicate the reversible capacity of the SiOC anode material depending on the composition. The highest capacity values are found for compositions containing mixed Si bonds (grey area) where silicon is tetrahedrally bonded to oxygen and carbon. Reproduced with permission from Ref. [399], © ICE Publishing 2012; Ref. [437].
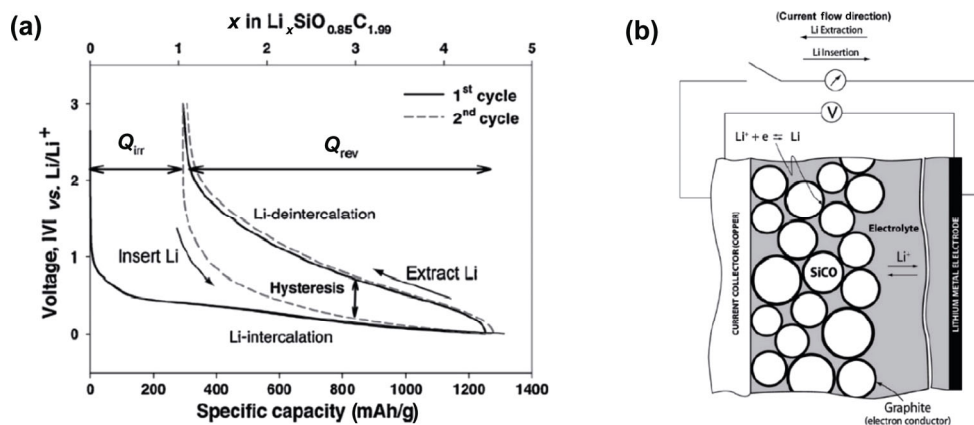
Fig. 19 (a) Insertion and extraction of lithium into polymer-derived SiOC and (b) a scheme of the microstructure of the SiOC electrode during cycling. Reproduced with permission from Ref. [444], © Elsevier B.V. 2010.

highest reversible capacity for samples pyrolyzed at 1000 ℃. The further works of Dahn's group focused on the effect of the chemical composition on the electrochemical performance of more than 60 different SiOC materials, with the composition of 14% Si and 80% C revealing the best electrochemical performance [437]. While those works focused on the impact of the elemental composition on the electrochemical behavior, the mechanism of lithium storage and lithium transport have not been addressed in detail [439–443].

Refs. [445–447] claim that the major lithiation site is the mixed bond configuration (tetrahedrally coordinated silicon from SiC_4 via SiC_3O, SiC_2O_2, and $SiCO_3$ to SiO_4). The reversible capacity of the specimen with mixed bonds of C, SiO_2, and SiC in SiOC compositional triangle is presented in Fig. 18. At the same time, the study of Ahn and Raj [444] describes the lithiation and delithiation process in SiOC as shown in Fig. 19. A hysteresis at a polarization potential between 250 and 500 mV is demonstrated by a coulometric titration technique [444]. It is a result of kinetics and thermodynamic limitations of the diffusion of Li ions at the surface of electrode and electrolyte. In contrary to these findings, Fukui *et al.* [448,449], Graczyk-Zajac *et al.* [450,451], Dibandjo *et al.* [52], Knozowski *et al.* [436,452], Kaspar *et al.* [453,454], Wilamowska *et al.* [455], and Pradeep *et al.* [456,457] demonstrated that the carbon phase is the major Li-ion storage host site. It has been shown that lithium is accommodated in interstitial and defect sites, edges of graphene sheets, and adsorbed on the interface of graphite nano-crystallites. ^{7}Li MAS NMR (nuclear magnetic resonance) measurements were applied to confirm that the carbon phase is the host site for

lithium storage by Fukui *et al.* [449] and Haaks *et al.* [458]. Sun and Zhao [459] investigated the atomistic origin of the performance of carbon-rich SiOC by first-principles theoretical approach, which demonstrates a two-step process of lithium insertion: (1) Li ions diffuse into nano-voids followed by (2) accommodation of the Li ions in the SiOC matrix and in the segregated carbon network. The atomistic model of SiOC and the overview of the supercell are presented in Fig. 20.

Kaspar *et al.* [460] investigated a polyorganosiloxane-derived SiOC anode pyrolyzed at temperatures from 900 to 2000 ℃ and demonstrated that the reversible capacity decreases with the rise of pyrolysis temperature and formation of crystalline SiC at temperatures exceeding 1200 ℃ (660 mAh/g for 900 ℃ to 80 mAh/g for 2000 ℃). The effect of the electrical conductivity on the capacity of SiOC was also investigated by Kaspar *et al.* [453], revealing that (1) a low carbon content exhibits high initially capacities but fading rapidly during cycling and (2) a carbon content beyond 20 wt% is beneficial for the conductivity and cycling stability.

Porous SiOC materials have also been investigated as materials for Li-ion batterie by various researchers. Dibandjo *et al.* [52] made a comparison between dense and porous SiOC anodes and found that the porous sample exhibits enhanced stable electrochemical performance. Pradeep *et al.* [457] synthesized a linear polysiloxane cross-linked with divinylbenzene (DVB) by hydrosilylation reaction catalyzed by Pt. After pyrolysis at 1000 ℃ under argon, the obtained porous SiOC with 180 m^2/g of specific surface area exhibits a high specific capacity over 600 mAh/g due to the porous structure providing enough fast ionic transport
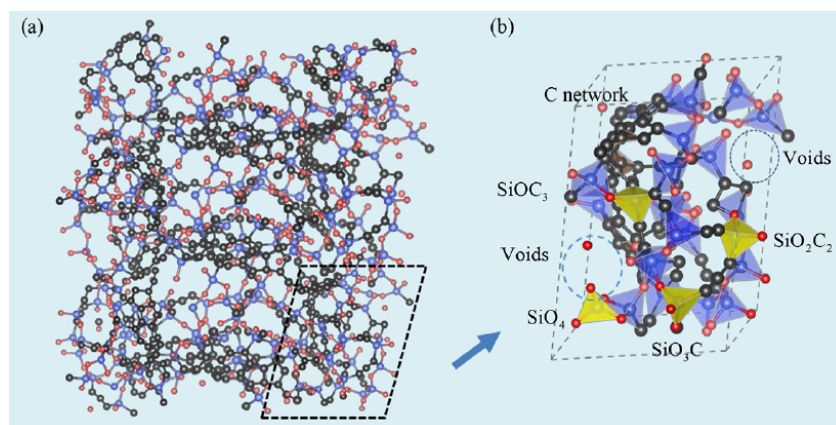
Fig. 20 Atomic model of SiOC. (a) Overview of the supercell; (b) unit cell shows a series of vertex-sharing tetrahedra (blue atoms: silicon atoms; red atoms: oxygen atoms; gray atoms: segregated carbon phase which forms the backbone of the network; blue dotted circles represent the nanovoids percolated in the lattice which contribute to the low density of the SiOC molecule). Reproduced with permission from Ref. [459], © American Chemical Society 2017.

paths and accommodating the structural changes during lithiation/delithiation. Fukui *et al.* [461] also developed a microporous SiOC composite material by pyrolyzing a blend of polysilane, $(Ph_2Si)_{0.85}(PhSi)_{0.15}$ (1) and polystyrene (1:1 in weight) at 1000 ℃, which shows a remarkable capacity of 600 mAh/g and a good cycle stability. Xia *et al.* [462] studied the impact of etching SiOC by KOH and found improved specific surface area of the material and enhanced electrochemical performance of the anode. Sang *et al.* [451,463] reported SiOC nanolayers wrapped 3D interconnected graphene sponge with deliberate porous mutli-layered sandwich-like structure, which shows a high initial discharge capacity (1280 mAh/g at 0.1 A/g) and high stability (701 mAh/g) after 100 cycles due to its improved electrical conductivity, accelerated ion insertion and endowed full utilization of active sites of lithium storage.

By introducing hydrogen during pyrolysis of polysiloxane precursors, the impact of pyrolysis atmosphere on SiOC was studied by Pradeep *et al.* [464]. It was found that 5% of H_2 admixture to the argon lead to a decreasing of the carbon content from 55.15 to 46.37 wt% and to an enhanced initial capacity from 568 to 704 mAh/g and coulombic efficiency from 63% to 67%. Shen and Raj [465] deposited thin films anodes of SiOC on copper with around 0.5–5 μm thickness which shows a capacity of 1100 mAh/g and a high efficiency of approximately 99%. The highlight of this material is a facile preparation method and lower cost due to lack of binder and conductive additive. Dong *et al.* [466] synthesized hard SiOC microbeads

by emulsifying cross-link and subsequent pyrolysis for anode and investigated its electrochemical performance. This processing approach enhanced the structural stability of the material leading to a discharge specific capacity of 805 mAh/g achieved after 300 cycles. Nitrogen-doped carbon fibers were also studied with SiOC as the matrix by Ma *et al.* [467]. The unique 3D conductive network and the existence of nitrogen result in improved electronic conductivity and electrochemical active sites of SiOC. Lim *et al.* [468] developed a novel silicone oil-derived SiOC anode by controlling free-carbon domain, which exhibits remarkable electrochemical performance including reversible capacity (550 mAh/g at 200 mA/g), cycle stability (95% capacity retention after 200 cycles at 200 mA/g). A polymer derived SiOC integrated with graphene aerogel was prepared by Shao *et al.* [469] via solvent assisted infiltration. The sample comprised of 19.8 wt% graphene in the SiOC matrix achieved the highest level of performance that the capacity retention was around 95% after 1000 cycles at a high current density of 1480 mA/g and over 99% of efficiency.

Blending SiOC with high-capacity elements like silicon or tin leads to a significant improvement of the electrochemical performance of the composite electrode. Silicon oxycarbide/tin nanocomposites (SiOC/Sn) were prepared via chemical modification of polysiloxane with tin(II)acetate and subsequent pyrolysis at 1000 ℃ by Kaspar *et al.* [112]. The obtained material demonstrates high initial capacity and excellent cycle stability. Kaspar *et al.* [470] also studied silicon oxycarbide/ nano-silicon composites and addressed the effect of the
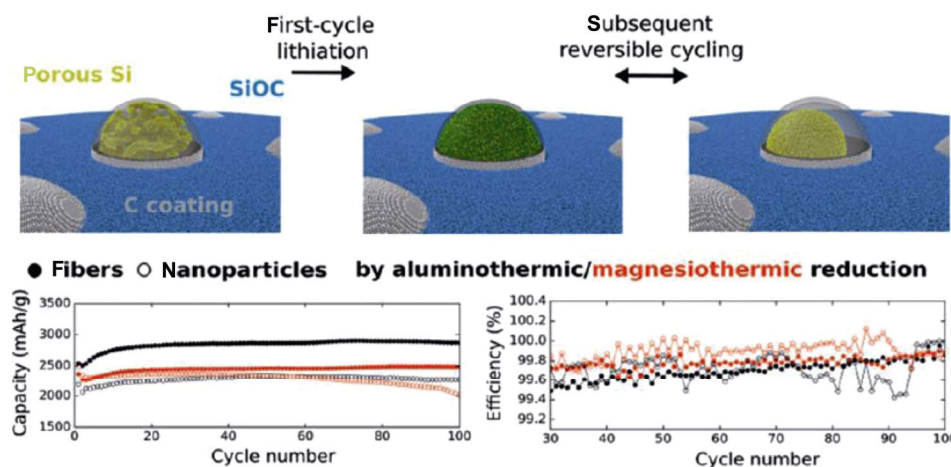
Fig. 21 Schematic diagram of mechanism of lithiation/delithiation of porous nano Si in a C/SiOC matrix and its electrochemical performance. Reproduced with permission from Ref. [110], © American Chemical Society 2017.

silicon crystallinity on the performance of the anode. These results show that composites of SiOC and crystalline Si exhibit higher, but faster decay capacity (905 mAh/g of reversible capacity) while the composite of SiOC and amorphous Si exhibits a lower reversible capacity of 704 mAh/g but a stable cycling property up to 100 cycles, which can be explained by the microstructural integrity of the composite comprised of SiOC and amorphous Si. Highly porous silicon embedded into a ceramic matrix has been designed and synthesized by Vrankovic *et al.* [110]. As shown in Fig. 21, the prepared material achieved a capacity of 2000–3000 mAh/g normalized to the amount of Si and above 99.5% coulombic efficiencies as well as almost 100% capacity retention after 100 cycles. The remarkable cycle stability is attributed to the porous structure of Si and the uniform ceramic networks which can effectively suppress the volume expansion of silicon and provide sufficient conductive paths. Xia *et al.* [471] studied the effect of $SnCl_2$ addition on the structure on the performance of SiOC anode by the synthesis of Sn/SiOC composites with varying Sn content via a sol–gel process. With the rise of the Sn content, the rate capability of Sn/SiOC composites increases first to a certain value but then decreases. A SiOC–Sb nanocomposite was fabricated by Dubey *et al.* [472]. The obtained material shows charge storage capacities within a range of 549–703 mAh/g under a current density of 74.4–2232 mA/g. ^{29}Si and ^{7}Li NMR measurements demonstrate that the introduction of Sb in SiOC matrix decreases the amount of free C in the SiOC matrix, resulting in different lithium-ion storage sites.

For polymer-derived SiCN anode, polysilazane-derived SiCN ceramics used as anode were described by Zank *et al.* [473] firstly in a patent in 1997 which shows that SiCN ceramics have reversible discharge capacities up to 560 mAh/g. SiCN materials were further suggested to be applied as a solid electrolyte by Liebau-Kunzmann *et al.* [474]. This work demonstrates the preferential formation of Li–N bonds in lithiation process which exhibits potential of SiCN for anode in LIB. Su *et al.* [475] investigated pure polymer-derived SiCN materials by pyrolyzing polysilylethylendiamine at 1000–1300 ℃. The obtained SiCN shows a discharge capacity of 754.9 mAh/g and an initial coulombic efficiency of 60.4%. However, fast capacity fading occurred in the subsequent cycles. To solve the issue, Feng [476] applied an additional heat treatment to the SiCN material, resulting in an enhanced discharge capacity and cycle stability. Carbon-rich SiCN materials have been extensively studied by Kaspar *et al.* [477], Graczyk-Zajac *et al.* [478], and Reinold *et al.* [479]. Their studies reveal that the presence of a free carbon phase improved the electrochemical performance significantly, and the molecular structure of the pre-ceramic polymer affects the electrochemical performance of the final material. Liu *et al.* [480] found that the chemical modification with divinylbenzene (DVB) can effectively increase the carbon content which is beneficial for a higher capacity of polyorganosilazane-derived SiCN from 136 to 574 mAh/g. Solid state NMR investigation realized by Baek *et al.* [481] shows that free carbon phase is a main storage site of lithium in the SiCN ceramics. Hard-carbon containing SiCN composites exhibiting

an excellent performance under high current density were investigated by Wilamowska *et al.* [482]. Graczyk-Zajac *et al.* [483,484] further investigated the lithium storage mechanism of the disordered hard-carbon SiCN by Raman spectroscopy and ^{7}Li MAS NMR. This study reveals that the adsorption-like process in disordered carbon is to a significant extent responsible for lithium storage in composites and more than 33% of lithium in the hard-carbon SiCN is adsorbed in ionic form at the surface and in pores of the composite. Feng *et al.* further studied the capacity fading mechanism of SiCN by using different poly-silyl-carbodiimides as precursor. They demonstrated that stable SEI layers and abundant free carbon result in excellent electrochemical performance. The composites of SiCN/graphite and SiCN/silicon also demonstrated improved electrochemical performance if compared with pure graphite and silicon, respectively [111,479–483,485]. Storch *et al.* [486] investigated the effect of the pyrolysis temperature on the electrochemical behavior of porous carbon-rich SiCN composite. This work shows that the sample pyrolyzed at 900 ℃ delivers a high initial charge capacity of 447 mAh/g and a capacity retention of 534 mAh/g after 100 cycle at a current of 72 mA/g.

Rohrer *et al.* [487] addressed various approaches regarding the stabilization of silicon and tin containing anodes embedded in a SiOCN matrix. In a review of Graczyk-Zajac *et al.* [435], irreversible and reversible lithium storage within SiOC and SiCN ceramics were discussed. Their results are as follows: (1) The first cycle discharge/charge capacities of SiOC materials nearly do not depend on the amount of free carbon. On the contrary, the capacity of SiCN increases with the amount of carbon and reaches a threshold value at around 50%. (2) Replacing O with N decreases the lithium storage capacity. Due to the more ionic character of Si–O bonds, lithium is more captured by O, which leads to a very high initial lithiation capacity even at low C content. (3) The more covalent character of Si–N bonds and lower electron density on the nitrogen atom result in less capture of Li in the ceramic matrix if O is replaced by N, thus leading to lower electrochemical performance of the anode of the LIB. Figures 22 and 23 show the dependence of the lithiation/delithiation capacity of SiOC- and SiCN-anode materials on the amount of free carbon and SiOC matrix or SiCN matrix, respectively. The results of this work also provide a reference for designing the optimal composition of PDC-based anode material.
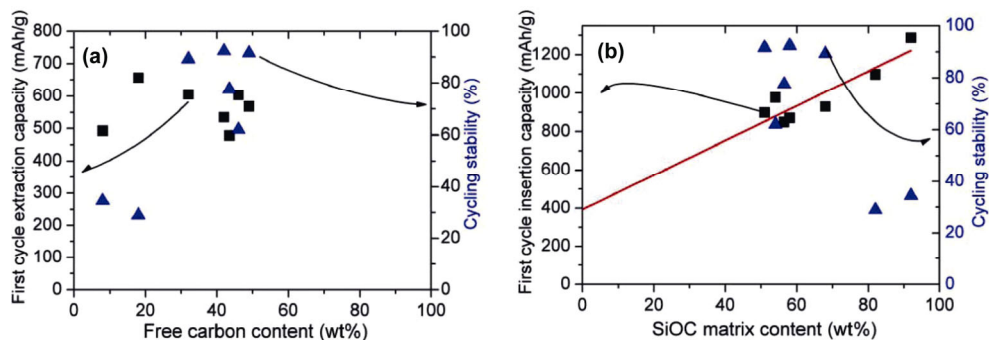
Fig. 22 Dependence of the lithiation/delithiation capacity of SiOC-derived materials on the amount of free carbon (a) and on the amount of SiOC matrix (b). Reproduced with permission from Ref. [435], © the authors 2015.
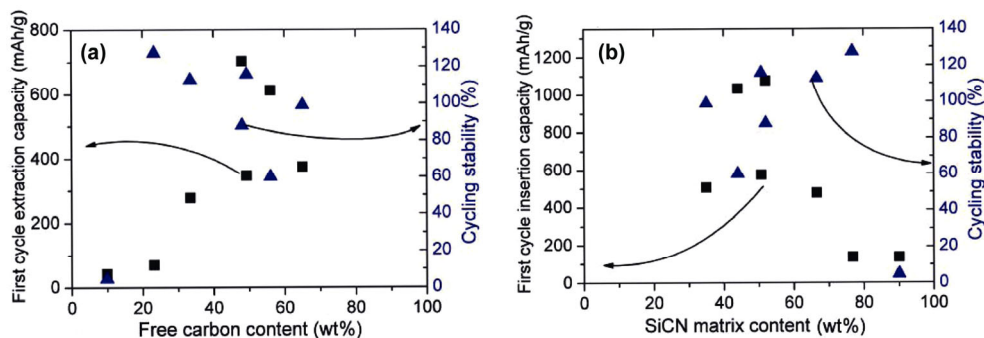
Fig. 23 Dependence of the lithiation/delithiation capacity of SiCN-derived materials on the amount of free carbon (a) and on the amount of SiCN matrix (b). Reproduced with permission from Ref. [435], © the authors 2015.

Despite many advantages, PDC anodes reveal one important drawback, namely a low coulombic efficiency which leads to lower economic benefits compared with commercial graphite anode. Thus, PDC anode is not the mainstream research direction up to now.

4.1.2 Cathode materials in lithium-based batteries

Li–S batteries are promising candidates for electrode materials for electrochemical energy storage devices due to their superior theoretical capacity of 1675 mAh/g and abundant resources as well as low cost. Nevertheless, "shuttle effect" and low conductivity of $5×10^{-28}$ S/m and volume expansion of 80%, result in fast capacity fading and low coulombic efficiency and seriously hinder their technical application [391,488]. Anode materials with sulfur dispersed in an electrically conducting microporous SiOC and porous carbon-rich SiCN ceramic matrix exhibit decreased "shuttle effect" and enhanced electrochemical performance. Weinberger *et al.* [489] synthesized highly microporous submicrometric carbon spheres by etching of a sol–gel derived SiOC, which has 0.63 cm^3/g of total pore volume that can accommodate sulfur for cathode. This composite

owns good cycle stability at a high current density of 500 mA/g, and the capacity retention is as high as 241 mAh/g up to 100 cycles and coulombic efficiency is close to 100% just after several cycles. The impact of the morphology of C-rich silicon carbonitride ceramic on the electrochemical performance was investigated by Qu *et al.* [490] via tunable pyrolysis temperature from 1000 to 1600 ℃. A schematic diagram of carbon-rich SiCN/S composite anode preparation is presented in Fig. 24. Their work demonstrates that C-rich SiCN ceramic matrix exhibits improved conductivity and stable cycling property because of the abundant free carbon phase. Best electrochemical performance has been identified for the sample pyrolyzed at 1000 ℃ with 66 wt% of sulfur loading in the composite.

Li–Se batteries are another promising candidates of high-capacity batteries due to the superior theoretical volumetric capacity of Se with 3253 mAh/cm^3 (based on density of 4.82 g/cm^3), and their substantial electrical conductivity (20 times that of sulfur) [491]. However, inferior cycle stability and low coulombic efficiency caused by poor structural stability and sluggish lithiation reaction kinetics of a Se cathode
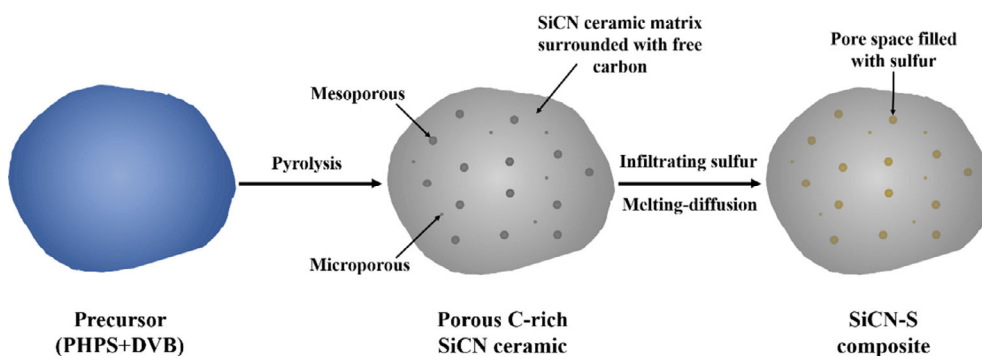
Fig. 24 Schematic diagram of carbon-rich SiCN/S cathode preparation. Reproduced with permission from Ref. [490], © Elsevier Ltd. 2021.
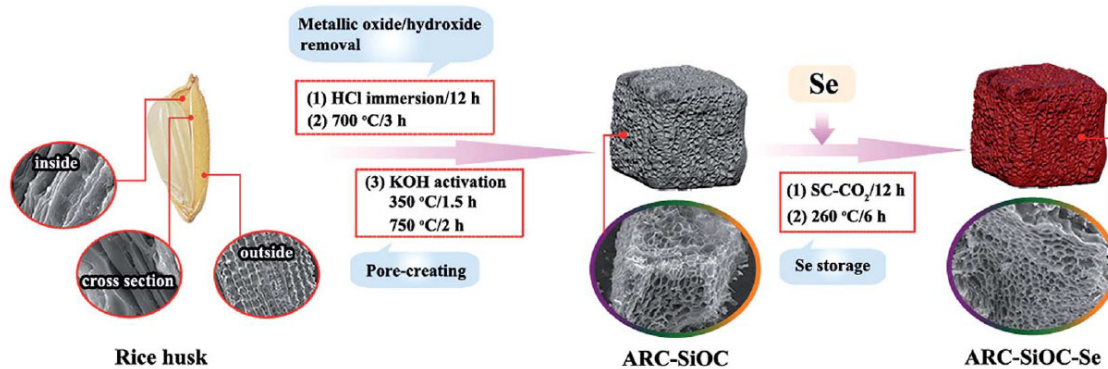
Fig. 25 Schematic of the synthesis of 3D porous SiOC/Se composite (ARC–SiOC = active rice husk carbon–SiOC matrix). Reproduced with permission from Ref. [491], © The Royal Society of Chemistry 2018.

hamper the practical application of Se cathodes [492,493]. Fang *et al.* [491] developed a SiOC/Se cathode derived from rice husks by a bio-templating method with the assistance of a supercritical CO_2 technique. A schematic of the synthesis of 3D porous SiOC/Se composite is presented in Fig. 25. The obtained 3D porous SiOC/Se cathode shows extremely high first areal capacity (8.1 mAh/cm^2 at 0.1 C) with a high Se loading (8 mg/cm^2) and remarkable capacity retention. The excellent properties are attributed to the unique 3D porous conductive network and SiOC units set in the porous carbon matrix, resulting in continuous electron/ion transport pathways as well as enhanced structural stability. Besides, trapping Se and Li_2Se by strong chemical adsorption and uniform distribution of infiltrated Se were also confirmed.

4.1.3 Anode materials in sodium-ion batteries

Due to the high abundance and low cost of sodium, combined with its low redox potential of −2.71 V (Na^+/Na) versus the standard hydrogen electrode, which is only 0.3 V above the one of Li^+/Li, sodium-ion batteries (NIBs) hold much promise for large-scale energy storage application. However, NIBs are less explored than Li-ion batteries and research for promising electrode materials is still a fundamental concern [494,495].

For Li-ion batteries, graphite is the most prominent anode material, because storing Li-ions by the reversible intercalation between their basal-planes and without structural degradation is possible. For Na-ions the overall thermodynamic balance is unfavorable and sodium forms graphite intercalation compounds to only a very limited extent [496]. Alternatively, non-graphitic disordered carbons have been intensively explored as potential anodes for reversible sodium storage. Stevens and Dahn [497] studied glucose-derived hard-carbon as NIB anode, providing a high reversible storage capacity of 300 mAh/g, but at relatively slow cycling current of C/80 with reference to NaC_6 stoichiometry. Significant improvement was achieved by Wenzel *et al.* [498], who investigated template prepared porous carbons, providing enhanced reversible capacity of 100–130 mAh/g at higher current rates of C/5–5C. However, the major drawback related to most disordered carbons is their weak cycling stability, serious capacity fading upon prolonged cycling, and a low-potential sodium insertion leading to a risk of the formation of dendritic plating. So far it is assumed that

storage of Na-ions within disordered carbon occurs similar to that of lithium, namely major storing sites are the edges of carbon and graphene layers, defect sites and micropores. However, this hypothesis has not been proven yet. Moreover, the experimental data [495,499,500] show that no direct analogy can be drawn between the storage performances of disordered carbons with respect to these two cations. In other words, the carbonaceous materials which fail in lithium storage can appear to be stable and reversible sodium hosts, while the materials which perform very well with respect to lithium ions might not be suitable to host sodium. Until now, this problem has not been analyzed in detail yet.

In recent years, PDC materials have been widely studied for application in LIBs due to their remarkable electrochemical properties and chemical and mechanical stability. However, until now only few studies pay attention to the utilization of PDCs in NIBs. Kaspar *et al.* [501] studied for the first time a SiOC(N)/hard carbon composite as anode material for NIBs with a focus on the influence of morphology of ceramic matrices on the electrochemical performance. They found a strong correlation of the electrochemical performance, porosity, and elemental composition of the SiOC(N) anode. For hard carbon of microporous nature, the addition of SiOC effectively enhanced the capacity from 44 to 201 mAh/g. A Sb-embedded SiOC anode was prepared by Lee *et al.* [502] by a "one pot pyrolysis" process at 900 ℃. Owing to the existence of free carbon, the composite shows a first desodiation capacity of about 510 mAh/g and a distinguished capacity retention over 97% even after 250 cycles. Kim *et al.* [503] also developed a free-carbon containing Sb/SiOC composite where the Sb nanoparticles are uniformly embedded in the ceramic matrix. This material yields 344.5 mAh/g of capacity retention after 150 cycles at 0.2 C and outstanding rate properties (197.5 mAh/g at 5 C) due to the presence of free carbon domains. Chandra and Kim [504] produced a SiCN material from silicone oil as anode for NIBs. The obtained sample calcined at 900 ℃ exhibits a remarkable reversible capacity of 160 mAh/g at 25 mA/g after 200 cycles and a high-rate performance. It is worth mentioning that the capacity decay of each cycle amounts only 0.09 mAh/g during 650 cycles. Chandra *et al.* [505] also investigated the mechanism related to Na ion storage in SiOCs by *ex situ* measurements and density functional theory simulations.

Their work reveals that the storage of Na ions mainly occurs in micropores, defects, and C-rich and O-rich ceramic phases. A functionalization of SiOC with MoS_2 is reported by Soares and Singh [117]. The MoS_2–SiOC composite anode exhibits an effectively improved cycle stability over 100 cycles. Another nitrogen-doped MoS_2/SiOC composite with hierarchical structure is prepared by Lim *et al.* [506]. Due to the enlargement of interspace and improved electronic conductivity as well as mechanical property, the hierarchical nitrogen-doped MoS_2/SiOC composite achieved a facile reversible cycle of Na ions during the operation of the battery, namely 540.7 mAh/g of reversible capacity and almost 100% of capacity retention, also including excellent rate capability at 10 A/g. Putra *et al.* [507] studied SiOC–graphene composites pyrolyzed from silicone oil and demonstrated their excellent performance. They also studied the effect of fluorinated ethylene carbonate in the electrolyte on the electrochemical performance. Chandra *et al.* [508] proposed a new strategy that synthesizes C- and O-rich SiOC composites by pyrolyzing C-rich precursor under H_2/Ar. The obtained SiOC delivered a high reversible capacity (234 mAh/g at 25 mA/g) and 160 mAh/g of reversible capacity after 140 cycles.

4.1.4 Anode materials in potassium-ion batteries

Practical application of potassium-ion batteries is significantly limited due to the large ionic radius of K, which causes a low ion diffusion rate and a huge volume expansion during insertion reaction. Nevertheless, potassium-ion batteries show a high energy density in line of material abundance as well as low cost [509]. Sang *et al.* [510] designed and prepared bi-continuous and nano-porous carbon spheres with continuous nanocarbon matrices and interconnected nanopores by etching carbon-rich SiOC ceramics. The achieved sample shows a high first reversible capacity (336 mAh/g at 0.1 A/g) as well as long cycle life and high-rate properties (191 mAh/g after 2000 cycles at 0.5 A/g) rationalized by the interconnected nanostructure, defective nature of carbon framework, and various oxygen-containing functional groups introduced after etching.

4. 2   Electrode materials in supercapacitors

Supercapacitors are electrochemical energy storage devices, necessary where the power requirement predominates the energy requirement. They are usually not constrained by ionic diffusion kinetics experienced in batteries and can run for a large number of cycles ($\sim 10^6$) at high charge and discharge currents. Nevertheless, the energy density of supercapacitors is usually limited by a specific surface aera of the electrode materials in practical applications, whereas the rate capability is affected by the insufficient electronic conductivity of the porous electrode [511–513]. Therefore, the choice of appropriate electrode materials is of importance to provide a sufficient device performance. Figure 26 shows a schematic of a supercapacitor containing porous electrode materials. Supercapacitor electrodes require high specific surface area and high electric conductivity in line with a good corrosion resistance, high temperature stability, controlled pore structure, processability and compatibility in composite materials, and a relatively low cost. All those properties can be easily obtained via effective tuning of polymer precursor of PDCs, what makes these ceramics a potential candidate for use in supercapacitors. Table 4 summarizes the electrochemical performance of various PDCs studied as electrodes in supercapacitors.

Equations (3) and (4) describe the relationship between the energy, power, and capacitance of a supercapacitor:

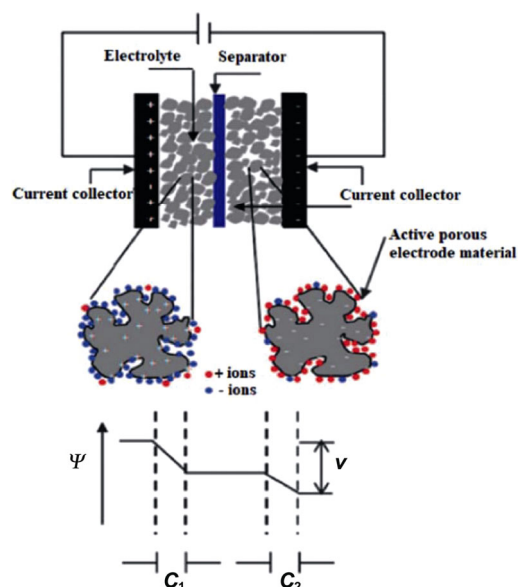Energy: $$W_{max} = \frac{1}{2} \times C_{total} \times U_{loaded}^2 \qquad (3)$$

Fig. 26   Schematic of porous electrode materials used in a supercapacitor. Reproduced with permission from Ref. [392], © The Royal Society of Chemistry 2009.

Table 4   **Electrochemical performance of PDC electrodes used in supercapacitors**

Specimen	Capacitance	Power density	Specific surface area	Capacity retention	Reference
SiOC	—	156 kW/kg	3.2 m^2/g	90% (75,000 cycles)	Halim *et al.* [118]
SiOC	78.93 F/g	—	—	86% (185 cycles)	Abass *et al.* [514]
SiOC	16.71 F/g	15 kW/kg	—	92.8% (5000 cycles)	Pazhamalai *et al.* [515]
SiOC	50 F/g	—	—	100% (2000 cycles)	Mujib *et al.* [516]
SiOC	243.3 F/g	—	1376 m^2/g	87.3% (5 mV of scan rate)	Kim *et al.* [517]
SiOC	27.2 mF/cm^2	9.3 kW/cm^2	—	90% (1000 cycles)	Oroanyanwu *et al.* [518]
S(B)iCN	269.52 F/g	—	—	124.60 F/g (1000 seconds test at 5 A/g)	David *et al.* [119]
SiCN	188 mF/cm	—	—	52.23 mF/cm^2 (1000 cycles at 5 mA/cm^2)	Reddy *et al.* [120]
SiCN	39 F/g	—	—	Almost 100% (7000 cycles)	Moyano *et al.* [519]

Power:
$$P_{max} = \frac{1}{4} \times \frac{U_{loaded}^2}{R_i} \qquad (4)$$

where C_{total} is the total capacitance, U_{loaded} is the voltage applied, and R_i is the internal DC resistance

4.2.1   SiOC electrodes in supercapacitors

Halim *et al.* [118] prepared a low-carbon SiOC composite by pyrolyzing silicone oil under argon in a temperature range from 700 to 1000 ℃. A pseudocapacitive behavior of the composite was confirmed by subsequent characterizations and the material demonstrated a power density of 156 kW/kg and maintained over 90% of energy density retention after 75,000 cycles. A SiOC composite with embedded boron nitride nanotubes and reduced graphene oxide was described by Abass *et al.* [514]. Their material exhibits high specific capacitance of 78.93 F/g at 1 A/g and a great cycling retention corresponding to 86% after 185 cycles, revealing that the presence of boron nitride nanotubes in the ceramic matrix affects the free carbon phase. Pazhamalai *et al.* [515] studied the carbothermal preparation of SiOC lamellae by using two-dimensional siloxene sheets and alginic acid as precursors for supercapacitors. The obtained sample shows a remarkable capacitance of about 16.71 F/g and an energy density of 20.89 Wh/kg as well as a power density of 15 kW/kg by a voltage window of 3.0 V due to its lamella-like SiOC nanostructure. Mujib *et al.* [516] investigated the electrochemical performance of SiOC ceramic fiber mats as electrodes for supercapacitors. The materials were fabricated by electrospinning which show a high splendid capacitance of 50 F/g with capacity retention around 100% after 2000 cycles. The obtained result demonstrated that higher pyrolysis temperature and longer pyrolysis time facilitate enhanced

electrochemical performance. Kim *et al.* [517] investigated the effect of surface oxygen functional group on the performance of porous SiC used as supercapacitor electrode. The porous SiC flakes with a high surface area of 1376 m^2/g were obtained by one-step carbonization of Si flakes and exhibit a high specific capacitance of 243.3 F/g at a scan rate of 5 mV/s and 85.6% of rate performance from 5 to 500 mV/s. Oroanyanwu *et al.* [518] studied SiC/SiOC/C nanocomposites fabricated via flash photothermal pyrolysis of cross-linked blend of polycarbosilanes and polysiloxanes. The prepared nanocomposites are thermally and oxidatively stable and show a capacitance as high as 27.2 mF/cm^2 at a scan rate of 10 mV/s at room temperature as well as excellent stability up to 1000 cycles.

4.2.2   SiCN electrodes in supercapacitors

David *et al.* [119] synthesized a boron-doped SiCN/carbon nanotube/graphene composite paper by vacuum filtration and thermal reduction for using as supercapacitor electrode. The composite paper delivers a high specific capacitance of up to 269.52 F/g at 5 A/g and a low ohmic resistance due to the unique self-supporting structure. Reddy *et al.* [120] reported high-performance hierarchical SiCN nanowires (diameter: 23–37 nm) used for supercapacitors. These nanowires show a capacitance of 188 mF/cm at a current density of 5 mA/cm. Another composite with SiCN matrix and embedded reduced graphene oxide was studied by Moyano *et al.* [519]. Their work showed that the obtained composite reaches a capacitance of 39 F/g and remains stable after 7000 cycles due to the characteristic hybrid cellular structure. Table 4 shows the electrochemical performance of electrodes prepared from PDCs used in supercapacitors.

4.2.3 SiOC as precursors for porous carbon as electrodes in supercapacitors

SiOC-derived carbons from a polyphenylsilsequioxane precursor prepared by Meier *et al.* [520] via pyrolysis and chlorination at different temperatures have large surface areas exceeding 2000 m^2/g and pore volume reaching to 1.4 cm^3/g, thus resulting in a considerable capacitance of 110 F/g and stable cyclability. Duan *et al.* [521] reported on micro/mesoporous SiOC derived carbons fabricated by chlorination and ammonia treatment of polymethyl(phenyl)siloxane. The obtained material shows a high specific capacitance up to 148.7 F/g as well as good capacitance retention around 94.3% after 2000 cycles at 1 A/g. Electrospinning and electrospraying were applied by Tolosa *et al.* [522] to form a SiOC-derived porous nano carbon as electrode for supercapacitors. Extremely high specific surface area up to 2394 m^2/g was achieved, leading to a high specific capacitance of 135 F/g at 10 mV/s and 63% of the capacitance retention at 100 A/g. Yang *et al.* [523] developed an ultra-high-surface-area meso-/microporous carbon by a new *in-situ* template method realizing an ultra-high specific surface area of 3122 m^2/g and large pore volume of 2.47 cm^3/g. Figure 27 shows the synthesis of polysiloxane-derived highly mesoporous carbon via NaOH etching and activation. The fabricated material exhibits a high energy density of 42 Wh/kg at a power density of 374 W/kg as well as an energy density retention of 21 Wh/kg at a power density of 30 kW/kg. Swain *et al.* [524] studied the performance of a SiOC derived nano-porous carbon hybrid with specific surface area of 1798 m^2/g and the prepared material exhibits a high specific capacitance of 333 F/g. Sun *et al.* [525] developed a composite with MnO$_2$ nanoneedles embedded in SiOC-derived

hierarchically porous carbon by a facile hydrothermal technology for electrode material for supercapacitors. With a large specific surface area of 1749.3 m^2/g and uniform distribution of MnO$_2$ nanoneedles, the hierarchically porous carbon used as electrode delivers a high capacitance of 255.8 F/g at 1 A/g in a three-electrode system. When fabricating a symmetrical coin cell supercapacitor, the material exhibits a distinguished energy density (12.6 Wh/kg at a power density of 3997.7 W/kg) and a remarkable capacitance retention of 92.2% after 2000 cycles [525].

4.3 Solid electrolyte/separator materials in lithium-ion batteries

Smith *et al.* [526] first synthesized a polyacrylonitrile (PAN)/polymer-derived ceramic hybrid nanofiber by combining PAN and ambient temperature-curable organopolysilazane via a single-step electrospinning process. The obtained membrane used as separator for LIBs shows excellent ionic conductivity. The composite separator with 30 wt% PDC has an increased ionic conductivity of 1.05 mS/cm compared to 0.29 mS/cm of pristine PAN separator and shows a stable cycling performance due to the presence of the ceramic phase on the surface of the membrane. The subsequent work of Smith *et al.* [527] further investigated the impact of the polymer structure and ceramic morphology on the performance of the PAN/polymer-derived ceramic hybrid nanofiber separator in LIBs. They found that the presence of tetraethyl orthosilicate (TEOS) pendant chain attached to the polysilazane (PSZ) backbone improved the interconnected amorphous networks, thus increasing electrolyte uptake and resulting in excellent cycling performance and superior ionic conductivity.
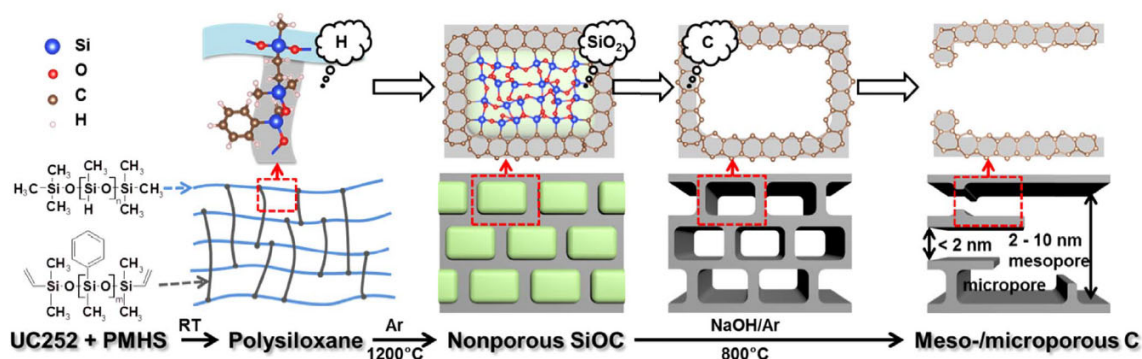

Fig. 27 Synthesis of polysiloxane-derived highly mesoporous carbon via NaOH etching and activation. Reproduced with permission from Ref. [523], © Elsevier Ltd. 2017.

4. 4 Gas diffusion layer and catalyst component in zinc–air batteries

Cycle life of rechargeable zinc–air batteries is affected by the oxygen diffusion rate. Thus, ideal architecture of gas diffusion layer determines its electrochemical performance. However, complex manufacturing process and low oxygen gas permeability of traditional commercial gas diffusion layer hamper the performance of zinc–air batteries. Property-tailorable PDC materials offer new solutions for enhanced architecture of gas diffusion layer for zinc–air batteries. Moni *et al.* [528] developed a porous conductive ceramic membrane derived from poly(methyl silsesquioxane) with a bilayered structure of 390 μm as well as an open porosity of 55% by a freeze tape casting technique. The obtained material was used as gas diffusion layer for zinc–air batteries. After introducing graphite and MWCNT as filler materials, a remarkable electrical conductivity of 5.59×10^{-3} S/cm was achieved. After coating with a commercial Pt–Ru/C catalyst, the as-prepared material exhibits excellent electrochemical performance due to the symmetric sponge-like structure facilitating the oxygen exchange rate and provides a short path for the kinetics.

5 Conclusions and perspectives

PDCs as a class of advanced ceramics with promising structural and functional properties for energy conversion and storage have received increasing attention in recent years. With respect to energy conversion systems, polymer-derived ceramic fibers are already on the market for a couple of decades. Taking advantage of the preceramic polymers, PDC approach offers solution to most of the problems associated with other processing methods for the fabrication of CMCs and T/EBCs. Moreover, several polymer-derived sensors (e.g., piezoresistive pressure sensors, temperature sensors, heat flux sensors, and hot-wire anemometers) used for *in situ* and real-time monitoring of the temperature/heat flux and dynamic pressure within the hot sections of gas turbine engines have been proposed and assessed. The short response time, wireless detection, excellent repeatability, stability, sensitivity, and accuracy ensure their future application in gas turbine engines. Regarding energy storage, several different PDC systems, such as SiCN,

SiCO, and SiCNO, as well as the composite materials consisting of a polymer-derived ceramic blended with carbon/silicon/tin have been thoroughly investigated. The PDC-based anode materials are proven to possess many desirable properties superior to or unobtainable with other materials. For instance, in addition to the tunable chemical and physical properties, the PDC-based anodes are chemically inert with respect to other battery components, able to minimize the agglomeration of lithium/sodium ions, lightweight but exhibiting excellent mechanical properties, possessing *in situ* formed free carbon network for electron conduction and lithium/sodium ion storage as well as showing superior exfoliation resistance. These remarkable features open a variety of new avenues regarding fundamental and applied research in the exciting fields of both PDCs and energy conversion and storage.

In the future, however, further studies in this field are still needed in order to facilitate these materials flowing out of the laboratory and into the markets. When employing the PDC approach to prepare CMCs and T/EBCs, the decomposition of preceramic polymers inevitably leads to shrinkage of the ceramic matrix and coatings during polymer-to-ceramic transformation, leading to formation of pores, voids, and micro-cracks. These defects are strongly detrimental to the thermomechanical properties and oxidation/corrosion resistance of CMCs and T/EBCs. In order to overcome this problem, further research has to be conducted from the following aspects: increasing the ceramic yield via molecular design or pyrolysis process optimization, taking multiple PIP process, introducing inert or active fillers to compensate the shrinkage as well as in conjunction with other fabricating methods, such as chemical vapor infiltration (CVI) and reactive melt infiltration (RMI). For the ceramic fibers, only a handful of ceramic fibers for use in CMCs have reached the market so far, and all of them are SiC-based fibers. Unfortunately, due to phase separation, grain growth, and carbothermal reactions, SiC-based ceramic fibers will lose their mechanical strength at high temperatures. Therefore, novel ceramic fibers with rather low oxygen content or with resistance to crystallization (e.g., SiBCN and novel SiHfBCN fibers) are highly demanded. In addition, for application in gas turbine engines, hydrothermal corrosion resistance of the Si-based fibers, CMCs, and T/EBCs at high temperatures is challenging. Thus, novel preceramic precursors should be synthesized in a bottom–up way

or via chemical modification of commercially available precursors in order to develop new Si-based PDCs with strongly enhanced hydrothermal corrosion resistance. Furthermore, the price and technological challenge to produce polymer-derived ceramic fibers should be remarkably reduced via further innovation in order to be affordable to more commercial customers.

It is wise to produce high-temperature sensors for gas turbine engines using PDCs because of their unique microstructures, tailorable electric properties, excellent thermal stability, high chemical durability, and superior oxidation resistance. However, they are still under development and produced on a laboratory scale. Within this context, precisely controlling the electric properties and shape of proposed PDC sensors, designing and fabricating wireless sensor technology, as well as testing and calibrating methods necessitate future fundamental and applied research.

For energy storage applications, despite that superior electrochemical performance such as energy density and cycling stability can be achieved by PDC-based electrodes, some challenging issues should be solved for large-scale commercial application. For instance, compared with commercial graphite anode, the coulombic efficiency of PDC anodes used for lithium/sodium batteries is lower, which leads to lower economic benefits. In order to solve this problem, the relationship between the capacity and the free carbon content should be further clarified, with a focus on diminishing first cycle irreversible capacity. In addition, the relatively high energy-cost of material processing and voltage hysteresis also hamper the widespread use of PDCs. Controlling particle size of PDC materials and introducing free carbon and nano-porous architecture could enhance structure stability and electrochemical performance. Research of in-depth structure–property–processing of PDCs for Li and Na storage, *in-situ* microscopy and spectroscopy characterization of the electrode/electrolyte interface of PDC electrodes should be the main research direction in the future [403]. Furthermore, the application of the PDCs as a stabilizing matrix for the anodes based on the volume-expanding elements like silicon or tin can be further developed as well.

Acknowledgements

References

[1]   Guillon O. *Advanced Ceramics for Energy Conversion and Storage*. Amsterdam: Elsevier, 2020.

[2]   Rao A. Sustainable energy conversion for electricity and coproducts: Principles, technologies, and equipment. Hoboken, NJ, USA: John Wiley & Sons, Inc., 2015.

[3]   Ainger F, Herbert J. The preparation of phosphorus–nitrogen compounds as non-porous solids. *Spec Ceram*, 1960: 168–182

[4]   Chantrell P, Popper P. Inorganic polymers and ceramics. *Spec Ceram* 1965: 67.

[5]   Yajima S, Hayashi J, Omori M. Continuous silicon carbide fiber of high tensile strength. *Chem Lett* 1975, **4**: 931–934.

[6]   Yajima S, Hasegawa Y, Okamura K, *et al*. Development of high tensile strength silicon carbide fibre using an organosilicon polymer precursor. *Nature* 1978, **273**: 525–527.

[7]   Blum YD, Platz RM, Crawford EJ. Glass strengthening by polymer-derived ceramic coatings. *J Am Ceram Soc* 1990, **73**: 170–172.

[8]   Torrey JD, Bordia RK. Processing of polymer-derived ceramic composite coatings on steel. *J Am Ceram Soc* 2007, **91**: 41–45.

[9]   Günthner M, Schütz A, Glatzel U, *et al*. High performance environmental barrier coatings, Part I: Passive filler loaded SiCN system for steel. *J Eur Ceram Soc* 2011, **31**: 3003–3010.

[10] Park CH, Joo YJ, Chung JK, *et al*. Morphology control of a silicon nitride thick film derived from polysilazane precursor using UV curing and IR heat treatment. *Adv Appl Ceram* 2017, **116**: 376–382.

[11] Colombo P, Gambaryan-Roisman T, Scheffler M, *et al*. Conductive ceramic foams from preceramic polymers. *J Am Ceram Soc* 2001, **84**: 2265–2268.

[12] Wen Q, Xu Y, Xu B, *et al*. Single-source-precursor synthesis of dense SiC/HfC$_x$N$_{1-x}$-based ultrahigh-

temperature ceramic nanocomposites. *Nanoscale* 2014, **6**: 13678–13689.

[13] Wen QB, Yu ZJ, Liu XM, *et al*. Mechanical properties and electromagnetic shielding performance of single-source-precursor synthesized dense monolithic SiC/HfC$_x$N$_{1-x}$/C ceramic nanocomposites. *J Mater Chem C* 2019, **7**: 10683–10693.

[14] Wen QB, Yu ZJ, Riedel R, *et al*. Significant improvement of high-temperature oxidation resistance of HfC/SiC ceramic nanocomposites with the incorporation of a small amount of boron. *J Eur Ceram Soc* 2020, **40**: 3499–3508.

[15] Wen QB, Feng Y, Yu ZJ, *et al*. Microwave absorption of SiC/ HfC$_x$N$_{1-x}$/C ceramic nanocomposites with HfC$_x$N$_{1-x}$-carbon core–shell particles. *J Am Ceram Soc* 2016, **99**: 2655–2663.

[16] Klatt E, Frass A, Frieß M, *et al*. Mechanical and microstructural characterisation of SiC– and SiBNC–fibre reinforced CMCs manufactured via PIP method before and after exposure to air. *J Eur Ceram Soc* 2012, **32**: 3861–3874.

[17] Poerschke DL, Braithwaite A, Park D, *et al*. Crystallization behavior of polymer-derived Si–O–C for ceramic matrix composite processing. *Acta Mater* 2018, **147**: 329–341.

[18] Chawla N, Tur YK, Holmes JW, *et al*. High-frequency fatigue behavior of woven-fiber-fabric-reinforced polymer-derived ceramic-matrix composites. *J Am Ceram Soc* 2005, **81**: 1221–1230.

[19] Jones R, Szweda A, Petrak D. Polymer derived ceramic matrix composites. *Compos A*: *Appl Sci Manuf* 1999, **30**: 569–575.

[20] Eckel ZC, Zhou C, Martin JH, *et al*. Additive manufacturing of polymer-derived ceramics. *Science* 2016, **351**: 58–62.

[21] Colombo P, Schmidt J, Franchin G, *et al*. Additive manufacturing techniques for fabricating complex ceramic components from preceramic polymers. *Am Ceram Soc Bull* 2017, **96**: 16–23.

[22] Verbeek W. Production of shaped articles of homogeneous mixtures of silicon carbide and nitride. U.S. patent 3 853 567, 1974.

[23] Verbeek W, Winter G. Formkoerper aus siliciumcarbid und verfahren zu ihrer herstellung. DE Patent 2236078, 1974.

[24] Winter G, Verbeek W, Mansmann M. Production of shaped articles of silicon carbide and silicon nitride. Google Patents, 1975. Available at https://patents.google.com/patent/US3892583A/en.

[25] Yajima S, Hayashi J, Omori M, *et al*. Development of a silicon carbide fibre with high tensile strength. *Nature* 1976, **261**: 683–685.

[26] Yajima S, Okamura K, Hayashi J, *et al*. Synthesis of continuous SiC fibers with high tensile strength. *J Am Ceram Soc* 1976, **59**: 324–327.

[27] Yajima S, Omori M, Hayashi J, *et al*. Simple synthesis of the continuous SiC fiber with high tensile strength. *Chem Lett* 1976, **5**: 551–554.

[28] Takamizawa M, Kobayashi T, Hayashida A. Organoborosilicon polymer and a method for the preparation thereof. U.S. patent 4 550 151, 1985.

[29] Takamizawa M, Kobayashi T, Hayashida A, *et al*. Method for the preparation of an inorganic fiber containing silicon, carbon, boron and nitrogen. Google Patents, 1986. Available at https://patents.google.com/patent/US4604367A/en.

[30] Greil P. Polymer derived engineering ceramics. *Adv Eng Mater* 2000, **2**: 339–348.

[31] Riedel R, Kienzle A, Dressler W, *et al*. A silicoboron carbonitride ceramic stable to 2,000 ℃. *Nature* 1996, **382**: 796–798.

[32] Riedel R, Passing G, Schönfelder H, *et al*. Synthesis of dense silicon-based ceramics at low temperatures. *Nature* 1992, **355**: 714–717.

[33] Riedel R, Kleebe HJ, Schönfelder H, *et al*. A covalent micro/nano-composite resistant to high-temperature oxidation. *Nature* 1995, **374**: 526–528.

[34] Funayama O, Nakahara H, Okoda M, *et al*. Conversion mechanism of polyborosilazane into silicon nitride-based ceramics. *J Mater Sci* 1995, **30**: 410–416.

[35] Colombo P, Mera G, Riedel R, *et al*. Polymer-derived ceramics: 40 years of research and innovation in advanced ceramics. *J Am Ceram Soc* 2010, **93**: 1805–1837.

[36] Wen QB, Yu ZJ, Riedel R. The fate and role of *in situ* formed carbon in polymer-derived ceramics. *Prog Mater Sci* 2020, **109**: 100623.

[37] Fu SY, Zhu M, Zhu YF. Organosilicon polymer-derived ceramics: An overview. *J Adv Ceram* 2019, **8**: 457–478.

[38] Ionescu E. Polymer-derived ceramics. In: *Ceramics Science and Technology*. Weinheim, Germany: Wiley-VCH Verlag GmbH & Co. KGaA, 2014: 457–500.

[39] Su Q, King S, Li LY, *et al*. Microstructure-mechanical properties correlation in irradiated amorphous SiOC. *Scripta Mater* 2018, **146**: 316–320.

[40] Stabler C, Roth F, Narisawa M, *et al*. High-temperature creep behavior of a SiOC glass ceramic free of segregated carbon. *J Eur Ceram Soc* 2016, **36**: 3747–3753.

[41] Mutin PH. Control of the composition and structure of silicon oxycarbide and oxynitride glasses derived from polysiloxane precursors. *J Sol Gel Sci Technol* 1999, **14**: 27–38.

[42] Laffon C, Flank AM, Lagarde P, *et al*. Study of Nicalon-based ceramic fibres and powders by EXAFS spectrometry, X-ray diffractometry and some additional methods. *J Mater Sci* 1989, **24**: 1503–1512.

[43] Takeda M, Saeki A, Sakamoto JI, *et al*. Effect of hydrogen atmosphere on pyrolysis of cured polycarbosilane fibers. *J Am Ceram Soc* 2004, **83**: 1063–1069.

[44] Mera G, Riedel R, Poli F, *et al*. Carbon-rich SiCN ceramics derived from phenyl-containing poly(silylcarbodiimides). *J Eur Ceram Soc* 2009, **29**: 2873–2883.

[45] Yu ZJ, Yang YJ, Mao KW, *et al*. Single-source-precursor synthesis and phase evolution of SiC–TaC–C ceramic nanocomposites containing core–shell structured TaC@C nanoparticles. *J Adv Ceram* 2020, **9**: 320–328.

[46] Yu ZJ, Lv X, Lai SY, *et al*. ZrC–ZrB$_2$–SiC ceramic nanocomposites derived from a novel single-source precursor with high ceramic yield. *J Adv Ceram* 2019, **8**: 112–120.

[47] Widgeon S, Mera G, Gao Y, *et al*. Effect of precursor on speciation and nanostructure of SiBCN polymer-derived ceramics. *J Am Ceram Soc* 2013, **96**: 1651–1659.

[48] Sorarù GD, Pederiva L, Latournerie J, *et al*. Pyrolysis kinetics for the conversion of a polymer into an amorphous silicon oxycarbide ceramic. *J Am Ceram Soc* 2002, **85**: 2181–2187.

[49] Peña-Alonso R, Mariotto G, Gervais C, *et al*. New insights on the high-temperature nanostructure evolution of SiOC and B-doped SiBOC polymer-derived glasses. *Chem Mater* 2007, **19**: 5694–5702.

[50] Naviroj M, Miller SM, Colombo P, *et al*. Directionally aligned macroporous SiOC via freeze casting of preceramic polymers. *J Eur Ceram Soc* 2015, **35**: 2225–2232.

[51] Vakifahmetoglu C, Colombo P. A direct method for the fabrication of macro-porous SiOC ceramics from preceramic polymers. *Adv Eng Mater* 2008, **10**: 256–259.

[52] Dibandjo P, Graczyk-Zajac M, Riedel R, *et al*. Lithium insertion into dense and porous carbon-rich polymer-derived SiOC ceramics. *J Eur Ceram Soc* 2012, **32**: 2495–2503.

[53] Riedel R, Greiner A, Miehe G, *et al*. The first crystalline solids in the ternary Si–C–N system. *Angew Chem Int Ed Engl* 1997, **36**: 603–606.

[54] Mera G, Navrotsky A, Sen S, *et al*. Polymer-derived SiCN and SiOC ceramics-structure and energetics at the nanoscale. *J Mater Chem A* 2013, **1**: 3826.

[55] Pham T, Kim DP, Lim TW, *et al*. Three-dimensional SiCN ceramic microstructures via nano-stereolithography of inorganic polymer photoresists. *Adv Funct Mater* 2006, **16**: 1235–1241.

[56] Kolb R, Fasel C, Liebau-Kunzmann V, *et al*. SiCN/C– ceramic composite as anode material for lithium ion batteries. *J Eur Ceram Soc* 2006, **26**: 3903–3908.

[57] Nghiem Q, Kim D, Kim DP. Synthesis of inorganic–organic diblock copolymers as a precursor of ordered mesoporous SiCN ceramic. *Adv Mater* 2007, **19**: 2351–2354.

[58] Yu ZJ, Li F, Zhu QK. Single-source-precursor synthesis and phase evolution of NbC–SiC–C ceramic nanocomposites with core–shell structured NbC@C and SiC@C nanoparticles. *Adv Powder Mater* 2021, https://doi.org/10.1016/j.apmate.2021.09.009.

[59] Chelliah NM, Singh H, Raj R, *et al*. Processing, microstructural evolution and strength properties of *in situ* magnesium matrix composites containing nano-sized polymer derived SiCNO particles. *Mater Sci Eng*: *A* 2017, **685**: 429–438.

[60] Terauds K, Sanchez-Jimenez PE, Raj R, *et al*. Giant piezoresistivity of polymer-derived ceramics at high temperatures. *J Eur Ceram Soc* 2010, **30**: 2203–2207.

[61] Chelliah NM, Padaikathan P, Surappa MK. Deformation mechanisms and texture evolution of *in situ* magnesium matrix composites containing polymer derived SiCNO dispersoids during hot compression. *Mater Sci Eng*: *A* 2018, **720**: 49–59.

[62] Duan RG, Mukherjee AK. Synthesis of SiCNO nanowires through heat-treatment of polymer-functionalized single-walled carbon nanotubes. *Adv Mater* 2004, **16**: 1106–1109.

[63] Schiavon MA, Armelin NA, Yoshida IVP. Novel poly(borosiloxane) precursors to amorphous SiBCO ceramics. *Mater Chem Phys* 2008, **112**: 1047–1054.

[64] Liebau V, Hauser R, Riedel R. Amorphous SiBCO ceramics derived from novel polymeric precursors. *Comptes Rendus Chimie* 2004, **7**: 463–469.

[65] Liao NB, Xue W, Zhou HM, *et al*. Molecular dynamics investigation of structure and high-temperature mechanical properties of SiBCO ceramics. *J Alloys Compd* 2014, **610**: 45–49.

[66] Cao YJ, Gao Y, Zhao R, *et al*. Coupling effect of temperature and stress on the electronic behavior of amorphous SiAlCO. *J Am Ceram Soc* 2016, **99**: 1881–1884.

[67] Cao YJ, An LN. Anomalous piezo-dielectricity of a polymer-derived amorphous silicoaluminum oxycarbide (SiAlCO). *Ceram Int* 2018, **44**: 1467–1470.

[68] Cao YJ, Yang XP, Zhao R, *et al*. Giant piezoresistivity in polymer-derived amorphous SiAlCO ceramics. *J Mater Sci* 2016, **51**: 5646–5650.

[69] Cao YJ, Yang XP, An LN. Electric conductivity and microstructure evolution of polymer-derived SiAlCO ceramics. *Ceram Int* 2016, **42**: 4033–4038.

[70] Wang YG, Fan Y, Zhang LG, *et al*. Polymer-derived SiAlCN ceramics resist oxidation at 1400 ℃. *Scripta Mater* 2006, **55**: 295–297.

[71] Wang YG, Fei WF, An LN. Oxidation/corrosion of polymer-derived SiAlCN ceramics in water vapor. *J Am Ceram Soc* 2006, **89**: 1079–1082.

[72] Dhamne A, Xu WX, Fookes BG, *et al*. Polymer-ceramic conversion of liquid polyaluminasilazanes for SiAlCN ceramics. *J Am Ceram Soc* 2005, **88**: 2415–2419.

[73] Wang YG, An LN, Fan Y, *et al*. Oxidation of polymer-derived SiAlCN ceramics. *J Am Ceram Soc* 2005, **88**: 3075–3080.

[74] Bernard S, Weinmann M, Cornu D, *et al*. Preparation of high-temperature stable SiBCN fibers from tailored single source polyborosilazanes. *J Eur Ceram Soc* 2005, **25**: 251–256.

[75] Gao Y, Mera G, Nguyen H, *et al*. Processing route dramatically influencing the nanostructure of carbon-rich SiCN and SiBCN polymer-derived ceramics. Part I: Low temperature thermal transformation. *J Eur Ceram Soc* 2012, **32**: 1857–1866.

[76] Zhang PF, Jia DC, Yang ZH, *et al*. Progress of a novel non-oxide Si–B–C–N ceramic and its matrix composites. *J Adv Ceram* 2012, **1**: 157–178.

[77] Kousaalya AB, Kumar R, Packirisamy S. Characterization of free carbon in the as-thermolyzed Si–B–C–N ceramic from a polyorganoborosilazane precursor. *J Adv Ceram* 2013, **2**: 325–332.

[78] Wen QB, Yu ZJ, Xu YP, *et al*. SiC/Hf$_y$Ta$_{1-y}$C$_x$N$_{1-x}$/C ceramic nanocomposites with Hf$_y$Ta$_{1-y}$C$_x$N$_{1-x}$–carbon core–shell nanostructure and the influence of the carbon-shell thickness on electrical properties. *J Mater Chem C* 2018, **6**: 855–864.

[79] Terauds K, Raj R. Limits to the stability of the amorphous nature of polymer-derived HfSiCNO compounds. *J Am Ceram Soc* 2013, **96**: 2117–2123.

[80] Ionescu E, Papendorf B, Kleebe HJ, *et al*. Phase separation of a hafnium alkoxide-modified polysilazane upon polymer-to-ceramic transformation—A case study. *J Eur Ceram Soc* 2012, **32**: 1873–1881.

[81] Yuan J, Hapis S, Breitzke H, *et al*. Single-source-precursor synthesis of hafnium-containing ultrahigh-temperature ceramic nanocomposites (UHTC–NCs). *Inorg Chem* 2014, **53**: 10443–10455.

[82] Yuan J, Luan XG, Riedel R, *et al*. Preparation and hydrothermal corrosion behavior of C$_f$/SiCN and C$_f$/SiHfBCN ceramic matrix composites. *J Eur Ceram Soc* 2015, **35**: 3329–3337.

[83] Luan XG, Yuan J, Wang JQ, *et al*. Laser ablation behavior of C$_f$/SiHfBCN ceramic matrix composites. *J Eur Ceram Soc* 2016, **36**: 3761–3768.

[84] Yuan J, Galetz M, Luan XG, *et al*. High-temperature oxidation behavior of polymer-derived SiHfBCN ceramic nanocomposites. *J Eur Ceram Soc* 2016, **36**: 3021–3028.

[85] Bill J, Aldinger F. Precursor-derived covalent ceramics. *Adv Mater* 1995, **7**: 775–787.

[86] Flores O, Bordia RK, Nestler D, *et al*. Ceramic fibers based on SiC and SiCN systems: Current research, development, and commercial status. *Adv Eng Mater* 2014, **16**: 621–636.

[87] Guo AR, Roso M, Modesti M, *et al*. Preceramic polymer-derived SiOC fibers by electrospinning. *J Appl Polym Sci* 2014, **131**: 39836.

[88] Barroso G, Li Q, Bordia RK, *et al*. Polymeric and ceramic silicon-based coatings—A review. *J Mater Chem A* 2019, **7**: 1936–1963.

[89] Hernández-Rodríguez P, López-Honorato E. Polymer derived SiC environmental barrier coatings with superwetting properties. *Ceram Int* 2017, **43**: 11289–11295.

[90] Günthner M, Wang KS, Bordia RK, *et al*. Conversion behaviour and resulting mechanical properties of polysilazane-based coatings. *J Eur Ceram Soc* 2012, **32**: 1883–1892.

[91] Liu J, Zhang LT, Liu QM, *et al*. Polymer-derived SiOC–barium–strontium aluminosilicate coatings as an environmental barrier for C/SiC composites. *J Am Ceram Soc* 2010, **93**: 4148–4152.

[92] Yoon BH, Lee EJ, Kim HE, *et al*. Highly aligned porous silicon carbide ceramics by freezing polycarbosilane/camphene solution. *J Am Ceram Soc* 2007, **90**: 1753–1759.

[93] Yoon BH, Park CS, Kim HE, *et al*. In situ synthesis of porous silicon carbide (SiC) ceramics decorated with SiC nanowires. *J Am Ceram Soc* 2007, **90**: 3759–3766.

[94] Zhang HX, D'Angelo Nunes P, Wilhelm M, *et al*. Hierarchically ordered micro/meso/macroporous polymer-derived ceramic monoliths fabricated by freeze-casting. *J Eur Ceram Soc* 2016, **36**: 51–58.

[95] Hanemann T, Ade M, Börner M, *et al*. Microstructuring of preceramic polymers. *Adv Eng Mater* 2002, **4**: 869–873.

[96] Lee HJ, Yoon TH, Kim DP. Fabrication of microfluidic channels derived from a UV/thermally cured preceramic polymer via a soft lithographic technique. *Microelectron Eng* 2007, **84**: 2892–2895.

[97] Martínez-Crespiera S, Ionescu E, Schlosser M, *et al*. Fabrication of silicon oxycarbide-based microcomponents via photolithographic and soft lithography approaches. *Sens Actuat A: Phys* 2011, **169**: 242–249.

[98] Yang H, Deschatelets P, Brittain ST, *et al*. Fabrication of high performance ceramic microstructures from a polymeric precursor using soft lithography. *Adv Mater* 2001, **13**: 54–58.

[99] Kaur S, Riedel R, Ionescu E. Pressureless fabrication of dense monolithic SiC ceramics from a polycarbosilane. *J Eur Ceram Soc* 2014, **34**: 3571–3578.

[100] Liu XM, Yu ZJ, Ishikawa R, *et al*. Single-source-precursor synthesis and electromagnetic properties of novel RGO–SiCN ceramic nanocomposites. *J Mater Chem C* 2017, **5**: 7950–7960.

[101] Toma L, Kleebe HJ, Müller MM, *et al*. Correlation between intrinsic microstructure and piezoresistivity in a SiOC polymer-derived ceramic. *J Am Ceram Soc* 2012, **95**: 1056–1061.

[102] Bechelany MC, Proust V, Gervais C, *et al*. In situ controlled growth of titanium nitride in amorphous silicon nitride: A general route toward bulk nitride nanocomposites with very high hardness. *Adv Mater* 2014, **26**: 6548–6553.

[103] Wang KS, Günthner M, Motz G, *et al*. High performance environmental barrier coatings, Part II: Active filler loaded SiOC system for superalloys. *J Eur Ceram Soc* 2011, **31**: 3011–3020.

[104] Nguyen MD, Bang JW, Bin AS, *et al*. Novel polymer-derived ceramic environmental barrier coating system for carbon steel in oxidizing environments. *J Eur Ceram Soc* 2017, **37**: 2001–2010.

[105] Wang KS, Unger J, Torrey JD, *et al*. Corrosion resistant polymer derived ceramic composite environmental barrier coatings. *J Eur Ceram Soc* 2014, **34**: 3597–3606.

[106] King D, Apostolov Z, Key T, *et al*. Novel processing approach to polymer-derived ceramic matrix composites. *Int J Appl Ceram Technol* 2018, **15**: 399–408.

[107] Zhao H, Chen LX, Luan XG, *et al*. Synthesis, pyrolysis of

a novel liquid SiBCN ceramic precursor and its application in ceramic matrix composites. *J Eur Ceram Soc* 2017, **37**: 1321–1329.

[108] Lewinsohn CA, Colombo P, Reimanis I, *et al*. Stresses occurring during joining of ceramics using preceramic polymers. *J Am Ceram Soc* 2001, **84**: 2240–2244.

[109] Colombo P, Sglavo V, Pippel E, *et al*. Joining of reaction-bonded silicon carbide using a preceramic polymer. *J Mater Sci* 1998, **33**: 2405–2412.

[110] Vrankovic D, Graczyk-Zajac M, Kalcher C, *et al*. Highly porous silicon embedded in a ceramic matrix: A stable high-capacity electrode for Li-ion batteries. *ACS Nano* 2017, **11**: 11409–11416.

[111] Reinold LM, Yamada Y, Graczyk-Zajac M, *et al*. The influence of the pyrolysis temperature on the electrochemical behavior of carbon-rich SiCN polymer-derived ceramics as anode materials in lithium-ion batteries. *J Power Sources* 2015, **282**: 409–415.

[112] Kaspar J, Terzioglu C, Ionescu E, *et al*. Stable SiOC/Sn nanocomposite anodes for lithium-ion batteries with outstanding cycling stability. *Adv Funct Mater* 2014, **24**: 4097–4104.

[113] Fukui H, Ohsuka H, Hino T, *et al*. Influence of polystyrene/phenyl substituents in precursors on microstructures of Si–O–C composite anodes for lithium-ion batteries. *J Power Sources* 2011, **196**: 371–378.

[114] Dahn JR, Wilson AM, Xing W, *et al*. Electrodes for lithium ion batteries using polysilazanes ceramic with lithium. Google Patents, 1997. Available at https://patents.google.com/patent/US5631106A/en.

[115] Seifollahi Bazarjani M, Hojamberdiev M, Morita K, *et al*. Visible light photocatalysis with c-WO$_{3-x}$/WO$_3$×H$_2$O nanoheterostructures *in situ* formed in mesoporous polycarbosilane–siloxane polymer. *J Am Chem Soc* 2013, **135**: 4467–4475.

[116] Kaspar J, Storch M, Schitco C, *et al*. SiOC(N)/hard carbon composite anodes for Na-ion batteries: Influence of morphology on the electrochemical properties. *J Electrochem Soc* 2015, **163**: A156–A162.

[117] Soares DM, Singh G. SiOC functionalization of MoS$_2$ as a means to improve stability as sodium-ion battery anode. *Nanotechnology* 2020, **31**: 145403.

[118] Halim M, Liu G, Ardhi REA, *et al*. Pseudocapacitive characteristics of low-carbon silicon oxycarbide for lithium-ion capacitors. *ACS Appl Mater Interfaces* 2017, **9**: 20566–20576.

[119] David L, Shareef KM, Abass MA, *et al*. Three-dimensional polymer-derived ceramic/graphene paper as a Li-ion battery and supercapacitor electrode. *RSC Adv* 2016, **6**: 53894–53902.

[120] Reddy IN, Sreedhar A, Reddy CV, *et al*. High performance hierarchical SiCN nanowires for efficient photocatalytic–photoelectrocatalytic and supercapacitor applications. *Appl Catal B: Environ* 2018, **237**: 876–887.

[121] Liu XM, Yu ZJ, Ishikawa R, *et al*. Single-source-precursor derived RGO/CNTs–SiCN ceramic nanocomposite with ultra-high electromagnetic shielding effectiveness. *Acta Mater* 2017, **130**: 83–93.

[122] Song Y, He LH, Zhang XF, *et al*. Highly efficient electromagnetic wave absorbing metal-free and carbon-rich ceramics derived from hyperbranched polycarbosilazanes. *J Phys Chem C* 2017, **121**: 24774–24785.

[123] Zhao WY, Shao G, Jiang MJ, *et al*. Ultralight polymer-derived ceramic aerogels with wide bandwidth and effective electromagnetic absorption properties. *J Eur Ceram Soc* 2017, **37**: 3973–3980.

[124] Yin XW, Kong L, Zhang LT, *et al*. Electromagnetic properties of Si–C–N based ceramics and composites. *Int Mater Rev* 2014, **59**: 326–355.

[125] Yu ZJ, Lv X, Mao KW, *et al*. Role of *in situ* formed free carbon on electromagnetic absorption properties of polymer-derived SiC ceramics. *J Adv Ceram* 2020, **9**: 617–628.

[126] Liew LA, Liu YP, Luo RL, *et al*. Fabrication of SiCN MEMS by photopolymerization of pre-ceramic polymer. *Sens Actuat A: Phys* 2002, **95**: 120–134.

[127] Schulz M. Polymer derived ceramics in MEMS/NEMS—a review on production processes and application. *Adv Appl Ceram* 2009, **108**: 454–460.

[128] Liew LA, Saravanan RA, Bright VM, *et al*. Processing and characterization of silicon carbon-nitride ceramics: Application of electrical properties towards MEMS thermal actuators. *Sens Actuat A: Phys* 2003, **103**: 171–181.

[129] Liu YP, Liew LA, Luo RL, *et al*. Application of microforging to SiCN MEMS fabrication. *Sens Actuat A: Phys* 2002, **95**: 143–151.

[130] Liew LA, Bright VM, Raj R. A novel micro glow plug fabricated from polymer-derived ceramics: *In situ* measurement of high-temperature properties and application to ultrahigh-temperature ignition. *Sens Actuat A: Phys* 2003, **104**: 246–262.

[131] Harshe R, Balan C, Riedel R. Amorphous Si(Al)OC ceramic from polysiloxanes: Bulk ceramic processing, crystallization behavior and applications. *J Eur Ceram Soc* 2004, **24**: 3471–3482.

[132] Ferraioli L, Ahn D, Saha A, *et al*. Intensely photoluminescent pseudo-amorphous SiliconOxyCarbo-Nitride polymer-ceramic hybrids. *J Am Ceram Soc* 2008, **91**: 2422–2424.

[133] Shimokawa Y, Fujiwara A, Ionescu E, *et al*. Synthesis and characterization of luminescent properties of ceramics derived from polysilylcarbodiimides. *J Ceram Soc Japan* 2014, **122**: 895–901.

[134] Su R, Huang ZF, Chen F, *et al*. Synthesis and luminescent properties of ternary Si–Ge–N nanowires. *CrystEngComm* 2016, **18**: 8787–8793.

[135] Zhang YJ, Quaranta A, Domenico Soraru G. Synthesis

and luminescent properties of novel Eu^{2+}-doped silicon oxycarbide glasses. *Opt Mater* 2004, **24**: 601–605.

[136] Cross T, Raj R, Prasad SV, *et al*. Mechanical and tribological behavior of polymer-derived ceramics constituted from SiC$_x$O$_y$N$_z$. *J Am Ceram Soc* 2006, **89**: 3706–3714.

[137] Cross TJ, Raj R, Cross TJ, *et al*. Synthesis and tribological behavior of silicon oxycarbonitride thin films derived from poly(urea)methyl vinyl silazane. *Int J Appl Ceram Technol* 2006, **3**: 113–126.

[138] Klaffke D, Wäsche R, Janakiraman N, *et al*. Tribological characterisation of siliconcarbonitride ceramics derived from preceramic polymers. *Wear* 2006, **260**: 711–719.

[139] Li ZB, Cao YJ, He JB, *et al*. Mechanical and tribological performances of C–SiC nanocomposites synthetized from polymer-derived ceramics sintered by spark plasma sintering. *Ceram Int* 2018, **44**: 14335–14341.

[140] Alvi SA, Akhtar F. High temperature tribology of polymer derived ceramic composite coatings. *Sci Rep* 2018, **8**: 15105.

[141] Vakifahmetoglu C, Buldu M, Karakuscu A, *et al*. High surface area carbonous components from emulsion derived SiOC and their gas sensing behavior. *J Eur Ceram Soc* 2015, **35**: 4447–4452.

[142] Hu LH, Raj R. Semiconductive behavior of polymer-derived SiCN ceramics for hydrogen sensing. *J Am Ceram Soc* 2015, **98**: 1052–1055.

[143] Karakuscu A, Ponzoni A, Ayana D, *et al*. High carbon-high porous SiOC glasses for room temperature NO$_2$ sensing. *Procedia Eng* 2014, **87**: 160–163.

[144] Ren XH, Ebadi S, Chen YH, *et al*. High-temperature characterization of SiCN ceramics for wireless passive sensing applications up to 500 ℃. In: Proceedings of the WAMICON 2011 Conference, 2011: 1–5.

[145] Gonzalo-Juan I, Detsch R, Mathur S, *et al*. Synthesis and *in vitro* activity assessment of novel silicon oxycarbide-based bioactive glasses. *Materials* 2016, **9**: 959.

[146] Ionescu E, Sen S, Mera G, *et al*. Structure, energetics and bioactivity of silicon oxycarbide-based amorphous ceramics with highly connected networks. *J Eur Ceram Soc* 2018, **38**: 1311–1319.

[147] Gawęda M, Jeleń P, Długoń E, *et al*. Bioactive layers based on black glasses on titanium substrates. *J Am Ceram Soc* 2018, **101**: 590–601.

[148] Riedel R, Mera G, Hauser R, *et al*. Silicon-based polymer-derived ceramics: Synthesis properties and applications—A review. *J Ceram Soc Japan* 2006, **114**: 425–444.

[149] Stabler C, Ionescu E, Graczyk-Zajac M, *et al*. Silicon oxycarbide glasses and glass-ceramics: "All-Rounder" materials for advanced structural and functional applications. *J Am Ceram Soc* 2018, **101**: 4817–4856.

[150] Bunsell AR, Piant A. A review of the development of three generations of small diameter silicon carbide fibres. *J Mater Sci* 2006, **41**: 823–839.

[151] Manoj Kumar BV, Kim YW. Processing of polysiloxane-derived porous ceramics: A review. *Sci Technol Adv Mater* 2010, **11**: 044303.

[152] Miele P, Bernard S, Cornu D, *et al*. Recent developments in polymer-derived ceramic fibers (PDCFs): Preparation, properties and applications—A review. *Soft Mater* 2007, **4**: 249–286.

[153] Vakifahmetoglu C, Zeydanli D, Colombo P. Porous polymer derived ceramics. *Mater Sci Eng*: *R*: *Rep* 2016, **106**: 1–30.

[154] Colombo P, Riedel R, Sorarù GD, *et al*. *Polymer Derived Ceramics: From Nano-Structure to Applications*. Lancaster, PA, USA: DEStech Publications, Inc., 2010.

[155] Riedel R, Bill J, Passing G. A novel carbon material derived from pyridine-borane. *Adv Mater* 1991, **3**: 551–552.

[156] Bhat S, Lauterbach S, Dzivenko D, *et al*. High-pressure high-temperature behavior of polymer derived amorphous B–C–N. *J Phys*: *Conf Ser* 2014, **500**: 182004.

[157] Bernard S, Miele P. Polymer-derived boron nitride: A review on the chemistry, shaping and ceramic conversion of borazine derivatives. *Materials*: *Basel* 2014, **7**: 7436–7459.

[158] Lei YP, Wang YD, Song YC, *et al*. Novel processable precursor for BN by the polymer-derived ceramics route. *Ceram Int* 2011, **37**: 3005–3009.

[159] Cornu D, Bernard S, Duperrier S, *et al*. Alkylaminoborazine-based precursors for the preparation of boron nitride fibers by the polymer-derived ceramics (PDCs) route. *J Eur Ceram Soc* 2005, **25**: 111–121.

[160] Lei YP, Wang YD, Xue JG, *et al*. Influence of pyrolysis conditions on fabrication of polymer-derived BN fiber for wave transparent application. *Compos B*: *Eng* 2013, **51**: 254–259.

[161] Salles V, Bernard S, Brioude A, *et al*. A new class of boron nitride fibers with tunable properties by combining an electrospinning process and the polymer-derived ceramics route. *Nanoscale* 2010, **2**: 215–217.

[162] Gervais C, Maquet J, Babonneau F, *et al*. Chemically derived BN ceramics: Extensive ^{11}B and ^{15}N solid-state NMR study of a preceramic polyborazilene. *Chem Mater* 2001, **13**: 1700–1707.

[163] Takahiro G, Hiroshi Y, Takaaki H, *et al*. Preparation of polyzirconoxane from zirconium oxychloride octahydrate and ethylene glycol as a precursor for zirconia ceramics. *Appl Organometal Chem* 2000, **14**: 119–126.

[164] Li XJ, Hector AL, Owen JR, *et al*. Evaluation of nanocrystalline Sn$_3$N$_4$ derived from ammonolysis of Sn(NEt$_2$)$_4$ as a negative electrode material for Li-ion and Na-ion batteries. *J Mater Chem A* 2016, **4**: 5081–5087.

[165] Baxter DV, Chisholm MH, Gama GJ, *et al*. Molecular routes to metal carbides, nitrides, and oxides. 2. Studies of the ammonolysis of metal dialkylamides and hexamethyldisilylamides. *Chem Mater* 1996, **8**: 1222–1228.

[166] Kurokawa Y, Ishizaka T, Suzuki M. Preparation of refractory nitride fibers by thermal decomposition of transition metal (Ti,Nb) alkoxide-cellulose precursor gel fibers in NH$_3$ atmosphere. *J Mater Sci* 2001, **36**: 301–306.

[167] Thorne K, Ting SJ, Chu CJ, *et al*. Synthesis of TiC via polymeric titanates: The preparation of fibres and thin films. *J Mater Sci* 1992, **27**: 4406–4414.

[168] Lang H, Seyferth D. Pyrolysis of metallocene complexes (ηC$_5$H$_4$R)$_2$MR: An organometallic route to metal carbide (MC) materials (M = Ti, Zr, Hf). *Appl Organomet Chem* 1990, **4**: 599–606.

[169] Preiss H, Schierhorn E, Brzezinka KW. Synthesis of polymeric titanium and zirconium precursors and preparation of carbide fibres and films. *J Mater Sci* 1998, **33**: 4697–4706.

[170] Tao XY, Qiu WF, Li H, *et al*. Synthesis of nanosized zirconium carbide from preceramic polymers by the facile one-pot reaction. *Polym Adv Technol* 2010, **21**: 300–304.

[171] Inzenhofer K, Schmalz T, Wrackmeyer B, *et al*. The preparation of HfC/C ceramics via molecular design. *Dalton Trans* 2011, **40**: 4741–4745.

[172] Sun YN, Yang CM, Lu Y, *et al*. Transformation of metallic polymer precursor into nanosized HfTaC$_2$ ceramics. *Ceram Int* 2020, **46**: 6022–6028.

[173] Tao XY, Xiang Z, Zhou S, *et al*. Synthesis and characterization of a boron-containing precursor for ZrB$_2$ ceramic. *J Ceram Sci Tech* 2016, **7**: 107–111.

[174] Tao XY, Zhou SX, Xiang ZM, *et al*. Fabrication of continuous ZrB$_2$ nanofibers derived from boron-containing polymeric precursors. *J Alloys Compd* 2017, **697**: 318–325.

[175] Wang H, Chen XB, Gao B, *et al*. Synthesis and characterization of a novel precursor-derived ZrC/ZrB$_2$ ultra-high-temperature ceramic composite. *Appl Organomet Chem* 2013, **27**: 79–84.

[176] Bernard S, Weinmann M, Gerstel P, *et al*. Boron-modified polysilazane as a novel single-source precursor for SiBCN ceramic fibers: Synthesis, melt-spinning, curing and ceramic conversion. *J Mater Chem* 2005, **15**: 289.

[177] Viard A, Fonblanc D, Schmidt M, *et al*. Molecular chemistry and engineering of boron-modified polyorganosilazanes as new processable and functional SiBCN precursors. *Chem Eur J* 2017, **23**: 9076–9090.

[178] Schuhmacher J, Weinmann M, Bill J, *et al*. Solid-state NMR studies of the preparation of Si−C−N ceramics from polysilylcarbodiimide polymers. *Chem Mater* 1998, **10**: 3913–3922.

[179] Viard A, Fonblanc D, Lopez-Ferber D, *et al*. Polymer derived Si–B–C–N ceramics: 30 years of research. *Adv Eng Mater* 2018, **20**: 1800360.

[180] Peuckert M, Vaahs T, Brück M. Ceramics from organometallic polymers. *Adv Mater* 1990, **2**: 398–404.

[181] Wynne KJ, Rice RW. Ceramics via polymer pyrolysisdagger. *Annu Rev Mater Sci* 1984, **14**: 297–334.

[182] Jaschke B, Klingebiel U, Riedel R, *et al*. Cyclosilazanes and borazines: Polymer precursors to silicon- and boron-containing ceramics. *Appl Organometal Chem* 2000, **14**: 671–685.

[183] Kroke E, Li YL, Konetschny C, *et al*. Silazane derived ceramics and related materials. *Mater Sci Eng*: *R*: *Rep* 2000, **26**: 97–199.

[184] Hector AL. Synthesis and processing of silicon nitride and related materials using preceramic polymer and non-oxide sol–gel approaches. *Coord Chem Rev* 2016, **323**: 120–137.

[185] Birot M, Pillot JP, Dunogues J. Comprehensive chemistry of polycarbosilanes, polysilazanes, and polycarbosilazanes as precursors of ceramics. *Chem Rev* 1995, **95**: 1443–1477.

[186] Kakimoto KI, Wakai F, Bill J, *et al*. Synthesis of Si–C–O bulk ceramics with various chemical compositions from polycarbosilane. *J Am Ceram Soc* 1999, **82**: 2337–2341.

[187] Su D, Li YL, An HJ, *et al*. Pyrolytic transformation of liquid precursors to shaped bulk ceramics. *J Eur Ceram Soc* 2010, **30**: 1503–1511.

[188] Choong Kwet Yive NS, Corriu RJP, Leclercq D, *et al*. Silicon carbonitride from polymeric precursors: Thermal cross-linking and pyrolysis of oligosilazane model compounds. *Chem Mater* 1992, **4**: 141–146.

[189] Lavedrine A, Bahloul D, Goursat P, *et al*. Pyrolysis of polyvinylsilazane precursors to silicon carbonitride. *J Eur Ceram Soc* 1991, **8**: 221–227.

[190] Kaur S, Cherkashinin G, Fasel C, *et al*. Single-source-precursor synthesis of novel V$_8$C$_7$/SiC(O)-based ceramic nanocomposites. *J Eur Ceram Soc* 2016, **36**: 3553–3563.

[191] Wang C, Wang J, Park CB, *et al*. Cross-linking behavior of a polysiloxane in preceramic foam processing. *J Mater Sci* 2004, **39**: 4913–4915.

[192] Yajima S, Hasegawa Y, Hayashi J, *et al*. Synthesis of continuous silicon carbide fibre with high tensile strength and high Young's modulus. *J Mater Sci* 1978, **13**: 2569–2576.

[193] Hasegawa Y, Okamura K. Synthesis of continuous silicon carbide fibre. *J Mater Sci* 1983, **18**: 3633–3648.

[194] Hasegawa Y. Synthesis of continuous silicon carbide fibre. *J Mater Sci* 1989, **24**: 1177–1190.

[195] Ichikawa H, Machino F, Mitsuno S, *et al*. Synthesis of continuous silicon carbide fibre. *J Mater Sci* 1986, **21**: 4352–4358.

[196] Ichikawa H. Polymer-derived ceramic fibers. *Annu Rev Mater Res* 2016, **46**: 335–356.

[197] Laine RM, Babonneau F. Preceramic polymer routes to silicon carbide. *Chem Mater* 1993, **5**: 260–279.

[198] Su ZM, Zhang LT, Li YC, *et al*. Rapid preparation of SiC fibers using a curing route of electron irradiation in a low oxygen concentration atmosphere. *J Am Ceram Soc* 2015, **98**: 2014–2017.

[199] Cramer NB, Reddy SK, Lu H, *et al*. Thiol-ene photopolymerization of polymer-derived ceramic precursors. *J Polym Sci A*: *Polym Chem* 2004, **42**: 1752–1757.

[200] He WQ, Chen LX, Peng F. Coating formed by SiBCN single source precursor via UV-photopolymerization. *Mater Lett* 2017, **206**: 121–123.

[201] Pham TA, Kim P, Kwak M, *et al*. Inorganic polymer photoresist for direct ceramic patterning by photolithography. *Chem Commun* 2007, **39**: 4021–4023.

[202] Schulz M, Börner M, Göttert J, *et al*. Cross linking behavior of preceramic polymers effected by UV- and synchrotron radiation. *Adv Eng Mater* 2004, **6**: 676–680.

[203] Zanchetta E, Cattaldo M, Franchin G, *et al*. Stereolithography of SiOC ceramic microcomponents. *Adv Mater* 2016, **28**: 370–376.

[204] Hundley JM, Eckel ZC, Schueller E, *et al*. Geometric characterization of additively manufactured polymer derived ceramics. *Addit Manuf* 2017, **18**: 95–102.

[205] Friedel T, Travitzky N, Niebling F, *et al*. Fabrication of polymer derived ceramic parts by selective laser curing. *J Eur Ceram Soc* 2005, **25**: 193–197.

[206] Zocca A, Gomes CM, Staude A, *et al*. SiOC ceramics with ordered porosity by 3D-printing of a preceramic polymer. *J Mater Res* 2013, **28**: 2243–2252.

[207] Zocca A, Colombo P, Gomes CM, *et al*. Additive manufacturing of ceramics: Issues, potentialities, and opportunities. *J Am Ceram Soc* 2015, **98**: 1983–2001.

[208] Tian XY, Zhang WG, Li DC, *et al*. Reaction-bonded SiC derived from resin precursors by Stereolithography. *Ceram Int* 2012, **38**: 589–597.

[209] De Hazan Y, Penner D. SiC and SiOC ceramic articles produced by stereolithography of acrylate modified polycarbosilane systems. *J Eur Ceram Soc* 2017, **37**: 5205–5212.

[210] Li S, Duan WY, Zhao T, *et al*. The fabrication of SiBCN ceramic components from preceramic polymers by digital light processing (DLP) 3D printing technology. *J Eur Ceram Soc* 2018, **38**: 4597–4603.

[211] Brinckmann SA, Patra N, Yao J, *et al*. Stereolithography of SiOC polymer-derived ceramics filled with SiC micronwhiskers. *Adv Eng Mater* 2018, **20**: 1800593.

[212] Hasegawa Y. Si–C fiber prepared from polycarbosilane cured without oxygen. *J Inorg Organomet Polym* 1992, **2**: 161–169.

[213] Rabe JA, Lipowitz J, Lu PP. Curing preceramic polymers by exposure to nitrogen dioxide. U.S. patent 5 051 215, 1991.

[214] Hasegawa Y. New curing method for polycarbosilane with unsaturated hydrocarbons and application to thermally stable SiC fibre. *Compos Sci Technol* 1994, **51**: 161–166.

[215] Hayashida A, Takamizawa M, Takeda Y. Preparation of hollow ceramic fibers. Google Patents, 1990. Available at https://patents.google.com/patent/US4948763A/en.

[216] Lipowitz J. Infusible preceramic polymers via plasma treatment. U.S. patent 4 743 662, 1988.

[217] Whinnery LL, Nichols MC, Wheeler DR, *et al*. Process for preparing silicon carbide foam. U.S. patent 5 668 188, 1997.

[218] Perale G, Giordano C, Daniele F, *et al*. A novel process for the manufacture of ceramic microelectrodes for biomedical applications. *Int J Appl Ceram Technol* 2008, **5**: 37–43.

[219] Narisawa M, Watase S, Matsukawa K, *et al*. White Si–O–C(–H) particles with photoluminescence synthesized by decarbonization reaction on polymer precursor in a hydrogen atmosphere. *Bull Chem Soc Jpn* 2012, **85**: 724–726.

[220] Dong SM, Chollon G, Labrugere C, *et al*. Characterization of nearly stoichiometric SiC ceramic fibres. *J Mater Sci* 2001, **36**: 2371–2381.

[221] Narisawa M, Funabiki F, Iwase A, *et al*. Effects of atmospheric composition on the molecular structure of synthesized silicon oxycarbides. *J Am Ceram Soc* 2015, **98**: 3373–3380.

[222] Chandra G, Martin TE. Rapid thermal process for obtaining silica coatings. E.P. patent 0 462 715, 1996.

[223] Krüger U, Ullrich R. Producing a ceramic layer by spraying polymer ceramic precursor particles onto a surface comprises using a cold gas spray nozzle. Siemens AG, German, 2006.

[224] Colombo P, Martucci A, Fogato O, *et al*. Silicon carbide films by laser pyrolysis of polycarbosilane. *J Am Ceram Soc* 2001, **84**: 224–226.

[225] Müller A, Herlin-Boime N, Ténégal F, *et al*. Comparison of Si/C/N pre-ceramics obtained by laser pyrolysis or furnace thermolysis. *J Eur Ceram Soc* 2003, **23**: 37–46.

[226] Wilden J, Fischer G. Laser synthesis of nanostructured ceramics from liquid precursors. *Appl Surf Sci* 2007, **254**: 1067–1072.

[227] Liu J, Qiao YL, Zhang P, *et al*. Synthesis of SiC ceramics from polysilazane by laser pyrolysis. *Surf Coat Technol* 2017, **321**: 491–495.

[228] Tangermann-Gerk K, Barroso G, Weisenseel B, *et al*. Laser pyrolysis of an organosilazane-based glass/ZrO$_2$ composite coating system. *Mater Des* 2016, **109**: 644–651.

[229] Wilden J, Bergmann JP, Schlichting S, *et al*. Direct laser pyrolysis of nanostructured micro components. In: Proceedings of the International Congress on Applications of Lasers & Electro-Optic, 2006: M1103.

[230] Ma RX, Erb D, Lu K. Flash pyrolysis of polymer-derived SiOC ceramics. *J Eur Ceram Soc* 2018, **38**: 4906–4914.

[231] Danko GA, Silberglitt R, Colombo P, *et al*. Comparison of microwave hybrid and conventional heating of preceramic polymers to form silicon carbide and silicon oxycarbide ceramics. *J Am Ceram Soc* 2004, **83**: 1617–1625.

[232] Zunjarrao SC, Dyjak P, Rahman A, *et al*. Microwave processing of actively seeded precursor for fabrication of polymer derived ceramics. *J Am Ceram Soc* 2016, **99**: 2260–2266.

[233] Pivin JC, Colombo P, Tonidandel M. Ion irradiation of preceramic polymer thin films. *J Am Ceram Soc* 1996, **79**: 1967–1970.

[234] Pivin JC, Colombo P, Sorarù GD. Comparison of ion irradiation effects in silicon-based preceramic thin films. *J Am Ceram Soc* 2000, **83**: 713–720.

[235] Pivin J, Colombo P. Ceramic coatings by ion irradiation of polycar bosilanes and polysiloxanes. Part II. Hardness and thermochemical stability. *Fuel Energy Abstr* 1998, **39**: 303.

[236] Pivin JC, Colombo P. Ceramic coatings by ion irradiation of polycarbosilanes and polysiloxanes: Part I Conversion mechanism. *J Mater Sci* 1997, **32**: 6163–6173.

[237] Tsukuda S, Seki S, Tagawa S, *et al*. Fabrication of nanowires using high-energy ion beams. *J Phys Chem B* 2004, **108**: 3407–3409.

[238] Srivastava SK, Avasthi DK, Pivin JC. Mechanism of H release from Si-based polymers under ion irradiation. *Nucl Instrum Methods Phys Res Sect B*: *Beam Interact Mater Atoms* 2002, **191**: 718–722.

[239] Pivin JC, Colombo P, Sendova-Vassileva M, *et al*. Ion-induced conversion of polysiloxanes and polycarbosilanes into ceramics: Mechanisms and properties. *Nucl Instrum Methods Phys Res Sect B*: *Beam Interact Mater Atoms* 1998, **141**: 652–662.

[240] Kumar A, Singh F, Pivin JC, *et al*. Photoluminescence studies of carbon clusters formed by irradiation of Si-based polymer. *Radiat Meas* 2005, **40**: 785–788.

[241] Liao NB, Xue W, Zhou HM, *et al*. Numerical investigation into the nanostructure and mechanical properties of amorphous SiBCN ceramics. *RSC Adv* 2013, **3**: 14458.

[242] Tomar V, Gan M, Kim HS. Atomistic analyses of the effect of temperature and morphology on mechanical strength of Si–C–N and Si–C–O nanocomposites. *J Eur Ceram Soc* 2010, **30**: 2223–2237.

[243] Kroll P. Searching insight into the atomistic structure of SiCO ceramics. *J Mater Chem* 2010, **20**: 10528.

[244] Amkreutz M, Frauenheim T. Understanding precursor-derived amorphous Si–C–N ceramics on the atomic scale. *Phys Rev B* 2002, **65**: 134113.

[245] Resta N, Kohler C, Trebin HR. Molecular dynamics simulations of amorphous Si–C–N ceramics: Composition dependence of the atomic structure. *J Am Ceram Soc* 2003, **86**: 1409–1414.

[246] Matsunaga K, Iwamoto Y. Molecular dynamics study of atomic structure and diffusion behavior in amorphous silicon nitride containing boron. *J Am Ceram Soc* 2004, **84**: 2213–2219.

[247] Bill J, Kamphowe TW, Müller A, *et al*. Precursor-derived Si–(B–)C–N ceramics: Thermolysis, amorphous state and crystallization. *Appl Organomet Chem* 2001, **15**: 777–793.

[248] Kleebe HJ, Turquat C, Sorarù GD. Phase separation in an SiCO glass studied by transmission electron microscopy and electron energy-loss spectroscopy. *J Am Ceram Soc* 2001, **84**: 1073–1080.

[249] Kleebe HJ, Blum YD. SiOC ceramic with high excess free carbon. *J Eur Ceram Soc* 2008, **28**: 1037–1042.

[250] Widgeon SJ, Sen S, Mera G, *et al*. ^{29}Si and ^{13}C solid-state NMR spectroscopic study of nanometer-scale structure and mass fractal characteristics of amorphous polymer derived silicon oxycarbide ceramics. *Chem Mater* 2010, **22**: 6221–6228.

[251] Scarmi A, Sorarù GD, Raj R. The role of carbon in unexpected visco(an)elastic behavior of amorphous silicon oxycarbide above 1273 K. *J Non-Cryst Solids* 2005, **351**: 2238–2243.

[252] Saha A, Raj R, Williamson DL. A model for the nanodomains in polymer-derived SiCO. *J Am Ceram Soc* 2006, **89**: 2188–2195 .

[253] Sen S, Stebbins JF. Phase separation, clustering, and fractal characteristics in glass: A magic-angle-spinning NMR spin-lattice relaxation study. *Phys Rev B* 1994, **50**: 822–830.

[254] Gabriel AO, Riedel R, Dressler W, *et al*. Thermal decomposition of poly(methylsilsesquicarbodiimide) to amorphous Si–C–N ceramics. *Chem Mater* 1999, **11**: 412–420.

[255] Iwamoto Y, Völger W, Kroke E, *et al*. Crystallization behavior of amorphous silicon carbonitride ceramics derived from organometallic precursors. *J Am Ceram Soc* 2004, **84**: 2170–2178.

[256] Michelle Morcos R, Mera G, Navrotsky A, *et al*. Enthalpy of formation of carbon-rich polymer-derived amorphous SiCN ceramics. *J Am Ceram Soc* 2008, **91**: 3349–3354.

[257] Mera G, Tamayo A, Nguyen H, *et al*. Nanodomain structure of carbon-rich silicon carbonitride polymer-derived ceramics. *J Am Ceram Soc* 2010, **93**: 1169–1175.

[258] Saha A, Raj R, Williamson DL, *et al*. Characterization of nanodomains in polymer-derived SiCN ceramics employing multiple techniques. *J Am Ceram Soc* 2005, **88**: 232–234.

[259] Liao NB, Xue W, Zhang M. Effect of carbon content on structural and mechanical properties of SiCN by atomistic simulations. *J Eur Ceram Soc* 2012, **32**: 1275–1281.

[260] Widgeon S, Mera G, Gao Y, *et al*. Nanostructure and energetics of carbon-rich SiCN ceramics derived from polysilylcarbodiimides: Role of the nanodomain interfaces. *Chem Mater* 2012, **24**: 1181–1191.

[261] Chen YH, Yang XP, Cao YJ, *et al*. Quantitative study on structural evolutions and associated energetics in polysilazane-derived amorphous silicon carbonitride ceramics. *Acta Mater* 2014, **72**: 22–31.

[262] Seitz J, Bill J, Egger N, *et al*. Structural investigations of Si/C/N–ceramics from polysilazane precursors by nuclear magnetic resonance. *J Eur Ceram Soc* 1996, **16**: 885–891.

[263] Traßl S, Suttor D, Motz G, *et al*. Structural characterisation of silicon carbonitride ceramics derived from polymeric precursors. *J Eur Ceram Soc* 2000, **20**: 215–225.

[264] Ionescu E, Kleebe HJ, Riedel R. Silicon-containing polymer-derived ceramic nanocomposites (PDC–NCs):

Preparative approaches and properties. *Chem Soc Rev* 2012, **41**: 5032.

[265] Kleebe HJ, Suttor D, Müller H, *et al*. Decomposition-crystallization of polymer-derived Si–C–N ceramics. *J Am Ceram Soc* 2005, **81**: 2971–2977.

[266] Kumar R, Cai Y, Gerstel P, *et al*. Processing, crystallization and characterization of polymer derived nano-crystalline Si–B–C–N ceramics. *J Mater Sci* 2006, **41**: 7088–7095.

[267] Zemanová M, Lecomte E, Šajgalík P, *et al*. Polysilazane derived micro/nano Si₃N₄/SiC composites. *J Eur Ceram Soc* 2002, **22**: 2963–2968.

[268] Gasch MJ, Wan J, Mukherjee AK. Preparation of a Si₃N₄/SiC nanocomposite by high-pressure sintering of polymer precursor derived powders. *Scripta Mater* 2001, **45**: 1063–1068.

[269] Xu TH, Ma QS, Chen ZH. High-temperature behavior of silicon oxycarbide glasses in air environment. *Ceram Int* 2011, **37**: 2555–2559.

[270] Ionescu E, Papendorf B, Kleebe HJ, *et al*. Polymer-derived silicon oxycarbide/hafnia ceramic nanocomposites. Part II: Stability toward decomposition and microstructure evolution at $T \gg 1000$ ℃. *J Am Ceram Soc* 2010, **93**: 1783–1789.

[271] Burns GT, Taylor RB, Xu YR, *et al*. High-temperature chemistry of the conversion of siloxanes to silicon carbide. *Chem Mater* 1992, **4**: 1313–1323.

[272] Le Coustumer P, Monthioux M, Oberlin A. Understanding Nicalon® fibre. *J Eur Ceram Soc* 1993, **11**: 95–103.

[273] Jansohn P. *Modern Gas Turbine Systems: High Efficiency, Low Emission, Fuel Flexible Power Generation*. Woodhead Publishing, 2013.

[274] Konegger T, Torrey J, Flores O, *et al*. Ceramics for sustainable energy technologies with a focus on polymer-derived ceramics. In: *Novel Combustion Concepts for Sustainable Energy Development*. Agarwal A, Pandey A, Gupta A, *et al*., Eds. New Delhi: Springer, 2014: 501–533.

[275] Asim N, Sopian K, Ahmadi S, *et al*. A review on the role of materials science in solar cells. *Renew Sustain Energy Rev* 2012, **16**: 5834–5847.

[276] Ameri T, Khoram P, Min J, *et al*. Organic ternary solar cells: A review. *Adv Mater* 2013, **25**: 4245–4266.

[277] Wright M, Uddin A. Organic–inorganic hybrid solar cells: A comparative review. *Sol Energy Mater Sol Cells* 2012, **107**: 87–111.

[278] Hu ZH, Wang J, Ma XL, *et al*. A critical review on semitransparent organic solar cells. *Nano Energy* 2020, **78**: 105376.

[279] Wang Y, Ruiz Diaz DF, Chen KS, *et al*. Materials, technological status, and fundamentals of PEM fuel cells —A review. *Mater Today* 2020, **32**: 178–203.

[280] Abdalla AM, Hossain S, Azad AT, *et al*. Nanomaterials for solid oxide fuel cells: A review. *Renew Sustain Energy Rev* 2018, **82**: 353–368.

[281] Majlan EH, Rohendi D, Daud WRW, *et al*. Electrode for

proton exchange membrane fuel cells: A review. *Renew Sustain Energy Rev* 2018, **89**: 117–134.

[282] Ren Z, Singh G. Nonoxide polymer-derived CMCs for "super" turbines. *Am Ceram Soc Bull* 2019, **98**: 34–39.

[283] Padture NP. Advanced structural ceramics in aerospace propulsion. *Nat Mater* 2016, **15**: 804–809.

[284] Perepezko JH. The hotter the engine, the better. *Science* 2009, **326**: 1068–1069.

[285] Clarke DR, Oechsner M, Padture NP. Thermal-barrier coatings for more efficient gas-turbine engines. *MRS Bull* 2012, **37**: 891–898.

[286] Information on https://www.powermag.com/another-world-record-for-combined-cycle-efficiency/.

[287] Spitsberg I, Steibel J. Thermal and environmental barrier coatings for SiC/SiC CMCs in aircraft engine applications. *Int J Appl Ceram Tec* 2004, **1**: 291–301.

[288] Yu ZJ, Luan XG, Riedel R. Editorial of the special issue on ultra-high temperature ceramic matrix composites. *J Eur Ceram Soc* 2016, **36**: 3551–3552.

[289] Ohnabe H, Masaki S, Onozuka M, *et al*. Potential application of ceramic matrix composites to aero-engine components. *Compos A*: *Appl Sci Manuf* 1999, **30**: 489–496.

[290] Naslain RR. The design of the fibre-matrix interfacial zone in ceramic matrix composites. *Compos A*: *Appl Sci Manuf* 1998, **29**: 1145–1155.

[291] Marshall DB, Cox BN. Integral textile ceramic structures. *Annu Rev Mater Res* 2008, **38**: 425–443.

[292] Dever JA, Nathal MV, DiCarlo JA. Research on high-temperature aerospace materials at NASA Glenn research center. *J Aerosp Eng* 2013, **26**: 500–514.

[293] Grady JE. CMC technology advancements for gas turbine engine applications. In: Proceedings of the American Ceramic Society's 10th Pacific Rim Conference on Ceramic and Glass Technology, 2013.

[294] Evans AG, Zok FW. The physics and mechanics of fibre-reinforced brittle matrix composites. *J Mater Sci* 1994, **29**: 3857–3896.

[295] Bansal NP, Lamon J. *Ceramic Matrix Composites*. Hoboken, NJ, USA: John Wiley & Sons, Inc., 2014.

[296] Kellner T. Made in rocket city: GE to mass-produce advanced space age material in the US for the first time. GE Reports, 2015. Available at https://www.designworldonline.com/ge-to-mass-produce-advanced-space-age-material-in-the-u-s-for-the-first-time/.

[297] Packirisamy S, Sreejith KJ, Devapal D, *et al*. Polymer-derived ceramics and their space applications. In: *Handbook of Advanced Ceramics and Composite*s. Cham: Springer International Publishing, 2020: 975–1080.

[298] Mainzer B, Lin CR, Jemmali R, *et al*. Characterization and application of a novel low viscosity polysilazane for the manufacture of C– and SiC–fiber reinforced SiCN ceramic matrix composites by PIP process. *J Eur Ceram Soc* 2019, **39**: 212–221.

[299] Song CK, Liu YS, Ye F, *et al*. Enhanced mechanical

property and tunable dielectric property of SiC$_f$/SiC–SiBCN composites by CVI combined with PIP. *J Adv Ceram* 2021, **10**: 758–767.

[300] Yajima S, Hayashi J, Omori M, *et al*. Development of a silicon carbide fibre with high tensile strength. *Nature* 1976, **261**: 683–685.

[301] Long X, Shao CW, Wang H, *et al*. Single-source-precursor synthesis of SiBNC–Zr ceramic nanocomposites fibers. *Ceram Int* 2016, **42**: 19206–19211.

[302] Nguyen VL, Proust V, Quievryn C, *et al*. Processing, mechanical characterization, and alkali resistance of SiliconBoronOxycarbide (SiBOC) glass fibers. *J Am Ceram Soc* 2014, **97**: 3143–3149.

[303] Bernard S, Cornu D, Miele P, *et al*. Polyborosilazane-derived ceramic fibers in the Si–B–C–N quaternary system for high-temperature applications. In: Proceedings of the Mechanical Properties and Performance of Engineering Ceramics and Composites: Ceramic Engineering and Science, Volume 26, 2005: 35–42.

[304] Ren Z, Singh G. Nonoxide polymer-derived CMCs for "super" turbines. *Am Ceram Soc Bull* 2019, **98**: 34–39.

[305] Ziegler G, Richter I, Suttor D. Fiber-reinforced composites with polymer-derived matrix: Processing, matrix formation and properties. *Compos A: Appl Sci Manuf* 1999, **30**: 411–417.

[306] Ionescu E, Linck C, Fasel C, *et al*. Polymer-derived SiOC/ZrO$_2$ ceramic nanocomposites with excellent high-temperature stability. *J Am Ceram Soc* 2010, **93**: 241–250.

[307] Proust V, Bechelany MC, Ghisleni R, *et al*. Polymer-derived Si–C–Ti systems: From titanium nanoparticle-filled polycarbosilanes to dense monolithic multi-phase components with high hardness. *J Eur Ceram Soc* 2016, **36**: 3671–3679.

[308] Wen QB, Luan XG, Wang L, *et al*. Laser ablation behavior of SiHfC-based ceramics prepared from a single-source precursor: Effects of Hf-incorporation into SiC. *J Eur Ceram Soc* 2019, **39**: 2018–2027.

[309] Ionescu E, Bernard S, Lucas R, *et al*. Polymer-derived ultra-high temperature ceramics (UHTCs) and related materials. *Adv Eng Mater* 2019, **21**: 1900269.

[310] Lee SH, Weinmann M, Aldinger F. Processing and properties of C/Si–B–C–N fiber-reinforced ceramic matrix composites prepared by precursor impregnation and pyrolysis. *Acta Mater* 2008, **56**: 1529–1538.

[311] Ding Q, Ni DW, Wang Z, *et al*. 3D C$_f$/SiBCN composites prepared by an improved polymer infiltration and pyrolysis. *J Adv Ceram* 2018, **7**: 266–275.

[312] Chen BW, Ding Q, Ni DW, *et al*. Microstructure and mechanical properties of 3D C$_f$/SiBCN composites fabricated by polymer infiltration and pyrolysis. *J Adv Ceram* 2021, **10**: 28–38.

[313] Ziegler G, Richter I, Suttor D. Fiber-reinforced composites with polymer-derived matrix: Processing, matrix formation and properties. *Compos A: Appl Sci Manuf* 1999, **30**: 411–417.

[314] Yuan Q, Chai ZF, Huang ZR, *et al*. A new precursor of liquid and curable polysiloxane for highly cost-efficient SiOC-based composites. *Ceram Int* 2019, **45**: 7044–7048.

[315] Xu TH, Ma QS, Chen ZH. High-temperature behavior of C$_f$/SiOC composites in inert atmosphere. *Mater Sci Eng: A* 2011, **530**: 266–270.

[316] Sreejith K, Rajasekhar B, Vijay V. Polymer-derived C$_f$/SiBOC ceramic matrix composites and a method of production thereof. Indian Patent Appl. No. 201841020417, 2018.

[317] Poerschke DL, Rossol MN, Zok FW. Intermediate temperature internal oxidation of a SiC/SiCN composite with a polymer-derived matrix. *J Am Ceram Soc* 2016, **99**: 3120–3128.

[318] Liu HT, Cheng HF, Wang J, *et al*. Effects of the single layer CVD SiC interphases on the mechanical properties of the SiC$_f$/SiC composites fabricated by PIP process. *Ceram Int* 2010, **36**: 2033–2037.

[319] Luo Z, Zhou XG, Yu JS. Mechanical properties of SiC/SiC composites by PIP process with a new precursor at elevated temperature. *Mater Sci Eng: A* 2014, **607**: 155–161.

[320] Wang JY, Yang ZH, Duan XM, *et al*. Microstructure and mechanical properties of SiC$_f$/SiBCN ceramic matrix composites. *J Adv Ceram* 2015, **4**: 31–38.

[321] Jones R, Szweda A, Petrak D. Polymer derived ceramic matrix composites. *Compos A: Appl Sci Manuf* 1999, **30**: 569–575.

[322] Poerschke DL, Rossol MN, Zok FW. Intermediate temperature internal oxidation of a SiC/SiCN composite with a polymer-derived matrix. *J Am Ceram Soc* 2016, **99**: 3120–3128.

[323] Luo Z, Zhou XG, Yu JS. Mechanical properties of SiC/SiC composites by PIP process with a new precursor at elevated temperature. *Mater Sci Eng: A* 2014, **607**: 155–161.

[324] Tian YL, Hu JD, Feng ZH, *et al*. Mechanical properties and high temperature failure mechanism of carbon fibers reinforced polysilazane-derived SiCN ceramic matrix composites via PIP process. *J Eur Ceram Soc* 2022, **42**: 890–897.

[325] Boitier G, Chermant JL, Vicens J. Understanding the creep behavior of a 2.5D C$_f$-SiC composite: II. Experimental specifications and macroscopic mechanical creep responses. *Mater Sci Eng: A* 2000, **289**: 265–275.

[326] Zhu SJ, Mizuno M, Kagawa Y, *et al*. Creep and fatigue behavior in Hi-Nicalon-fiber-reinforced silicon carbide composites at high temperatures. *J Am Ceram Soc* 1999, **82**: 117–128.

[327] Kopeliovich D. Advances in the manufacture of ceramic matrix composites using infiltration techniques. In: *Advances in Ceramic Matrix Composites*. Amsterdam: Elsevier, 2014: 79–108.

[328] Kumagawa K, Yamaoka H, Shibuya M, *et al*. Fabrication and mechanical properties of new improved Si–M–C–(O) tyranno fiber. In: Proceedings of the 22nd Annual

Conference on Composites, Advanced Ceramics, Materials, and Structures: A: Ceramic Engineering and Science Proceedings, Volume 19, 2014: 65–72.

[329] Kumagawa K, Yamaoka H, Shibuya M, *et al*. Thermal stability and chemical corrosion resistance of newly developed continuous Si–Zr–C–O tyranno fiber. In: Proceedings of the 21st Annual Conference on Composites, Advanced Ceramics, Materials, and Structures: A: Ceramic Engineering and Science Proceedings, Volume 18, 2008: 113–118.

[330] Liu Y, Chen KZ, Dong FB, *et al*. Effects of hydrolysis of precursor on the structures and properties of polymer-derived SiBN ceramic fibers. *Ceram Int* 2018, **44**: 10199–10203.

[331] Long X, Wu ZY, Shao CW, *et al*. High-temperature oxidation behavior of SiBN fibers in air. *J Adv Ceram* 2021, **10**: 768–777.

[332] Bai HW, Wen G, Huang XX, *et al*. Synthesis and structural characterization of SiBOC ceramic fibers derived from single-source polyborosiloxane. *J Eur Ceram Soc* 2011, **31**: 931–940.

[333] Toreki W, Batich CD, Sacks MD, *et al*. Polymer-derived silicon carbide fibers with low oxygen content and improved thermomechanical stability. *Compos Sci Technol* 1994, **51**: 145–159.

[334] Sacks MD, Morrone AA, Scheiffele GW, *et al*. Characterization of polymer-derived silicon carbide fibers with low oxygen content, near-stoichiometric composition, and improved thermomechanical stability. In: *Ceramic Engineering and Science Proceedings*. Hoboken, NJ, USA: John Wiley & Sons, Inc., 2009: 25–35.

[335] Evans AG, Zok FW. The physics and mechanics of fibre-reinforced brittle matrix composites. *J Mater Sci* 1994, **29**: 3857–3896.

[336] Motz G, Bordia RK. Processing, structure and properties of ceramic fibers. In: *Handbook of Textile Fibre Structure*. Amsterdam: Elsevier, 2009: 378–424.

[337] Viard A, Miele P, Bernard S. Polymer-derived ceramics route toward SiCN and SiBCN fibers: From chemistry of polycarbosilazanes to the design and characterization of ceramic fibers. *J Ceram Soc Jpn* 2016, **124**: 967–980.

[338] Viard A, Fonblanc D, Lopez-Ferber D, *et al*. Polymer derived Si–B–C–N ceramics: 30 years of research. *Adv Eng Mater* 2018, **20**: 1800360.

[339] Padture NP, Gell M, Jordan EH. Thermal barrier coatings for gas-turbine engine applications. *Science* 2002, **296**: 280–284.

[340] Padture NP. Environmental degradation of high-temperature protective coatings for ceramic-matrix composites in gas-turbine engines. *npj Mater Degrad* 2019, **3**: 11.

[341] Opila EJ. Oxidation kinetics of chemically vapor-deposited silicon carbide in wet oxygen. *J Am Ceram Soc* 1994, **77**: 730–736.

[342] Luan XG, Xu XM, Wang L, *et al*. Self-healing enhancing tensile creep of 2D-satin weave SiC/(SiC–SiBCN)$_x$ composites in wet oxygen environment. *J Eur Ceram Soc* 2020, **40**: 3509–3519.

[343] Lee KN, Fox DS, Eldridge JI, *et al*. Upper temperature limit of environmental barrier coatings based on mullite and BSAS. *J Am Ceram Soc* 2003, **86**: 1299–1306.

[344] Gadow R, Kern F. Liquid-phase coating of carbon fibers with pre-ceramic polymer precursors: Process and applications. *Adv Eng Mater* 2002, **4**: 883–886.

[345] Schütz A, Günthner M, Motz G, *et al*. Characterisation of novel precursor-derived ceramic coatings with glass filler particles on steel substrates. *Surf Coat Technol* 2012, **207**: 319–327.

[346] Günthner M, Kraus T, Dierdorf A, *et al*. Advanced coatings on the basis of Si(C)N precursors for protection of steel against oxidation. *J Eur Ceram Soc* 2009, **29**: 2061–2068.

[347] Liu J, Zhang LT, Hu F, *et al*. Polymer-derived yttrium silicate coatings on 2D C/SiC composites. *J Eur Ceram Soc* 2013, **33**: 433–439.

[348] Günthner M, Kraus T, Krenkel W, *et al*. Particle-filled PHPS silazane-based coatings on steel. *Int J Appl Ceram Technol* 2009, **6**: 373–380.

[349] Barroso GS, Krenkel W, Motz G. Low thermal conductivity coating system for application up to 1000 ℃ by simple PDC processing with active and passive fillers. *J Eur Ceram Soc* 2015, **35**: 3339–3348.

[350] Shah SR, Raj R. Multilayer design and evaluation of a high temperature environmental barrier coating for Si-based ceramics. *J Am Ceram Soc* 2007, **90**: 516–522.

[351] Zhao G, Hu P, Zhou S, *et al*. Ordered silica nanoparticles grown on a three-dimensional carbon fiber architecture substrate with siliconborocarbonitride ceramic as a thermal barrier coating. *ACS Appl Mater Interfaces* 2016, **8**: 4216–4225.

[352] Hasemann G, Baumann T, Dieck S, *et al*. Polymer-derived ceramics as innovative oxidation barrier coatings for Mo-Si-B alloys. *Metall Mater Trans A* 2015, **46**: 1455–1460.

[353] Kappa M, Kebianyor A, Scheffler M. A two-component preceramic polymer system for structured coatings on metals. *Thin Solid Films* 2010, **519**: 301–305.

[354] Gong X, An LN, Xu CY. Wireless passive sensor development for harsh environment applications. In: Proceedings of the IEEE International Workshop on Antenna Technology, 2012: 140–143.

[355] Tregay GW, Calabrese PR,. Kaplin PL, *et al*. Optical fiber sensor for temperature measurement from 600 to 1900 ℃ in gas turbine engines. In: Proceedings of SPIE - The International Society for Optical Engineering 1589, 1991: 38–47.

[356] Bhattacharya A, Srinivasa Rao R, Ghanashyam Krishna M. Characterization of Yb$_2$O$_3$ based optical temperature sensor for high temperature applications. *Sens Actuat A: Phys* 2007, **134**: 348–356.

[357] Zhang LG, Wang YS, Wei Y, *et al*. A silicon carbonitride ceramic with anomalously high piezoresistivity. *J Am Ceram Soc* 2008, **91**: 1346–1349.

[358] Riedel R, Toma L, Janssen E, *et al*. Piezoresistive effect in SiOC ceramics for integrated pressure sensors. *J Am Ceram Soc* 2010, **93**: 920–924.

[359] Wang YS, Zhang LG, Fan Y, *et al*. Stress-dependent piezoresistivity of tunneling-percolation systems. *J Mater Sci* 2009, **44**: 2814–2819.

[360] Ma BS, Wang YG. Fabrication of dense polymer-derived silicon carbonitride ceramic bulks by precursor infiltration and pyrolysis processes without losing piezoresistivity. *J Am Ceram Soc* 2018, **101**: 2752–2759.

[361] Li N, Cao YJ, Zhao R, *et al*. Polymer-derived SiAlOC ceramic pressure sensor with potential for high-temperature application. *Sens Actuat A*: *Phys* 2017, **263**: 174–178.

[362] Ricohermoso III E, Rosenburg F, Klug F, *et al*. Piezoresistive carbon-containing ceramic nanocomposites—A review. *Open Ceram* 2021, **5**: 100057.

[363] Shao G, Jiang JP, Jiang MJ, *et al*. Polymer-derived SiBCN ceramic pressure sensor with excellent sensing performance. *J Adv Ceram* 2020, **9**: 374–379.

[364] Nagaiah NR, Kapat JS, An L, *et al*. Novel polymer derived ceramic-high temperature heat flux sensor for gas turbine environment. *J Phys*: *Conf Ser* 2006, **34**: 458–463.

[365] Seo D, Jung S, Lombardo SJ, *et al*. Fabrication and electrical properties of polymer-derived ceramic (PDC) thin films for high-temperature heat flux sensors. *Sens Actuat A*: *Phys* 2011, **165**: 250–255.

[366] Zhao R, Shao G, Cao YJ, *et al*. Temperature sensor made of polymer-derived ceramics for high-temperature applications. *Sens Actuat A*: *Phys* 2014, **219**: 58–64.

[367] Nagaiah NR, Sleiti AK, Rodriguez S, *et al*. A novel design and analysis of a MEMS ceramic hot-wire anemometer for high temperature applications. *J Phys*: *Conf Ser* 2006, **34**: 277–282.

[368] Cheng HT, Shao G, Ebadi S, *et al*. Evanescent-mode-resonator-based and antenna-integrated wireless passive pressure sensors for harsh-environment applications. *Sens Actuat A*: *Phys* 2014, **220**: 22–33.

[369] Ren XH, Ebadi S, Chen YH, *et al*. Characterization of SiCN ceramic material dielectric properties at high temperatures for harsh environment sensing applications. *IEEE Trans Microw Theory Tech* 2013, **61**: 960–971.

[370] Li Y, Yu YX, San HS, *et al*. Wireless passive polymer-derived SiCN ceramic sensor with integrated resonator/antenna. *Appl Phys Lett* 2013, **103**: 163505.

[371] Wen L, Li F, Cheng HM. Carbon nanotubes and graphene for flexible electrochemical energy storage: From materials to devices. *Adv Mater* 2016, **28**: 4306–4337.

[372] Guo YG, Hu JS, Wan LJ. Nanostructured materials for electrochemical energy conversion and storage devices. *Adv Mater* 2008, **20**: 2878–2887.

[373] Mai LQ, Tian XC, Xu X, *et al*. Nanowire electrodes for electrochemical energy storage devices. *Chem Rev* 2014, **114**: 11828–11862.

[374] Han S, Wu DQ, Li S, *et al*. Porous graphene materials for advanced electrochemical energy storage and conversion devices. *Adv Mater* 2014, **26**: 849–864.

[375] Chen KF, Song SY, Liu F, *et al*. Structural design of graphene for use in electrochemical energy storage devices. *Chem Soc Rev* 2015, **44**: 6230–6257.

[376] Wang H, Yang Y, Guo L. Nature-inspired electrochemical energy-storage materials and devices. *Adv Energy Mater* 2017, **7**: 1601709.

[377] Chen S, Qiu L, Cheng HM. Carbon-based fibers for advanced electrochemical energy storage devices. *Chem Rev* 2020, **120**: 2811–2878.

[378] Mackanic DG, Chang TH, Huang Z, *et al*. Stretchable electrochemical energy storage devices. *Chem Soc Rev* 2020, **49**: 4466–4495.

[379] Zahir N, Magri P, Luo W, *et al*. Recent advances on graphene quantum dots for electrochemical energy storage devices. *Energy Environ Mater* 2021, https://doi.org/10.1002/eem2.12167.

[380] Tarascon JM, Armand M. Issues and challenges facing rechargeable lithium batteries. *Nature* 2001, **414**: 359–367.

[381] Scrosati B, Garche J. Lithium batteries: Status, prospects and future. *J Power Sources* 2010, **195**: 2419–2430.

[382] Bruce P, Scrosati B, Tarascon JM. Nanomaterials for rechargeable lithium batteries. *Angew Chem Int Ed* 2008, **47**: 2930–2946.

[383] Fergus JW. Recent developments in cathode materials for lithium ion batteries. *J Power Sources* 2010, **195**: 939–954.

[384] Ji LW, Lin Z, Alcoutlabi M, *et al*. Recent developments in nanostructured anode materials for rechargeable lithium-ion batteries. *Energy Environ Sci* 2011, **4**: 2682.

[385] Zhang WJ. A review of the electrochemical performance of alloy anodes for lithium-ion batteries. *J Power Sources* 2011, **196**: 13–24.

[386] Kim SW, Seo DH, Ma XH, *et al*. Electrode materials for rechargeable sodium-ion batteries: Potential alternatives to current lithium-ion batteries. *Adv Energy Mater* 2012, **2**: 710–721.

[387] Jian ZL, Han WZ, Lu X, *et al*. Superior electrochemical performance and storage mechanism of $Na_3V_2(PO_4)_3$ cathode for room-temperature sodium-ion batteries. *Adv Energy Mater* 2013, **3**: 156–160.

[388] Sun J, Lee HW, Pasta M, *et al*. A phosphorene–graphene hybrid material as a high-capacity anode for sodium-ion batteries. *Nat Nanotechnol* 2015, **10**: 980–985.

[389] Ji XL, Lee KT, Nazar LF. A highly ordered nanostructured carbon–sulphur cathode for lithium–sulphur batteries. *Nat Mater* 2009, **8**: 500–506.

[390] Yin YX, Xin S, Guo YG, *et al*. Lithium-sulfur batteries: Electrochemistry, materials, and prospects. *Angew Chem Int Ed* 2013, **52**: 13186–13200.

[391] Manthiram A, Fu YZ, Chung SH, *et al*. Rechargeable lithium–sulfur batteries. *Chem Rev* 2014, **114**: 11751–11787.

[392] Zhang LL, Zhao XS. Carbon-based materials as supercapacitor electrodes. *Chem Soc Rev* 2009, **38**: 2520–2531.

[393] Raza W, Ali F, Raza N, *et al*. Recent advancements in supercapacitor technology. *Nano Energy* 2018, **52**: 441–473.

[394] Wang Y, Shi ZQ, Huang Y, *et al*. Supercapacitor devices based on graphene materials. *J Phys Chem C* 2009, **113**: 13103–13107.

[395] Cheng FY, Chen J. Metal–air batteries: From oxygen reduction electrochemistry to cathode catalysts. *Chem Soc Rev* 2012, **41**: 2172.

[396] Kim J, Gwon O, Kwon O, *et al*. Synergistic coupling derived cobalt oxide with nitrogenated holey two-dimensional matrix as an efficient bifunctional catalyst for metal–air batteries. *ACS Nano* 2019, **13**: 5502–5512.

[397] Steele BC, Heinzel A. Materials for fuel-cell technologies. *Nature* 2001, **414**: 345–352.

[398] Cano ZP, Banham D, Ye SY, *et al*. Batteries and fuel cells for emerging electric vehicle markets. *Nat Energy* 2018, **3**: 279–289.

[399] Bhandavat R, Pei ZJ, Singh G. Polymer-derived ceramics as anode material for rechargeable Li-ion batteries: A review. *Nanomater Energy* 2012, **1**: 324–337.

[400] Information on https://www.iea.org/publications/freepublications/publication/EV_PHEV_Roadmap.pdf.

[401] Thomas BR. *Linden's Handbook of Batteries*, 4th edn. New York: McGraw-Hill Education, 2011.

[402] Whittingham MS. Electrical energy storage and intercalation chemistry. *Science* 1976, **192**: 1126–1127.

[403] Rolison DR, Nazar LF. Electrochemical energy storage to power the 21st century. *MRS Bull* 2011, **36**: 486–493.

[404] Yabuuchi N, Kubota K, Dahbi M, *et al*. Research development on sodium-ion batteries. *Chem Rev* 2014, **114**: 11636–11682.

[405] Fan XM, Hu GR, Zhang B, *et al*. Crack-free single-crystalline Ni-rich layered NCM cathode enable superior cycling performance of lithium-ion batteries. *Nano Energy* 2020, **70**: 104450.

[406] Nayak PK, Yang LT, Brehm W, *et al*. From lithium-ion to sodium-ion batteries: Advantages, challenges, and surprises. *Angew Chem Int Ed* 2018, **57**: 102–120.

[407] Li M, Lu J, Chen ZW, *et al*. 30 years of lithium-ion batteries. *Adv Mater* 2018, **30**: 1800561.

[408] Liu X, Huang JQ, Zhang Q, *et al*. Nanostructured metal oxides and sulfides for lithium-sulfur batteries. *Adv Mater* 2017, **29**: 1601759.

[409] Sun YT, Liu XR, Jiang YM, *et al*. Recent advances and challenges in divalent and multivalent metal electrodes for metal–air batteries. *J Mater Chem A* 2019, **7**: 18183–18208.

[410] Staffell I, Scamman D, Velazquez Abad A, *et al*. The role of hydrogen and fuel cells in the global energy system. *Energy Environ Sci* 2019, **12**: 463–491.

[411] Mukherjee S, Ren ZK, Singh G. Molecular polymer-derived ceramics for applications in electrochemical energy storage devices. *J Phys D: Appl Phys* 2018, **51**: 463001.

[412] Mera G, Navrotsky A, Sen S, *et al*. Polymer-derived SiCN and SiOC ceramics—Structure and energetics at the nanoscale. *J Mater Chem A* 2013, **1**: 3826.

[413] Francis A. Progress in polymer-derived functional silicon-based ceramic composites for biomedical and engineering applications. *Mater Res Express* 2018, **5**: 062003.

[414] Wu F, Maier J, Yu Y. Guidelines and trends for next-generation rechargeable lithium and lithium-ion batteries. *Chem Soc Rev* 2020, **49**: 1569–1614.

[415] Kim T, Song WT, Son DY, *et al*. Lithium-ion batteries: Outlook on present, future, and hybridized technologies. *J Mater Chem A* 2019, **7**: 2942–2964.

[416] Choi JW, Aurbach D. Promise and reality of post-lithium-ion batteries with high energy densities. *Nat Rev Mater* 2016, **1**: 16013.

[417] Agubra V, Fergus J. Lithium ion battery anode aging mechanisms. *Materials: Basel* 2013, **6**: 1310–1325.

[418] Smart MC, Ratnakumar BV. Effects of electrolyte composition on lithium plating in lithium-ion cells. *J Electrochem Soc* 2011, **158**: A379–A389.

[419] Ratnakumar BV, Smart MC. Lithium plating behavior in lithium-ion cells. *ECS Trans*, 2010, **25**: 241–252.

[420] Bhattacharyya R, Key B, Chen HL, *et al*. *In situ* NMR observation of the formation of metallic lithium microstructures in lithium batteries. *Nat Mater* 2010, **9**: 504–510.

[421] Honbo H, Takei K, Ishii Y, *et al*. Electrochemical properties and Li deposition morphologies of surface modified graphite after grinding. *J Power Sources* 2009, **189**: 337–343.

[422] Markervich E, Salitra G, Levi MD, *et al*. Capacity fading of lithiated graphite electrodes studied by a combination of electroanalytical methods, Raman spectroscopy and SEM. *J Power Sources* 2005, **146**: 146–150.

[423] Ning G, Haran BL, Popov BN. Capacity fade study of lithium-ion batteries cycled at high discharge rates. *J Power Sources* 2003, **117**: 160–169.

[424] Markovsky B, Rodkin A, Cohen YS, *et al*. The study of capacity fading processes of Li-ion batteries: Major factors that play a role. *J Power Sources* 2003, **119–121**: 504–510.

[425] Levi MD, Wang C, Gnanaraj JS, *et al*. Electrochemical behavior of graphite anode at elevated temperatures in organic carbonate solutions. *J Power Sources* 2003, **119–121**: 538–542.

[426] Gnanaraj JS, Levi MD, Levi E, *et al*. Comparison between the electrochemical behavior of disordered carbons and graphite electrodes in connection with their structure. *J Electrochem Soc* 2001, **148**: A525.

[427] Markovsky B, Levi MD, Aurbach D. The basic electroanalytical behavior of practical graphite-lithium

intercalation electrodes. *Electrochimica Acta* 1998, **43**: 2287–2304.

[428] Aurbach D, Levi MD, Levi E, *et al*. Common electroanalytical behavior of Li intercalation processes into graphite and transition metal oxides. *J Electrochem Soc* 1998, **145**: 3024–3034.

[429] Lu J, Chen ZW, Pan F, *et al*. High-performance anode materials for rechargeable lithium-ion batteries. *Electrochem Energy Rev* 2018, **1**: 35–53.

[430] Feng K, Li M, Liu WW, *et al*. Silicon-based anodes for lithium-ion batteries: From fundamentals to practical applications. *Small* 2018, **14**: 1702737.

[431] Zuo XX, Zhu J, Müller-Buschbaum P, *et al*. Silicon based lithium-ion battery anodes: A chronicle perspective review. *Nano Energy* 2017, **31**: 113–143.

[432] Bargeron CB, Benson RC, Jette AN, *et al*. Oxidation of hafnium carbide in the temperature range 1400 to 2060 ℃. *J Am Ceram Soc* 1993, **76**: 1040–1046.

[433] Li GD, Xiong X, Huang BY, *et al*. Oxidized characteristic and oxidized mechanism of TaC coating. *Chin J Nonferrous* 2007, **17**: 360–367. (in Chinese)

[434] Mera G, Gallei M, Bernard S, *et al*. Ceramic nanocomposites from tailor-made preceramic polymers. *Nanomaterials*: *Basel* 2015, **5**: 468–540.

[435] Graczyk-Zajac M, Reinold LM, Kaspar J, *et al*. New insights into understanding irreversible and reversible lithium storage within SiOC and SiCN ceramics. *Nanomaterials*: *Basel* 2015, **5**: 233–245.

[436] Knozowski D, Graczyk-Zajac M, Trykowski G, *et al*. Silicon oxycarbide-graphite electrodes for high-power energy storage devices. *Materials* 2020, **13**: 4302.

[437] Xing WB, Wilson AM, Eguchi K, *et al*. Pyrolyzed polysiloxanes for use as anode materials in lithium-ion batteries. *J Electrochem Soc* 1997, **144**: 2410–2416.

[438] Wilson AM, Reimers JN, Fuller EW, *et al*. Lithium insertion in pyrolyzed siloxane polymers. *Solid State Ion* 1994, **74**: 249–254.

[439] David L, Bhandavat R, Barrera U, *et al*. Polymer-derived ceramic functionalized MoS_2 composite paper as a stable lithium-ion battery electrode. *Sci Rep* 2015, **5**: 9792.

[440] Xing WB, Wilson AM, Zank G, *et al*. Pyrolysed pitch-polysilane blends for use as anode materials in lithium ion batteries. *Solid State Ion* 1997, **93**: 239–244.

[441] Wilson AM, Zank G, Eguchi K, *et al*. Polysiloxane pyrolysis. *Chem Mater* 1997, **9**: 1601–1606.

[442] Wilson AM, Zank G, Eguchi K, *et al*. Pyrolysed silicon-containing polymers as high capacity anodes for lithium-ion batteries. *J Power Sources* 1997, **68**: 195–200.

[443] Wilson A. Pyrolysed pitch-polysilane blends for use as anode materials in lithium ion batteries II: The effect of oxygen. *Solid State Ion* 1997, **100**: 259–266.

[444] Ahn D, Raj R. Thermodynamic measurements pertaining to the hysteretic intercalation of lithium in polymer-derived silicon oxycarbide. *J Power Sources* 2010, **195**: 3900–3906.

[445] Ahn D, Raj R. Cyclic stability and C-rate performance of amorphous silicon and carbon based anodes for electrochemical storage of lithium. *J Power Sources* 2011, **196**: 2179–2186.

[446] Sanchez-Jimenez PE, Raj R. Lithium insertion in polymer-derived silicon oxycarbide ceramics. *J Am Ceram Soc* 2010, **93**: 1127–1135.

[447] Saha A, Raj R, Williamson DL. A model for the nanodomains in polymer-derived SiCO. *J Am Ceram Soc* 2006, **89**: 2188–2195.

[448] Fukui H, Harimoto Y, Akasaka M, *et al*. Lithium species in electrochemically lithiated and delithiated silicon oxycarbides. *ACS Appl Mater Interfaces* 2014, **6**: 12827–12836.

[449] Fukui H, Ohsuka H, Hino T, *et al*. A Si–O–C composite anode: High capability and proposed mechanism of lithium storage associated with microstructural characteristics. *ACS Appl Mater Interfaces* 2010, **2**: 998–1008.

[450] Graczyk-Zajac M, Toma L, Fasel C, *et al*. Carbon-rich SiOC anodes for lithium-ion batteries: Part I. Influence of material UV-pre-treatment on high power properties. *Solid State Ion* 2012, **225**: 522–526.

[451] Graczyk-Zajac M, Vrankovic D, Waleska P, *et al*. The Li-storage capacity of SiOC glasses with and without mixed silicon oxycarbide bonds. *J Mater Chem A* 2018, **6**: 93–103.

[452] Knozowski D, Graczyk-Zając M, Vrankovic D, *et al*. New insights on lithium storage in silicon oxycarbide/carbon composites: Impact of microstructure on electrochemical properties. *Compos B*: *Eng* 2021, **225**: 109302.

[453] Kaspar J, Graczyk-Zajac M, Choudhury S, *et al*. Impact of the electrical conductivity on the lithium capacity of polymer-derived silicon oxycarbide (SiOC) ceramics. *Electrochimica Acta* 2016, **216**: 196–202.

[454] Kaspar J, Graczyk-Zajac M, Riedel R. Determination of the chemical diffusion coefficient of Li-ions in carbon-rich silicon oxycarbide anodes by electro-analytical methods. *Electrochimica Acta* 2014, **115**: 665–670.

[455] Wilamowska M, Pradeep VS, Graczyk-Zajac M, *et al*. Tailoring of SiOC composition as a way to better performing anodes for Li-ion batteries. *Solid State Ion* 2014, **260**: 94–100.

[456] Pradeep VS, Graczyk-Zajac M, Riedel R, *et al*. New insights in to the lithium storage mechanism in polymer derived SiOC anode materials. *Electrochimica Acta* 2014, **119**: 78–85.

[457] Pradeep VS, Ayana DG, Graczyk-Zajac M, *et al*. High rate capability of SiOC ceramic aerogels with tailored porosity as anode materials for Li-ion batteries. *Electrochimica Acta* 2015, **157**: 41–45.

[458] Haaks M, Kaspar J, Franz A, *et al*. 7Li NMR studies of lithium ion dynamics in polymer-derived silicon oxycarbide ceramics. *Solid State Ion* 2016, **287**: 28–35.

[459] Sun H, Zhao KJ. Atomistic origins of high capacity and high structural stability of polymer-derived SiOC anode materials. *ACS Appl Mater Interfaces* 2017, **9**: 35001–35009.

[460] Kaspar J, Graczyk-Zajac M, Riedel R. Lithium insertion into carbon-rich SiOC ceramics: Influence of pyrolysis temperature on electrochemical properties. *J Power Sources* 2013, **244**: 450–455.

[461] Fukui H, Ohsuka H, Hino T, *et al*. Preparation of microporous Si–O–C composite material and its lithium storage capability. *Chem Lett* 2009, **38**: 86–87.

[462] Xia KD, Wu ZX, Xuan CJ, *et al*. Effect of KOH etching on the structure and electrochemical performance of SiOC anodes for lithium-ion batteries. *Electrochimica Acta* 2017, **245**: 287–295.

[463] Sang ZY, Zhao ZH, Su D, *et al*. SiOC nanolayer wrapped 3D interconnected graphene sponge as a high-performance anode for lithium ion batteries. *J Mater Chem A* 2018, **6**: 9064–9073.

[464] Pradeep VS, Graczyk-Zajac M, Wilamowska M, *et al*. Influence of pyrolysis atmosphere on the lithium storage properties of carbon-rich polymer derived SiOC ceramic anodes. *Solid State Ion* 2014, **262**: 22–24.

[465] Shen J, Raj R. Silicon-oxycarbide based thin film anodes for lithium ion batteries. *J Power Sources* 2011, **196**: 5945–5950.

[466] Dong BB, Han YH, Wang T, *et al*. Hard SiOC microbeads as a high-performance lithium-ion battery anode. *ACS Appl Energy Mater* 2020, **3**: 10183–10191.

[467] Ma MB, Wang HJ, Li X, *et al*. Free-standing SiOC/nitrogen-doped carbon fibers with highly capacitive Li storage. *J Eur Ceram Soc* 2020, **40**: 5238–5246.

[468] Lim H, Kim H, Kim SO, *et al*. Novel approach for controlling free-carbon domain in silicone oil-derived silicon oxycarbide (SiOC) as an anode material in secondary batteries. *Chem Eng J* 2021, **404**: 126581.

[469] Shao GF, Hanaor DAH, Wang J, *et al*. Polymer-derived SiOC integrated with a graphene aerogel as a highly stable Li-ion battery anode. *ACS Appl Mater Interfaces* 2020, **12**: 46045–46056.

[470] Kaspar J, Graczyk-Zajac M, Lauterbach S, *et al*. Silicon oxycarbide/nano-silicon composite anodes for Li-ion batteries: Considerable influence of nano-crystalline vs. nano-amorphous silicon embedment on the electrochemical properties. *J Power Sources* 2014, **269**: 164–172.

[471] Xia KD, Qu L, Liu X, *et al*. Effect of SnCl$_2$ addition on the structure and lithium storage performance of SiOC anodes. *Appl Surf Sci* 2020, **506**: 144775.

[472] Dubey RJ, Sasikumar PVW, Cerboni N, *et al*. Silicon oxycarbide-antimony nanocomposites for high-performance Li-ion battery anodes. *Nanoscale* 2020, **12**: 13540–13547.

[473] Zank GA, Dahn JR, Wilson AM, *et al*. Electrodes for lithium ion batteries using polysilazanes ceramic with lithium. U.S. Patent 5631106(A), 1997.

[474] Liebau-Kunzmann V, Fasel C, Kolb R, *et al*. Lithium containing silazanes as precursors for SiCN: Li ceramics—A potential material for electrochemical applications. *J Eur Ceram Soc* 2006, **26**: 3897–3901.

[475] Su D, Li YL, Feng Y, *et al*. Electrochemical properties of polymer-derived SiCN materials as the anode in lithium ion batteries. *J Am Ceram Soc* 2009, **92**: 2962–2968.

[476] Feng Y. Electrochemical properties of heat-treated polymer-derived SiCN anode for lithium ion batteries. *Electrochimica Acta* 2010, **55**: 5860–5866.

[477] Kaspar J, Mera G, Nowak AP, *et al*. Electrochemical study of lithium insertion into carbon-rich polymer-derived silicon carbonitride ceramics. *Electrochimica Acta* 2010, **56**: 174–182.

[478] Graczyk-Zajac M, Mera G, Kaspar J, *et al*. Electrochemical studies of carbon-rich polymer-derived SiCN ceramics as anode materials for lithium-ion batteries. *J Eur Ceram Soc* 2010, **30**: 3235–3243.

[479] Reinold LM, Graczyk-Zajac M, Gao Y, *et al*. Carbon-rich SiCN ceramics as high capacity/high stability anode material for lithium-ion batteries. *J Power Sources* 2013, **236**: 224–229.

[480] Liu GW, Kaspar J, Reinold LM, *et al*. Electrochemical performance of DVB-modified SiOC and SiCN polymer-derived negative electrodes for lithium-ion batteries. *Electrochimica Acta* 2013, **106**: 101–108.

[481] Baek SH, Reinold LM, Graczyk-Zajac M, *et al*. Lithium dynamics in carbon-rich polymer-derived SiCN ceramics probed by nuclear magnetic resonance. *J Power Sources* 2014, **253**: 342–348.

[482] Wilamowska M, Graczyk-Zajac M, Riedel R. Composite materials based on polymer-derived SiCN ceramic and disordered hard carbons as anodes for lithium-ion batteries. *J Power Sources* 2013, **244**: 80–86.

[483] Graczyk-Zajac M, Wimmer M, Xu YP, *et al*. Lithium intercalation into disordered carbon/SiCN composite. Part 2: Raman spectroscopy and ^{7}Li MAS NMR investigation of lithium storage sites. *J Solid State Electrochem* 2017, **21**: 47–55.

[484] Graczyk-Zajac M, Wimmer M, Neumann C, *et al*. Lithium intercalation into SiCN/disordered carbon composite. Part 1: Influence of initial carbon porosity on cycling performance/capacity. *J Solid State Electrochem* 2015, **19**: 2763–2769.

[485] Feng Y, Dou SM, Wei YZ, *et al*. Preparation and capacity-fading investigation of polymer-derived silicon carbonitride anode for lithium-ion battery. *ACS Omega* 2017, **2**: 8075–8085.

[486] Storch M, Vrankovic D, Graczyk-Zajac M, *et al*. The influence of pyrolysis temperature on the electrochemical behavior of porous carbon-rich SiCN polymer-derived ceramics. *Solid State Ion* 2018, **315**: 59–64.

[487] Rohrer J, Vrankovic D, Cupid D, *et al*. Si- and Sn-containing SiOCN-based nanocomposites as anode materials for lithium ion batteries: Synthesis, thermodynamic

characterization and modeling. *Int J Mater Res* 2017, **108**: 920–932.

[488] Ng SF, Lau MYL, Ong WJ. Lithium-sulfur battery cathode design: Tailoring metal-based nanostructures for robust polysulfide adsorption and catalytic conversion. *Adv Mater* 2021, https://doi.org/10.1002/adma.202008654.

[489] Weinberger M, Munding J, Lindén M, *et al*. Template-derived submicrometric carbon spheres for lithium-sulfur and sodium-ion battery electrodes. *Energy Technol* 2018, **6**: 1797–1804.

[490] Qu FM, Graczyk-Zajac M, Vrankovic D, *et al*. Effect of morphology of C-rich silicon carbonitride ceramic on electrochemical properties of sulfur cathode for Li–S battery. *Electrochimica Acta* 2021, **384**: 138265.

[491] Fang RY, Xia Y, Liang C, *et al*. Supercritical CO_2-assisted synthesis of 3D porous SiOC/Se cathode for ultrahigh areal capacity and long cycle life Li–Se batteries. *J Mater Chem A* 2018, **6**: 24773–24782.

[492] Zeng LC, Li WH, Jiang Y, *et al*. Recent progress in Li–S and Li–Se batteries. *Rare Met* 2017, **36**: 339–364.

[493] Jin J, Tian XC, Srikanth N, *et al*. Advances and challenges of nanostructured electrodes for Li–Se batteries. *J Mater Chem A* 2017, **5**: 10110–10126.

[494] Vaalma C, Buchholz D, Weil M, *et al*. A cost and resource analysis of sodium-ion batteries. *Nat Rev Mater* 2018, **3**: 18013.

[495] Palomares V, Serras P, Villaluenga I, *et al*. Na-ion batteries, recent advances and present challenges to become low cost energy storage systems. *Energy Environ Sci* 2012, **5**: 5884.

[496] Sangster J. C–Na (carbon–sodium) system. *J Phase Equilibria Diffusion* 2007, **28**: 571–579.

[497] Stevens DA, Dahn JR. High capacity anode materials for rechargeable sodium-ion batteries. *J Electrochem Soc* 2000, **147**: 1271.

[498] Wenzel S, Hara T, Janek J, *et al*. Room-temperature sodium-ion batteries: Improving the rate capability of carbon anode materials by templating strategies. *Energy Environ Sci* 2011, **4**: 3342.

[499] Palomares V, Casas-Cabanas M, Castillo-Martínez E, *et al*. Update on Na-based battery materials. A growing research path. *Energy Environ Sci* 2013, **6**: 2312.

[500] Slater MD, Kim D, Lee E, *et al*. Sodium-ion batteries. *Adv Funct Mater* 2013, **23**: 947–958.

[501] Kaspar J, Storch M, Schitco C, *et al*. SiOC(N)/hard carbon composite anodes for Na-ion batteries: Influence of morphology on the electrochemical properties. *J Electrochem Soc* 2015, **163**: A156–A162.

[502] Lee Y, Lee KY, Choi W. One-pot synthesis of antimony-embedded silicon oxycarbide materials for high-performance sodium-ion batteries. *Adv Funct Mater* 2017, **27**: 1702607.

[503] Kim D, Kim H, Lim H, *et al*. A facile control in free-carbon domain with divinylbenzene for the high-

rate-performing Sb/SiOC composite anode material in sodium-ion batteries. *Int J Energy Res* 2020, **44**: 11473–11486.

[504] Chandra C, Kim J. Silicon oxycarbide produced from silicone oil for high-performance anode material in sodium ion batteries. *Chem Eng J* 2018, **338**: 126–136.

[505] Chandra C, Cahyadi HS, Alvin S, *et al*. Revealing the sodium storage mechanism in high-temperature-synthesized silicon oxycarbides. *Chem Mater* 2020, **32**: 410–423.

[506] Lim H, Yu S, Choi W, *et al*. Hierarchically designed nitrogen-doped MoS_2/silicon oxycarbide nanoscale heterostructure as high-performance sodium-ion battery anode. *ACS Nano* 2021, **15**: 7409–7420.

[507] Putra RN, Halim M, Ali G, *et al*. High-rate sodium insertion/extraction into silicon oxycarbide-reduced graphene oxide. *New J Chem* 2020, **44**: 14035–14040.

[508] Chandra C, Devina W, Alvin S, *et al*. New strategy for increasing sodium-ion uptake in silicon oxycarbides. *Chem Eng J* 2021, **404**: 126520.

[509] Li Z, Dong Y, Feng J, *et al*. Controllably enriched oxygen vacancies through polymer assistance in titanium pyrophosphate as a super anode for Na/K-ion batteries. *ACS Nano* 2019, **13**: 9227–9236.

[510] Sang ZY, Su D, Wang JS, *et al*. Bi-continuous nanoporous carbon sphere derived from SiOC as high-performance anodes for PIBs. *Chem Eng J* 2020, **381**: 122677.

[511] Jiang YQ, Liu JP. Definitions of pseudocapacitive materials: A brief review. *Energy Environ Mater* 2019, **2**: 30–37.

[512] Poonam, Sharma K, Arora A, *et al*. Review of supercapacitors: Materials and devices. *J Energy Storage* 2019, **21**: 801–825.

[513] Muzaffar A, Ahamed MB, Deshmukh K, *et al*. A review on recent advances in hybrid supercapacitors: Design, fabrication and applications. *Renew Sustain Energy Rev* 2019, **101**: 123–145.

[514] Abass MA, Syed AA, Gervais C, *et al*. Synthesis and electrochemical performance of a polymer-derived silicon oxycarbide/boron nitride nanotube composite. *RSC Adv* 2017, **7**: 21576–21584.

[515] Pazhamalai P, Krishnamoorthy K, Sahoo S, *et al*. Carbothermal conversion of siloxene sheets into silicon-oxy-carbide lamellae for high-performance supercapacitors. *Chem Eng J* 2020, **387**: 123886.

[516] Mujib SB, Cuccato R, Mukherjee S, *et al*. Electrospun SiOC ceramic fiber mats as freestanding electrodes for electrochemical energy storage applications. *Ceram Int* 2020, **46**: 3565–3573.

[517] Kim M, Oh I, Kim J. Influence of surface oxygen functional group on the electrochemical behavior of porous silicon carbide based supercapacitor electrode. *Electrochimica Acta* 2016, **196**: 357–368.

[518] Okoroanyanwu U, Bhardwaj A, Einck V, *et al*. Rapid preparation and electrochemical energy storage applications

of silicon carbide and silicon oxycarbide ceramic/carbon nanocomposites derived via flash photothermal pyrolysis of organosilicon preceramic polymers. *Chem Mater* 2021, **33**: 678–694.

[519] Moyano JJ, Mosa J, Aparicio M, *et al*. Strong and light cellular silicon carbonitride—Reduced graphene oxide material with enhanced electrical conductivity and capacitive response. *Addit Manuf* 2019, **30**: 100849.

[520] Meier A, Weinberger M, Pinkert K, *et al*. Silicon oxycarbide-derived carbons from a polyphenylsilsequioxane precursor for supercapacitor applications. *Microporous Mesoporous Mater* 2014, **188**: 140–148.

[521] Duan LQ, Ma QS, Mei L, *et al*. Fabrication and electrochemical performance of nanoporous carbon derived from silicon oxycarbide. *Microporous Mesoporous Mater* 2015, **202**: 97–105.

[522] Tolosa A, Krüner B, Jäckel N, *et al*. Electrospinning and electrospraying of silicon oxycarbide-derived nanoporous carbon for supercapacitor electrodes. *J Power Sources* 2016, **313**: 178–188.

[523] Yang J, Wu HL, Zhu M, *et al*. Optimized mesopores enabling enhanced rate performance in novel ultrahigh surface area meso-/microporous carbon for supercapacitors. *Nano Energy* 2017, **33**: 453–461.

[524] Swain IP, Pati S, Behera SK. A preceramic polymer derived nanoporous carbon hybrid for supercapacitors. *Chem Commun* 2019, **55**: 8631–8634.

[525] Sun HY, Pan JM, Yan XH, *et al*. MnO_2 nanoneedles loaded on silicon oxycarbide-derived hierarchically porous carbon for supercapacitor electrodes with enhanced electrochemical performance. *Ceram Int* 2019, **45**: 24802–24810.

[526] Smith SA, Park JH, Williams BP, *et al*. Polymer/ceramic co-continuous nanofiber membranes via room-curable organopolysilazane for improved lithium-ion battery performance. *J Mater Sci* 2017, **52**: 3657–3669.

[527] Smith SA, Williams BP, Joo YL. Effect of polymer and ceramic morphology on the material and electrochemical properties of electrospun PAN/polymer derived ceramic composite nanofiber membranes for lithium ion battery separators. *J Membr Sci* 2017, **526**: 315–322.

[528] Moni P, Deschamps A, Schumacher D, *et al*. A new silicon oxycarbide based gas diffusion layer for zinc–air batteries. *J Colloid Interface Sci* 2020, **577**: 494–502.

Erratum

Erratum to: Si-based polymer-derived ceramics for energy conversion and storage

Qingbo WEN^{a,†}, Fangmu QU^{c,†}, Zhaoju YU^{b,*},
Magdalena GRACZYK-ZAJAC^{c,d,*}, Xiang XIONG^{a}, Ralf RIEDEL^{c}

^{a}*State Key Laboratory of Powder Metallurgy, Central South University, Changsha 410083, China*
^{b}*College of Materials, Key Laboratory of High-Performance Ceramic Fibers (Xiamen University), Ministry of Education, Xiamen 361005, China*
^{c}*Technische Universität Darmstadt, Institut für Materialwissenschaft, Otto-Berndt-Straße 3, D-64287, Darmstadt, Germany*
^{d}*EnBW Energie Baden-Württemberg AG, Durlacher Allee 93, 76131 Karlsruhe, Germany*

Erratum to

The online version of the original article can be found at
https://doi.org/10.1007/s40145-021-0562-2

---

† Qingbo Wen and Fangmu Qu contributed equally to this work.

* Corresponding authors.

E-mail: Z. Yu, zhaojuyu@xmu.edu.cn;
        M. Graczyk-Zajac, m.graczyk-zajac@enbw.com

Polymer-Derived Ceramic Aerogels to Immobilize Sulfur for Li-S Batteries

Andrea Zambotti, Fangmu Qu,* Giacomo Costa, Magdalena Graczyk-Zajac, and Gian Domenico Sorarù

Lithium–sulfur batteries are among the promising high-capacity candidates owing to the superior theoretical capacity of sulfur, when compared with conventional cathodes such as LiCoO$_2$. However, several issues must be addressed before these batteries can be considered fully operational. Major issues regard the insulating nature of sulfur and the so-called shuttle effect of soluble polysulfides, which dramatically reduces the cathode capacity upon cycling. Herein, three carbon-containing polymer-derived ceramic aerogels are characterized belonging to the Si-C-O and Si-C-N systems, infiltrated with sulfur to work as cathodes for Li-S batteries. The electrochemical performances are evaluated in relation to the microstructural and chemical features of such materials. In particular, the effect of the pore size of the ceramic matrices on the shuttling behavior of polysulfides is investigated. Despite the high initial specific capacities exceeding hundreds of mAh g^{-1}, all types of cathodes show stable capacities in the 60–120 mAh g^{-1} range after 100 cycles.

A. Zambotti, G. Costa, G. D. Sorarù
Department of Industrial Engineering
Glass & Ceramics Laboratory
University of Trento
Via Sommarive 9, 38123 Trento, Italy

F. Qu, M. Graczyk-Zajac
Institute of Materials ScienceDarmstadt University of Technology
Otto-Berndt-Str. 3, 64287 Darmstadt, Germany
E-mail: fangmu.qu@stud.tu-darmstadt.de

M. Graczyk-Zajac
Research and Development
EnBW Energie Baden-Württemberg AG
Durlacher Allee 93, 76131 Karlsruhe, Germany

G. D. Sorarù
National Research Council of Italy (ICMATE-CNR)
Institute of Condensed Matter Chemistry and Technologies for Energy
Via Marini 6, I-16149 Genoa, Italy

The ORCID identification number(s) for the author(s) of this article can be found under https://doi.org/10.1002/ente.202300488.

1. Introduction

As demonstrated in the pioneering work of Yajima in the mid-70s, nonoxide ceramics such as SiC can be obtained via pyrolysis of Si-containing preceramic polymers.[1] Since then, the so-called polymer-derived ceramic (PDC) route has been demonstrated for a large number of binary (Si-C; B-N), ternary (Si-C-O, Si-C-N), and quaternary (Si-B-C-O; Si-B-C-N, Si-Ti-O-C) ceramic compositions.[2–4] The PDC route also allows processing components with difficult-to-obtain microstructure and/or shape: fibers,[5] foams,[6] aerogels,[7] and microlattices/honeycombs.[8]

Taking advantage of the high chemical and thermal stability of PDC aerogels and from their easy tailorable composition and porosity (i.e., total porosity and pore size),[9,10] they have been proposed for different applications like matrices for thermal energy storage (TES) to confine high temperature melting and chemically aggressive phase change materials (PCM)[11,12] or as sorbents for water purification.[13,14] Polymer-derived silicon oxycarbides have also shown higher lithium storage capacity compared to conventional graphite-based anodes[15] and SiOC aerogels displayed also very high lithium reversible capacity at very high charging/discharging rates, namely, 300 mAh g^{-1} at 20 C.[16]

Nowadays lithium-ion batteries are used in portable electronics and cars and are proposed as backup storage for many intermittent renewable energy sources.[17,18] However, researchers are still working to improve the performance of these devices either to increase the specific capacity or by substituting rare and health-hazardous elements, like Co present in most of the cathode materials, with safer ones. A possible solution to these problems is to use sulfur as cathode material in Li-S batteries.[19] Sulfur has a higher theoretical specific capacity, 1,675 mAh g^{-1} compared to 150–220 mAh g^{-1} for common cathode materials, it is nontoxic, abundant, and available on the earth's crust. However, sulfur cathodes suffer from other problems: sulfur is electrically insulating and shows a rapid capacity fading related to the high solubility of lithium polysulfides in the liquid electrolyte which results in the well-known "shuttle effect." Moreover, during the lithiation, the volume of sulfur increases by around 80%, leading to electrode disintegration during cycling.[20] To overcome these limitations, sulfur is often confined in a conductive C-based matrix. Based on the idea that porosity also plays a pivotal role in blocking or reducing the diffusion of

ADVANCED
SCIENCE NEWS

www.advancedsciencenews.com

Energy Technology
Generation, Conversion, Storage, Distribution

www.entechnol.de

lithium polysulfides from the cathode to the anode, many different forms of porous carbon having different pore sizes and amount of porosity (active C, carbon nanotubes, C aerogels, C fibers mats, etc.) have been studied.[21] Porous C-rich Si-based PDCs have been also investigated as a confinement material in S cathodes.[22–24]

In this work, we studied the electrochemical performance of three different sulfur/PDC cathodes. For two of them sulfur is contained in PDCs aerogels belonging to the Si-O-C and Si-C-N systems, respectively, obtained via CO_2 supercritical drying[9,25] while in the third one sulfur is confined in a mesoporous SiOC processed via the "polymeric spacer" method.[26] The composite cathodes have been electrochemically characterized and their performances are discussed and related to the chemical composition and microstructure of the PDCs scaffold.

2. Experimental Section

2.1. Synthesis of PDC Aerogel

Synthesis of the PDC aerogels followed published procedures.[16,25] Commercial polysiloxane (polyhydromethylsiloxane, PHMS, CAS: 63148-57-2, ABCR, Karlsruhe, Germany) and polysilazane (Durazane 1800 CAS: 503590-70-3, DurXtreme, Ulm, Germany) were chosen as precursors for the synthesis of Si-O-C and Si-C-N aerogels, respectively. Divinylbenzene (DVB, CAS: 1321-74-0, technical grade 80%, Sigma-Aldrich, Saint Louis, MO, USA) was used as crosslinker. Platinum divinyltetramethyldisiloxane complex in xylene (Karstedt's catalyst, CAS: 68478–92–2), with Pt content of $\approx$2% (Sigma–Aldrich, Saint Louis, MO, USA) was further diluted to obtain a solution containing 0.1 wt% of catalyst. Cyclohexane (Carlo Erba, CAS: 110-82-7, Milano, Italy) was used as solvent. Crosslinking was obtained via hydrosilylation reactions between the Si-H bonds of the Si-polymer and the vinyl groups of DVB in the presence of Pt catalyst.[27] The preceramic polymer (PHMS or Durazane) was mixed with DVB in cyclohexane and then Pt catalyst was added. The amounts of the reagents used for the synthesis are reported in **Table 1**. The mixture was magnetically stirred for 5 min and then poured into the Teflon container of a pressure reactor (Parr Digestion Vessel 4749, Parr Instrument Company, Moline, IL, USA). The reactor was then heated at 180 °C/24 h to complete the curing of the gel. At the end of the crosslinking process, the wet gel was solvent exchanged in cyclohexane (2 times a day for 3 days) before loading into the reactor for CO_2 supercritical drying. Preceramic aerogels were pyrolyzed at 1,000 °C/1 h, 10 °C min^{-1}, in flowing Ar (100 mL min^{-1}) using alumina boats in an alumina tube furnace (Lindberg Blu, USA).

2.2. Synthesis of Mesoporous SiOC

Synthesis of the mesoporous SiOC via the "polymeric spacer" method is reported in detail elsewhere.[26] In this case, PHMS (CAS: 63148-57-2, ABCR, Karlsruhe, Germany) is reacted, via hydrosilylation reactions, with a vinyl-terminated polydimethylsiloxane having an average molecular weight of 9,400 DA, viscosity 200 cSt. (Vy-PDMS, CAS: 68083-19-2, Gelest, Morrisville, PA, USA) and with 1,3,5,7-tetravinyl-1,3,5,7-tetramethylcyclotetrasiloxane 95% (TVTMS, CAS: 27342-69-4, ABCR, Karlsruhe, Germany) used as crosslinker enhancer. The vinyl-terminated PDMS serves the double purpose of solvent, at the initial stage of the synthesis, and as a size-controlling templating agent. Indeed, during pyrolysis, vinyl-PDMS decomposes almost completely and leaves a porous SiOC with pore size related to its MW. Details of the synthesis are reported in Table 1. Mesoporous SiOC samples were obtained after pyrolysis at 800 °C/1 h using the same furnace and pyrolysis conditions (heating rate and atmosphere) as the PDC aerogels.

In both cases, for the synthesis of the aerogels and of the mesoporous SiOC, the manipulation of the reagents was performed under gentle Ar flow to prevent reaction with oxygen and moisture.

2.3. Preparation of the Porous PDC/S Composite Cathodes

To produce the composite electrodes, a recipe proposed by Qu et al.[23] was followed. In brief, the porous SiOCs were first milled using a mortar to obtain fine powders and, after that, a quantity of sulfur doubled in weight with respect to the SiOC was added and the powders were further milled to homogenize the mixture. The SiOC/S powders were then loaded into a pressure reactor (Parr digestion vessel) which was placed inside an oven at 155 °C for 24 h. At these conditions, sulfur is in its liquid state and can flow into the pores of the ceramic matrix.

Once the thermal treatment was completed, the mixture was extracted from the vessel and grounded to obtain a composite powder which was further used to produce the electrodes for testing. Accordingly, a slurry containing 85 wt% PDC-sulfur composite, 10 wt% polyvinylidene fluoride, PVDF, as a binder, and 5% super P carbon black (Timcal Ltd) was prepared. Methyl-2-pyrrolidone (NMP, BASF) was utilized as a solvent of the slurry. Aluminum foil (Alfa Aesar) was employed as contact over which the slurry was pasted and consequently dried (in the oven, at 40 °C for 24 h). Electrodes of 10 mm diameter were punched out of the deposited material to serve as ready-to-use cathodes. Swagelok cells were assembled in a T-cell configuration,

Table 1. Amounts of reagents used in the synthesis of the preceramic samples.

Sample	Preceramic polymer	Crosslinker	DVB/Preceramic polymer [wt wt^{-1}]	TVTMS/ PHMS [wt wt^{-1}]	Vinyl-PDMS/ PHMS [wt wt^{-1}]	Pt catalyst [μl g^{-1} of preceramic polymer]	Cyclohexane [vol%]
SiOC-A	PHMS	DVB	2	–	–	200	90
SiCN-A	Durazane 1800	DVB	2	–	–	100	90
spSiOC	PHMS	TVTMS	–	0.04	1.5	20*	–

*Pt 2% (not diluted).

**ADVANCED
SCIENCE NEWS**

www.advancedsciencenews.com

Energy Technology

Generation, Conversion, Storage, Distribution

www.entechnol.de

separating the cathode and a 0.75 mm thick lithium foil (anode) with an A-grade quartz membrane. As a liquid electrolyte, we utilized 1 M lithium bis(trifluoromethanesulfonyl) imide, LiTFSI, dissolved in a mixture of 1,3-dioxolane, DOL, and dimethoxymethane, DME, in a 1:1 volume ratio. To reduce shuttle effects in the testing of the cells, 0.1 M LiNO₃ was added to the electrolyte solution. A total of two tests per composite cathode were performed to check for reproducibility of the electrochemical measurements.

2.4. Characterization Techniques

Porosity, pore size distribution, and specific surface area (SSA) of the porous SiOC were investigated by recording N_2 adsorption and desorption isotherms. Experiments were carried out with an Autosorb iQ analyzer (Anton-Paar, Gratz, AU) in the $10^{-6} \leq P/P^0 \leq 1$ range. A nonlocal density functional theory (NLDFT) approach on the adsorption branch of the isotherm was utilized for the pore size distribution in the mesopore-micropore range, imposing an adsorption model that of silica with cylindrical pores. All calculations were made using the Quantachrome ASiQwin software.

A Gemini SUPRA 40 FE-SEM scanning electron microscope (Carl Zeiss, Germany) was used to investigate the morphology of the porous ceramic SiOC. Micrographs were obtained after sputtering the sample surface with an Au/C film to prevent charging during the observation.

Thermogravimetric and differential thermal analysis (TGA/DTA) measurements were performed using a Netzsch STA 409 instrument. The main objective of this measurement was to estimate the amount of sulfur in the composites. The thermal evolution of the aerogel-sulfur composites was carried out under 100 cc min⁻¹ pure air flow, heating about 50 mg of material with a 10 °C min⁻¹ rate up to a temperature of 1,000 °C.

C and Si contents of the ceramic samples were analyzed by Mikroanalytisches Labor Pascher (Remagen-Bandorf, Germany). Carbon was analyzed based on combustion techniques while silicon was measured using inductively coupled plasma atomic emission spectroscopy.

X-ray diffractograms, XRD, were collected using a Rigaku D-Max diffractometer (Rigaku, Tokyo, Japan) in the Bragg–Brentano configuration with CuKα radiation operating at 40 kV and 30 mA. The scanning range was $2\theta = 10$–60 with a step rate of 0.05° and an acquisition time of 5s per point.

The electrochemical performance was analyzed using galvanostatic cycling with potential limitation (GCPL) on VMP-multipotentiostat (Biologic Science Instruments, France) and controlled constant temperature of 25 °C. Cells were cycled by GCPL in a potential range of 1.2–3.6 V with a current of 83.5 mA g⁻¹. For electrodes fabrication, 85 wt% SiCN-S composite as active material, 10 wt% polyvinylidene fluoride (PVDF) as binder, and 5 wt% carbon black (Super P, Timcal Ltd, Switzerland) as conduction additive were mixed with N-Methyl-2-pyrrolidone (NMP, BASF, Germany) to form slurry. Then the slurry was pasted onto an aluminum foil by a doctor blade and then dried at 40 °C in the oven for 24 h until NMP completely evaporated. After cutting and then drying in a Büchi glass oven (Labortechnik AG, Germany) for 24 h, electrodes with 10 mm of diameter were obtained. Afterward,

Swagelok cells were assembled in an argon-filled glove box without air contact. Lithium foil (0.75 mm thickness, Alfa Aesar, Germany) was used as the counter and QMA (Whatmann, UK) as separator. Electrolyte contained 1 M lithium bis(trifluoromethanesulfonyl) imide (LiTFSI) dissolved in a mixture of 1,3-dioxolane (DOL) and dimethoxymethane (DME) with a volume ratio 1:1. Besides, 0.1 M of LiNO₃ was added into the electrolyte to alleviate the shuttle effect.

Galvanostatic charge/discharge measurements were performed at a low rate of C/20, corresponding to a current of 83.5 mA per gram of sulfur (the specific capacity of the active material was assumed to be 1,670 mAh g⁻¹). The potential range of the measurement was fixed between 1.2 and 3.6 V. The charge/discharge profiles were built point by point knowing the voltage and the inserted/extracted charge capacity. The total specific capacity refers to the total electrode mass. Furthermore, the coulombic efficiency was calculated as the ratio between delithiation (charge) and lithiation (discharge) capacities.

Extended cycling stability was evaluated either by repeating the galvanostatic charge/discharge measurements for 100 cycles at C/20 rate and by increasing, after five cycles, the rate from C/20 to C/10, C/5, C/2, and C and then by repeating the test at C/20 rate. Finally, cyclic voltammetry was performed to assess the nature of redox reactions occurring in the PDC-derived Li-S batteries by imposing scan rates of 0.02 mV s⁻¹.

The electrochemical impedance spectroscopy (EIS) was obtained also by VMP-multipotentiostat (Biologic Science Instruments, France) at a voltage of 10 mV from 100 kHz to 10 mHz at room temperature.

3. Result and Discussion

3.1. Characterization of the Porous Ceramics before and after Sulfur Infiltration

Figure 1 reports the adsorption/desorption isotherms and the corresponding pore size distribution curves recorded on the starting porous samples before sulfur infiltration. SiOC-A and SiCN-A show type IV and type II isotherms, respectively, SiOC-A having a clear H1 hysteresis loop.[28] Compared to SiOC-A, SiCN-A shows a lower total porosity volume (0.15 vs 0.60 cm³ g⁻¹), and the hysteresis is shifted to higher relative pressure due to the formation of large mesopores/macropores. The pore size distribution curves (Figure 1b) confirm that SiCN-A has pores larger than SiOC-A (ca 70 vs 20 nm). The adsorption/desorption isotherm of the mesoporous spSiOC sample is of type IV with H2 hysteresis loop, revealing that the mesopores have an ink-bottle shape. In this case, the total porosity is 0.32 cm³ g⁻¹ and the pore size distribution curve, obtained from the adsorption branch of the isotherm, shows two maxima, one in the micropore range (ca 1 nm) and the other in the mesopore regime at 6 nm. The specific surface area (SSA) of the three types of porous ceramics follows a trend closely related to their pore size distribution: spSiOC, which presents a fine porosity spanning between 1 and 10 nm, is characterized by an SSA of 455 m² g⁻¹; on the contrary, SiCN-A has a low SSA of 46 m² g⁻¹ due to its macroporous characteristic. Finally, SiOC-A aerogels present an SSA of 161 m² g⁻¹ in accordance with
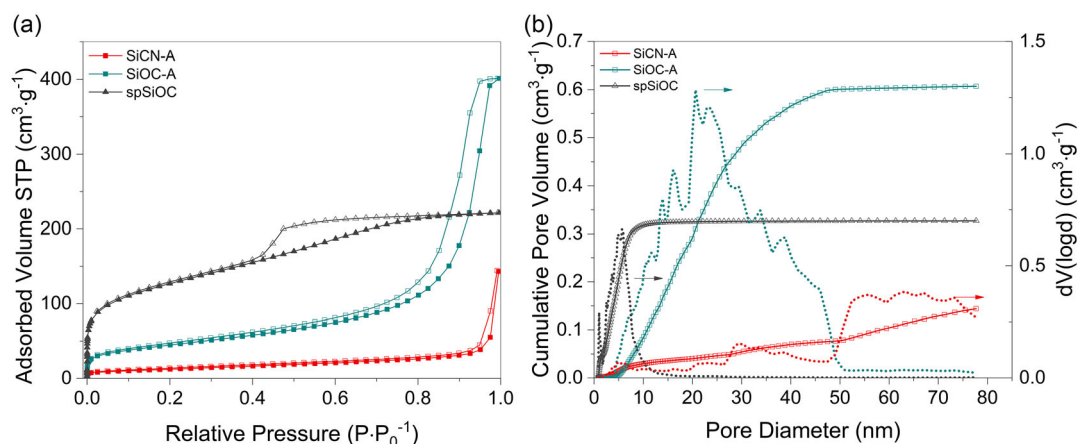
Figure 1. a) N_2 physisorption isotherms and b) DFT pore size distributions recorded on the porous ceramics before the sulfur infiltration.

Table 2. Results from the Ads/Des analysis of the three porous PDCs.

Sample	Isotherm	Hysteresis loop	SSA [m² g⁻¹]	DFT pore volume [cc g⁻¹]	Pore size [nm]
SiOC-A	Type IV	H1	161	0.60	20
SiCN-A	Type II	–	46	0.15	70
spSiOC	Type IV	H2	455	0.32	1 and 6

its intermediate values of pore size distribution. Details of the results obtained from the N_2 adsorption/desorption analysis are reported in **Table 2**.

SEM pictures of the fracture surfaces of the porous samples help in characterizing the nanostructure of the ceramic scaffolds (**Figure 2**). Accordingly, the two aerogel samples are both formed by colloidal particles, as is typical for these materials.[9] SiOC-A sample shows finer individual particles and smaller pore size compared to the SiCN-A one. From the SEM picture taken at the highest magnification (Figure 2, top right), the particle size
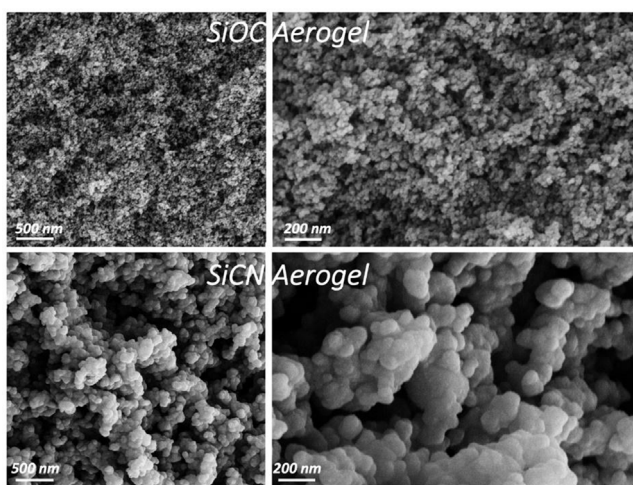
for SiOC-A can be estimated in the range of a few tens of nanometers while for SiCN-A sample (Figure 2, bottom right) particles of a hundred (or more) nm can easily be found. Likewise, pore sizes of SiCN aerogel can reach several hundred of nanometers. For both aerogels and specifically for SiCN-A, SEM demonstrates the presence of macropores (pore size > 50 nm, according to IUPAC definition), implying that the total pore volume estimated from the N_2 sorption analysis is probably underestimated, in particular for SiCN-A.

SEM acquisitions on the mesoporous spSiOC ceramic (**Figure 3**) reveal only a rough surface, in agreement with the very fine porosity of this sample disclosed by the N_2 sorption analysis. No macropores have been seen in this sample and accordingly, the pore volume extracted from the N_2 analysis (0.32 cm³ g⁻¹) should be very close to the total actual pore volume.

As reported in many studies, the amorphous polymer-derived, Si-based ceramic network contains a free carbon phase that controls many functional properties, including electrical conductivity.[29,30] It is therefore important, for the application envisaged in this study, to quantify the amount of free C which correlates, as a first approximation, to the electrical conductivity.[31] The amount of free carbon can be estimated by performing a TGA in air-flow.[32] The weight loss, measured in the temperature range 400–700 °C, is associated with the reaction $C + O_2 \rightarrow CO_2$ and it is therefore a direct measure of the amount of free C present in the ceramic. TGA curves of the three porous samples before sulfur infiltration are shown in **Figure 4**a. The two

Figure 2. SEM picture showing the nanostructure of the ceramic aerogels: SiOC (top) and SiCN (bottom).
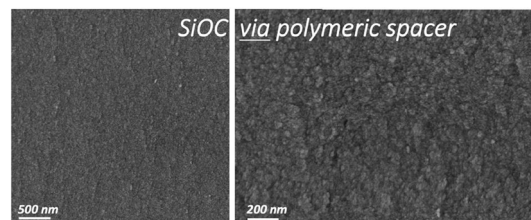

Figure 3. SEM of the fracture surface of the mesoporous SiOC obtained via "polymeric spacer." Porosity is indirectly observed from the roughness of the fracture surface which is clearly seen in the picture at the highest magnification (150.000 X).
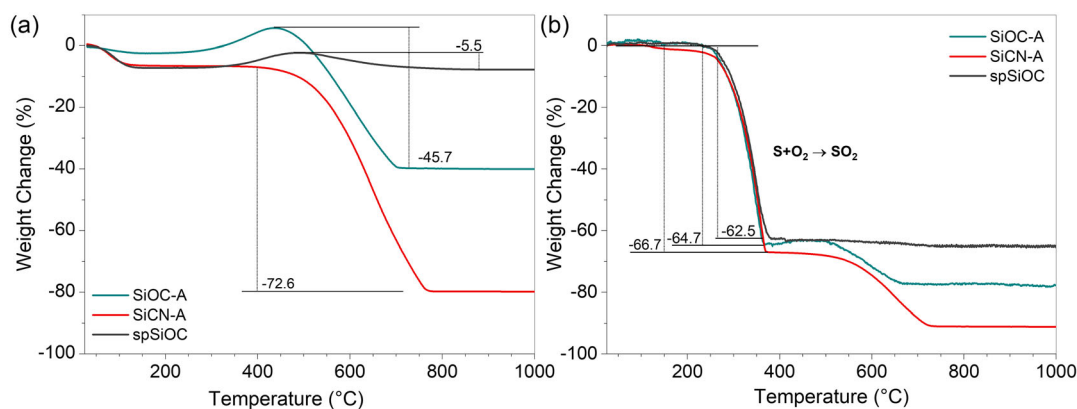
ADVANCED
SCIENCE NEWS

www.advancedsciencenews.com

Energy Technology
Generation, Conversion, Storage, Distribution

www.entechnol.de

Figure 4. TGA curves recorded in airflow on the porous ceramics a) before and b) after sulfur infiltration.

aerogels, SiOC-A and SiCN-A, show a weight loss of 45.7 and 72.6%, respectively, which correspond to the amount of free C in the two systems. Mesoporous spSiOC has a lower amount of free C being the weight loss, in this case, of only 5.5% (**Table 3**). The TGA curves of the two SiOC systems show also an additional small weight increase before the free C oxidation, in the temperature range 350–450 °C. Such a thermogravimetric effect has been already reported in the literature and is generally explained by the oxidation of Si-CHx groups, which leads to Si-O-Si bonds, accordingly, explaining the weight increase.[33,34] Thermogravimetric curves recorded in flowing air for the three sulfur/PDC composites are shown in Figure 4b. The curves show a steep weight loss within 62% and 67% in the temperature range 200–400 °C which is due to the oxidation of S to SO_2 and demonstrate that the sulfur content of the PDC/S composites is very close to the expected one (**Table 4**). Then, the weight loss step from ≈500 to ≈700 °C is assigned to the oxidation of free C and agrees quite well with the value of C_{free} previously estimated. Chemical analyses of the carbon and silicon fractions in neat

ceramic aerogels are given in Table 3. Here, for the SiOC-A and SiCN-A carbon is lower at around 2–3 wt% when compared with previous data. For the spSiOC sample, C_{free} measured by TGA is lower compared to the total C provided via chemical analysis, suggesting that, for this sample, most of the C is bonded to the network via Si-C bonds.

X-ray diffraction analysis demonstrates the amorphous character of the PDC scaffold, and after sulfur infiltration, XRD confirms the presence of crystalline S_8 (Figure S1, Supporting Information).

3.2. Electrochemical Performances of the PDCs Cathodes

Galvanostatic cycling with potential limitation (GCPL) tests were first run in a discharge configuration, with the as-prepared cathodes already filled with nonlithiated sulfur. First lithiation and delithiation profiles are depicted in **Figure 5**, where it is evident that SiOC-A-derived cathodes perform better than SiCN and spSiOC in terms of initial specific capacity. As a matter of fact, the first discharge of the SiOC-A cathode shows a capacity of 909 mAh g^{-1}, while those of the SiCN-A and spSiOC cathodes give a value of ≈704 and 671 mAh g^{-1}, respectively. Clear lithiation plateaus are visible in all kinds of cathodes at around 2.3 and 2.0 V, these occurring as a consequence of the formation of high-order soluble polysulfides (e.g., Li_2S_8, Li_2S_4) and low-order solid polysulfides (e.g., Li_2S_2).[35] The final steep potential loss is ascribable to the conversion into solid Li_2S, where the cathode is considered discharged. The following charge ends up with specific capacities of 837, 565, and 610 mAh g^{-1}, for SiOC-A, SiCN-A, and spSiOC, respectively. A consistent loss in specific capacity is nevertheless observed in all cases, suggesting a dissolution of polysulfides in the electrolyte during the first lithiation.

Extended cycling stability was defined with an imposed C/20 rate in the 1–100 cycles range and relative results are given in **Figure 6**a. As a first comment, it is clear that a consistent loss of capacity occurs in all the PDC cathodes, showing a stabilization of the specific capacity with the ongoing measurement. After 100 cycles, the SiOC-A, SiCN-A, and spSiOC cathodes retain 112, 62, and 126 mAh g^{-1}, respectively, corresponding to a total retention of 12%, 9%, and 19%, respectively, of the initial capacity. Some information on the shuttle effect can be retrieved from

Table 3. TGA measured amounts of C_{free} (wt%) in the porous PDCs. Chemical analyses of carbon and silicon fractions in the neat ceramic samples are given, too.

Sample	Thermogravimetry C_{free} [wt%]	Chemical analysis	
		C [wt%]	Si [wt%]
SiOC-A	45.7	43.6 ± 0.4	26.1 ± 0.0
SiCN-A	72.6	68.60 ± 0.9	9.5 ± 0.1
spSiOC	5.5	14.8 ± 0.1	42.4 ± 0.1

Table 4. TGA measured amounts of infiltrated S (wt%) in the PDC/S composites.

Sample	Thermogravimetry	
	C_{free} [wt%]	S [wt%]
SiOC-A/S	–	64.7
SiCN-A/S	–	66.7
spSiOC/S	–	62.5

ADVANCED
SCIENCE NEWS
www.advancedsciencenews.com

Energy Technology
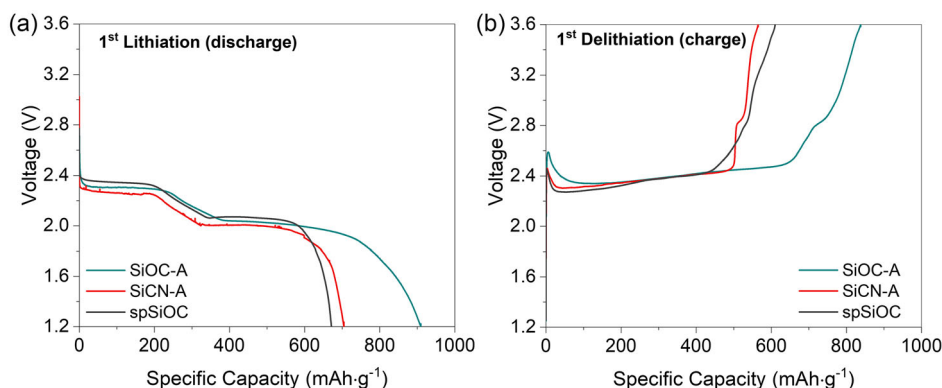Generation, Conversion, Storage, Distribution
www.entechnol.de

Figure 5. Galvanostatic discharge/charge curves of SiOC-A, SiCN-A, and spSiOC-based cathodes during: a) lithiation corresponding to the first discharge of the Li-S cell and b) first delithiation (first charge of the Li-S cell).
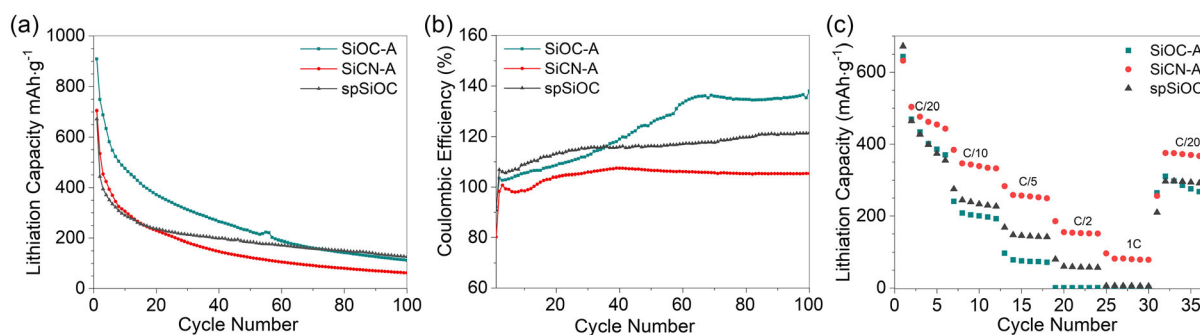

Figure 6. a) Extended constant rate cyclic stability, b) coulombic efficiency in the 2-100 cycles range, and c) variable rate cycling of the two prepared cathodes.

the extended cycling stability by plotting the cycle-by-cycle coulombic efficiency. As a matter of fact, it has been demonstrated that efficiencies outbreaking 100% are observed when soluble polysulfides are shuttled toward the anode, where sulfur oxidation releases the excess charge responsible for the efficiency boost.[22,23]

We report the coulombic efficiency of SiOC-A, SiCN-A, and spSiOC in Figure 6b. Evidently, silicon oxycarbide-based cathodes show an increase in the efficiency toward 140% and 120% for the SiOC-A and spSiOC, respectively, which remain stable from the 60th and 30th cycle on, respectively. The reason for the efficiency over 100% is an increasing degree of shuttling effect. Namely, the long-chain polysulfides migrate to the Li anode, are chemically reduced, diffuse back to the cathode, and are further oxidized to a long-chain polysulfide, leading to a long charge (delithiation) process with efficiency losses. The shuttling phenomenon does not appear to largely affect the potential/capacity transient of SiCN-A cathode. From here, we could derive a hypothesis on the effect of the chemical composition of the scaffold material being the SiCN more suitable to hinder the shuttle phenomena than SiOC. As a matter of fact, it is known that nitrogen-containing cathodes are able to strongly chemisorb polysulfides at the nitrogen sites, so the shuttling effect is largely hindered.[36] This also signifies that the chemical composition of a matrix material may be advantageous over the present porosity. On the other side, the better electrochemical performance of

spSiOC compared to SiOC-A could be related to its smaller pore size and to its ink-bottle shape which, evidently, can more efficiently hamper the shuttle behavior compared to the larger mesopores present in SiOC-A. Similar pore size effects have been observed in a recent work, where microporosity is addressed as a major factor in limiting shuttling phenomena compared with mesoporosity, in hierarchical porous carbon nanoparticles.[24]

Figure 6c displays the variable rate cycling of the cathodes, where the SiCN-A cathode shows superior charge/discharge ability at fast charging/discharging rates. The rate performance is primarily determined by the ionic and electronic conductivity of the matrix material. High free carbon content leads to higher electrical conductivity of SiCN-A sample, thus providing pathways for better transport of ions and electrons and enhanced performance of this material at high-rate charge/discharge tests. In contrast, the slightly better performance of the spSiOC compared to SiOC-A at high rates is more difficult to explain, indeed, the same two parameters (free C content and pore size) should suggest an opposite trend. A possible explanation might reside in the large SSA of this material, which might be beneficial for fast Li$^+$ adsorption directly at the contact interface.

Finally, cyclic voltammetry was employed as an analytical method to define the ability of the cathodes to withstand cyclability from an electrochemical point of view, investigating the nature of redox reactions occurring at their interface.
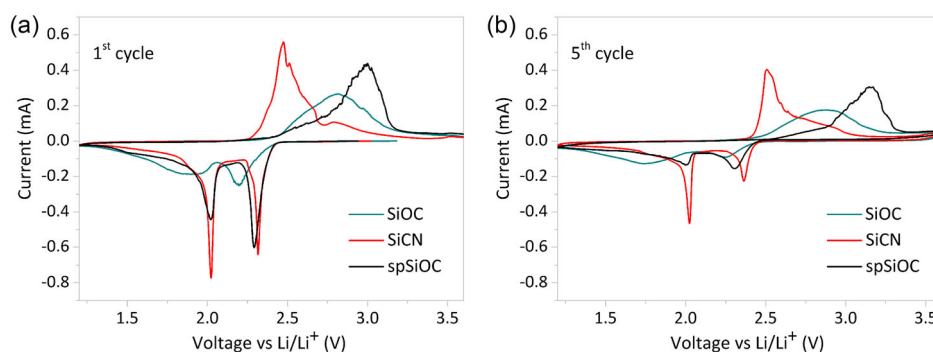
ADVANCED
SCIENCE NEWS
www.advancedsciencenews.com

Energy Technology
Generation, Conversion, Storage, Distribution
www.entechnol.de

Figure 7. Cyclic voltammetry of the a) first and b) fifth cycles of the sulfur-containing PDC cathodes.

Figure 7a,b reports the first and fifth voltammetric cycles, respectively. As a reference point, positive current refers to the sulfur oxidation reaction (charge), and negative current to the reduction one (discharge). The first cathodic (discharge) peak appears at 2.3 corresponding to the conversion of S_8 to high-order polysulfides (Li_2S_x, $4 < x < 8$). The second cathodic peak appears at 2.0 V and corresponds to the further reduction of polysulfides to insoluble Li_2S_2 and Li_2S. During the oxidation process, a main anodic peak should appear at 2.4 V, attributed to the conversion of lithium sulfide to S_8. Usually, it consists of the overlap of two peaks corresponding to oxidation of the species reduced within two cathodic peaks. For SiCN-A both oxidation and reduction peaks are quite sharp, and the distance between them is the lowest among all the investigated materials. This signifies that SiCN-A presents the lowest ohmic losses, attributed to a high carbon content providing a good electrical conductivity. Cathodic and anodic peaks registered for SiOC-A are much broader and significantly shifted toward negative (around 100 mV) and positive (around 400 mV) direction, respectively. This signifies a much higher polarization related to the ohmic drop compared with the one of SiCN-A. This feature can be attributed to a lower amount of free carbon, leading to a lower conductivity. The broad peaks can also be correlated to dissolution and diffusion of polysulfides, which is boosted for this material (compare Figure 6b).

The CV curve registered for spSiOC is quite atypical. While cathodic peaks almost superimpose with those of SiCN-A, the anodic peak is shifted significantly into the positive direction (>600 mV). According to literature reports,[37] this feature can be attributed to the presence of a high amount of long-chain polysulfides which delithiate first at higher potentials.

In spSiOC, the rather high SSA and ordered pore structure might also trigger a pseudocapacitive response of the cathode.[38] Such behavior emerges when charged ions are mainly adsorbed onto the surface of the material, rather than in its bulk.[39] If we consider that spSiOC is provided with a smaller amount of carbon compared to other aerogels, but with a much higher SSA, its sharp peaks in the cyclic voltammetry might be indicative of surface adsorption. This especially holds when considering that for ultramicroporous materials with very fine porosity, it is not possible to discriminate the bulk of the solid from its surface, and this applies also to sulfur dispersed in such a fine matrix. Likewise, if we consider the rate capacity measurements, the spSiOC scaffold presents smaller drops in the capacity compared to the other SiOC aerogel, a behavior that might be predominantly ascribed to surface adsorption, instead of Li^+ migration toward the bulk of sulfur.

Table 5 shows the comparison of electrochemical performances of silicon-based positive LIS electrodes that can be compared with the result presented in this article. As a matter of fact, the overall capacity and stability of Si-based scaffolds for Li-S batteries seem to be promising when synthesizing SiC, SiOC, or SiCN with nanostructured features presenting large fractions of carbon and not necessarily large SSAs. Compared to this work, optimized reversible capacities have been reported to outreach 500 mAh g^{-1}) even after 400 cycles, suggesting that polymer-derived ceramic aerogels might be engineered to boost their performances. Compared to other electrode materials, ceramic aerogels have the advantage of being able to accommodate large volume variations thanks to their solid colloidal structure, thus partially solving the issues related to sulfur expansion.

Table 5. Comparative table of electrochemical performances of similar cathode materials for Li-S battery storage.

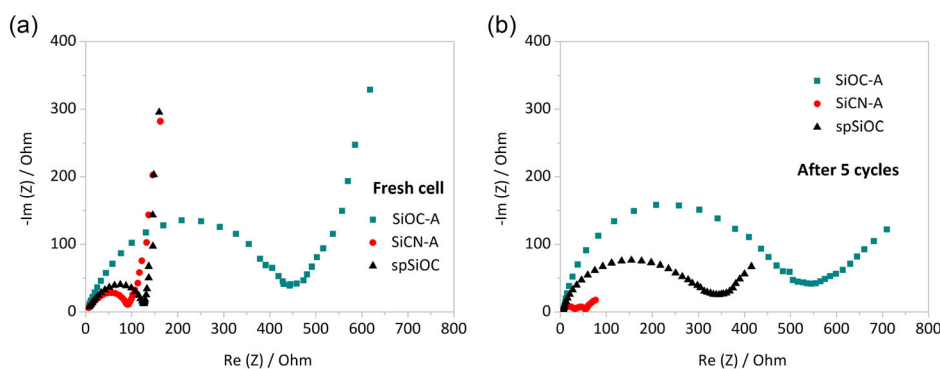| Sulfur host material	Sulfur content [wt%]	SSA [m^2 g^{-1}]	Initial capacity [mAh g^{-1}]	Reversible capacity [mAh g^{-1}]	Number of cycles	References
SiOC-A/S	64.7	161	909	112	100	This work
SiCN-A/S	66.7	46	704	62	100	This work
spSiOC/S	62.5	455	671	126	100	This work
HPCN11	76	2789	1129	590	400	[24]
SiCN-S-1000	66.6	72	722	313	40	[23]
SiOCN-5/S- CP	70	38.2	1015	374	500	[40]
S-CNTs/SiC	75.6	61.6	1008	316	400	[41]

Figure 8. Nyquist plots of all samples a) before and b) after five cycles.

The electrochemical impedance spectroscopy (EIS) measurements were performed on the freshly assembled cell after five cycles (**Figure 8**). The diameter of the semicircle at the high-frequency region is attributed to the charge-transfer resistance (R_{ct}) of the material and the slope of the spectrum at the low frequencies is associated with the electrolyte resistance (R_e). The equivalent circuit of the lithium-sulfur battery is shown in **Figure 9** and all resistance values of the samples before and after five cycles are listed in **Table 6**. Before electrochemical cycling, the diameters of the semicircle of SiCN-A and spSiOC are much smaller than SiOC-A. Especially for SiCN-A, the value of R_{ct} of it is 100.3 Ohm, the lowest charge-transfer resistance compared to other samples. After five cycles, the charge-transfer resistance of SiOC-A and spSiOC increases to 464 Ohm and 289.8 Ohm from 460.5 and 127.8 Ohm, respectively, which is indicated by bigger corresponding semicircles and the spectra fitting results. Besides, the increased R_e of SiOC-A to 5.498 Ohm reveals a higher ions diffusion resistance of the electrolyte. However, for SiCN-A, not only the ion diffusion resistance decreases to almost 0, but also the charge-transfer resistance within the electrode diminishes significantly to
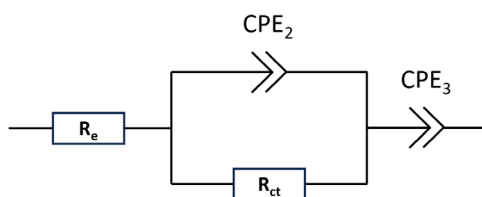
22.95 Ohm. We attribute this behavior to a better distribution of sulfur in big pores of SiCN-A being a consequence of cycling and the sulfur volume changes related to this process. Elemental analysis results have also shown that SiCN-A contains the highest amount of carbon, thus the sulfur volume changes during cycling possibly causing also a rearrangement of a free carbon phase leading to a higher conductivity. Moreover, the low charge transfer resistance probably enables the good rate capability of the materials, as shown in Figure 6c.

4. Conclusion

In conclusion to this work, polymer-derived ceramic SiOC and SiCN aerogels were successfully synthesized and utilized as scaffolds for sulfur containment in Li-S batteries. Their electrochemical performances were studied together with those of a porous SiOC ceramic with a peculiar ink bottle-shaped fine mesoporosity obtained via selective degradation of molecular spacers. Results show that despite the impressive initial capacities shown by all of the scaffolds, SiOC and SiCN materials present capacities fading toward the 110–60 mAh g^{-1} range, losing around 90% of their first specific capacity. Despite the smaller pore volume, SiCN-A possesses a major fraction of free carbon as compared to the other scaffolds, which eventually guarantees good electrical conductivity, and the presence of nitrogen in the ceramic network further retains the efficiency toward chemisorption of a fraction of polysulfides.

For what concerns SiOC scaffolds, results indicate that a fine porosity (1–10 nm wide) might be the key for partially hinder shuttling phenomena in Si-based compounds. As a matter of fact, large mesopores of SiOC-A ($\approx$20 nm) can be associated with severe shuttling and efficiency losses, while fine pores of spSiOC result in a damped degradation and faster charge/discharge abilities.

Further studies concerning the use of microporous PDCs with ink bottle-shaped pores will clarify whether these might result in a better retainment of the initial capacity of these novel Li-S cathodes.

Figure 9. The equivalent circuits of the battery. R_e is associated with the resistance of the electrolyte, R_{ct} represents the charge transfer resistances, and CPE$_2$ and CPE$_3$ are the constant phase elements.

Supporting Information

Supporting Information is available from the Wiley Online Library or from the author.

Table 6. Resistance list of all samples. R_e and R_{ct} represent the resistance of electrolytes and the charge transfer before cycling. R_e' and R_{ct}' represent the resistance of the electrolyte and the charge transfer after five cycles.

	R_e [Ohm]	R_{ct} [Ohm]	R_e' [Ohm]	R_{ct}' [Ohm]
SiOC-A/S	2.221	460.5	5.498	464
SiCN-A/S	2.438	100.3	$\approx$0	22.95
spSiOC/S	3.611	127.8	2.99	289.8

Acknowledgements

Conflict of Interest

The authors declare no conflict of interest.

Data Availability Statement

The data that support the findings of this study are available on request from the corresponding author. The data are not publicly available due to privacy or ethical restrictions.

Keywords

[1] S. Yajima, J. Hayashi, M. Omori, *Chem. Lett.* **1975**, *4*, 931.

[2] P. Colombo, G. Mera, R. Riedel, G. D. Sorarù, *J. Am. Ceram. Soc.* **2010**, *93*, 1805.

[3] A. Viard, D. Fonblanc, D. Lopez-Ferber, M. Schmidt, A. Lale, C. Durif, M. Balestrat, F. Rossignol, M. Weinmann, R. Riedel, S. Bernard, *Adv. Eng. Mater.* **2018**, *20*, 1800360, .

[4] A. L. Hector, *Coord. Chem. Rev.* **2016**, *323*, 120.

[5] H. Ichikawa, *Annu. Rev. Mater. Res.* **2016**, *46*, 335.

[6] P. Colombo, *J. Eur. Ceram. Soc.* **2008**, *28*, 1389.

[7] E. Zera, R. Campostrini, P. R. Aravind, Y. Blum, G. D. Sorarù, *Adv. Eng. Mater.* **2014**, *16*, 814.

[8] Z. C. Eckel, C. Zhou, J. H. Martin, A. J. Jacobsen, W. B. Carter, T. A. Schaedler, *Science (80-).* **2016**, *351*, 58.

[9] G. D. Sorarù, E. Zera, R. Campostrini, *Handbook of Sol-Gel Science and Technology* **2016**, https://doi.org/10.1007/978-3-319-19454-7.

[10] S. Aguirre-Medel, P. Jana, P. Kroll, G. D. Sorarù, *Materials* **2018**, *11*, 2589 .

[11] A. Zambotti, F. Valentini, E. Lodi, A. Pegoretti, V. Tyrpekl, S. Kohúteková, G. D. Sorarù, M. Kloda, M. Biesuz, *J. Alloys Compd.* **2021**, *895*, 162592.

[12] A. Zambotti, E. Caldesi, M. Pellizzari, F. Valentini, A. Pegoretti, A. Dorigato, G. Speranza, K. Chen, M. Bortolotti, G. D. Sorarù, M. Biesuz, *J. Eur. Ceram. Soc.* **2021**, *41*, 5484.

[13] M. C. Bruzzoniti, M. Appendini, B. Onida, M. Castiglioni, M. D. Bubba, L. Vanzetti, P. Jana, G. D. Sorarù, L. Rivoira, *Environ. Sci. Pollut. Res.* **2018**, *25*, 10619.

[14] A. Zambotti, A. Bruni, M. Biesuz, G. D. Sorarù, L. Rivoira, M. Castiglioni, B. Onida, M. C. Bruzzoniti, *SSRN Electron J.* **2023**, *11*, 109771.

[15] H. Fukui, H. Ohsuka, T. Hino, K. Kanamura, *ACS Appl. Mater. Interfaces.* **2010**, *2*, 999.

[16] P. Vallachira Warriam Sasikumar, E. Zera, M. Graczyk-Zajac, R. Riedel, G. D. Soraru, B. Dunn, *J. Am. Ceram. Soc.* **2016**, *99*, 2977.

[17] M. Li, J. Lu, Z. Chen, K. Amine, *Adv. Mater.* **2018**, *30*, 1800561.

[18] G. E. Blomgren, *J. Electrochem. Soc.* **2017**, *164*, A5019.

[19] Y. X. Yin, S. Xin, Y. G. Guo, L. J. Wan, *Angew. Chem., Int. Ed.* **2013**, *52*, 13186.

[20] A. Eftekhari, D. W. Kim, *J. Mater. Chem. A* **2017**, *5*, 17734.

[21] J. Chai, J. Du, Q. Li, N. Han, W. Zhang, B. Tang, *Energy Fuels.* **2021**, *35*, 15455.

[22] F. Qu, Z. Yu, M. Krol, N. Chai, R. Riedel, M. Graczyk-Zajac, *Nanomaterials* **2022**, *12*, 1283.

[23] F. Qu, M. Graczyk-Zajac, D. Vrankovic, N. Chai, Z. Yu, R. Riedel, *Electrochim. Acta.* **2021**, *384*, 138265.

[24] S. Eun, M. Ji, J. Park, J. W. Lee, D. W. Yoon, Y. Kim, J. H. Kim, Y. C. Kang, D. S. Jung, *Chem. Eng. J.* **2023**, *465*, 143035.

[25] V. L. Nguyen, E. Zera, A. Perolo, R. Campostrini, W. Li, G. D. Sorarù, *J. Eur. Ceram. Soc.* **2015**, *35*, 3295.

[26] Y. Blum, G. D. Sorarù, A. P. Ramaswamy, D. Hui, S. M. Carturan, *J. Am. Ceram. Soc.* **2013**, *96*, 2785.

[27] Y. D. Blum, D. B. MacQueen, H. J. Kleebe, *J. Eur. Ceram. Soc.* **2005**, *25*, 143.

[28] F. Rouquerol, J. Rouquerol, K. S. W. Sing, P. Llewellyn, G. Maurin, *Adsorption by Powders and Porous Solids*, Academic Press **2014**.

[29] Q. Wen, Z. Yu, R. Riedel, *Prog. Mater. Sci.* **2020**, *109*, 100623.

[30] F. Dalcanale, J. Grossenbacher, G. Blugan, M. R. Gullo, A. Lauria, J. Brugger, H. Tevaearai, T. Graule, M. Niederberger, J. Kuebler, *J. Eur. Ceram. Soc.* **2014**, *34*, 3559.

[31] J. Kaspar, M. Graczyk-Zajac, S. Choudhury, R. Riedel, *Electrochim. Acta.* **2016**, *216*, 196.

[32] M. Graczyk-Zajac, D. Vrankovic, P. Waleska, C. Hess, P. V. Sasikumar, S. Lauterbach, H.-J. Kleebe, G. D. Sorarù, *J. Mater. Chem. A* **2018**, *6*, 93.

[33] M. Narisawa, K. Terauds, R. Raj, Y. Kawamoto, T. Matsui, A. Iwase, *Scr. Mater.* **2013**, *69*, 602.

[34] G. D. Sorarù, C. Tavonatti, L. Kundanati, N. Pugno, M. Biesuz, *J. Am. Ceram. Soc.* **2020**, *103*, 6519.

[35] X. Zhang, H. Xie, C.-S. Kim, K. Zaghib, A. Mauger, C. M. Julien, *Mater. Sci. Eng. R: Rep.* **2017**, *121*, 1.

[36] J. Song, M. L. Gordin, T. Xu, S. Chen, Z. Yu, H. Sohn, J. Lu, Y. Ren, Y. Duan, D. Wang, *Angew. Chem.,– Int. Ed.* **2015**, *54*, 4325.

[37] X. Huang, Z. Wang, R. Knibbe, B. Luo, S. A. Ahad, D. Sun, L. Wang, *Energy Technol.* **2019**, *7*, 1801001.

[38] M. Mastragostino, F. Soavi, C. Arbizzani, *Adv. Lithium-Ion Batter.* **2002**, *481*, https://doi.org/10.1007/0-306-47508-1_17.

[39] K. Brezesinski, J. Wang, J. Haetge, C. Reitz, S. O. Steinmueller, S. H. Tolbert, B. M. Smarsly, B. Dunn, T. Brezesinski, *J. Am. Chem. Soc.* **2010**, *132*, 6982.

[40] J. Q. Lu, J. L. Hu, H. X. Zhong, Y. L. Ren, L. Z. Zhang, *J. Alloys Compd.* **2021**, *860*, 157903.

[41] J. Y. Wang, W. J. Wang, H. P. Li, T. Z. Tan, X. Wang, Y. Zhao, *J. Nanopart. Res.* **2019**, *21*, 113.

Supplementary Material -.Polymer-derived ceramic aerogels to immobilize sulfur for Li-S batteries.

Andrea Zambotti[1], , Fangmu Qu[2,*], Giacomo Costa[1], Magdalena Graczyk-Zajac[2,3], Gian Domenico Sorarù[1,4]
[1]Department of Industrial Engineering, Glass & Ceramics Laboratory, University of Trento, Via Sommarive 9, 38123 Trento, Italy
[2]Institute of Materials Science, Darmstadt University of Technology, Otto-Berndt-Str. 3, 64287 Darmstadt, Germany
[3]EnBW Energie Baden-Württemberg AG Durlacher Allee 93 76131 Karlsruhe, Germany
[4] Natl Res Council Italy ICMATE CNR, Inst Condensed Matter Chem & Technol Energy, Via Marini 6, I-16149 Genoa, Italy
*Corresponding author: fangmu.qu@stud.tu-darmstadt.de

Figure S1 reports the XRD patterns of sulfur-containing ceramic scaffolds. All diffraction peaks correspond to the orthorhombic symmetry of the S_8 sulfur phase (COD code: 9011363), confirming that crystalline sulfur is present within the porous supports.
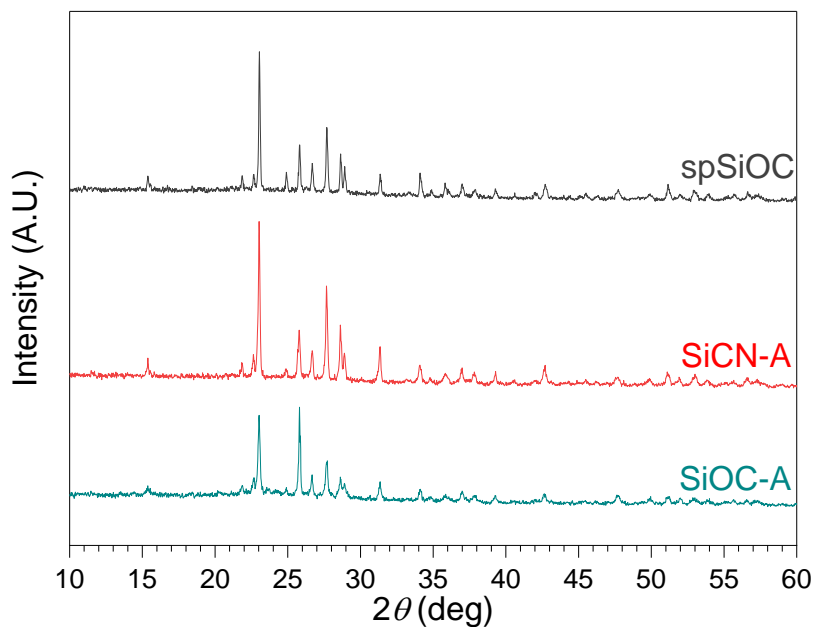

Figure S 1: X-ray diffraction patterns of ceramic scaffolds loaded with sulfur.

In-situ formed porous silicon carbonitride/boron nitride composites to boost cathode performance in lithium sulfur batteries

Fangmu Qu [a,*], Zhaoju Yu [b,c,**], Marc Widenmeyer [a], Chuanmu Tian [a], Ruijuan Yan [a,d], Honghong Tian [a], Alexander Kempf [a], Dario M. De Carolis [a], Jan P. Hofmann [a], Anke Weidenkaff [a,e], Ralf Riedel [a], Magdalena Graczyk-Zajac [a,f]

[a] *Institute of Materials Science, Technical University of Darmstadt, Peter-Grünberg-Str. 2, Darmstadt 64287, Germany*
[b] *College of Materials, Key Laboratory of High-Performance Ceramic Fibers (Xiamen University), Ministry of Education, Xiamen 361005, China*
[c] *College of Materials, Xiamen Key Laboratory of Electronic Ceramic Materials and Devices, Xiamen University, Xiamen 361005, China*
[d] *Max Planck Institute for Chemical Physics of Solids, Nöthnitzer Str. 40, Dresden 01187, Germany*
[e] *Fraunhofer Research Institution for Materials Recycling and Resource Strategy (IWKS), Brentanostr. 2a, Alzenau 63755, Germany*
[f] *EnBW Energie Baden-Württemberg AG, Durlacher Allee 93, Karlsruhe 76131, Germany*

ARTICLE INFO

ABSTRACT

Carbon-rich polymer-derived SiCN ceramic matrix serves as a stabilizing host for sulfur cathodes due to its robust, stress-accommodating properties and well-conductive carbon network. Herein, novel SiCN-BN composites are synthesized through the annealing of a polymer-derived SiCN ceramic alongside boric acid and urea. The prepared cathodes exhibit significantly improved electrochemical performance after sulfur immobilization within the resulting composites. Of particular note is the material annealed at 950 °C, designated as SiCN-BN-950/S. It exhibits a reversible capacity of 445 mAh/g showcasing 62% capacity retention over 60 cycles, using electrodes with an areal density of 3.5–3.8 mg/cm^2 and a sulfur loading of 66 wt%. Its good cycling stability is attributed to the remarkable synergistic interplay between BN on the surface and disordered carbon present within the SiCN ceramic matrix. The presence of BN enables effective polar adsorption of polysulfides, while the in-situ formed porous carbon contributes to enhanced electrical conductivity. This combination significantly elevates the overall electrochemical performance of the sulfur cathode. The successful utilization of these novel SiCN-BN composites, a remarkable advancement in sulfur cathode technology, opens up possibilities for further enhancing the efficiency and stability of energy storage systems.

1. Introduction

Lithium-ion batteries (LIBs) make our modern life extremely convenient. However, their theoretical energy density became a bottleneck, which cannot keep up with the ever-growing demand of energy markets [1–3]. The emerging and crucial work nowadays is to develop a new battery system with improved electrochemical performance at low-cost. As one of the most promising candidates for the replacement of LIB, the lithium sulfur battery (LSB) exhibits a higher energy density (2600 Wh/kg) [4] and a superior theoretical capacity (1675 mAh/g) [5] for the sulfur cathode. In addition, the abundant reserves and low price of sulfur make it suitable for large-scale commercial production and application [6–8]. Nevertheless, the electrically insulating property of the active sulfur, the final reduction products Li_2S_2 and Li_2S, the volume expansion of the sulfur during charge/discharge processes and the deadly "shuttle effect" caused by the dissolution of redox intermediates in polar electrolytes give currently rise to poor cycling stability of the LSB, thus severely hampering its potential practical application [9–13]. Therefore, developing a novel LSB architecture with a stable electrochemical performance is still a great challenge.

Extensive research has been taken to overcome the above-mentioned fatal drawbacks of the LSB. The current research focuses on improving the microstructure of the sulfur cathode host [14–16], and on designing new separators to hinder the polysulfide shuttling [17,18]. Carbon

---

* Corresponding author.
** Corresponding author at: College of Materials, Key Laboratory of High-Performance Ceramic Fibers (Xiamen University), Ministry of Education, Xiamen 361005, China.
E-mail addresses: fangmu.qu@stud.tu-darmstadt.de (F. Qu), zhaojuyu@xmu.edu.cn (Z. Yu).

materials such as porous carbon, graphene, and carbon nanotubes (CNTs) are widely investigated to stabilize sulfur cathodes. This is due to their excellent conductive network, which provides enough electron and ion pathways for redox reactions, and also due to their abundant interior space which enable them to accommodate sulfur and to be a barrier towards the electrolyte to a certain degree [19–22]. However, the interactions of various carbon materials and polysulfides are mainly non-polar physical adsorption based on Van-der-Waals interaction since carbon materials are non-polar while polysulfides are polar species. This represents a relatively weak confinement compared with polar physical adsorption [23,24]. Therefore, plenty of polar sulfides [25–27], as well as oxides [28,29] and nitrides [15,16,30] of metals and nonmetals have been studied as skeleton host or additives for sulfur cathodes. They can provide efficient polar physical adsorption to immobilize lithium polysulfides formed in the redox reactions during the battery cycling. Regrettably, the polar materials mentioned above are usually characterized by a low specific surface area and a poor electrical conductivity [23]. These drawbacks lead to a low sulfur loading and impaired redox reaction caused by obstructed electron and ion pathways, resulting in unsatisfactory electrochemical performance.

Combining non-polar and polar physical adsorption for polysulfides is a comprehensive strategy. Boron nitride (BN) nanosheets are an effective adsorbent for various substances, like organic pollutants and also polar polysulfides, due to the B–N bond polarity and a suitable specific surface area resulting from its nanostructure [23,31]. Its high thermal conductivity and stability make it a good additive which is not involved in the chemical reaction between lithium and sulfur, avoiding thus the production of additional by-products [32–34]. The only obstacle of applying BN in sulfur cathodes is its insulating property. Therefore, He et al. [23] synthesized a paragenesis hybrid of BN and CNTs as sulfur host for LSB which demonstrated a strong interaction between the BN/CNTs hybrid and sulfur. The strong interaction results from the monoclinic phase that sulfur assumes in the BN/CNTs hybrid host, differing from the generally reported orthorhombic phase. The combination of non-conductive but strong adsorptive BN and well conductive CNTs exhibits high specific capacity (1374 mAh/g at 0.2 C, (1 C =1675 mAh/g)) and impressive cycling stability. Deng et al. [35] and Sun et al. [36] prepared BN/graphene and BN/Ketjen black, respectively. A remarkable electrochemical performance due to the strong synergistic effect between the BN nanosheets and the carbon nanomaterials – hindering the "shuttle effect" of polysulfides – has been achieved in these works. Nevertheless, in all these studies, nanomaterials of high-cost and unsuitable for large-scale production and commercialization have been used.

In our previous works [37–39], we have demonstrated that the polymer-derived SiCN ceramic matrix is a suitable sulfur host material providing a stable, conductive, and porous network for an efficient sulfur encapsulation. Introducing a polar adsorption mechanism for polysulfides in form of BN nanosheets on the ceramic surface represents a chance of a further enhancement of the electrochemical performance of the porous SiCN matrix for sulfur cathodes. Thus, in this work, we synthesized porous SiCN-BN composites to explore the effect of BN-nanosheets on the electrochemical performance of the resulting Li-S cell.

2. Experimental part

2.1. Fabrication of C-rich SiCN ceramic matrix

50 g of perhydropolysilazane/Di-n-butylether (PHPS/DBE, DURA-ZANE 2250, Merck Performance Materials GmbH, Wiesbaden, Germany) solution was cross-linked with 65 g of divinylbenzene (DVB, 80%, mixture of isomers, Sigma-Aldrich, Burlington, MA, USA) in an argon protected flask at 120 ℃ for 6 h in the presence of the platinum (0)-1,3-divinyl-1,1,3,3-tetramethyldisiloxane complex catalyst (~Pt 2% in xylene, Sigma-Aldrich, Burlington, MA, USA). The obtained cross-linked

product was pyrolyzed subsequently in a tube furnace at 1000 ℃ under Ar for 3 h. Finally, the C-rich SiCN was ball-milled (zirconia ball, dry milled in air, 30 Hz, 60 min) and sieved (40 μm).

2.2. Synthesis of SiCN-BN composites

35 g of urea (ACS reagent, ≥ 99%, Sigma-Aldrich, Burlington, MA, USA), 1.75 g of boric acid (ACS reagent, ≥ 99.8%, Sigma-Aldrich, Burlington, MA, USA), and 0.6 g of obtained C-rich SiCN (1000 °C) ceramic were dispersed in 200 mL deionized water. The mixture was heated to 70 ℃ under stirring for 5 h to complete evaporation of water. Afterwards, the solid precipitate was put into a graphite crucible and then into a tube furnace and annealed at 950 ℃, 1100 °C, and 1250 °C under Ar for 5 h. The final products were denoted as SiCN-BN-950, SiCN-BN-1100, and SiCN-BN-1250, respectively.

2.3. Preparation of SiCN-BN/S composites

10 min ball milling (identical parameters as 2.1) was applied to form a uniform dispersion of sulfur (sublimed, 100 mesh, 99.5%, Alfa Aesar, Germany) in SiCN-BN-950 with a mass ratio of 1:2 (66.6 wt% sulfur). Then, the mixture was put into a Teflon sealed autoclave and heated to 160 ℃ in an oven for 24 h. After grinding the composite, SiCN-BN-950/S was obtained. SiCN-BN-1100/S and SiCN-BN-1250/S were prepared using an analogous procedure.

2.4. Characterization

A STOE STADIP X-ray diffractometer (XRD) was used to investigate the crystal structure of all SiCN-BN composites. The device was equipped with monochromatic Mo-$K\alpha_1$ radiation and the testing range of 2θ is 5–45°. N_2 adsorption/desorption measurements were carried out using a 3 P sync400 with nitrogen at 77 K to get linear Brunauer–Emmett–Teller (BET) plots to determine the specific surface area and porosity of the SiCN-BN ceramic matrix. Raman spectra were recorded with a Horiba HR800 Micro-Raman spectrometer equipped with an Ar-ion laser to analyze the carbon phase of the ceramic composites. The wavelength of the laser is 514.5 nm and testing range is 1000–2000 cm^{-1}. Fourier transform infrared (FTIR) spectra of all SiCN-BN composites were recorded by using KBr pellets on a Varian 670-FTIR spectrometer in transmission geometry. The total carbon content in all SiCN-BN composites was analyzed by using a Leco-200 hot-gas extraction (elemental analysis). Other quantitative elemental analysis for boron, nitrogen, and oxygen were performed by Mikroanalytisches Labor Pascher (Remagen, Germany). Specifically, boron was detected using inductively coupled plasma atomic emission spectroscopy (ICP-AES); nitrogen was detected by changes in thermal conductivity and oxygen was detected by the CO_2 IR-absorption bands during carbothermal fusion in He atmosphere. After introducing S into the SiCN-BN composites, the materials morphology and corresponding element distribution were investigated by scanning electron microscopy via a Philips XL30 FEG equipped with 30 mm^2 SDD detector under 15 keV acceleration voltage (SEM). X-ray photoelectron spectroscopy (XPS) was conducted using a hemispherical energy analyzer (PHOIBOS 150, Focus 500 with XR50M) under a pressure < 10^{-9} mbar, employing monochromatized Al Kα line (1486.74 eV) as the X-ray source. Survey spectra were obtained with a pass energy of 20 eV, while detailed spectra were obtained at 10 eV. Binding energy was calibrated using the core lines of copper, silver, and gold, and peaks were fitted using CasaXPS software with a Shirley background.

2.5. Electrochemical measurement

Electrochemical performance of all samples was investigated by using a Swagelok cell setup. For fabricating the cathode electrode, firstly, the slurry which consisted of 85 wt% SiCN-BN/S composite as active material, 10 wt% polyvinylidenflourid (PVDF) as binder, 5 wt%

carbon black as conductive agent, and 1–2 mL of N-Methyl-2-pyrrolidone (NMP) as solvent, was printed on a carbon-coated aluminum foil (16 μm of aluminum foil, 2 μm of carbon, AFT ELECTRONIC CO., LTD. BOLUO, China) by a doctor blade and then dried at 40 °C for 24 h to evaporate the solvent. The thickness of the electrode material layer is 120 μm and the sulfur content of the electrode material is around 56 wt %. Afterwards, the electrode foil was cut into 10 mm diameter electrodes. These electrodes were then put into a vacuum dryer (Büchi Labortechnik AG, Germany) at 60 °C for 24 h. The areal density of sulfur in cathode is between 3.5–3.8 mg/cm². Swagelok cells were assembled with the obtained electrodes as cathode, lithium foil (0.75 mm thickness, Alfa Aesar, Germany) as the anode, QMA glass fiber (Whatmann, UK) as separator, a mixture of 1,3-dioxolane (DOL) and dimethoxymethane (DME) with a volume ratio of 1:1 dissolving 1 M lithium bis (trifluoromethanesulfonyl)imide (LiTFSI) and 0.1 M LiNO₃ as electrolyte (180 μL). The cell assembly was performed in an argon-filled glovebox. The galvanostatic cycling at a current density of 83.5 mA/g (0.05 C, 1 C =1675 mAh/g) and rate capacity (0.05 C, 0.1 C, 0.2 C, 0.5 C, 1 C, 2 C) measurements were performed by a Neware BTS-4000 battery test system (Neware, China) in a potential window of 1–3 V. Cyclic voltammetry (CV) plots were recorded by VMP-multipotentiostat (Biologic Science Instruments, France) with a scan rate of 0.02 mV/s and the same voltage range of 1–3 V. All measurements were collected at a constant temperature of 25 ℃.

3. Results and discussion

3.1. X-ray diffraction

To evaluate the phase composition of the SiCN-BN ceramics, XRD was performed. Fig. 1 shows the XRD patterns of the pure BN (commercial powder, ~1 μm, 98%, Sigma-Aldrich, Burlington, MA, USA), SiCN (1000 ℃) ceramic matrix, and SiCN-BN composites. Pure BN powder exhibits a series of characteristic reflections of a layered hexagonal BN structure. Among them, three relatively strong peaks present clear at $2\theta = 12.2°$, $18.8°$, and $32.8°$, corresponding to the (002), (100), and (110) planes of standard crystalline BN (JCPDS no. 85–1068) [35, 40]. The pure SiCN material shows an amorphous characteristic. For SiCN-BN-950, SiCN-BN-1100, and SiCN-BN-1250, the reflection at $2\theta = 12.2°$ gradually forms with the increase of pyrolysis temperature from 950 °C to 1250 °C. It is worth noting that there is a small shift left compared with pure BN. This probably originates from its overlap with the broad reflex of the amorphous ceramic matrix. Besides, the sample synthesized at 1250 °C also exhibits the reflections of the (100) and

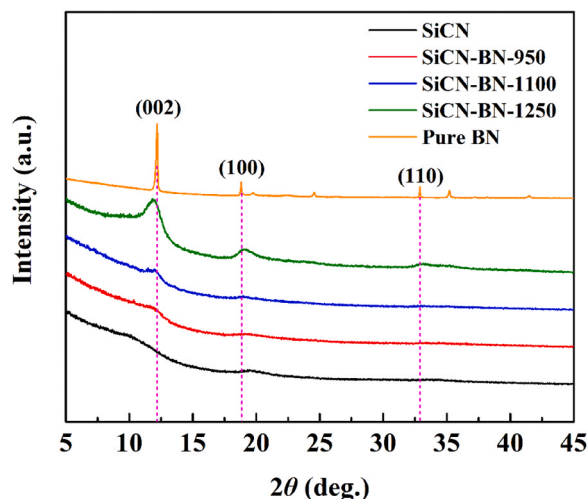(110) planes of BN at $2\theta = 18.8°$ and $32.8°$. It reveals that increasing pyrolysis temperature is beneficial for the formation of crystalline boron nitride. The peak shift compared with commercial BN could be attributed to

3.2. Fourier transform infrared spectroscopy

To further confirm the existence of the BN in the synthesized composites, Fourier transform infrared (FTIR) spectroscopy measurements were performed and the results are shown in Fig. 2. Sample SiCN presents clear Si–N and Si–C bonds between 400 cm⁻¹ to 1000 cm⁻¹ [41]. Compared with the sample SiCN, all SiCN-BN composites clearly exhibit two characteristic peaks of hexagonal BN at 780 cm⁻¹ and 1400 cm⁻¹ corresponding to the B–N bending and B–N stretching modes, respectively. This is consistent with previous studies [23]. The result confirms the presence of BN in the composites. Besides, with the increase of the annealing temperature, the intensity of BN peaks increases. Additionally, for all SiCN-BN samples, there are a typical vibration of Si–O at 480 cm⁻¹ [42] and a broad peak between 3000 cm⁻¹ and 3700 cm⁻¹ attributed to the water molecules or the O–H stretching vibrations, usually present in the BN composite systems [23,43].

3.3. Elemental analysis

The results of the elemental analysis are shown in Table 1a, b. The change in elemental composition during the annealing procedure is mainly due to the following potential reactions: [44–50]

$$H_3BO_3 \rightarrow HBO_2 + H_2O\,(T > 140°C) \tag{1}$$

$$4HBO_2 \rightarrow H_2B_4O_7 + H_2O\,(T > 180°C) \tag{2}$$

$$CO(NH_2)_2 + H_2O \rightarrow CO_2 + 2NH_3\,(200 \sim 400°C) \tag{3}$$

$$C + H_2O \rightarrow CO + H_2\,(T > 200°C) \tag{4}$$

$$C + CO_2 \rightarrow 2CO\,(450 \sim 1000°C) \tag{5}$$

$$H_2B_4O_7 \rightarrow 2B_2O_3 + H_2O\,(T > 530°C) \tag{6}$$

$$B_2O_3 + 2NH_3 \rightarrow 2BN + 3H_2O\,(T = 900°C) \tag{7}$$

$$B_2O_3 + CO(NH_2)_2 \rightarrow 2BN + CO_2 + 2H_2O\,(T > 1000°C) \tag{8}$$

Compared with the pure SiCN, the C content of sample SiCN-BN-950 decreases from 67.5 wt% to 29.5 wt% due to the carbothermal

Fig. 1. XRD patterns of SiCN-BN samples annealed at three different temperatures compared to SiCN (1000 ℃) and pure BN diffractograms.

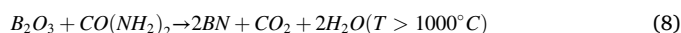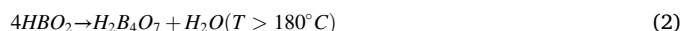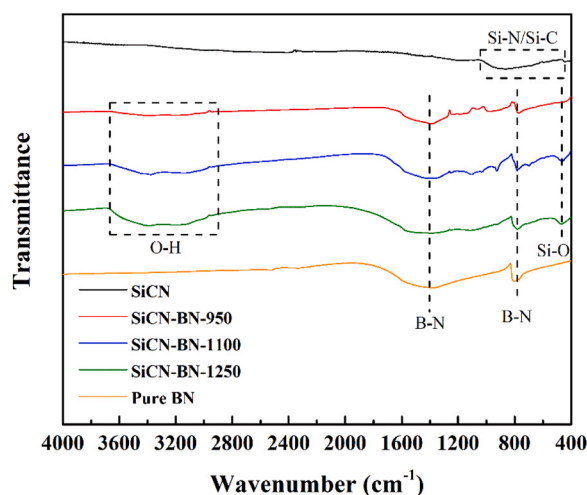**Fig. 2.** FTIR spectra of SiCN-BN samples annealed at three different temperatures compared to SiCN (1000 ℃) and pure BN.

Table 1a

Results of elemental analysis. Possible trace amount of hydrogen present in the SiCN ceramic has been considered as negligible.

Sample	SiCN	SiCN-BN-950	SiCN-BN-1100	SiCN-BN-1250
Si wt%	20.5	15.3	19.2	22.9
C wt%	67.5	29.5	6.8	0.5
N wt%	4.8	17.7	18.9	22.3
B wt%	-	14.4	23.1	25.7
O wt%	7.2	23.1	32.0	28.6

Table 1b

Result of element analysis after normalization based on Si.

Sample	SiCN	SiCN-BN-950	SiCN-BN-1100	SiCN-BN-1250
Si	1	1	1	1
C	3.29	1.93	0.35	0.02
N	0.23	1.16	0.98	0.97
B	-	0.94	1.20	1.12
O	0.35	1.51	1.67	1.25

reductions (4) and (5) enabled by the products (CO_2 and H_2O) of the reactions (1−3). Besides, the content of B and N increase to 14.4 wt% and 17.7 wt% from 0 wt% and 4.76 wt%, respectively. After normalization on the Si wt%, based on the assumption that silicon does not lose during annealing, the increase or decrease in the content of various elements is clearer. The increased content of oxygen might be attributed to the replacement of nitrogen with oxygen (originating from water fromed in reaction (1,2,6,7,8)) in the SiCN network. Furthermore, the oxygen partly originates from the annealing environment of SiCN-BN composites, which is the alumina furnace. In this way the silicon-bonded nitrogen and also carbon in SiCN matrix are partly replaced with oxygen. Subsequent XPS analysis also confirmed this. When the samples are stored in the air, this Si–O bonds might attract humidity, leading to the O–H formation. This is supported by the increased O–H bond detected for SiCN-BN composites in FTIR measurement. Increasing the annealing temperature to 1100 ℃ and 1250 ℃ causes little changes in the contents of B and N, but the carbon content of the composites further decreased to 6.8 wt% at 1100 °C and even 0.5 wt% at 1250 °C. We rationalize this in a view of the progress of the reactions(4), (5) and (8). At temperatures exceeding 1000 °C, the reaction (8) continues. More CO_2 and H_2O are generated, what further intensifies the carbothermal reduction reaction leading to a further consumption of free carbon in the composites.

3.4. X-ray photoelectron spectroscopy

The covalent bonding in SiCN and SiCN-BN-950 was further investigated by X-ray photoelectron spectroscopy (XPS) and the corresponding high-resolution spectra are plotted in Fig. 3a-j (The element survey spectra is plotted in Supplementary Information). For both SiCN and SiCN-BN-950, the C 1 s spectra can be fitted by six components, corresponding to the expected C–Si, C≡C, C–C, C≡N, C–N, C–O features [51,52]. Among them, the C–C/C≡C species of the carbon phase is the main component. After annealing, the content of C≡N and C–N increases compared to the other species, most significantly the C≡N component. Combined with the decrease in the relative content of C≡C, it can be inferred, that N replaced parts of sp^2 C in the ceramic matrix. The introduced N might be derived directly from urea, or it might be derived from the annealing product BN, or other N intermediates. We deem the increase in C–N/C≡N content to be beneficial for electrochemical performance by inhibiting the shuttling of polysulfide compounds due to the increase of N in C network. In B 1 s spectrum, SiCN-BN-950 shows two peaks at 191.3 eV and 193 eV, however, SiCN showing no peak at all. The peak at 191.3 eV derives from the BN component [23,36]. It indicates that the BN is present on the surface of the ceramic matrix after the annealing. Another peak originates from the

presence of B_2O_3 which usually remains in BN system [23,36,53].

Besides, the N 1 s spectrum of SiCN can be fitted into three typical components corresponding to the N–Si at 397.7 eV, N–C at 399.5 eV and N≡C at 400.8 eV [51,53,54]. The N 1 s spectrum of SiCN-BN-950 exhibits one more peak of N–B at 399.6 eV. The decrease in the relative content of N–Si and the increase in the relative content of C–N/C≡N are consistent with the C 1 s spectrum fitting results. Both B 1 s and N 1 s XPS spectra confirm the existence of BN in SiCN ceramic matrix. In the O 1 s spectrum, compared with SiCN, the relative content of O–Si in SiCN-BN-950 increases based on O–C content [51,55]. Besides, there is an extra peak for SiCN-BN-950 at 535 eV which can be attributed to O–B derived from B_2O_3 as expected [23,36,53,56]. For the Si 2p spectra, both samples show Si–C, Si–N, Si–O at 101.9/101.3 eV, 101.3/102.6 eV, 104.1/103.5 eV, respectively [51,52,54,55]. The decrease of relative content of Si–C, the increase of relative content of Si–N and Si–O, they all indicate that the C in the ceramic matrix has been replaced by N and O during the annealing. These findings are consistent with the results of elemental analysis.

3.5. N_2 adsorption-desorption isotherms

N_2 adsorption-desorption isotherms are shown in Fig. 4a. Linear BET (Brunauer–Emmett–Teller) plots were obtained from N_2 adsorption isotherm and used to determine the specific surface area (SSA) and pore size distribution of all prepared samples. The isotherms of all measured samples cannot be distinguished into one typical isotherm type. The isotherms are consistent with the beginning stage of type II and type IV. As the relative pressure continues to increase at a relative high-pressure region ($p/p_0 > 0.4$), all isotherms exhibit a slim reversible hysteresis loop, indicating a capillary condensation of nitrogen in mesoporous structure (type IV) [37,57,58].

For SiCN-BN-1250 the hysteresis is visible only at high relative pressures. However, when the relative pressure approaches to 1, the adsorption curves tending toward infinity reveal the presence of macropores in samples SiCN, SiCN-BN-950 and SiCN-BN-1100 (type II). It indicates that the materials possess a hybrid structure consisting of mesopores and macropores [59–61]. The pore size distribution shown in Fig. 4b further reveals that all measured samples contain pores in a size range of 2 ~ 180 nm. All samples reveal a mesoporous character, SiCN-BN-1100 reveals a significant amount of small mesopores (3 ~ 10 nm) which are formed due to the carbothermal reduction (compare the results of the elemental analysis). Table 2 presents detailed SSA, total pore volume (V_t), average pore diameter (APD) as well as the isotherm type of all investigated samples. When the annealing procedure starts and temperature increases from 950 to 1250 ℃, SSA and V_t of all samples show an overall decreasing trend. The pore volume decreasing in the raw from SiCN to SiCN-BN-1250 signifies that BN covering the surface of the ceramic partly block the pores present. The low pore volume of 0,06 cm^3/g, a low surface area of 8.5 m^2/g in line with the shape of the isotherm (very short multilayer adsorption part) of the SiCN-BN-1250 underline that the material presents to a high extent a nonporous character with only some big mesoporous present. This might be correlated with the crystallization of BN (compare Fig. 1) at this temperature leading to pore closing.

3.6. Scanning electron microscopy

The morphology of the SiCN/S ceramic and SiCN-BN/S composites as well as their elemental distribution were observed by SEM and energy dispersive X-ray spectroscopy (EDS). The images shown in Fig. 5 reveal that in both, SiCN/S ceramic and SiCN-BN/S composites, particles exhibited irregular rough surfaces. Through EDS mapping analysis, the presence of uniformly distributed sulfur, within the given resolution limit, was confirmed in all SiCN-BN/S composites. It proves again that the applied method is suitable to obtain a uniform distribution of sulfur in the ceramic matrix.
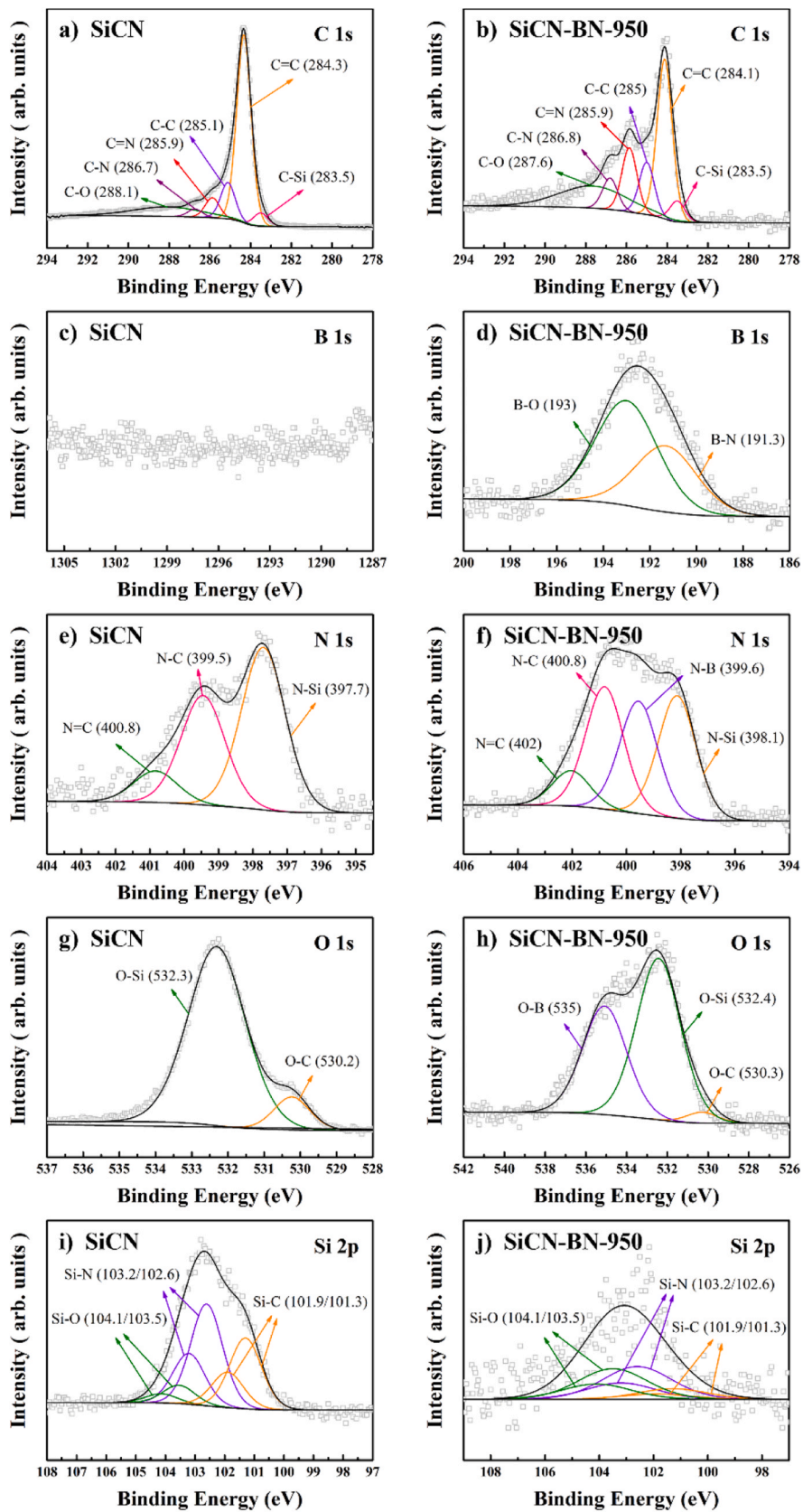
Fig. 3. XPS spectra of SiCN and SiCN-BN-950: (a,b) C 1 s, (c,d) B 1 s, (e,f) N 1 s, (g,h) O 1 s, (i,j) Si 2p.
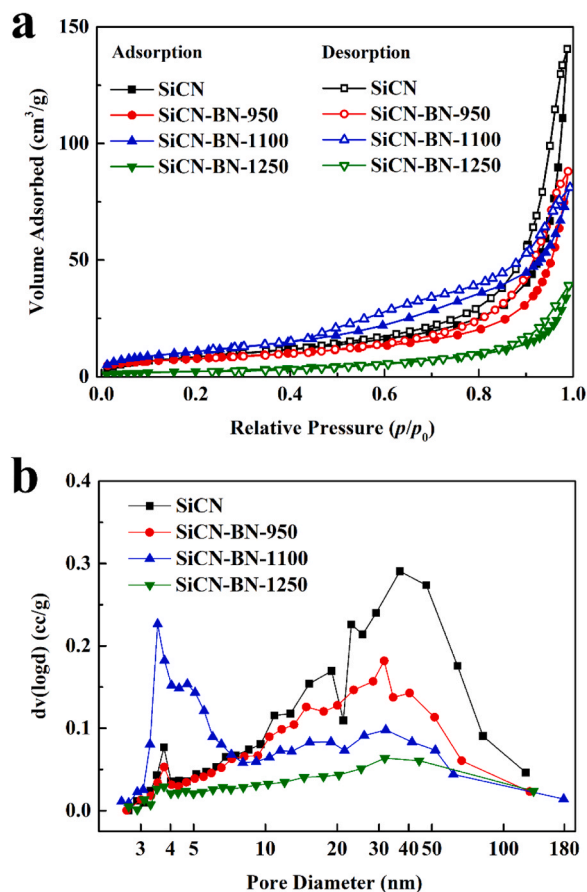
Fig. 4. Nitrogen adsorption-desorption isotherms (a) and pore size distribution (b) of SiCN ceramic and SiCN-BN composites.
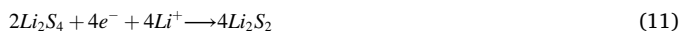
Table 2
Summary of the results obtained from BET analysis.

Sample	SiCN	SiCN-BN-950	SiCN-BN-1100	SiCN-BN-1250
SSA (m^2/g)	32.3	27.6	40.7	8.5
V_t (cm^3/g)	0.22	0.14	0.12	0.06
APD (nm)	26.9	19.7	12.0	26.5
Isotherm type	II + IV	II + IV	II + IV	II + IV

3.7. Galvanostatic discharge/charge measurements

The initial lithiation/delithiation processes recorded for all investigated samples are plotted in Fig. 6. Both SiCN/S ceramics and SiCN-BN/S composites exhibit distinct discharge (lithiation) voltage plateaus, prominently situated at approximately 2.4 V and 2.1 V. Additionally, a single charge (delithiation) voltage plateau is evident around 2.3 V. These voltage plateaus are unequivocally attributed to the electrochemical sulfur reactions. The first voltage plateau at 2.4 V represents the electrochemical reduction reaction of sulfur to form soluble lithium polysulfides Li_2S_x ($4 < x < 8$) (reactions (9) and (10)). The second voltage plateau at 2.1 V is attributed to the further reduction conversion of the polysulfides Li_2S_x to solid Li_2S_2 and Li_2S [62,63] (reactions (11) and (12)). The redox reaction equations can be expressed as follows [38]:

$$S_8 + 2e^- + 2Li^+ \longrightarrow Li_2S_8 \tag{9}$$

$$Li_2S_8 + 2e^- + 2Li^+ \longrightarrow 2Li_2S_4 \tag{10}$$

$$2Li_2S_4 + 4e^- + 4Li^+ \longrightarrow 4Li_2S_2 \tag{11}$$

$$4Li_2S_2 + 8e^- + 8Li^+ \longrightarrow 8Li_2S \tag{12}$$

During the delithiation process, the negative sulfur in solid Li_2S_2 and Li_2S is oxidized to elemental sulfur and the lithium ions return to the counter electrode through the electrolyte. A cycle is completed. Among all samples, no matter initial lithiation or initial delithiation process, the SiCN shows a relative low polarization, which is attributed to its highest free carbon content supported by element analysis.

The initial discharge capacity as well as a corresponding columbic efficiency of the sample SiCN/S and SiCN-BN/S are shown in Table 3. Despite the initial discharge capacity of the sample SiCN-BN-950/S being slightly lower compared to the sample SiCN/S, its initial coulombic efficiency is close to 100%, indicating a high reversibility of the sulfur cathode. Regarding the sample SiCN-BN-1100/S, the obviously increased initial discharge and charge capacity are attributed to its significantly increased number of small mesopores and degree of graphitization of carbon according to the result of BET and Raman (see Supplementary Information), respectively. The initial coulombic efficiency of sample SiCN-BN-1100/S changed little representing the closer reversibility with that of sample SiCN-BN-950/S during the first cycle. As for the sample SiCN-BN-1250/S, in turn reduced mesopores and continued oxidation of the porous carbon according to the results of BET and elemental analysis contribute to the composite exhibiting a compounded adverse effect, resulting in deteriorative initial discharge capacity and coulombic efficiency.

3.8. Extended cycling performance

Fig. 7a-c show the extended cycling discharge/charge specific capacity, and coulombic efficiency of both SiCN/S and SiCN-BN/S (see also the values listed in Table 3). Despite that sample SiCN-BN-950/S shows the lowest initial discharge capacity of 716 mAh/g, it surpasses those of samples SiCN-BN-1100/S and SiCN-BN-1250/S from the second cycle and even surpasses that of SiCN/S starting from the 4th cycle. The sample SiCN-BN-950/S retained the highest discharge capacity in all subsequent cycles, with more than 600 mAh/g over the first 23 cycles. After 60 cycles, its reversible capacity was 445 mAh/g, whereas SiCN/S had only 319 mAh/g. The capacity retentions after 60 cycles of SiCN-BN-950/S and SiCN/S were 62% and 41%, respectively. This reveals that the introduction of BN into the ceramic matrix significantly enhances the cycling stability of SiCN-BN-950/S. This is mainly attributed to the synergy between BN and the porous free carbon for the polysulfides capturing. Therefore, the "shuttle effect" was suppressed during electrochemical reactions. As concerns the samples SiCN-BN-1100/S and SiCN-BN-1250/S, their extended discharge capacities are very close to each other but significantly lower than SiCN/S. Besides, they also present relatively lower capacity retentions after 60 cycles of only 24% and 31%, respectively. This is also expected because an increased annealing temperature leads to significantly decreased porous free carbon resulting in an impaired synergy with BN insufficient for surpassing the "shuttle effect". After 15 cycles, the charge capacity of the samples SiCN-BN-1100/S and SiCN-BN-1250/S fluctuates due to the increased "shuttle effect" resulting from the diminished performance gain from porous carbon [6,21,37,63]. The coulombic efficiencies of samples SiCN-BN-950/S and SiCN/S exhibited remarkable stability over 90% in 60 cycles, whereas the SiCN-BN-1100/S and SiCN-BN-1250/S presented unstable fluctuations with efficiencies between 80% and 90% originating from the increased "shuttle effect".

The rate capabilities of all samples are shown in Fig. 7d. Although the sample SiCN-BN-950/S was unremarkable at the lowest cycling currents of 0.05 C, its discharge capacity surpassed all other samples from the 0.1 C cycle and remained the best in all subsequent cycles. This signifies that the synergy of BN and porous free carbon also resulted in a superior rate performance of the composites. Interestingly, starting from 0.2 C, the sample SiCN/S presented the lowest rate capacity performance, which indicated it underperforms under high current. Therefore, it
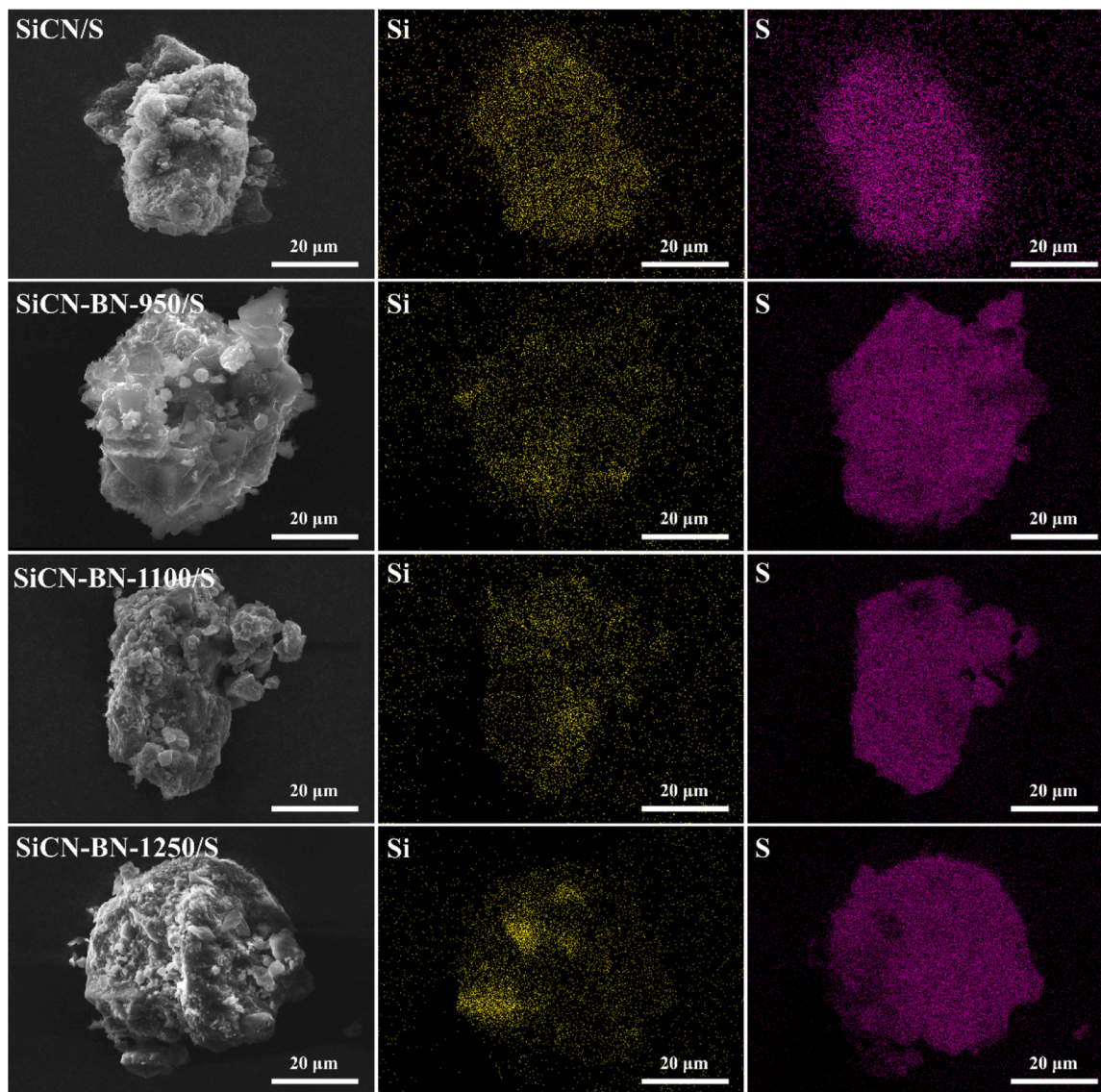
Fig. 5. SEM images and elemental mapping of SiCN/S and all SiCN-BN/S composites (yellow represents Si and purple represents S).
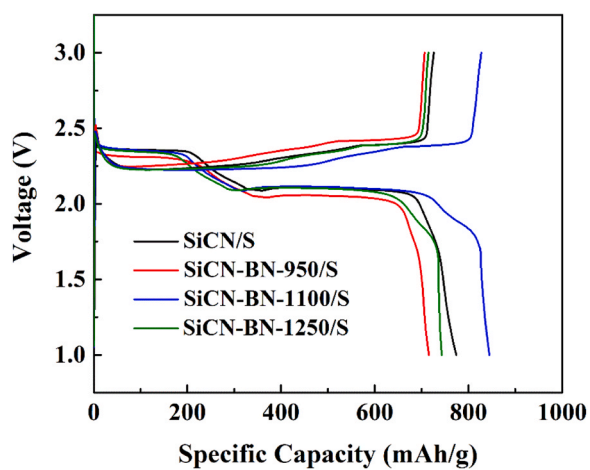

Fig. 6. Lithiation curves and delithiation curves of SiCN/S and all SiCN-BN/S samples.

Table 3
Electrochemical parameters of the sulfurized SiCN samples.

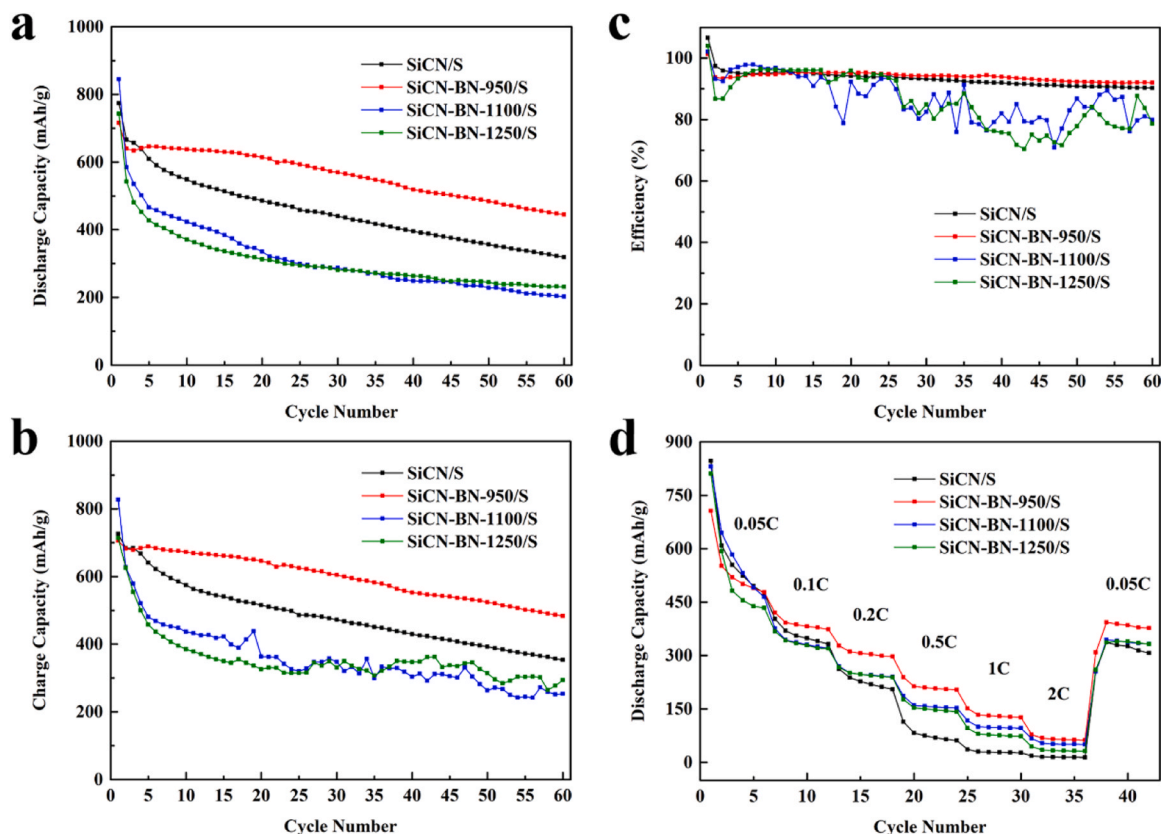| Sample	Initial discharge Capacity (mAh/g)	Initial Coulombic Efficiency (%)	Reversible Capacity after 60 Cycle (mAh/g)	Capacity Retention (%)
SiCN/S	774	107	319	41
SiCN-BN-950/S	716	101	445	62
SiCN-BN-1100/S	845	102	202	24
SiCN-BN-1250/S	743	104	231	31

Fig. 7. Cycling performance of the SiCN/S and SiCN-BN/S. Discharge capacity (a), charge capacity (b), efficiency (c), and rate capacity (d).

reveals that the existence of BN indeed increased rate cycling performance of the samples.

3.9. Cyclic Voltammetry

Cyclic voltammetry measurements show two typical cathodic peaks and one anodic peak of sulfur (refer to Fig. 8). They signify two sequential reduction processes: the transformation of S_8 molecules into soluble polysulfides Li_2S_x ($4 < x < 8$), followed by their conversion into solid Li_2S_2 and Li_2S. Additionally, the oxidation process of lithium sulfide to elemental sulfur is evident [37], a pattern being consistent with the previously discussed galvanostatic discharge/charge profiles. During the initial cycle, SiCN-BN-950/S exhibits higher potential positions of 2.06 V and 2.33 V (2.05 V and 2.33 V for SiCN/S and SiCN-BN-1100/S, and 2.05 V and 2.32 V for SiCN-BN-1250/S, respectively) as well as the highest current density of the cathodic peaks, revealing the strongest reduction reaction of sulfur and minimal cathodic polarization compared to other samples. Conversely, the anodic peak of SiCN-BN-950/S is shifted to a higher potential of 2.42 V compared to SiCN/S (2.38 V), while its current density remained higher. This suggests a slight increase in the electrode polarization possibly due to a decreased carbon content and the incorporation of insulating BN. However, the intensity of oxidation reaction notably increased due to the BN-polysulfides interaction. With an increase in annealing temperature to 1100 °C, the cathodic peak (2.05 V) is shifted leftward, the anodic peak (2.44 V) is shifted rightward, and the peak intensity decreased. All these indicate a higher electrode polarization due to the greatly reduced carbon phase (referring to the elemental analysis). For SiCN-BN-1250/S, its cathodic and anodic peaks do not further significantly deviate from the equilibrium electrode potential compared to the sample SiCN-BN-1100/S, yet current density further decreased, indicating weaker electrochemical reactions. During the third cycle (see Fig. 8b), the sample SiCN-BN-950/S consistently demonstrates the

lowest anodic peak potential (2.47 V) and the strongest current density in both reduction and oxidation processes, suggesting superior stability. In contrast, SiCN/S exhibits pronounced rightward shifting (2.55 V, even more pronounced for the samples SiCN-BN-1100/S and SiCN-BN-1250/S), indicating enhanced polarization and compromised stability over the cycles. As for the samples SiCN-BN-1100/S and SiCN-BN-1250/S, not only the rightward shifting of the anodic peak but also the decreased current intensity, they both reveal further weakened electrochemical reactions compared to the sample SiCN-BN-950/S. Notably, the incorporation of BN at 950 °C improves polysulfides capture and overall electrochemical performance. However, elevating annealing temperature to 1100 °C or even 1250 °C lead to carbon consumption (verified by elemental analysis), causing weakening in electrochemical performance.

4. Conclusions

In this study, a porous SiCN-BN composite has been successfully synthesized through a two-step process involving polysilazane pyrolysis and subsequent annealing with urea and boric acid. This innovative approach initiates the in-situ growth of BN sheets within the porous carbon-rich SiCN ceramic matrix. The annealing temperature was adjusted in order to obtain SiCN-BN composites. Remarkably, the SiCN-BN-950/S composite exhibits enhanced electrochemical performance in comparison to unmodified porous SiCN. It delivers a consistent stable reversible capacity of 445 mAh/g, retaining 62% of its capacity after 60 cycles with a high active material areal density of 3.5–3.8 mg/cm² and 66 wt% sulfur loading. Furthermore, all prepared SiCN-BN/S composites displayed an improved rate capacity at elevated current densities (from 0.2 C) compared to the pristine SiCN/S counterpart. This observation highlights the microstructural stability provided by BN during cycling under high currents. We rationalize the enhanced electrochemical performance as follows: 1) the BN-modified SiCN ceramic
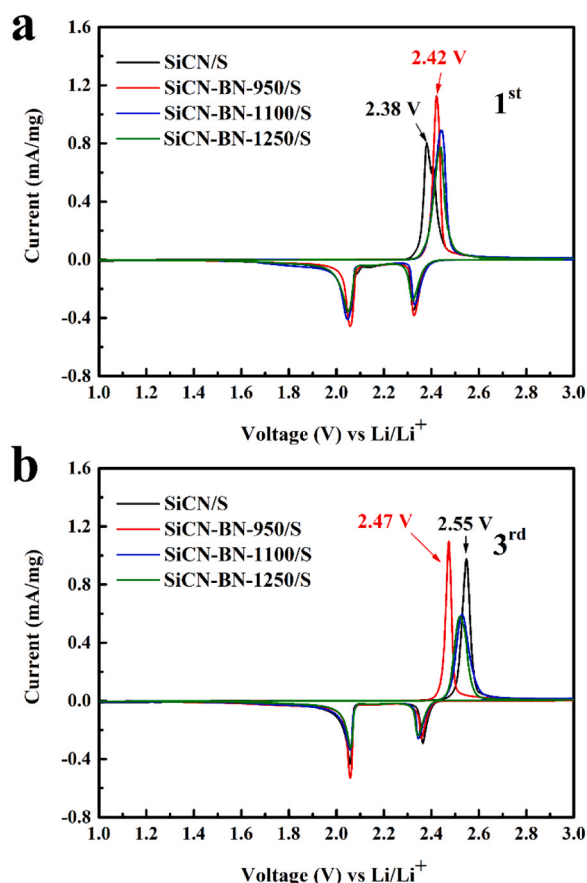
Fig. 8. Cyclic voltammograms of SiCN/S and SiCN-BN/S in the first (a) and the third (b) cycle.

matrix offers remarkable structural and chemical stability, 2) the porous SiCN ceramic matrix provides an efficient network for trapping polysulfides, 3) the porous BN nanosheets assist the SiCN in stabilizing sulfur through polar B–N bonds, facilitating polysulfides trapping (polar physisorption), 4) the composite's porosity accommodates high sulfur loading and 5) a synergistic effect between BN and carbon-rich SiCN ceramic matrix contributes to an excellent electrochemical performance (SiCN-BN/S). Furthermore, this work introduces a straightforward route for sulfur cathodes in LSB, emphasizing its practical significance.

CRediT authorship contribution statement

Zhaoju Yu: Writing – review & editing, Supervision. **Fangmu Qu:** Writing – review & editing, Writing – original draft, Validation, Software, Resources, Methodology, Investigation, Funding acquisition, Formal analysis, Data curation, Conceptualization. **Ruijuan Yan:** Formal analysis, Data curation. **Jan P. Hofmann:** Resources, Writing – review & editing. **Marc Widenmeyer:** Writing – review & editing, Formal analysis, Data curation. **Magdalena Graczyk-Zajac:** Writing – review & editing, Supervision, Resources, Project administration, Methodology, Investigation, Funding acquisition, Formal analysis, Conceptualization. **Ralf Riedel:** Writing – review & editing, Supervision, Resources, Project administration, Funding acquisition, Conceptualization. **Chuanmu Tian:** Data curation, Funding acquisition, Resources, Software, Writing – review & editing. **Alexander Kempf:** Writing – review & editing, Funding acquisition, Data curation. **Honghong Tian:** Investigation, Formal analysis, Data curation. **Anke Weidenkaff:** Writing – review & editing, Resources. **Dario M. De Carolis:** Writing – review & editing, Investigation.

Declaration of Competing Interest

All authors disclosed no relevant relationships.

Data availability

Data will be made available on request.

Appendix A. Supporting information

Supplementary data associated with this article can be found in the online version at doi:10.1016/j.jallcom.2024.174021.

References

[1] M. Li, J. Lu, Z. Chen, K. Amine, 30 years of lithium-ion batteries, Adv. Mater. 30 (2018) 1800561.
[2] J.B. Goodenough, Y. Kim, Challenges for rechargeable Li batteries, Chem. Mater. 22 (2010) 587–603.
[3] T.L. Kulova, V.N. Fateev, E.A. Seregina, A.S. Grigoriev, A brief review of post-lithium-ion batteries, Int. J. Electrochem. Sci. 15 (2020) 7242–7259.
[4] A. Manthiram, Y. Fu, Y.-S. Su, Challenges and prospects of lithium-sulfur batteries, Acc. Chem. Res. 46 (2013) 1125–1134.
[5] Y.-X. Yin, S. Xin, Y.-G. Guo, L.-J. Wan, Lithium-sulfur batteries: electrochemistry, materials, and prospects, Angew. Chem. -Int. Ed. 52 (2013) 13186–13200.
[6] A. Manthiram, Y. Fu, S.-H. Chung, C. Zu, Y.-S. Su, Rechargeable lithium-sulfur batteries, Chem. Rev. 114 (2014) 11751–11787.
[7] Z. Cheng, et al., Bilayer functional interlayer coupling defect and Li-ion channel for high-performance Li-S batteries, Electrochim. Acta 436 (2022) 141377.
[8] H. Li, et al., Cooperative catalysis of polysulfides in lithium-sulfur batteries through adsorption competition by tuning cationic geometric configuration of dual-active sites in spinel oxides, Angew. Chem. Int. Ed. 62 (2023) e202216286.
[9] Z.W. Seh, Y. Sun, Q. Zhang, Y. Cui, Designing high-energy lithium-sulfur batteries, Chem. Soc. Rev. 45 (2016) 5605–5634.
[10] R. Fang, et al., More reliable lithium-sulfur batteries: status, solutions and prospects, Adv. Mater. 29 (2017) 1606823.
[11] H. Asano, et al., Enhancing the reversibility of Li deposition/dissolution in sulfur batteries using high-concentration electrolytes to develop anode-less batteries with lithium sulfide cathode, J. Power Sources 554 (2023) 232323.
[12] S. Kim, Y.A. Chart, S. Narayanan, M. Pasta, Thin solid electrolyte separators for solid-state lithium-sulfur batteries, Nano Lett. 22 (2022) 10176–10183.
[13] R. Yan, et al., Origin and acceleration of Insoluble Li2S2–Li2S reduction catalysis in ferromagnetic atoms-based lithium-sulfur battery cathodes, Angew. Chem. Int. Ed. 62 (2023) e202215414.
[14] Y.-J. Yen, et al., Selective chemisorption of polysulfides by porous molecular crystal: cathode host materials for lean-electrolyte lithium-sulfur cells with high electrochemical stability, J. Power Sources 565 (2023) 232891.
[15] Z. Sun, et al., Conductive porous vanadium nitride/graphene composite as chemical anchor of polysulfides for lithium-sulfur batteries, Nat. Commun. 8 (2017) 14627.
[16] Z. Cui, C. Zu, W. Zhou, A. Manthiram, J.B. Goodenough, Mesoporous titanium nitride-enabled highly stable lithium-sulfur batteries, Adv. Mater. 28 (2016) 6926–6931.
[17] J. Yu, et al., Design of filamentous conductive catalyst as separator coating for high-efficiency lithium-sulfur batteries, Chem. Eng. J. 479 (2024) 147870.
[18] Y.-C. Lin, Y.-H. Wu, J.-M. Ting, S.-H. Chung, Stable lithium–sulfur cell separator with a high-entropy metal oxide modification, Energy Fuels 37 (2023) 15162–15169.
[19] Y. Chen, et al., Advances in lithium–sulfur batteries: from academic research to commercial viability, Adv. Mater. 33 (2021) 2003666.
[20] Q. Pang, X. Liang, C.Y. Kwok, L.F. Nazar, Advances in lithium–sulfur batteries based on multifunctional cathodes and electrolytes, Nat. Energy 1 (2016) 16132.
[21] R. Fang, et al., The regulating role of carbon nanotubes and graphene in lithium-ion and lithium–sulfur batteries, Adv. Mater. 31 (2019) 1800863.
[22] Y. Qu, et al., Three-electrode in mono-electrolyte for integrated photo-assisted lithium sulfur battery, J. Power Sources 555 (2023) 232374.
[23] B. He, et al., Paragenesis BN/CNTs hybrid as a monoclinic sulfur host for high rate and ultra-long life lithium–sulfur battery, J. Mater. Chem. A 6 (2018) 24194–24200.

[24] H. Kang, M.J. Park, Thirty-minute synthesis of hierarchically ordered sulfur particles enables high-energy, flexible lithium-sulfur batteries, Nano Energy 89 (2021) 106459.

[25] B. Zhao, Z. Ren, Z. Li, G. Tan, J. Xie, Encapsulate lithium sulfide cathodes with carbon-doped MoS2 for fast kinetics in lithium-sulfur batteries, a theoretical study, Acta Mater. 242 (2023) 118441.

[26] A. Kızılaslan, A. Waleed Majeed Al-Ogaili, H. Akbulut, NiCo5S8 structure with unique morphology as a cathode active material for all-solid-state lithium-sulfur batteries, Chem. Eng. J. 450 (2022) 138050.

[27] S.S. Zhang, D.T. Tran, Pyrite FeS2 as an efficient adsorbent of lithium polysulphide for improved lithium-sulphur batteries, J. Mater. Chem. A 4 (2016) 4371–4374.

[28] Z. Wei Seh, et al., Sulphur–TiO2 yolk–shell nanoarchitecture with internal void space for long-cycle lithium–sulphur batteries, Nat. Commun. 4 (2013) 1331.

[29] X. Liang, L.F. Nazar, In situ reactive assembly of scalable core–shell sulfur–MnO2 composite cathodes, ACS Nano 10 (2016) 4192–4198.

[30] T. Zhou, et al., Twinborn TiO2-TiN heterostructures enabling smooth trapping-diffusion-conversion of polysulfides towards ultralong life lithium-sulfur batteries, Energy Environ. Sci. 10 (2017) 1694–1703.

[31] D.R. Deng, et al., Enhanced adsorptions to polysulfides on graphene-supported BN nanosheets with excellent Li–S battery performance in a wide temperature range, ACS Nano 12 (2018) 11120–11129.

[32] K. Uosaki, et al., Boron nitride nanosheet on gold as an electrocatalyst for oxygen reduction reaction: theoretical suggestion and experimental proof, J. Am. Chem. Soc. 136 (2014) 6542–6545.

[33] D. Golberg, et al., Boron nitride nanotubes and nanosheets, ACS Nano 4 (2010) 2979–2993.

[34] W. Lei, D. Portehault, D. Liu, S. Qin, Y. Chen, Porous boron nitride nanosheets for effective water cleaning, Nat. Commun. 4 (2013) 1777.

[35] D.R. Deng, et al., Enhanced adsorptions to polysulfides on graphene-supported BN nanosheets with excellent Li-S battery performance in a wide temperature range, ACS Nano 12 (2018) 11120–11129.

[36] C. Sun, et al., Highly catalytic boron nitride nanofiber in situ grown on pretreated ketjenblack as a cathode for enhanced performance of lithium–sulfur batteries, ACS Appl. Energy Mater. 3 (2020) 10841–10853.

[37] F. Qu, et al., Effect of morphology of C-rich silicon carbonitride ceramic on electrochemical properties of sulfur cathode for Li-S battery, Electrochim. Acta 384 (2021) 138265.

[38] F. Qu, et al., Electrochemical performance of carbon-rich silicon carbonitride ceramic as support for sulfur cathode in lithium sulfur battery, Nanomaterials 12 (2022) 1283.

[39] L.M. Reinold, M. Graczyk-Zajac, Y. Gao, G. Mera, R. Riedel, Carbon-rich SiCN ceramics as high capacity/high stability anode material for lithium-ion batteries, J. Power Sources 236 (2013) 224–229.

[40] C. Huang, et al., Stable colloidal boron nitride nanosheet dispersion and its potential application in catalysis, J. Mater. Chem. A 1 (2013) 12192–12197.

[41] Y. Feng, et al., Preparation and capacity-fading investigation of polymer-derived silicon carbonitride anode for lithium-ion battery, Acs Omega 2 (2017) 8075–8085.

[42] A. Zambotti, et al., Synthesis and thermal evolution of polysilazane-derived SiCN (O) aerogels with variable C content stable at 1600 °C, Ceram. Int. 47 (2021) 8035–8043.

[43] J. Xiong, et al., Boron nitride mesoporous nanowires with doped oxygen atoms for the remarkable adsorption desulfurization performance from fuels, ACS Sustain. Chem. Eng. 4 (2016) 4457–4464.

[44] G. Kaur, S. Kainth, R. Kumar, P. Sharma, O.P. Pandey, Reaction kinetics during non-isothermal solid-state synthesis of boron trioxide via boric acid dehydration, React. Kinet., Mech. Catal. 134 (2021) 347–359.

[45] S. Aghili, M. Panjepour, M. Meratian, Kinetic analysis of formation of boron trioxide from thermal decomposition of boric acid under non-isothermal conditions, J. Therm. Anal. Calorim. 131 (2018) 2443–2455.

[46] M. Koebel, E.O. Strutz, Thermal and hydrolytic decomposition of urea for automotive selective catalytic reduction systems: thermochemical and practical aspects, Ind. Eng. Chem. Res. 42 (2003) 2093–2100.

[47] H. Hiller, R. Reimert, H.-M. Stönner, in Ullmann's Encyclopedia of Industrial Chemistry, Wiley-VCH, Weinheim, 2011.

[48] D.R. Lide. in CRC Handbook of Chemistry and Physics, ninetieth ed., Taylor & Francis, 2009.

[49] S. Balcı, N.A. Sezgi, E. Eren, Boron oxide production kinetics using boric acid as raw material, Ind. Eng. Chem. Res. 51 (2012) 11091–11096.

[50] S. Rudolph, Boron nitride, Am. Ceram. Soc. Bull. 73 (1994) 89–90.

[51] K. Yamamoto, Y. Koga, S. Fujiwara, XPS studies of amorphous SiCN thin films prepared by nitrogen ion-assisted pulsed-laser deposition of SiC target, Diam. Relat. Mater. 10 (2001) 1921–1926.

[52] S.L. Ma, B. Xu, K.W. Xu, X.L. Wu, P.K. Chu, Annealing behavior and hardness enhancement of amorphous SiCN thin films, J. Vac. Sci. Technol. A 25 (2007) 1407–1410.

[53] D.J. Joyner, D.M. Hercules, Chemical bonding and electronic structure of B2O3, H3BO3, and BN: an ESCA, Auger, SIMS, and SXS study, J. Chem. Phys. 72 (2008) 1095–1108.

[54] N.B. Laidani, V.L. Nguyen, G.D. Sorarù, N-doped polymer-derived Si(N)OC: the role of the N-containing precursor, J. Mater. Res. 30 (2015) 770–781.

[55] A. Vashisth, et al., Mechanical size effects of amorphous polymer-derived ceramics at the nanoscale: experiments and ReaxFF simulations, Nanoscale 11 (2019) 7447–7456.

[56] D. Schild, S. Ulrich, J. Ye, M. Stüber, XPS investigations of thick, oxygen-containing cubic boron nitride coatings, Solid State Sci. 12 (2010) 1903–1906.

[57] J.T. Lee, et al., Sulfur-infiltrated micro- and mesoporous silicon carbide-derived carbon cathode for high-performance lithium sulfur batteries, Adv. Mater. 25 (2013) 4573–4579.

[58] N. Kang, et al., Cathode porosity is a missing key parameter to optimize lithium-sulfur battery energy density, Nat. Commun. 10 (2019) 4597.

[59] S. Fu *et al.*, Accurate characterization of full pore size distribution of tight sandstones by low-temperature nitrogen gas adsorption and high-pressure mercury intrusion combination method. 9, 80-100 (2021).

[60] M. Melzi d'Eril, et al., Effect of ultra-fast pyrolysis on polymer-derived SiOC aerogels and their application as anodes for Na-ion batteries, Open Ceram. 14 (2023) 100354.

[61] M. Thommes *et al.*, Physisorption of gases, with special reference to the evaluation of surface area and pore size distribution (IUPAC Technical Report). 87, 1051-1069 (2015).

[62] K. Amine, R. Kanno, Y. Tzeng, Rechargeable lithium batteries and beyond: progress, challenges, and future directions, MRS Bull. 39 (2014) 395–401.

[63] U. Gulzar, et al., Nitrogen-doped single-walled carbon nanohorns as a cost-effective carbon host toward high-performance lithium–sulfur batteries, ACS Appl. Mater. Interfaces 10 (2018) 5551–5559.